Manifestations and Effects of Dipolar Coupling in Erbium-Based Molecular Magnets

Orlova, Angelica Philippovna

2024

UNIVERSITY OF CALIFORNIA SAN DIEGO

Manifestations and Effects of Dipolar Coupling in Erbium-Based Molecular Magnets

A Dissertation submitted in partial satisfaction of the requirements
for the degree Doctor of Philosophy

in

Chemistry

by

Angelica P. Orlova

Committee in charge:

Professor Jeffrey Dennis Rinehart, Chair
Professor Julio Guerrero Barreiro
Professor Joshua S. Figueroa
Professor Alina M. Schimpf
Professor Mark Young

2024

The Dissertation of Angelica P. Orlova is approved, and it is acceptable
in quality and form for publication on microfilm and electronically.

University of California San Diego

2024

DEDICATION

To JMM, the electricity to my magnetism

TABLE OF CONTENTS

LIST OF FIGURES

LIST OF TABLES

ACKNOWLEDGEMENTS

The Rinehart Lab (as I knew them): *Jeff, Max′, Max″, Tara, Kyle, Phil, Ben, Alex, Jeremy, and Zach – thank you for an excellent environment within which to do science.*

Jeff: There’s no one I would rather talk about the fourth dimension with. You hold the record for the number of times someone has made me laugh and spit my food out; in fact, I think you are the only one to do so. Thank you for encouraging me to stretch my brain, embracing my abstract ideas and giving them space and time (see: spacetime, Minkowski flavor), and letting me do and try all of the things I wanted during the time of this degree, all while offering an excellent soundtrack (and sound system). I started this because I had so many questions about the world, and you entertained all of them (including those not directly related to magnetism) and encouraged me to pursue and research the answers of those we could not answer. For that, I am immensely grateful. I cannot imagine a better manifestation of a PhD.

Max′: It was your enthusiasm for magnetism and science that drove my decision to join the lab, don’t ever forget that! You have a presence more powerful than you know, kindness in every corner of your heart, and a brain full of exciting and meaningful thoughts. Thank you for teaching me with patience, kindness, and grace; thank you for dancing, being silly, listening to music too loud, believing in souls, the hundreds of late-night conversations philosophizing our existence (it is a doctorate of philosophy after all…), always being open to talk and think about the nuances of magnetism (and life), celebrating the big and little things, sticky mango rice deliveries, sticky note messages, and the many many laughs. It’s been a pleasure to work with you and watch you grow as a scientist and as a human. Thanks for letting me borrow our delocalized braincell to write this.

Tara: Thank you for your consistent kindness, genuine light, and always remembering the little things. While we didn't directly work together, you brought a light to the lab that everyone has seen and recognized. You give without expecting anything back, and I hope you know that everyone around you appreciates that.

Kyle: Thank you also for your steady supply of MeOH that I've borrowed with permission (see: stolen) and your computer mouse that I've been using for the past 3ish years. I still think of it as yours, but I've adopted it and given it a good life – it has traveled with me across the US, and to at least three other countries. Thank you for being my on-call Quantum Design expert, and being open to answer any science questions, even before your QD days.

Phil: Since that conversation we had while working in the glovebox together, I find it hard to believe that you should be in the office that doesn't believe in souls. Perhaps it's a spectrum and I should revise the "definition" of soul-believers. Thanks for making that solenoid coil with me and being continually curious and interested in the speakeasies that I've sampled.

Max″ (Maxwell): Thank you for your patience with me as we both learned together. You've taught me a great deal about mentorship, teamwork, and collaboration. I have no doubt that you will continue to be an exceptional scientist; you approach the world with curiosity, wonder, and excitement – don't ever lose that.

To my committee: Drs. Jeffrey Rinehart, Alina Schimpf, Joshua Figueroa, Julio Barreiro, and Mark Young – thank you for your support, guidance, and curiosity towards my work throughout this journey.

To the Figs (as I knew them): Adam, Ritchie, Sean, Krista, Myles, Mikey, Vincent – thank you for the honorary Figueroa member title, status, hundreds of coffees, drinks, and hot pots. You were excellent (and significantly better-funded) neighbors who always had the knowledge and resources to assist me when needed. Ritchie and Mickey, thank you for the crystallographic help; Mickey you are still saved in my phone as “The Jedi”. Myles, thank you for quickly teaching me to take no shit and be myself. Vincent, your laser pointer journeyed with me to many conferences and exams, with your excellent energy attached to it. Maybe you will finally save my name in your phone after this. Ritchie and Sean – thank you for the excellent meals and desserts at *Ritchie’s Restaurant and Sean’s Sweets*; your Yelp reviews are off the charts. Krista, you were my saving grace in countless times and situations. Scientifically speaking, kudos for the IR help in your glovebox (I confess my true love to you in a following section).

To the X-ray magicians: Dr. Milan Gembicky and Dr. Jake Bailey – thank you for the education, support, good conversation, and espresso. Milan, thanks for all that nitrogen you used on my temperature study, the excellent hiking suggestions, and a couple long drives. Your enthusiasm for crystallography and life, and the balance that you have found between the two is refreshing and encouraging.

The Keck Laboratory & Dr. Robert Konecny: while we’ve never met in person, I owe a great deal of gratitude to Dr. Konecny and his managing of the supercomputer cluster; much of this work would not have been possible without time on it.

Dr. Paul Jasien, thank you for accepting my gifts of banana bunches and salt-free pretzels so that I could pester you about what photons might look like (amongst other things). You’ve set the foundation for my research work and encouraged my questioning of the world. I am deeply grateful for your mentorship, advisership, and support throughout the years.

Jacques Coulombe, I have a lot of gratitude for our past, especially your openness towards talking about how mathematics holds the underlying answers to our world. It took me some time, but I'm seeing it now.

Dr. Doran Spencer, thank you for hearing and believing me when many others did not. I've pondered what academia would be like without eyesight and my conclusion was that it would have been difficult, at best. Thank you for keeping my speculation from becoming reality.

Моя дорогая семья: вы поддерживали меня в этом научном путешествии с самого раннего возраста. Вы научили меня, что я должна продвигаться по миру и задавать о нем вопросы. Именно это и привело меня к этому моменту. **Мама**, ты научила меня раскладывать все по маленьким полочкам в моем мозгу. Так вот, это самый большой набор информации, который я когда-либо раскладывала по полочкам, и не только для себя, но, надеюсь, и для других. С самого раннего детства ты поощряла меня использовать моё воображение. Способность воображать и создавать в уме, а затем создавать и формулировать в физическом мире - это основы науки. Только недавно я осознала, насколько тесно связаны воображение и наука. Нужно уметь представить себе свою идею мысль так, что это вызвало бы её существование. У меня есть такая возможность благодаря тебе. **Папа**, ты научил меня сомневаться во всем, что меня окружает, но не в себе. Ты научил меня продолжать учиться, продолжать понимать окружающий мир. Так вот, это мое понимание небольшого уголка науки, и не только для себя, но, надеюсь, и для других. Самый важный урок, который вы оба мне преподали, - это то, что вы всегда на моей стороне. Я храню эти слова в своем сердце и применяю их во всех моих отношениях. Знать, что те, кто тебя любят, неизменно на твоей стороне, - самое большое утешение для души. Я стараюсь дарить это чувство тем, кто мне дорог. **Давид**, ты научил меня учить, понимать мир с другой точки зрения и помнить, что значит познавать мир с детства. **Моя дорогая бабушка**, ты научила меня, что женщина может включать в себя и науку, и женственность. Мы не должны идти на компромисс со своими возможностями.

My Dearest Friends (& Colleagues): *Amy, Krista, Chris, Sean, Stephanie, Jocelyn & Jason, Devonte', Jules – thank you for your love, consistent support, adventures in every spare moment, curiosity, and open-mindedness towards understanding each other and the world we share.*

To my wives, Amy and Krista: The most important thing you've both taught me about is healthy love. Not only are you both exceptional scientists, but you are also exceptional humans. I have the utmost respect for you both, gratitude for your existence, our chance meeting, and our tenured friendship. Thank you for the endless love and support, the flowers, the gifts, the adventures, the sunset dinners at the gliderport, the wife dinners (especially Amy's tofu magic, even when she made me make it so it wouldn't get under her fancy nails), letting me give you tattoos, and so many more shenanigans that do not fit into the parameter space of thesis acknowledgments (but y'all know). Amy, you've taught me about kindness and gentleness, with myself and others. Krista, you've taught me about toughness and perseverance (and general badassery). I wouldn't be here without you both.

Sean: It's not often that you meet someone and create a whole new calendar together; in fact, it's so uncommon that this has only happened to me once, and it was with you (kudos to Krista for the introduction). Thank you for three years of playlists (and counting), engineering the strongest pillars known to us, collaborating on the manufacturing of microscale tethers and a deterministic approach towards sunscreen application, making art in my living room(s), experimenting with pop-rocks, banana bread, and breathing (in remembrance), and determining the most appropriately aggressive way to eat an ice cream cone (backwards). I will never see a salt and vinegar chip or a funky patterned shirt and not think of you.

Jocelyn & Jason: Thank you both for every moment we've spent talking about all aspects of science and life. Thank you for your curiosity, your openness, our origami making evenings, our hikes, and for dancing into the mornings with me. You both have been in my life since our early scientist days, and I cherish our friendship immensely!

Chris: My dude! All of the things I will write here, you already know, but I think that's a good thing. Thank you for being you. Thank you for being here from the start and through and through. Thank you for listening, being so open to every question and conversation, whether it was on my ramblings about science, souls, brains, poetry, music, imagination…(what haven't we talked about?!), and for always having a pair of concert tickets up your sleeve and some good tunes to boogie to. Thank you for listening to me talk (ramble) about shapes and letting me turn our living room into an art studio – this has been the biggest freedom of the past few years. You've taught me so much: about how music is put together (because of you, I see all the layers (!); and you know how much I love the layers), about the longevity and pathways of friendship, the intricacies of creation and perspective, and that mayonnaise belongs in banana muffins. Thank you for reminding me of our accidentally collected, and yet greatly relevant, fridge commandments: (1) you are beautiful, (2) whatever you're feeling is alright, and (3) we can always start again. Thank you for reminding me of who I am when I couldn't remember.

Jules: You are the only person who can see and understand this fully for what it is: for the science, the process, the version of me who put it together, and the version of me that exists outside of this work. You have been my muse, my inspiration, and my unfaltering support in science, love, art, and every aspect of existence since the day we met. There has never been a person who so effortlessly changed my perspective on the world through their mere existence. Consequently, there are no appropriate words to describe my gratitude, appreciation, or adoration of you, but let me try in French: *Te connaître m'a donné envie de vivre. Tu es toutes mes raisons. Je te kiffe de ouf!* For everything else that cannot be bound by language: I know you know.

Chapter 2 is directly adapted from material as it appears in the Journal of the American Chemical Society: Orlova, A.P., Hilgar, J.D., Bernbeck, M.G., Gembicky, M., Rinehart, J.D., "Intuitive Control of Low-Energy Magnetic Excitations via Directed Dipolar Interactions in a Series of Er(III)-Based Complexes," *J. Amer. Chem. Soc.* **2022**. 144 (25), 11316. The dissertation author was the primary researcher and author of this paper.

Chapter 3 is directly adapted from material as it appears in the Journal of the American Chemical Society: Orlova, A.P., Varley, M.S., Bernbeck, M.G., Kirkpatrick, K.M., Bunting, P.C., Gembicky, M., Rinehart, J.D., "Molecular Network Approach to Anisotropic Ising Lattices: Parsing Magnetization Dynamics in Erbium Systems with 0-3 Dimensional Spin Interactivity," *J. Amer. Chem. Soc.* **2023**. 145 (40), 22265. The dissertation author was the primary researcher and author of this paper.

Chapter 4 is directly adapted from material as it appears in the Journal of the American Chemical Society: Orlova, A.P., Bernbeck, M.G., Rinehart, J.D., "Designing Quantum Spaces of Higher Dimensionality from a Tetranuclear Erbium-Based Single-Molecule Magnet," *J. Amer. Chem. Soc.* **2024**. The dissertation author was the primary researcher and author of this paper.

VITA

2017 B.S., Biochemistry, *summa cum laude*, California State University San Marcos

2021 M.S., Chemistry, University of California San Diego

2024 Ph.D., Chemistry, University of California San Diego

PUBLICATIONS

Orlova, A. P., Bernbeck, M. G., Rinehart, J. D.; "Designing Quantum Spaces of Higher Dimensionality from a Tetranuclear Erbium-Based Single-Molecule Magnet," *J. Am. Chem. Soc.* 2024. https://doi.org/10.1021/jacs.4c06600.

Bernbeck, M. G., **Orlova, A. P.**, Hilgar, J. D., Gembicky, M., Ozerov, M., Rinehart, J. D.; "Dipolar Coupling as a Mechanism for Fine Control of Magnetic States in ErCOT-Alkyl Molecular Magnets" *J. Am. Chem. Soc.* 2024, 146, 11, 7243. https://doi.org/10.1021/jacs.3c10412.

Orlova, A. P., Varley, M.S., Bernbeck, M. G., Kirkpatrick, K.M., Bunting, P.C., Gembicky, M., Rinehart, J. D.; "A Molecular Network Approach to Anisotropic Ising Lattices: Parsing Magnetization Dynamics in Er^{3+} Systems with 0 – 3 Dimensional Spin Interactivity," *J. Am. Chem. Soc.* 2023, 145, 40, 22265. https://10.1021/jacs.3c08946.

Orlova, A. P., Hilgar, J.D., Bernbeck, M. G., Gembicky, M., Rinehart, J. D.; "Intuitive Control of Low-Energy Magnetic Excitations via Directed Dipolar Interactions in a Series of Er(III)-Based Complexes," *J. Am. Chem. Soc.* 2022, 144, 25, 11316. https://doi.org/10.1021/jacs.2c03236.

Orlova, A. P., Jasien, P.G., "Halogen Bonding in Self-Assembling Systems: A Comparison of Intra- and Interchain Binding Energies," *Comput. Theor. Chem.* 2018, 1139, 63. https://doi.org/10.1016/j.comptc.2018.07.004.

FIELD OF STUDY

Major Field: Chemistry
Studies in Inorganic Chemistry & Magnetochemistry
Professor Jeffrey Rinehart

ABSTRACT OF THE DISSERTATION

Manifestations and Effects of Dipolar Coupling in Erbium-Based Molecular Magnets

by

Angelica P. Orlova
Doctor of Philosophy in Chemistry
University of California San Diego, 2024
Professor Jeffrey Rinehart, Chair

The focus of this dissertation is the thorough analysis of the effects of dipolar coupling on magnetic relaxation behavior within erbium-based molecular magnets. Utilizing the Er-COT unit as the starting point and building block, we investigate intra- and inter-molecular dipolar coupling motifs generated with analogous highly anisotropic building block units. Each chapter holds a specific focus, organized as follows:

Chapter 1 offers a brief introduction to molecular magnetism, followed by an overview of topics necessary towards understanding magnetic relaxation in the scope of this work, including energy perturbations, relaxation dynamics, and anisotropy; an introduction to the Er-COT unit and

coupling schemes in lanthanide-based molecular magnetism, and the motivation for investigating dipolar coupled systems. The chapter concludes with extended chapter summaries for the remainder of this work.

Chapter 2 focuses on the role and effects of *intra*molecular dipolar coupling in a series of compounds of increasing nuclearity. This work demonstrates the ability of intramolecular dipolar coupling to control quantum tunnelling of magnetization, and thus the rate and mechanism of magnetic relaxation. This chapter utilizes an expanded frequency space magnetometry technique to garner new insights into magnetic relaxation by visualizing, fitting, and analyzing multiple relaxation regimes. The chapter concludes with an intuitive model of thought based on a simple vector addition model, within which spin interactions can be estimated directly from a crystal structure.

Chapter 3 discusses the effects of *inter*molecular dipolar coupling within a series of identical single-ion magnets within varied crystal packing environments. This work depicts the propensity of intermolecular dipolar coupling to drive dramatic differences in resulting magnetic behavior and seeks to shed light on the relationship between single-ion magnetism and solid-state magnetism. This chapter applies a novel fitting methodology to quantify additional parameters from isothermal magnetization data for downstream analysis.

Chapter 4 presents the analysis of a highly symmetric, near-tetrahedral tetranuclear single-molecule magnet to discuss the effects of crystallographic symmetry on the resulting dipole-coupled spin-space symmetry. This chapter discusses the ensuing available rhombic dodecahedral quantum space of this molecule, composed of octahedral and cubic subspaces, and makes connections to theoretically proposed quantum Cayley networks upon hypercubes.

Chapter 1 A Brief Introduction

1.1 A Brief Introduction to Molecular Magnetism

Molecular magnetism is a field of study that investigates the magnetic properties of molecules capable of exhibiting slow magnetic relaxation. This work focuses specifically on the properties and characteristics of lanthanide molecular magnets, which hold a unique position in the field due to their distinctive electronic structure. The lanthanides are characterized by their partially filled f-orbitals and high degree of spin-orbit coupling, contributing to large magnetic moments and complex energy perturbations, especially upon application of crystal field, giving rise to magnetic anisotropy. The primary objective of research in f-element molecular magnetism is to understand and control the magnetic properties of these complex systems. This involves synthesizing new f-element complexes, characterizing their magnetic behavior, and exploring their potential applications. Methodologies typically include X-ray crystallography for structural analysis, SQUID magnetometry for magnetic measurements, and complimentary *ab initio* computational techniques for probing electronic and magnetic structures.

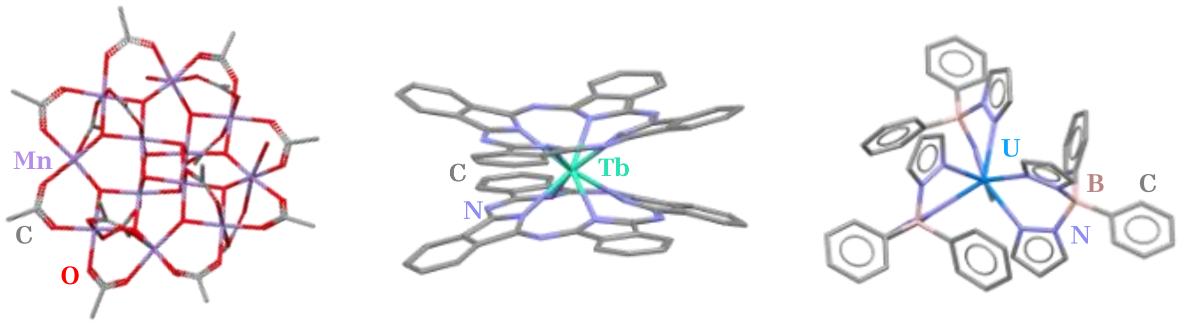

Mn_{12} cluster **$[TbPc_2]^-$** **$U(Ph_2BPz_2)_3$**

Figure 1.1: Historically relevant molecular magnets, as described in the text. Left to right: the first transition metal, lanthanide, and actinide molecular magnets. Elements are color coordinated to labels in the text; hydrogens have been omitted for clarity.

Historically, observation of magnetic behaviors in a single-molecule magnet (SMM) occurred in a Mn_{12} acetate cluster in the early 90s,[1-3] demonstrating that individual molecules could exhibit magnetic bistability, analogous to bulk materials. Key milestones include the synthesis of the first lanthanide-based SMM by Ishikawa and coworkers[4-5] in 2003 and the discovery of the first actinide system to display slow magnetic relaxation by Rinehart and Long in 2009 (Figure 1.1).[6] Furthermore, an ongoing pursuit to reach operational temperatures above liquid nitrogen has yielded many exceptional resulting molecular magnets, reaching hysteresis temperatures of 60[7] and 80 K,[8] with recent work[9] showing coercive fields of up to 14 tesla at 60 K. Much of this work is done with intent to functionalize these materials towards applications in quantum information science, quantum computing, spintronics, and quantum sensing technologies.[10-16] We will not delve into these compounds in detail as they are comprehensively featured in numerous publications and theses in molecular magnetism and extensive reviews and perspectives are now available that provide more in-depth and thorough coverage of these topics.[17-20]

1.2 Energy Perturbations, Relaxation Dynamics, and Anisotropy

The active electronic structure of most lanthanide-based molecular magnets can be thought of as a series of progressively smaller perturbations on an f-orbital basis, beginning with the interelectronic repulsion, followed by spin-orbit coupling, and finally, splitting driven by the application of the ligand (or crystal) field.[21] An example of such a structure is demonstrated in Figure 1.2 for trivalent erbium (Er^{3+}), as is relevant to this work. Trivalent erbium is a $4f^{11}$ system with total spin, S = 3/2, and total angular momenta, L = 6, for which the LS coupling scheme is applied to give J = 15/2. The term symbol for the spin-orbit coupled term for Er^{3+} is $^4I_{15/2}$ with the ground state being the J = 15/2 state due to having a more than half filled shell. The spin-orbit coupled manifold is further split by the application of a crystal field, to yield an energy manifold of 8 doubly degenerate Kramers doublets (KDs) related by time-reversal symmetry: M_J = ±15/2, ±13/2, ±11/2, ±9/2, ±7/2, ±5/2, ±3/2, ±1/2. This is due to the Kramers' degeneracy theorem,[22-23] which states that fermionic, half-integer total spin systems will have two eigenstates related to each other by time-reversal symmetry. This generates a double-welled energy potential responsible for time-dependent magnetic relaxation whose energy levels can be modulated by choice of lanthanide and ligand field.

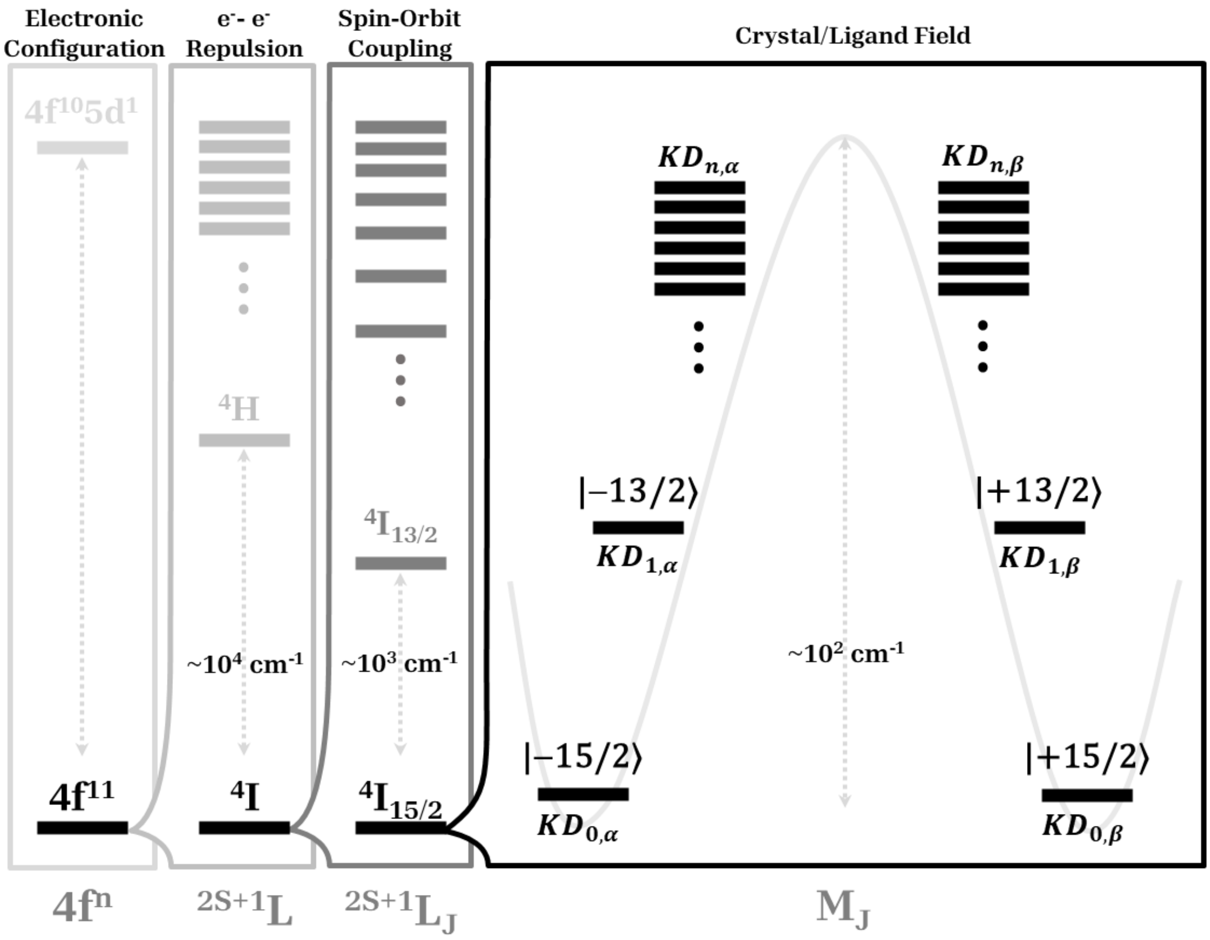

Figure 1.2: Iterative energy perturbations for an Er^{3+}, $4f^{11}$ system. Left to right: electronic configuration of ground $4f^{11}$ system; electron-electron repulsion with ^4I ground term; spin-orbit coupling, yielding a $^4I_{15/2}$ ground term; further split through an application of a crystal/ligand field into M_J substates (Kramers Doublets, KD_n), related by time-reversal symmetry (α, β).

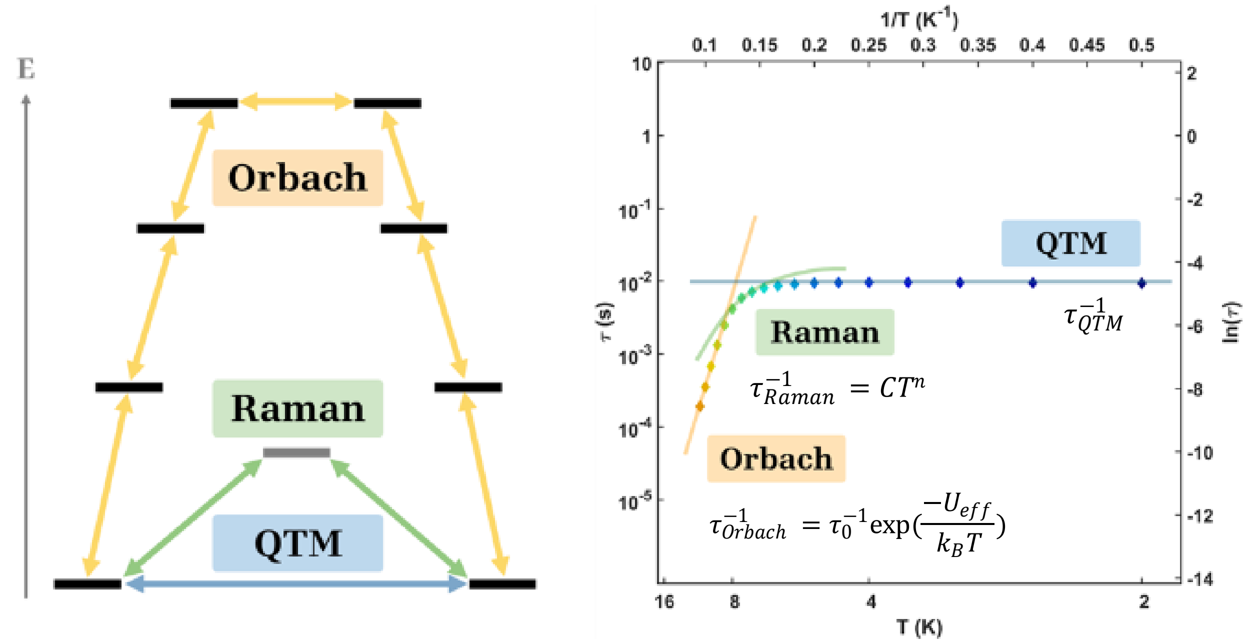

Figure 1.3: Left, diagram depicting commonly seen relaxation mechanisms in lanthanide-based molecular magnetism, showing Orbach (yellow), Raman (green), and QTM (blue) mechanism. Right, Arrhenius plot of relaxation times (diamonds are extracted τ values from time-dependent magnetic data) with corresponding relaxation regimes. Inset shows typically employed fitting equations for those relaxation regimes.

Relaxation mechanisms in lanthanide-based molecular magnetism typically fall into three main categories: Orbach, Raman, and QTM. The Orbach[24] relaxation regime (Figure 1.3, yellow) is a temperature-dependent, over-barrier process governed by the absorption or emission of phonons to traverse the energy barrier generated by the M_J states. This is often represented by an Arrhenius law, which allows for the extraction of U_{eff}, or the thermal barrier to relaxation, a parameter frequently used to quantify the behavior of a molecular magnet. When fit to extracted time-dependent magnetometry data, plotted as the logarithm of relaxation time (τ) versus temperature, the Orbach mechanism generates a linear, clearly temperature-dependent region, depicted by the yellow lines fit to data in Figure 1.3, right. Raman relaxation (Figure 1.3, green) is a two-phonon process which involves the excitement to a virtual state, bypassing the effective barrier. This regime is represented by a power law dependence on temperature and is often seen as the curved, intermediate region between the Orbach, higher-temperature regime and the low-temperature quantum tunneling regime (shown in green in Figure 1.3, right). The last relaxation regime is responsible for the lowest-temperature relaxation and is deemed QTM, or quantum tunneling of magnetization (Figure 1.3, blue). This is a temperature-independent relaxation regime, occurring between the lowest ground states, bypassing any energetic barrier. This is represented by a linear, temperature-independent region shown in blue in Figure 1.3, right. The chapters in this work, especially Chapter 2, will focus on the meaning and implications of deviations from temperature-independent QTM regimes at low temperatures. In this chapter, we propose that these deviations arise from magnetic dipolar coupling interactions, and we fit magnetic time-dependent data with a second Arrhenius law to describe this process. Importantly, the magnetic dipole coupling describes a further perturbation on the quantum states of the system – not necessarily the energy exchange mechanism leading to relaxation – often likely to be largely phonon-mediated. Other couplings that occur in the range of the crystal field splitting, including coupling to local vibrational modes, are generally higher energy, harder to control and predict, and thus minimally relevant in the presence of directional couplings such as the anisotropic dipole-dipole interactions studied here. The interested reader is directed to other works[25-28] that offer comprehensive discussions on all investigated relaxation processes present in molecular magnets.

At this point, it's pertinent to say a few words on anisotropy, a term that will be used throughout this work as a design principle towards synthetically structuring molecular magnets. Magnetic anisotropy is used to describe the difference in magnetic properties of an object based on its direction. If an object is fully isotropic, this means that its response will not vary, regardless of direction. If an object is highly anisotropic, that means that its response will differ greatly in one direction. In lanthanide-based molecular magnets, anisotropy can be encouraged through

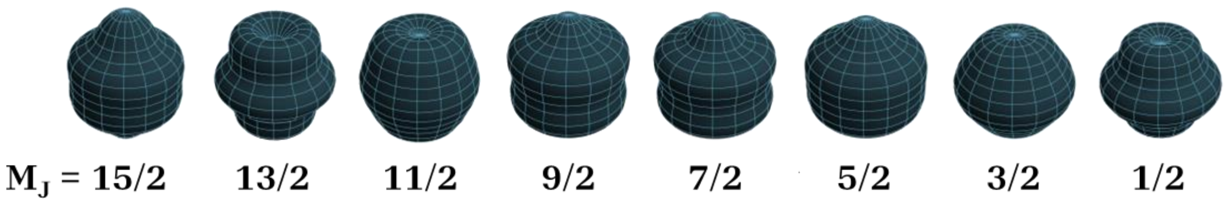

Figure 1.4: Depiction of total 4f charge densities for M_J states of the Er^{3+} ion.

choice of lanthanide and choice of appropriate ligand field, the combination of which will design a unique energy perturbation diagram, as was discussed previously (Figure 1.2). The concept of single-ion or magnetocrystalline anisotropy can be adopted to great effect in the fundamental design of single-molecule magnets,[29] where anisotropy begins at the single-ion level of the lanthanide of interest, around which the crystal field can be designed to stabilize the M_J state(s) of interest (typically the highest M_J state). Depicted in Figure 1.4 (adapted from visualizations by Kragskow[30]) are the angular dependencies of the total 4f charge density for the M_J states of the Er^{3+} ion of the J = 15/2 ground state, constructed based on derivations by Sievers.[31] This figure depicts the highest $M_J = 15/2$ state as having a prolate electron density that should be stabilized by an equatorial anionic coordination environment. This design principle should encourage high anisotropy in the ground state, leading to an Ising-type[32] spin system where the spins are restricted to align along a single axis (typically chosen to be the z-axis) with minimal contribution (~ 0) along both x- and y-axes. The application of these design principles to create and maintain anisotropy in erbium-based compounds is discussed in great detail in the following section and will be present throughout this work. The goals will be to use these principles to construct a fundamental building unit of well-defined, strongly oriented anisotropy by which to design and study increasingly complex spin interactions.

1.3 The Highly Anisotropic Building Block: Er-COT and Co.

Investigations into the erbium-cyclooctatetraene motif (Er-COT, Figure 1.5), both as a chemical curiosity and an anisotropic building unit, have spanned numbers of years, many of which are directly attributed to my colleagues in the Rinehart laboratory (especially Drs. Bernbeck and Hilgar). The first investigations into the Er-COT motif were synthetic and crystallographic in nature, with the first structure deposited into the CCDC being an erbium-bisCOT motif with bridging potassium ions published[33] in 1991 by Xia and coworkers. Following, Zhang, et. al.[34] synthesized (2,4-C_7H_{11})(Ln-COT)·THF congeners with neodymium and erbium in 1994, and Evans, et. al. reported[35] on the synthesis of some (Cp*)(Ln-COT) metallocenes in 2000, which included samarium, dysprosium, and erbium. Some years later, Roesky's group published a handful of works on substituted[36] Er-COT compounds, and those with modified coordination spheres to include chiral phosphanylamides[37] and bis(phosphinimino)methanides.[38] The first magnetic characterization of an Er-COT motif would take place eleven years after Evans' initial crystallographic characterization, in a work published by Jiang and coworkers from Gao's group[39] on the single-ion magnetic properties of (Cp*)(Er-COT), which opened the field to further investigations of this unit. Following, works by Meihaus[40] of the Long group and LeRoy[41-43] from Murugesu's group took over the Er-COT magnetic literature, both publishing respective PhD

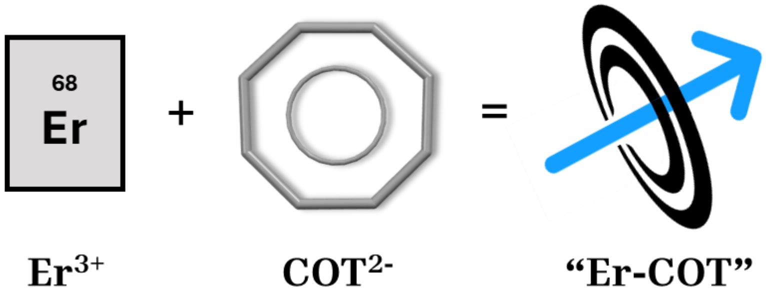

Figure 1.5: The erbium-cyclooctatetraene motif.

theses[44-45] in 2015 featuring magnetic characterization and analysis of Er-COT compounds and their derivatives.

This repository of work depicted the Er-COT motif as a magnetically interesting and potentially tenacious unit towards retaining its magnetic anisotropy, and thus set the stage for work done in the Rinehart group to further investigate this system.[46-50] In the years following, our group has demonstrated a number of curious phenomena with the Er-COT motif: (1) the Er-COT unit is a "metal-ligand pair" that upholds magnetic anisotropy, (2) two Er-COT units within a molecule can ferromagnetically couple, and (3) the cant angle of magnetic units with respect to one another drastically changes relaxation behaviors.

Taken together, these works depicted that the Er-COT unit is synthetically friendly and fairly resistant to changes in coordination environment, meaning that modifications to the remaining coordination sphere had minimal effects on the magnetic anisotropy of the unit. This allowed for the formation of a continuously growing library of compounds utilizing the Er-COT unit as a building block that upheld these design principles, while refining the ways in which it can be used to generate configurable interactions of highly anisotropic, Ising-like systems (Figure 1.6).

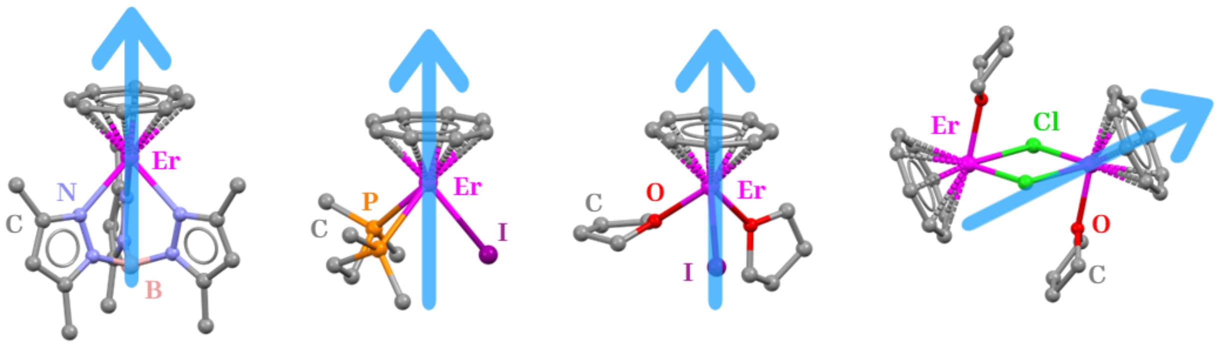

Figure 1.6: Selected compounds synthesized in the Rinehart group from references 46-50. Elements are color coordinated to labels in the figure; hydrogens have been omitted for clarity. Blue arrows represent the real-space tether of the anisotropy axis, generated by the Er-COT motif within these structures.

This lends itself to significant intuition in the analysis of these systems since there is a real-space tether of the magnetic anisotropy axis, as depicted by the blue arrows in Figures 1.5 and 1.6. Furthermore, evidence of ferromagnetic coupling and influence of cant angle between magnetic centers points towards the utility of controlled dipolar coupling effects, as dipolar coupling is defined by distance and angle between interacting units. Following these discoveries, it was pertinent to understand just how such units couple and how these coupling behaviors affect magnetic relaxation dynamics. As such, we looked towards coupling schemes in molecular magnetism and began investigations into the role dipolar coupling could play in modifying magnetic relaxation.

1.4 Coupling Schemes in Lanthanide Molecular Magnetism

Coupling within lanthanide-based molecular magnets exists in a number of flavors, the most commonly discussed being dipolar coupling and exchange coupling (Figure 1.7). Dipolar coupling is a long-range, through-space coupling interaction, driven by the mutual interactions of the magnetic dipoles present on each magnetic center.[51] This interaction is inherent to every crystal system with more than one neighboring magnetic center. Exchange coupling, or orbital exchange,

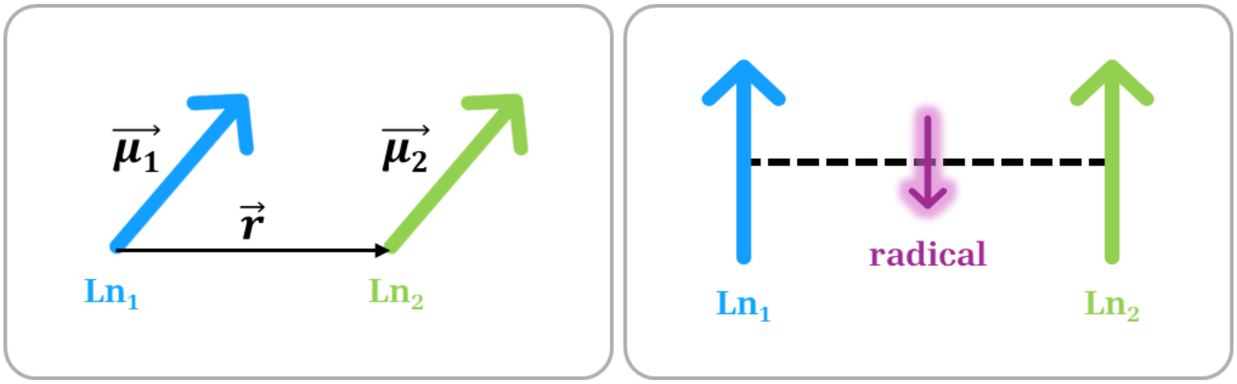

Figure 1.7: Simplified depiction of through-space dipolar coupling (left) and radical-bridged exchange coupling (right).

refers to the indirect coupling interactions enforced by Pauli exclusion between two or more magnetic centers. In molecular systems, this is typically mediated by a formally diamagnetic bridging ligand (known as superexchange) but can also occur through direct orbital overlap. Superexchange coupling is often discussed in the context of transition metal compounds due to the presence of accessible d-orbitals, which can interact with p-orbitals of, e.g. oxygen bridging ligands.[52] Intuitively, one may think that adding more "spin" into a system of interest would immediately improve upon its magnetic characteristics and relaxation dynamics, however, the answer bears significantly more complexity. This complexity becomes especially evident in lanthanide systems, as the f-orbitals of lanthanides are highly contracted,[53] complicating matters of both direct and ligand-bridged orbital overlap. Strategies to overcome such matters in f-element complexes employ radical bridges, such as N_2^{3-}, whose diffuse orbitals can penetrate the contracted 4f orbitals of lanthanides.[54-56] This strategy, however, is itself not without complications. Radical bridged chemistry is notoriously synthetically challenging and also bears potential to destroy the single-ion anisotropy of the mononuclear system through with the introduction of the radical crystal field (and its attached magnetic counterpart).

This brings us to the motivation for studying magnetic dipolar coupling, an interaction that is based solely on the relative orientation between two (or more) magnetic moments and is inherent to every molecular system with neighboring units. This interaction is based on the distance between two spin centers, as well as the angle(s) between them, and is introduced in detail in Chapter 2. Dipolar interactions are often touted as detrimental to slow magnetic relaxation and are looked to be eliminated, however, in our eyes, this was simply evidence towards the fact that they can have substantial effects on magnetic relaxation and warrant further investigation. We were interested in designing systems in which dipolar coupling could play a beneficial role towards magnetic relaxation behaviors, which meant eliminating other coupling regimes, leaving dipolar coupling as the main focus. From a chemical design perspective, this meant implementing the simplest system of study that can serve as a foundational framework. Ideally, this system needed to be synthetically accessible, chemically intuitive, modifiable, and easily interpreted, and also allowing for further expansion of complexity and scalability. As such, the focus of this thesis is work done with highly anisotropic erbium-based systems which offer the necessary characteristics for this study. Chapter 2 incorporates Er-COT units to investigate *intra*molecular dipolar coupling in mono-, di-, and tri-nuclear compounds; this chapter also demonstrates that the dipoles of these systems can be interpreted intuitively from crystal structures. Chapter 3 focuses on long-range *inter*molecular dipolar coupling by modifying the crystallographic organizational motifs of identical mononuclear magnetic units. The intent of this chapter is to show the true impact of dipolar coupling on the resulting magnetic properties in well-designed systems and begin to parse magnetic behaviors arising from 0-D versus 3-D magnetism. Chapter 4 focuses on designing and interpreting more complex systems of higher nuclearity and generating quantum spin spaces of interest through dipolar coupling means.

1.5 Chapter Summaries

Chapter 2: The intent of this work was to determine the impacts of *intra*molecular magnetic dipolar coupling in Ising-type systems on controlling quantum tunneling of magnetization, and thus, the rate and mechanism of magnetic relaxation. This was accomplished through a joint synthetic and theoretical study on a series of highly anisotropic erbium-based molecular magnets of increasing nuclearity (1, 2, and 3 magnetic centers). We were able to show that dipolar coupled energy perturbations on the order of ~1 cm^{-1}, evidenced and fit in time-domain, phase-dependent AC susceptometry data, are able to substantially modify relaxation dynamics and increase magnetic relaxation times. To collect magnetometry data on timescales necessary for these compounds, we implemented an expanded frequency space technique (allowing collection down to 10^{-5} Hz, whereas it was previously only possible to collect data down to 10^{-1} Hz). This method generates long-timescale square waveforms constructed in DC (direct current) or VSM (vibrating sample magnetometry) scan modes on the magnetometer, from which time-dependent data can be extracted and fit. Characterization techniques employed during this work included static and dynamic air-free SQUID magnetometry, X-ray diffraction, infra-red spectroscopy, NMR spectroscopy, elemental analysis, air-free and water-free synthesis of the compounds, and computational studies completed at the CASSCF (complete active space, self-consistent field) level.

Chapter 3: The intent of this work was to understand the effects of long-range intermolecular magnetic dipolar coupling in highly anisotropic lanthanide molecular magnets and understand the relationship between single-ion magnetism (0-D) and solid-state magnetism (3-D). This was accomplished by generating three different lattices with varied dipolar interactions, while maintaining the identity of the magnetic unit. We showed a three-fold increase in magnetic relaxation times between lattices and saw features typically only present/discussed in solid-state magnetic materials, thereby seeking to connect the chemical and physical approaches to magnetism. To aid us in this study, we applied a novel fitting methodology to quantify additional parameters from isothermal magnetization data. Characterization techniques employed during this work included static and dynamic air-free SQUID magnetometry, infra-red spectroscopy, elemental analysis, air-free and water-free synthesis of the compounds, X-ray diffraction and varied-temperature X-ray diffraction studies, and computational studies completed at the CASSCF level.

Chapter 4: The intent of this work was to expand the utility of magnetic dipolar coupling to generate spin spaces of interest, understand the effects of crystallographic symmetry on resulting quantum spin spaces, and make connections to fields in quantum information science. This was accomplished through the synthesis and analysis of a highly symmetric, near-tetrahedral tetranuclear molecular magnet, the curiosity of which arises from the nature of the local anisotropy which fixes the moments of each ion along the diagonals of a cube, enforcing a limited, high symmetry restriction on possible coupling geometries. We leverage this symmetry to discover new ways in which the spatial and spin symmetry manifest in the quantum structure and measurable properties of the system. Curiously still, the experimentally derived low-temperature dipole-coupled quantum space holds a direct connection to previously theoretically proposed quantum Cayley networks upon hypercubes, potentially providing evidence for a four-dimensional manifestation of magnetism, projected down to 3-D. Characterization techniques employed during this work included static and dynamic air-free SQUID magnetometry, infra-red spectroscopy, elemental analysis, air-free and water-free synthesis of the compounds, X-ray diffraction, and numerous computational studies completed at the CASSCF level.

1.6 References

1. Sessoli, R.; Tsai, H. L.; Schake, A. R.; Wang, S. Y.; Vincent, J. B.; Folting, K.; Gatteschi, D.; Christou, G.; Hendrickson, D. N., High-Spin Molecules - [Mn12o12(O2cr)16(H2o)4]. *J Am Chem Soc* **1993,** *115* (5), 1804-1816.

2. Sessoli, R.; Gatteschi, D.; Caneschi, A.; Novak, M. A., Magnetic Bistability in a Metal-Ion Cluster. *Nature* **1993,** *365* (6442), 141-143.

3. Caneschi, A.; Gatteschi, D.; Sessoli, R.; Barra, A. L.; Brunel, L. C.; Guillot, M., Alternating-Current Susceptibility, High-Field Magnetization, and Millimeter Band Epr Evidence for a Ground S = 10 State in [Mn12o12(Ch3coo)16(H2o)4].2ch3cooh.4h2o. *J Am Chem Soc* **1991,** *113* (15), 5873-5874.

4. Ishikawa, N., Single molecule magnet with single lanthanide ion. *Polyhedron* **2007,** *26* (9-11), 2147-2153.

5. Ishikawa, N.; Sugita, M.; Ishikawa, T.; Koshihara, S.; Kaizu, Y., Lanthanide double-decker complexes functioning as magnets at the single-molecular level. *J Am Chem Soc* **2003,** *125* (29), 8694-8695.

6. Rinehart, J. D.; Long, J. R., Slow Magnetic Relaxation in a Trigonal Prismatic Uranium(III) Complex. *J Am Chem Soc* **2009,** *131* (35), 12558.

7. Goodwin, C. A. P.; Ortu, F.; Reta, D.; Chilton, N. F.; Mills, D. P., Molecular magnetic hysteresis at 60 kelvin in dysprosocenium. *Nature* **2017,** *548* (7668), 439-442.

8. Guo, F. S.; Day, B. M.; Chen, Y. C.; Tong, M. L.; Mansikkamaki, A.; Layfield, R. A., Magnetic hysteresis up to 80 kelvin in a dysprosium metallocene single-molecule magnet. *Science* **2018,** *362* (6421), 1400.

9. Gould, C. A.; McClain, K. R.; Reta, D.; Kragskow, J. G. C.; Marchiori, D. A.; Lachman, E.; Choi, E. S.; Analytis, J. G.; Britt, R. D.; Chilton, N. F.; Harvey, B. G.; Long, J. R., Ultrahard magnetism from mixed-valence dilanthanide complexes with metal-metal bonding. *Science* **2022,** *375* (6577), 198.

10. National Academies of Sciences, E.; Medicine, *Advancing Chemistry and Quantum Information Science: An Assessment of Research Opportunities at the Interface of Chemistry and Quantum Information Science in the United States*. The National Academies Press: Washington, DC, 2023; p 226.

11. Gaita-Ariño, A.; Luis, F.; Hill, S.; Coronado, E., Molecular spins for quantum computation. *Nature Chemistry* **2019,** *11* (4), 301-309.

12. Wang, Y. C.; Hu, Z. X.; Sanders, B. C.; Kais, S., Qudits and High-Dimensional Quantum Computing. *Front Phys-Lausanne* **2020,** *8*.

13. Hymas, K.; Soncini, A., Molecular spintronics using single-molecule magnets under irradiation. *Phys Rev B* **2019,** *99* (24).

14. Natterer, F. D.; Yang, K.; Paul, W.; Willke, P.; Choi, T. Y.; Greber, T.; Heinrich, A. J.; Lutz, C. P., Reading and writing single-atom magnets. *Nature* **2017,** *543* (7644), 226.

15. Ganzhorn, M.; Wernsdorfer, W., Molecular Quantum Spintronics Using Single-Molecule Magnets. *Nanosci Technol* **2014**, 319-364.

16. Bogani, L.; Wernsdorfer, W., Molecular spintronics using single-molecule magnets. *Nat Mater* **2008,** *7* (3), 179-186.

17. Christou, G., Single-molecule magnets: a molecular approach to nanoscale magnetic materials. *Polyhedron* **2005,** *24* (16), 2065-2075.

18. Layfield, R. A., Organometallic Single-Molecule Magnets. *Organometallics* **2014,** *33* (5), 1084-1099.

19. Woodruff, D. N.; Winpenny, R. E. P.; Layfield, R. A., Lanthanide Single-Molecule Magnets. *Chemical Reviews* **2013,** *113* (7), 5110-5148.

20. Meihaus, K. R.; Long, J. R., Actinide-based single-molecule magnets. *Dalton Transactions* **2015,** *44* (6), 2517-2528.

21. Sorace, L.; Gatteschi, D., Electronic Structure and Magnetic Properties of Lanthanide Molecular Complexes. In *Lanthanides and Actinides in Molecular Magnetism*, Layfield, R. A.; Murugesu, M., Eds. Wiley: 2015; pp 1-26.

22. Klein, M. J., On a Degeneracy Theorem of Kramers. *Am J Phys* **1952,** *20* (2), 65-71.

23. Kramers, H. A., General theory of the paramagnetic rotation in crystals. *P K Akad Wet-Amsterd* **1930,** *33* (6/10), 959-972.
24. Orbach, R., Spin-Lattice Relaxation in Rare-Earth Salts. *Proc R Soc Lon Ser-A* **1961,** *264* (1318), 458.

25. Liddle, S. T.; van Slageren, J., Improving f-element single molecule magnets. *Chemical Society Reviews* **2015,** *44* (19), 6655-6669.

26. Chiesa, A.; Cugini, F.; Hussain, R.; Macaluso, E.; Allodi, G.; Garlatti, E.; Giansiracusa, M.; Goodwin, C. A. P.; Ortu, F.; Reta, D.; Skelton, J. M.; Guidi, T.; Santini, P.; Solzi, M.; De Renzi, R.; Mills, D. P.; Chilton, N. F.; Carretta, S., Understanding magnetic relaxation in single-ion magnets with high blocking temperature. *Phys Rev B* **2020,** *101* (17).

27. Rousset, E.; Piccardo, M.; Boulon, M. E.; Gable, R. W.; Soncini, A.; Sorace, L.; Boskovic, C., Slow Magnetic Relaxation in Lanthanoid Crown Ether Complexes: Interplay of Raman and Anomalous Phonon Bottleneck Processes. *Chem-Eur J* **2018,** *24* (55), 14768-14785.

28. Giansiracusa, M.; Gransbury, G.; Chilton, N.; Mills, D., Single Molecule Magnets. In *Encyclopedia of Inorganic and Bioinorganic Chemistry*, John Wiley & Sons Ltd.: Online, 2021; Vol. eibc2784.

29. Rinehart, J. D.; Long, J. R., Exploiting single-ion anisotropy in the design of f-element single-molecule magnets. *Chem Sci* **2011,** *2* (11), 2078-2085.

30. Kragskow, J., Lanthanide Ion 4f Electron Densities. 2022; Vol. 2024, p a plot of visualized 4f charge densities.

31. Sievers, J., Asphericity of 4f-shells in their Hund's rule ground states. *Zeitschrift für Physik B Condensed Matter* **1982,** *45* (4), 289-296.

32. Ising, E., Beitrag zur Theorie des Ferromagnetismus. *Zeitschrift für Physik* **1925,** *31* (1), 253-258.

33. Xia, J.; Jin, Z.; Chen, W., Synthesis and crystal structure of a new lanthanide cyclooctatetraene complex (η8-C8H8)Er(μ-η8-C8H8)K(μ-η8-C8H8)Er(μ-η8-C8H8)K(THF)4. *Journal of the Chemical Society, Chemical Communications* **1991,** (17), 1214-1215.

34. Zhang, S.; Jin, J.; Wei, G.; Chen, W.; Liu, J., Syntheses and molecular structure of (C8H8)Ln(2,4-C7H11) · THF (Ln □ Nd, Er). *Journal of Organometallic Chemistry* **1994,** *483* (1), 57-60.

35. Evans, W. J.; Johnston, M. A.; Clark, R. D.; Ziller, J. W., Variability of (ring centroid)–Ln–(ring centroid) angles in the mixed ligand C5Me5/C8H8 complexes (C5Me5)Ln(C8H8) and [(C5Me5)Yb(THF)](μ-η8:η8-C8H8)[Yb(C5Me5)]. *Journal of the Chemical Society, Dalton Transactions* **2000,** (10), 1609-1612.

36. Panda, T. K.; Benndorf, P.; Roesky, P. W., Substituted cyclooctatetraene complexes of yttrium and erbium with bis(phosphinimino)methanides - Synthesis and structure. *Z Anorg Allg Chem* **2005,** *631* (1), 81-84.

37. Panda, T. K.; Gamer, M. T.; Roesky, P. W., Yttrium and Lanthanide Complexes Having a Chiral Phosphanylamide in the Coordination Sphere. *Inorganic Chemistry* **2006,** *45* (2), 910-916.

38. Panda, T. K.; Zulys, A.; Gamer, M. T.; Roesky, P. W., Cyclooctatetraene Complexes of Yttrium and the Lanthanides with Bis(phosphinimino)methanides: Synthesis, Structure, and Hydroamination/Cyclization Catalysis1. *Organometallics* **2005,** *24* (9), 2197-2202.

39. Jiang, S.-D.; Wang, B.-W.; Sun, H.-L.; Wang, Z.-M.; Gao, S., An Organometallic Single-Ion Magnet. *J Am Chem Soc* **2011,** *133* (13), 4730-4733.

40. Meihaus, K. R.; Long, J. R., Magnetic Blocking at 10 K and a Dipolar-Mediated Avalanche in Salts of the Bis(η8-cyclooctatetraenide) Complex [Er(COT)2]−. *J Am Chem Soc* **2013,** *135* (47), 17952-17957.

41. Le Roy, J. J.; Korobkov, I.; Murugesu, M., A sandwich complex with axial symmetry for harnessing the anisotropy in a prolate erbium(iii) ion. *Chem Commun* **2014,** *50* (13), 1602-1604.

42. Le Roy, J. J.; Ungur, L.; Korobkov, I.; Chibotaru, L. F.; Murugesu, M., Coupling Strategies to Enhance Single-Molecule Magnet Properties of Erbium–Cyclooctatetraenyl Complexes. *J Am Chem Soc* **2014,** *136* (22), 8003-8010.

43. Ungur, L.; Le Roy, J. J.; Korobkov, I.; Murugesu, M.; Chibotaru, L. F., Fine-tuning the Local Symmetry to Attain Record Blocking Temperature and Magnetic Remanence in a Single-Ion Magnet**. *Angew Chem Int Edit* **2014,** *53* (17), 4413-4417.

44. Roy, J. J. L. The Pursuit of High Blocking Temperature Single Molecule Magnets using 4f/5f Cyclooctatetraenyl Complexes. University of Ottawa Ottawa, Canada, 2015.

45. Meihaus, K. R. Slow Magnetic Relaxation in f-Element Complexes: A Tale of Dipolar Interactions, Symmetry, and Magnetic Hysteresis. University of California, Berkeley Berkeley, CA, 2015.

46. Bernbeck, M. G.; Hilgar, J. D.; Rinehart, J. D., Probing axial anisotropy in dinuclear alkoxide-bridged Er-COT single-molecule magnets. *Polyhedron* **2020,** *175*.

47. Hilgar, J. D.; Butts, A. K.; Rinehart, J. D., A method for extending AC susceptometry to long-timescale magnetic relaxation. *Phys Chem Chem Phys* **2019,** *21* (40), 22302-22307.

48. Hilgar, J. D.; Bernbeck, M. G.; Rinehart, J. D., Million-fold Relaxation Time Enhancement across a Series of Phosphino-Supported Erbium Single-Molecule Magnets. *J Am Chem Soc* **2019,** *141* (5), 1913-1917.

49. Hilgar, J. D.; Bernbeck, M. G.; Flores, B. S.; Rinehart, J. D., Metal-ligand pair anisotropy in a series of mononuclear Er-COT complexes. *Chem Sci* **2018,** *9* (36), 7204-7209.

50. Hilgar, J. D.; Flores, B. S.; Rinehart, J. D., Ferromagnetic coupling in a chloride-bridged erbium single-molecule magnet. *Chem Commun* **2017,** *53* (53), 7322-7324.

51. Chen, Y.-C.; Tong, M.-L., Single-molecule magnets beyond a single lanthanide ion: the art of coupling. *Chem Sci* **2022,** *13* (30), 8716-8726.

52. Pavarini, E.; Koch, E.; Scalettar, R.; Martin, R. M., *The Physics of Correlated Insulators, Metals, and Superconductors Modeling and Simulation, Vol. 7*. 2017.

53. Cotton, F. A.; Wilkinson, G., *Advanced Inorganic Chemistry*. 5th ed.; Wiley-Interscience: New York, 1988.

54. Rajeshkumar, T.; Rajaraman, G., Is a radical bridge a route to strong exchange interactions in lanthanide complexes? A computational examination. *Chem Commun* **2012,** *48* (63), 7856-7858.

55. Demir, S.; Zadrozny, J. M.; Nippe, M.; Long, J. R., Exchange Coupling and Magnetic Blocking in Bipyrimidyl Radical-Bridged Dilanthanide Complexes. *J Am Chem Soc* **2012,** *134* (45), 18546-18549.

56. Rinehart, J. D.; Fang, M.; Evans, W. J.; Long, J. R., Strong exchange and magnetic blocking in N23−-radical-bridged lanthanide complexes. *Nature Chemistry* **2011,** *3* (7), 538-542.

Chapter 2 Intuitive Control of Low-Energy Magnetic Excitations via Directed Dipolar Interactions in a Series of Er(III)-Based Complexes

Dipolar coupling is rarely invoked as a driving force for slow relaxation dynamics in lanthanide-based single-molecule magnets, though it is often the strongest mechanism available for mediating inter-ion magnetic interactions in such species. Indeed, for multinuclear lanthanide complexes, the magnitude and anisotropy of the dipolar interaction can be considerable given their ability to form highly directional, high-moment ground states. Herein we present a mono-, di-, and tri-nuclear erbium-based single-molecule magnet sequence, $([\mathrm{Er}-\mathrm{TiPS_2COT}]^+)_n$ $(n = 1-3)$, wherein a drastic reduction in the allowedness of magnetic relaxation pathways is rationalized within the framework of the dipole-dipole interactions between angular momentum quanta. The resulting design principles for multinuclear molecular magnetism arising from intramolecular dipolar coupling interactions between highly anisotropic magnetic states present a nuanced justification of the relaxation dynamics in complex manifolds of individual quantized transitions. Experimental evidence for the validity of this model is provided by coupling the relaxation dynamics to an AC magnetic field across an unprecedented frequency range for molecular magnetism ($10^3 - 10^{-5}$ Hz). The combination of slow dynamics and multiple, low-energy transitions leads to a number of noteworthy phenomena, including a lanthanide single-molecule magnet with three well-defined relaxation processes observable at a single temperature.

2.1 Introduction

The field of molecular magnetism seeks synthetic control over the temporal and spatial flow of magnetic information at the molecular level. One aspect of this control has been the manipulation of the characteristic magnetic relaxation timescale away from that of isotropic paramagnetism.[1] In this research field, known as Single-Molecule Magnetism (SMM), perturbations to a bistable spin ground state are used to generate an energy barrier which prevents direct relaxation between opposite orientations of the magnetic moment.[2-4] Advances in synthetic technique and theoretical understanding in this field have led to slowing of paramagnetic relaxation by a factor of 10^9 or more at liquid nitrogen temperatures.[5] In recent years, the challenge of manipulating the relaxation time has grown more nuanced as the many underlying factors controlling magnetic relaxation have become better understood.[6-10] Molecular-level magnetic design has many interesting prospects, especially if the design principles form the basis of a building-block approach to more complex or hierarchical magnetic structures.

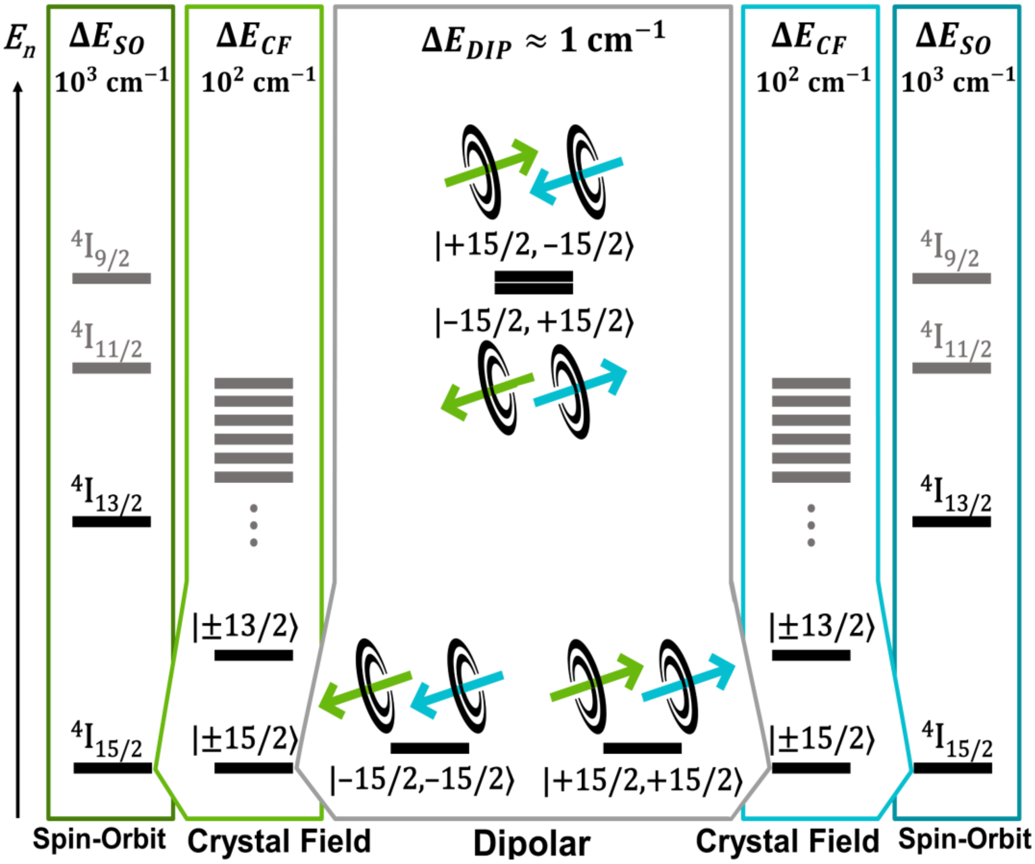

Figure 2.1. Idealized perturbative scheme for a dinuclear interaction between two magnetic centers, each with the general electronic structure of the $[\mathrm{ErCOT}]^+$ unit. The center energy splitting represents a pure magnetic dipolar interaction between pseudo-spin $\tilde{s} = ½$ Kramers doublets with $g_x = g_y = 0$. Green and blue arrows represent single-ion anisotropy axes with the arrow direction representing the composition of magnetic ground state orientations for individual eigenstates.

Two of the major challenges in rational assembly of magnetic building units are (1) maintenance of the desired magnetic properties under the mutable electronic structure conditions of assembly and (2) predicting the net interaction caused by a manifold of magnetic interaction pathways. To overcome the first challenge, we have used the erbium(III) cyclooctatetraenide-based building unit ($[ErCOT]^+$) which can function as a reliable source of axial anisotropy in the presence of a wide range of ligands. Fundamentally, $[ErCOT]^+$ directs single-ion anisotropy by a combination of favorable crystal field interactions between Er^{3+} and COT^{2-} and minimal energy-level restructuring from the preferred tripodal arrangement of the remaining coordination sites.[11-16] The $[ErCOT]^+$ building unit offers a tangible, versatile, synthetic connection between real-space and spin-space for the design of magnetic structures that largely conserve single-ion anisotropy oriented along the Er-COT vector ($\vec{r}_\perp$).

In this work, we extend our approach to demonstrate how control over the single-ion anisotropy axis can be leveraged for chemical intuition over more complex interactions in molecular clusters. For this study, the solubility and steric bulk of the 1,4-bis(triisopropylsilyl)cyclooctatetraenide ($TiPS_2COT^{2-}$) anion are utilized to direct the single-ion anisotropy of Er^{3+} in mono-, di-, and trinuclear complexes. These three molecules, with progressively more complex intramolecular interactions, are used to demonstrate how a simple heuristic (Figure 2.1) yields a structurally intuitive model that is surprisingly consistent with both magnetic and computational data. These results highlight that while the dipole-dipole magnetic interaction is often considered inconsequential or detrimental to control of magnetic relaxation, in properly controlled cases,[17] it can drastically and reliably alter the allowed-ness of transitions, presenting a reliable means of control over complex low-energy state manifolds.

2.2 Experimental

As a basis for our analysis of molecular magnetic relaxation at the anisotropic dipolar limit, we synthesized mononuclear (η^8-1,4-bis(triisopropylsilyl)cyclooctatetraenyl)-iodo-bis(tetrahydrofuran)-erbium (**1**), dinuclear bis(η^2-iodo)-bis((η^8-1,4-bis(triisopropylsilyl)cyclooctatetraenyl)-tetrahydrofuran-erbium) (**2**), and trinuclear (μ_2-iodo)-bis(μ_3-iodo)-tris(η^8-1,4-bis(triisopropylsilyl)cyclooctatetraenyl-erbium) (**3**). Briefly, synthesis of **1** is achieved by addition of dipotassium 1,4-bis(triisopropylsilyl)-cyclooctatetraenide (K_2TiPS_2COT) to an erbium triiodide suspension (−30° C, THF). After extraction into THF and filtration, a vapor diffusion with pentane yields pink needles of **1**. Dissolution of **1** into benzene, and crystallization from a benzene/pentane layering yields the dinuclear complex **2**, as red-orange plates. The trinuclear form, **3**, is synthesized via slow addition of trimethylaluminum (TMA, −30° C, toluene) to **1** or **2**. Pentane trituration of the resulting oil, followed by crystallization out of a concentrated hexane solution (−30° C), leads to orange crystals of **3** (Figure 2.2). Quantitative

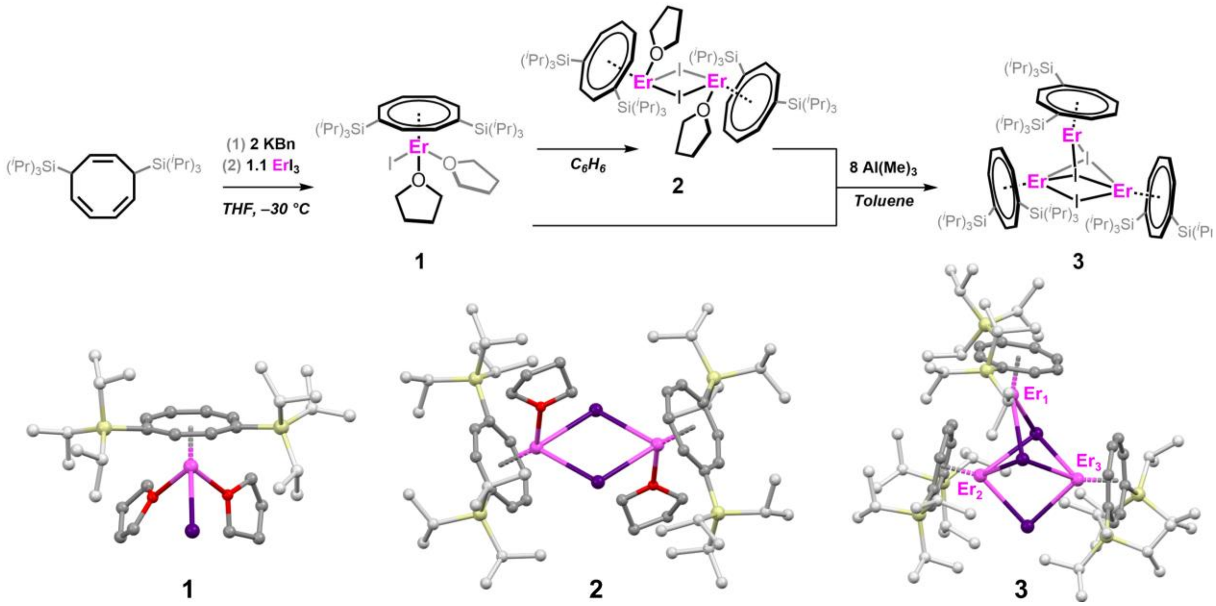

Figure 2.2. Synthetic scheme of **1**, **2**, and **3** (*top*). Solid states structures of **1**, **2**, and **3** with spheres representing erbium (light pink), iodine (purple), silicon (light yellow), oxygen (red), and carbon (gray). Hydrogen atoms have been omitted and triisopropylsilyl groups have been lightened for clarity (*bottom*).

solid-state structural information was obtained from single-crystal X-ray diffraction data collected with a Mo anode source (Figure 2.2). Similar to analogous complexes synthesized with the unsubstituted cyclooctatetraenide anion (COT^{2-}),[13,18-29] mononuclear **1** and dinuclear **2** adopt piano-stool and inversion-symmetric [μ_2-I]$_2$ geometries, respectively. Compound **3** adopts a low symmetry trinuclear structure with three crystallographically unique Er^{3+} centers. Two Er^{3+} centers are nearly collinear, bridged by three iodide ligands. The third erbium center is bridged by two iodide ligands and participates in a nearly orthogonal configuration in relation to the former two metal centers. Devoid of coordinating solvent, $TIPS_2COT^{2-}$ completes the coordination sphere for each metal center. Erbium centers within **2** are separated by 4.8 Å, whereas the distances between erbium centers in **3** vary between 3.9 – 4.6 Å (Tables 2.1, 2.2, Supplemental Tables S.2.1, S.2.2). The nearest intramolecular Er-Er distances are approximately double those seen intermolecularly for both compounds.

Table 2.1: Selected distances (Å) for **2** and averages between both fragments in the unit cells. $\vec{r}_{\perp}$ represents the distance between the COT centroid and erbium, $\vec{r}$ is the internuclear distance between the two erbium centers.

	$\vec{r}_{\perp}$	$\vec{r}$
Fragment 1	1.7476(3)	4.7873(7)
Fragment 2	1.7517(3)	4.8264(7)
Averages	1.7497(3)	4.8069(7)

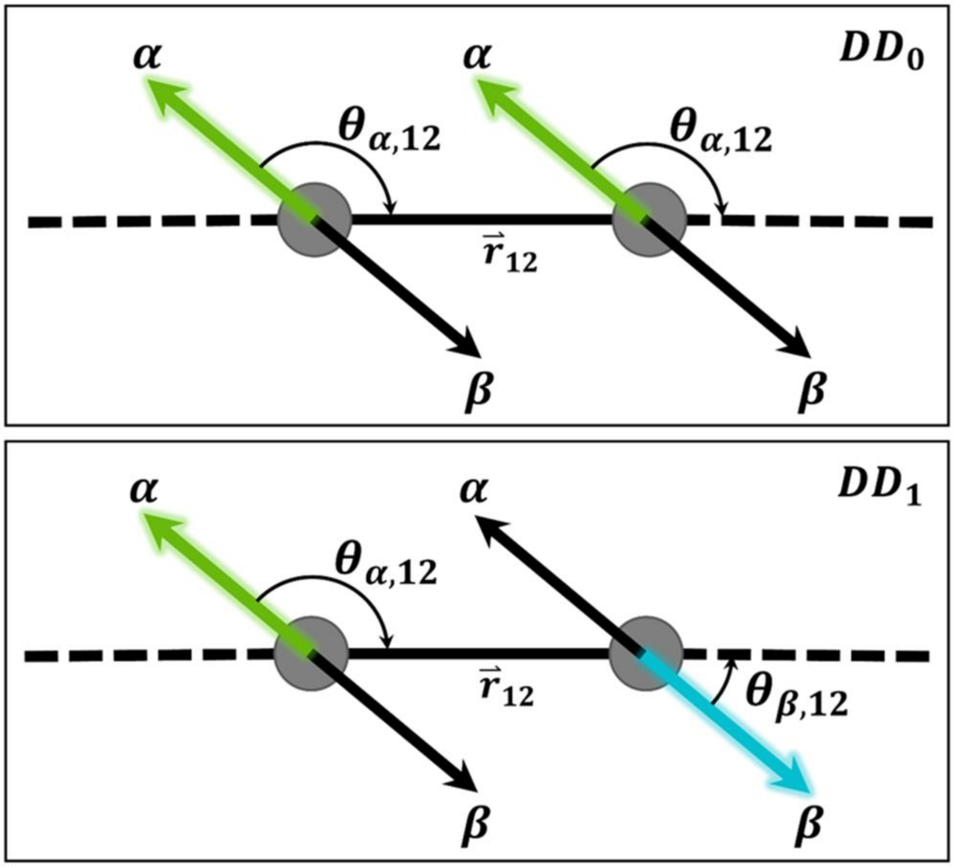

Figure 2.3 Simplified graphic of crystal structure of **2**, demonstrating angular projection of the Er-COT vector ($\vec{\boldsymbol{r}}_{\perp,\mathbf{n}}$) onto the internuclear axis ($\vec{\boldsymbol{r}}$) between magnetic centers (gray) making up the ground ($\boldsymbol{DD_0}$) and excited ($\boldsymbol{DD_1}$) dipole doublet states. The terms $\boldsymbol{\alpha_{n_i}}$ and $\boldsymbol{\beta_{n_i}}$ represent the spin polarization of the single-ion Kramers wavefunctions as orthogonal basis elements located on Er center n_i. Angles $\boldsymbol{\theta_{\alpha_{n_i},\vec{r}_{n_in_j}}}$ and $\boldsymbol{\theta_{\beta_{n_i},\vec{r}_{n_in_j}}}$ represent the angle between $\boldsymbol{\alpha_{n_i}}$ and $\vec{\boldsymbol{r}}_{n_in_j}$ as tabulated below. Parameters are denoted with subscripts corresponding to their respective erbium centers and the internuclear axis the moment is being projected onto.

As discussed previously,[1,11,13] the Er–COT vector ($\vec{r}_\perp$) can be used as a fully structural, real-space proxy for the single-ion anisotropy axis in these compounds. As such, their magnetic behavior is befitting discussion under the lens of dipolar coupling. The magnetic dipole-dipole equation (Eq. 1) depends on magnetic moments ($\vec{\mu}$) and the internuclear unit vector ($\hat{n} = \vec{r}/r$), where r is the magnitude of $\vec{r}$.

$$E_{dip} = -\frac{\mu_{Bohr}^2}{r^3}[3(\vec{\mu}_1 \cdot \hat{n}_{12})(\vec{\mu}_2 \cdot \hat{n}_{12}) - \vec{\mu}_1 \cdot \vec{\mu}_2] \qquad (Eq.\ 1)$$

In our analysis, two structural parameters are chosen due to their connection to the dipolar term in magnetic interactions *(vide infra)*: the internuclear erbium distance (r) and the angle from the projection of $\vec{r}_{\perp}$ onto $\vec{r}$ (θ; Figure 2.3, Table 2.2, shown for **2**). These purely structural parameters provide an intuitive and simple approximation of the type of coupling expected to be present in the ground and excited dipolar states. In the discussion, these structural, real-space parameters will be used to predict and rationalize the computationally predicted (spin-space) splitting of the single-ion states by the dipole-dipole interaction and justify the nature and magnitude of the time-dependence in the magnetic results. Importantly, the success of this model demonstrates how the full versatility of synthetic design can be brought to bear on quantum challenges currently lacking a diversity of candidate materials.

Table 2.2 Tabulated angles, $\boldsymbol{\theta_\alpha}$ and $\boldsymbol{\theta_\beta}$, of the projection of moment represented by the Er-COT vector ($\vec{\boldsymbol{r}}_{\perp,\mathbf{n}}$) onto the internuclear axis ($\vec{\boldsymbol{r}}$) between magnetic centers making up the ground and excited dipole doublets of **2**.

$\boldsymbol{DD_0}$	**Fragment 1**	**Fragment 2**	**Averages**
$\theta_{\alpha,12}$	144.914(15)	144.140(15)	144.527(15)
$\theta_{\alpha,12}$	144.914(15)	144.140(15)	144.527(15)
$\boldsymbol{DD_1}$	**Fragment 1**	**Fragment 2**	**Averages**
$\theta_{\alpha,12}$	144.914(15)	144.140(15)	144.527(15)
$\theta_{\beta,12}$	35.086(15)	25.860(15)	35.473(15)

2.3 Results

2.3.1 Static Magnetic Properties

Temperature-dependent magnetic susceptibility data were collected on crushed microcrystalline samples between $T = 2–300$ K at an applied field of $H_0 = 100$ Oe. Field-cooled susceptibility data (FC, $\chi_M T$) were collected by subjecting samples to an external field of $H = H_0$ as the temperature was lowered to $T = 2\ K$ with subsequent data collection occurring as the temperature was incremented back up to $T = 300\ K$. Zero-Field Cooled susceptibility data (ZFC, $\chi_M T$) were collected in a similar fashion, but without the biasing field during the initial cooling. As an added precaution, active removal of remnant magnetic fields was put into effect prior to measurement by linearly ramping the field to $H = 1$ T with subsequent oscillations about $H = 0$ T of diminishing magnitude. Behavior of $\chi_M T$ for **1–3** is represented as a susceptibility-temperature product ($\chi_M T$) to highlight deviations from Curie paramagnetism (Figure 2.4).

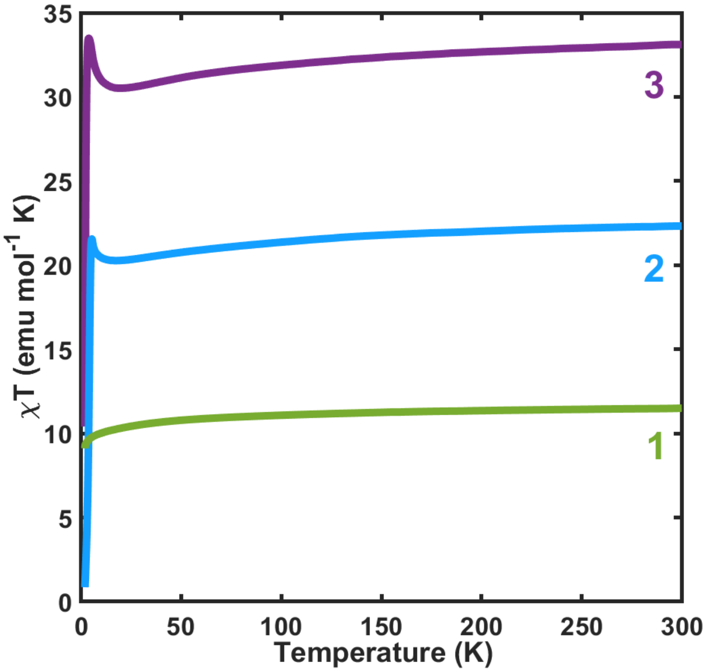

Figure 2.4: Zero-field cooled magnetic susceptibility data plotted as χT vs. T for **1–3** collected between T = 2–300 K under an applied field of H = 100 Oe.

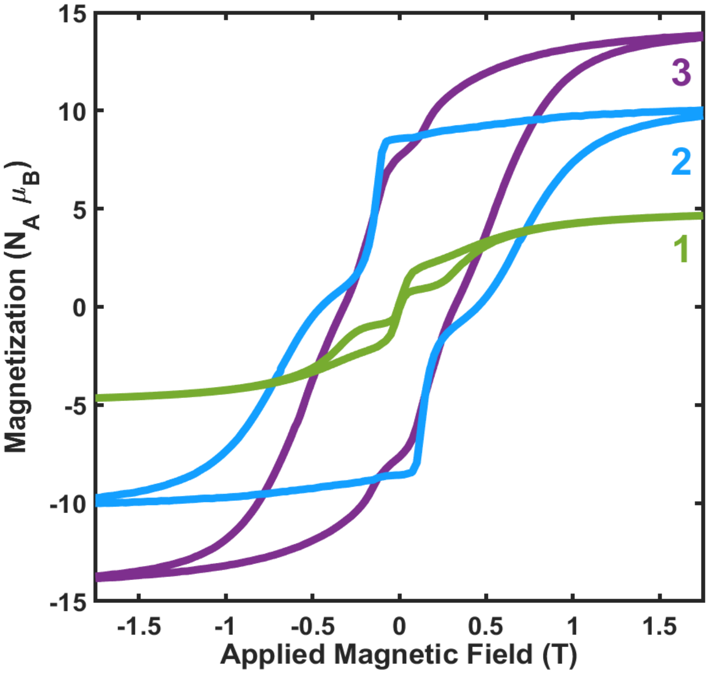

Figure 2.5: Isothermal magnetization of **1** (green), **2** (blue), and **3** (purple) at 2 K with H_C = 0.00, 0.45, and 0.32 T, respectively. Data were collected at a 50 Oe s^{-1} magnetic field sweep rate.

Analysis of the $\chi_M T$ product for $\mathbf{1}$–$\mathbf{3}$ at $T = 300\ K$ shows near-quantitative agreement with a Landé g-factor description[30] of an isotropic $J = 15/2$ state (100.0, 97.0, and 96.0 % of the full value for $\mathbf{1} - \mathbf{3}$, respectively). As T is lowered, each data set shows a monotonic decrease in $\chi_M T$ corresponding to thermal depopulation of higher-energy Kramers doublets of the $J = 15/2$ spin-orbit manifold. At low temperatures, multinuclear complexes $\mathbf{2} - \mathbf{3}$ display markedly different behavior compared to mononuclear $\mathbf{1}$. The multinuclear complexes display a sharp upturn in $\chi_M T$ as internuclear coupling begins to dominate changes to the Boltzmann distribution. With continued lowering of temperature, the ZFC data of $\mathbf{2} - \mathbf{3}$ reach maxima ($\mathbf{2}$, $\chi_M T$ = 21.6 emu K mol^{-1}, T = 5.4 K; **3,** $\chi_M T$ = 33.5 emu K mol^{-1}, T = 3.9 K). A divergence in FC/ZFC behavior is observed near the maxima, with both **2** and **3** displaying abrupt drops in ZFC magnetization. This behavior is indicative of magnetic blocking on the measurement timescale. The low temperature magnetism of $\mathbf{2-3}$ contrasts with observations for mononuclear $\mathbf{1}$, where $\chi_M T$ simply declines monotonically with T over the entire measurement range.

To further probe the magnetic blocking behavior, isothermal magnetization measurements were collected with a scan rate of $dH/dt = 50\ \mathrm{Oe/s}$. At $T\ =\ 2$ K, each compound reaches magnetic saturation ($M_{sat} =\ 5.0, 10.5,$ and $14.7\ N_A\mu_B$ for $\mathbf{1-3}$, respectively) with applied fields above $H\ =\ 4$ T. Consistent with the absence of evidence for magnetic blocking in its FC/ZFC susceptibility curves, $\mathbf{1}$ displays butterfly-shaped hysteresis with negligible remanent magnetization ($M_r = M_{H=0} = 0$) at our scan rate. Also consistent with divergences observed in ZFC/FC $\chi_M T$ data, **2** and **3** display open hysteresis with coercive fields of $H_c =\ 0.45$ and 0.32 T, respectively (Figure 2.5).

2.3.2 Dynamic Magnetic Properties

Magnetic relaxation dynamics in the $\nu_{AC} = 10^{-1} - 10^{3}$ Hz regime were probed using standard AC magnetometry techniques. Additional longer-timescale relaxation dynamics ($\nu_{AC} = 10^{-1} - 10^{-5}\mathrm{Hz}$) were probed via a previously described method of coupling the magnetic relaxation response to low-frequency square-wave drive fields (Figure 2.6, top).[14] Temperature and frequency-dependence of the AC susceptibility response of **1**–**3** is decomposed into in-phase (χ_M') and out-of-phase (χ_M'') components of the molar magnetic susceptibility and fit to an extended Debye model, which sums up one, two, or three modified Debye functions for **1**–**3**, respectively.[31-34] This model captures inhomogeneous broadening of the relaxation distribution (α), as well as the presence of one or more characteristic relaxation times for the magnetization (τ). Compound **1** displays highly homogeneous relaxation, with the α parameter very close to zero

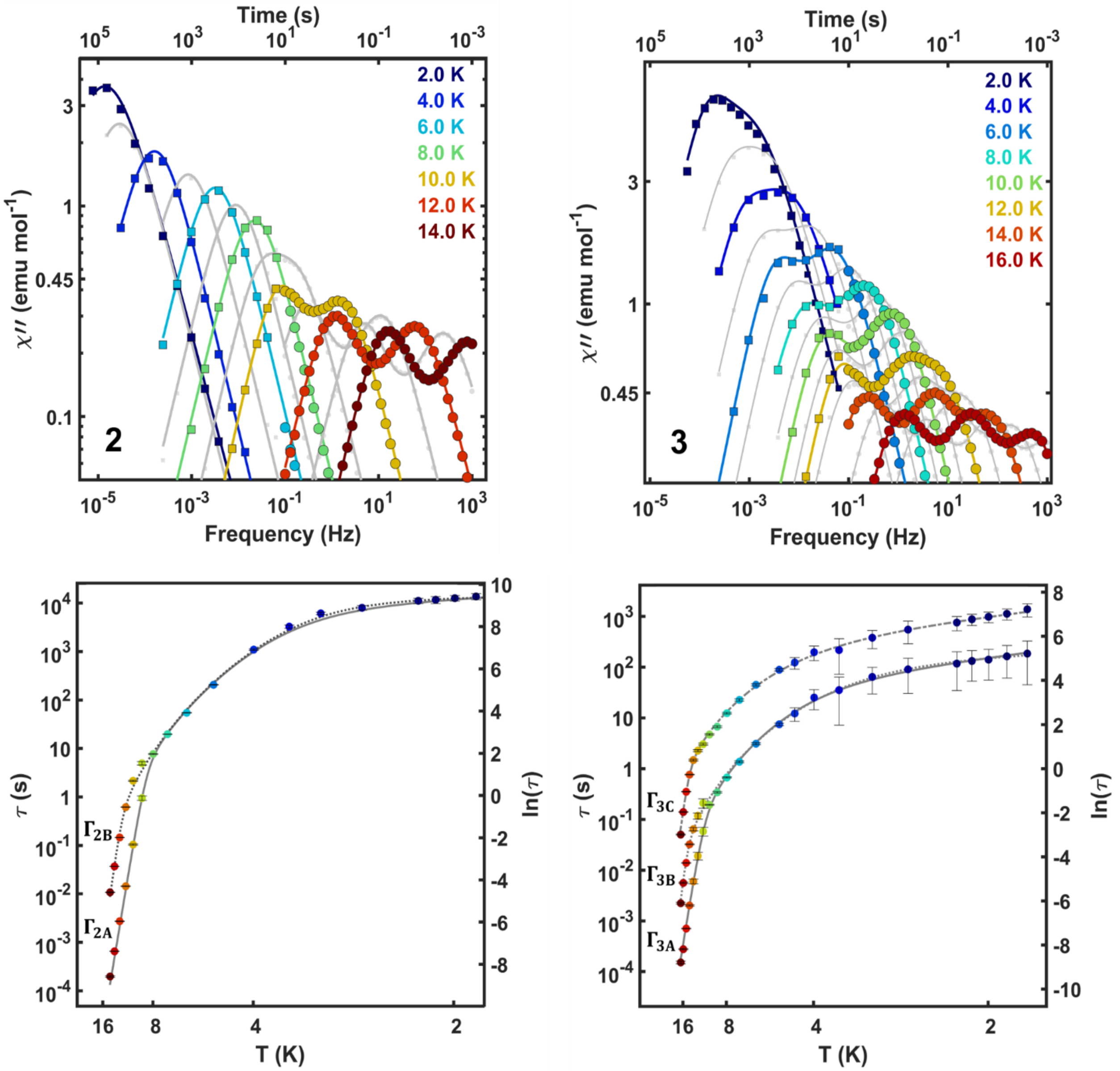

Figure 2.6: Top, plots of AC out-of-phase susceptibility (χ'') for **2** (left) and **3** (right). Data points are susceptibilities measured via standard AC measurements (circles) and extracted from Fourier analysis of VSM data (squares). Lines represent fits to an extended Debye model. For clarity, odd-temperature data are grayed out. Bottom, Arrhenius plots of relaxation times versus temperature for **2** (left) and **3** (right). Gray lines are fits to a multi-term relaxation model, Equation 7. For reference, in the text, each process (**Γ**) is subscripted with the associated molecule (**2-3**) and indexed alphabetically from shortest to longest timescale. Error bars demonstrate upper and lower error limits of τ values.

over a broad temperature range and a single, well-defined relaxation process. In contrast, multiple relaxation processes are present for $\mathbf{2-3}$ (Figure 2.6, Top, AC Susceptibility; Bottom, Arrhenius plots). Two relaxation processes were resolved within the measured range of $T = 9 – 14$ K for **2**, with subsequent merging to a single resolvable process at lower temperatures. Three distinct relaxation processes were observed for **3** from $T = 14 - 17$ K with the faster two merging at lower temperatures and the slowest remaining distinct down to $T = 2$ K (Figure 2.6). These data are consistent with a model for multiple relaxation times of intramolecular origin proposed by Ho and Chibotaru.[34] Importantly, the model predicts that when multiple relaxation processes contribute significantly within the measured frequency range, one can be parameterized as the sum of rates of individual processes (Orbach, Raman, etc.), whereas the second process will solely depend on another Orbach relaxation rate. We see this to be consistent with our experimental findings, such that the relaxation processes $\boldsymbol{\Gamma_{2A}}$ and $\boldsymbol{\Gamma_{2B}}$ (and $\boldsymbol{\Gamma_{3A}}$, $\boldsymbol{\Gamma_{3B}}$, $\boldsymbol{\Gamma_{3C}}$) differ in their respective Orbach regimes.

2.3.3 Computational Findings

Further understanding of the connection between the spatial arrangement of magnetic centers within each molecule and the resulting magnetic properties was garnered through computational modeling. The basic approach was to use the OpenMolcas computational package for ab initio calculation of the electronic structure of $\mathbf{1-3}$ including the crucial effects of spin-orbit coupling.[35,36] Subsequently, the SINGLE_ANISO module within OpenMolcas was employed to formulate pseudospin Hamiltonians describing the low-lying state manifold at single spin centers. For **1**, this represents a model for the magnetic behavior of the molecule, while for $\mathbf{2-3}$, it represents the electronic structure of each spin center of the cluster in the absence of any coupling perturbation from other spin centers. In $\mathbf{2-3}$, the POLY_ANISO module of OpenMolcas was used to model the nature and strength of interactions between single-ion magnetic centers.[37] Roughly, these steps can be considered a computational realization of the heuristic perturbations introduced in Figure 2.1. Input structural geometries for these calculations were taken from atom position refinements against crystallographic data and were not optimized further. As expected for a mononuclear structure based on the [ErCOT]$^+$ building unit,[12,13,15] **1** possesses a strongly axial ground state $(KD_0; c_J|\pm M_J\rangle = 0.98|\pm\frac{15}{2}\rangle)$ where c_J is the coefficient of the largest contributor from the M_J basis to the ground state Kramers doublet, KD_0. It should be noted that the axial ground state projection into real-space is anticipated by the structural parameter, θ, discussed above, with only a minor deviation represented by the cant angle $\left(\theta_{cant,\mathbf{1}} = 1.6°\right)$. The bistable ground Kramers doublet, KD_0, is separated from the first excited doublet, KD_1 $(0.93|\pm\frac{13}{2}\rangle)$, by a

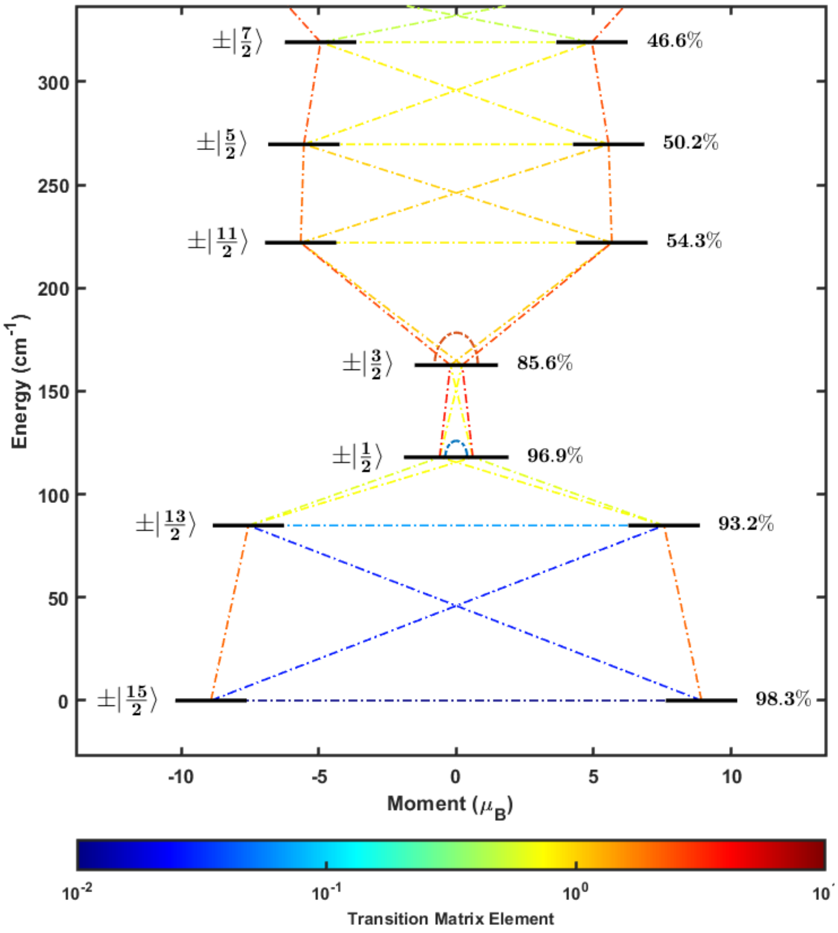

Figure 2.7: Calculated spectrum of the seven lowest energy Kramers states for **1**. States are represented by black lines and are labeled by their largest $\pm M_J$ component (left) and the percentage of that component (right). Transverse magnetic moment matrix elements (dashed lines) are colored according to their respective values (colorbar).

crystal field energy of $85\,\mathrm{cm}^{-1}$; the second excited Kramers doublet is found at $118\,\mathrm{cm}^{-1}$ (KD_2: $0.97|\pm\frac{1}{2}\rangle$); and the third at $163\,\mathrm{cm}^{-1}$ (KD_3: $0.86|\pm\frac{3}{2}\rangle$); (Figure 2.7, Tables 2.3 – 2.4).

Table 2.3: *J* = 15⁄2 manifold spectrum of **1** and **[1]**.

	1		**[1]**	
KD_n, n =	M_z (μ_B)	E (cm^{-1})	M_z (μ_B)	E (cm^{-1})
0	8.93	0.00	8.93	0.00
1	7.56	84.85	7.62	89.12
2	0.60	117.92	6.10	133.99
3	0.21	162.62	0.29	180.44
4	5.66	221.98	5.75	239.27
5	5.55	269.65	4.96	287.84
6	4.94	319.19	4.90	337.75
7	7.06	350.44	6.98	365.98

Table 2.4: Calculated cant angles and *g*-values of **1** and **[1]**.

g	**1**	**[1]**
gX	0.006429	0.005064
gY	0.009390	0.007700
gZ	17.851200	17.861155
θ_{cant}	1.60°	1.08°

As proof-of-concept, and to simplify further computational load, we completed identical calculations on a truncated version of **1**, replacing the triisopropylsilyl groups with hydrogen atoms placed according to a standard riding model[38,39] (referred to as **[1]**). Aligning with previous findings,[14,40,41] symmetry-lowering substitutions on COT^{2-} appear to play a negligible role in modulating the cylindrical p-electron density needed to stabilize prolate $M_J = \pm\frac{15}{2}$ states on the Er^{3+} ion ($\theta_{cant,[\mathbf{1}]} = 1.1°$; $\theta_{cant,\mathbf{1}} = 1.6°$; Table 2.4). With this in mind, triisopropylsilyl groups were substituted with hydrogen atoms in the ab initio calculations for **2** and **3** placed according to a standard riding model, (hereafter referred to as **[2]** and **[3]**).

Averages of the moduli of the transition matrix elements connecting eigenstates through a Zeeman perturbation ($\|T_{ij}\|$) are tabulated for states within the $J = \frac{15}{2}$ manifold for **[1]-[3]** (see Associated Supplementary Content, Section 2.6.4). As discussed in prior work,[42] the magnitude of the magnetic moment matrix terms correlates to the probabilities of those transitions. In this work, we will utilize the following notation in our discussion of transitions between states:

$$KD_{n,\alpha} \overset{\|T_{ij}\|}{\underset{\longrightarrow}{\longleftarrow}} KD_{n,\beta} \;\; (Eq. 2)$$

where n is the KD state, α and β are Kramers doublet components related by time-reversal, and $\|T_{ij}\|$ is the average magnetic moment matrix element for that transition. As seen in **[1]**, there is a relatively low intrinsic probability for QTM transitions within the ground state,

$$KD_{0,\alpha} \overset{10^{-3}}{\underset{\longrightarrow}{\longleftarrow}} KD_{0,\beta} \;\; (Eq. 3),$$

and first excited state,

$$KD_{1,\alpha} \overset{10^{-2}}{\underset{\longrightarrow}{\longleftarrow}} KD_{1,\beta} \;\; (Eq. 4).$$

In the absence of internuclear interactions, the inversion symmetric erbium centers in **[2]** display low-energy Kramers landscapes roughly equivalent to the mononuclear compound $\left(KD_0\text{: } 0.99 \left|\pm\frac{15}{2}\right\rangle;\ KD_1, 96\ \text{cm}^{-1}\text{: } 0.98 \left|\pm\frac{13}{2}\right\rangle;\ KD_2, 194\ \text{cm}^{-1}\text{: } 0.98 \left|\pm\frac{1}{2}\right\rangle;\right.$ $\left.KD_3, 240\ \text{cm}^{-1}\text{: } 0.86|\pm\frac{3}{2}\rangle\right)$. A similar correlation between the electronic and physical structure is seen as well $\left(\theta_{cant,[\mathbf{2}]} = 1.4°;\ \text{Associated Supplemental Content, Section 2.6.4}\right)$:

$$KD_{0,\alpha} \overset{10^{-5}}{\underset{\longrightarrow}{\longleftarrow}} KD_{0,\beta} \;\; (Eq. 5)$$

and

$$KD_{1,\alpha} \overset{10^{-4}}{\underset{\longrightarrow}{\longleftarrow}} KD_{1,\beta} \ \ (Eq. 6).$$

It's important to note that the $[ErCOT]^{+}$-based anisotropy is not wholly inert to crystal field perturbations. The single iodine and two THF ligands of **[1]** can be expected to lead to differences in mixing terms when compared to the two iodine and one THF ligand present in **[2]**. Although they can be significant in excited states, these differences are minimized in dipolar coupling between KD_0 states where our analysis focuses.

Several computational models of trinuclear **3** were generated utilizing complex **[3]** due to its low symmetry and three crystallographically distinct Er^{3+} centers. For each Er^{3+} center, a separate single-ion calculation was completed, the results of which yielded three distinct energy manifolds (see Associated Supplemental Content, Section 2.6.4). All three centers exhibit nearly pure ground and first excited Kramers doublets with state mixing in further excited states as expected for $[ErCOT]^{+}$-based subunits. The robust nature of the $[ErCOT]^{+}$ anisotropy building unit to crystal field perturbation is evident in the small range of KD_1 energy predictions (E_{KD_1} = $99(1), 81(0), 95(2)\ \text{cm}^{-1}$ for $[\mathbf{3}]_{\boldsymbol{Er1}}$, $[\mathbf{3}]_{\boldsymbol{Er2}}$, $[\mathbf{3}]_{\boldsymbol{Er3}}$, respectively), when averaged between both fragments in the unit cell. In each case θ remains predictive of the local axiality with minor cant angles predicted in spin-space ($\theta_{cant,[\mathbf{3}]_{1-3}} = 3.4°, 6.5°, 2.7°$). Note that while the single ion ground states (KD_0) of $\mathbf{1-3}$ are of nearly pure $M_J = \pm 15/2$ composition, it is still preferrable to use the α and β notation to avoid confusion between local and global spin orientations, and we will continue to utilize this notation in our discussion of the dipole doublets (DD_n) generated by POLY_ANISO and introduced in the following section. This will become especially important in the discussion of **3**, where three non-collinear spins must be tracked.

2.4 Discussion

Relaxation dynamics in multinuclear lanthanide complexes has been a topic of interest since the first multi-nuclear Dy-based clusters were shown to display slow relaxation.[43] Unless coupling pathways are carefully engineered,[44-47] single-ion effects remain dominant, due to the localized nature of the 4f orbitals. Although minor in terms of the overall energetics, the intramolecular magnetic coupling can induce a quantized molecular form of exchange biasing[48] wherein the local magnetocrystalline anisotropy barrier is kept largely static, yet QTM pathways are drastically restructured.[49-51] Within this context, we will discuss the merits of describing $\mathbf{1-3}$ through the progressive perturbative approach summarized in Figure 2.1. This model allows for rationalization of exchange-biasing behavior as well as a surprisingly intuitive understanding of the low-energy magnetic manifolds of highly anisotropic, dipolar-coupled systems.

Critically, the behavior of **1** provides a magnetic building unit for descriptions of the more complex clusters, $\mathbf{2-3}$. In **1**, the observation of a single-relaxation process with a transition from over-barrier ($U_{eff} = 82(2)\ \mathrm{cm}^{-1}$) to through barrier relaxation at relatively fast timescales is consistent with single-ion anisotropy of Er^{3+} with COT^{2-} ligation. Interestingly, the relaxation dynamics of **1** closely mimic those of $Er(COT)I(THF)_2$, ($U_{eff} = 95\ \mathrm{cm}^{-1}$),[12] indicating that any TiPS-induced perturbation of the ring electronic structure have negligible effect on the SMM properties. Within the context of our perturbative model, the ground Kramers doublet of **2**, KD_0, can be considered as the interaction of two high-purity $M_J = \pm 15/2$ doublets via the magnetic dipole interaction. As observed via AC magnetic relaxation measurements, two temperature-dependent Orbach processes are present ($T > 9$ K; $\mathbf{\Gamma_{2A}}$ and $\mathbf{\Gamma_{2B}}$, Figure 2.6, left). Below $T = 9$ K, the timescale of the AC resonance merges into a single process with sublinear Arrhenius temperature dependence indicative of Raman-type relaxation. Below $T = 3$ K, a region of linear temperature dependence is once again observed, with a large increase in the characteristic attempt time. To describe the low temperature relaxation barrier and to properly fit the dynamic magnetic data, we've implemented a second Arrhenius-type relaxation term in the multi-term relaxation equation typically used to fit magnetic data (Equation 7). Herein, D_{eff}, describes the dipolar barrier and τ_D, the dipolar attempt time (analogous to U_{eff} and τ_0 at higher temperatures):

$$\tau^{-1} = \tau_0^{-1} exp\left(\frac{-U_{eff}}{k_B T}\right) + CT^n + \tau_D^{-1} exp\left(\frac{-D_{eff}}{k_B T}\right) \qquad (Eq. 7)$$

Extraction of these parameters from the fitting of experimental relaxation data for **2** begins to shed light on the nature of the dipolar interaction, which brings about a small, low temperature dipolar relaxation barrier ($D_{eff} = 0.63(4)\ \text{cm}^{-1}$) and a lengthy dipolar attempt time ($\tau_D = 9.2(4) \times 10^3\ s$; Table 2.5; also see Associated Supplemental Content, Section 2.6.4).

To further probe the viability of the dipole interaction as the defining perturbation controlling long-timescale magnetic dynamics, the splitting of the KD_0 manifold by internuclear dipolar coupling was treated using the POLY_ANISO module of OpenMolcas. The emergence of a weakly-temperature dependent linear region at low temperatures is consistent with the interpretation of a dipolar splitting to give new eigenstates (referred to here as dipole doublets, DD_n, to differentiate them from the rigorously degenerate single-ion Kramers doublets, KD_n). The overwhelmingly axial nature of the single-ion states ($g_x = 0.0002; g_y = 0.0002; g_z = 17.9130$) results in minimal mixing which is responsible for the doublet interpretation instead of the singlet-triplet formalism appropriate for interaction of isotropic spin states. The nature and magnitude of the splitting of these states induced by the dipolar interaction is determined by the anisotropy of the single-ion moments and their collective projection onto the internuclear axis (Eq. 1) to yield a ferro- or antiferromagnetic coupling interaction.

Table 2.5: Best-fit, calculated, and predicted relaxation parameters of **1-3**. Fit parameters for **1** are extracted from a multi-term relaxation mechanism equation (Eq. S.2.2), where τ is the fitted relaxation time, τ_0 is the attempt time, U_{eff} is the effective barrier, C is the effective Raman relaxation coefficient, n is the Raman exponent, and *QTM* is the quantum tunneling relaxation term. Fit parameters for **2** and **3** follows Eq. 7, where the QTM term has been replaced with a dipolar term where τ_D is the dipole attempt time, and D_{eff} is the dipolar effective barrier. Calculated values show the dipole doublet energy splittings computed from ab initio electronic structure data of **[2]** and **[3]**. Predicted energy splittings use crystallographic parameters of **2** and **3** (see Discussion).

		Fit (*experimental*)						Calculated (*ab initio*)		Predicted (*empirical*)
Compound	Process	U_{eff} (cm^{-1})	τ_0 (s)	C	n	QTM				
1	Γ_1	82(2)	$4.6(7) \times 10^{-9}$	$2.5(8) \times 10^{-5}$	7.5(3)	$9.9(1) \times 10^{-3}$				
Compound	Process	U_{eff} (cm^{-1})	τ_0 (s)	C	n	D_{eff} (cm^{-1})	τ_D (s)	Dipole Doublet	ΔE_{calc} (cm^{-1})	ΔE_{pred} (cm^{-1})
2	Γ_{2A}	138(2)	$2.6(6) \times 10^{-10}$	$1.5(4) \times 10^{-7}$	6.7(2)	0.63(4)	$9.2(4) \times 10^{3}$	**DD₁**	0.65	0.62
	Γ_{2B}	152(1)	$2.5(3) \times 10^{-9}$	$8.7(6) \times 10^{-8}$	6.8(0)					
3	Γ_{3A}	139(1)	$1.3(1) \times 10^{-9}$	$4.0(0) \times 10^{-5}$	5.0(0)	0.26(5)	$1.5(5) \times 10^{2}$	**DD₁**	0.22	0.41
	Γ_{3B}	169(1)	$2.0(2) \times 10^{-9}$					**DD₂**	1.11	1.27
	Γ_{3C}	196(0)	$4.0(7) \times 10^{-9}$	$6.9(0) \times 10^{-6}$	4.5(0)	2.90(1)	$1.5(0) \times 10^{2}$	**DD₃**	2.83	2.79

With a significant projection of the anisotropy axes in **[2]** onto the internuclear axis, the ground state is expected to correspond to the ferromagnetic orientation. We see this to be corroborated by the calculational output of POLY_ANISO and the upturn in χT vs. T in the static magnetic data (Figure 2.4): the ground state of **[2]** is associated with a largely ferromagnetic composition $(DD_0;\ M_Z = \pm 18)$, and the excited dipole state $(DD_1; M_Z = 0)$ with an antiferromagnetic composition (Figure 2.8-a). Furthermore, the dipole splitting for a transition between the ground dipole doublet (DD_0) and the excited dipole doublet (DD_1) of **[2]** estimated from fitting the relaxation data $(D_{eff} = 0.63(4)\ \mathrm{cm}^{-1})$ and that computed ab initio $(\Delta E_{calc} = 0.65\ \mathrm{cm}^{-1})$ are in excellent agreement (Figure 2.8, Table 2.5, see Associated Supplemental Content, Section 2.6.4). Excitingly, these data can also be interpreted via the real-space orientation of single-ion anisotropy centers through a dipolar coupling mechanism utilizing only two structural parameters. Thus, we can begin to understand, predict, and even design, dipolar interactions to drastically alter the nature of transitions between states without large perturbations to their energy.

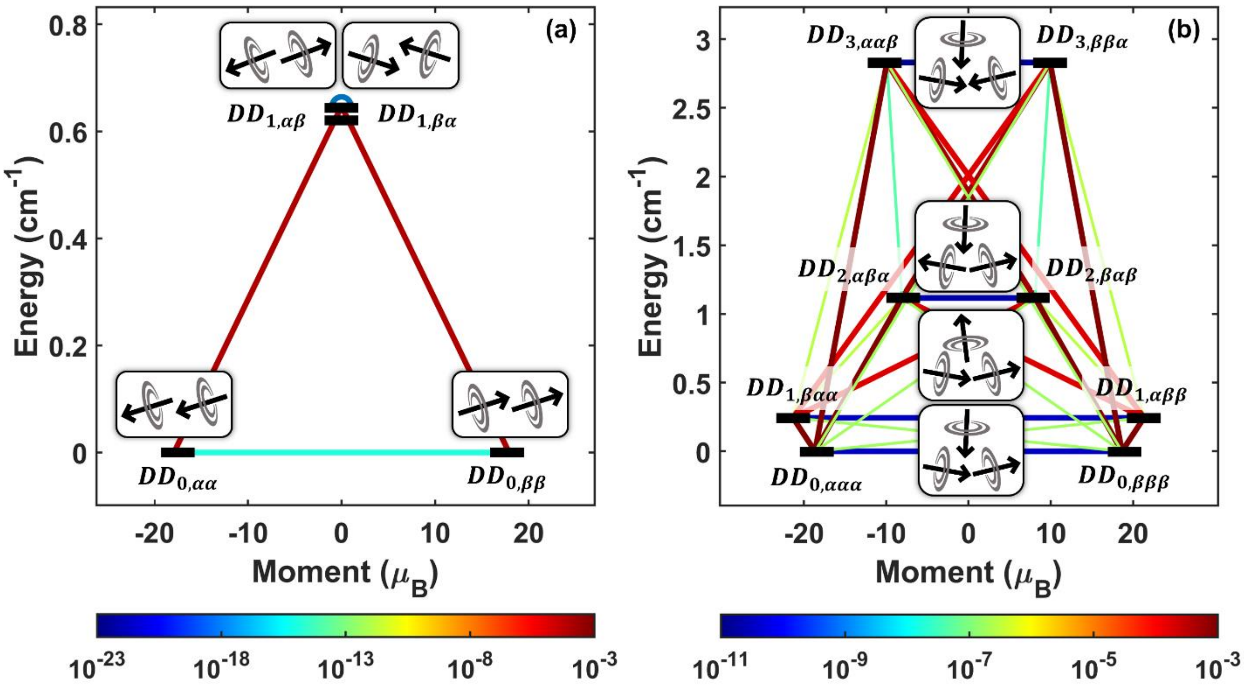

Figure 2.8: Calculated energy states of the magnetic dipole interaction Hamiltonian and representative Ising configurations for [2] and [3]. The Hamiltonian bases correspond to the four and eight pseudospin ½ single-ion states for [2] (a) and [3] (b), respectively. The g-factors were calculated at the CASSCF level. Ground and highest-excited state configurations for both species correspond to maximal net-ferromagnetic and net-antiferromagnetic interactions, respectively. Calculations were performed on structures with triisopropylsilyl groups replaced with hydrogen atoms. States are represented by black lines. Transverse magnetic moment elements (colored lines) are colored according to their magnitude (colorbar). α and β are dipole doublet components related by time-reversal, as discussed in the text. Dipole components for [3] are labeled in order according to Figure 2.2, starting at the upper Er-1 center and progressing counter-clockwise: $DD_{n,Er1,Er2,Er3}$.

A simple and intuitive calculation appears to be able to predict and approximate the nature of coupling present in **2**, utilizing only two crystallographically derived structural parameters: the internuclear erbium distance, r, and the angle, θ, from the projection of the Er-COT vector ($\vec{r}_\perp$) onto $\vec{r}$. Associating $\vec{r}_\perp$ as the real-space indicator of the anisotropy axis yields a proportional, empirically parameterized version of the dipolar equation:

$$E_{dip} = -\frac{\mu_B^2\mu^2}{r^3}[3\cos\theta_1\cos\theta_2 - \cos(\Delta\theta)] \qquad (Eq. 8)$$

In these pair-wise dipolar interactions, θ_1 and θ_2 are angles from the projections of moment onto the internuclear axis. $\Delta\theta$ is the difference between angles θ_1 and θ_2, and r is the magnitude of the internuclear vector. For example, when $\theta_1 = \theta_2 = 0°$, a maximally ferromagnetically coupled ground state is obtained, whereas when θ_1 = 0° and $\theta_2 = 180°$ the antiferromagnetically coupled state is favored. Sample calculations, figures, and angle tabulations are provided in the Associated Supplemental Content, Section 2.6.2.

Use of our experimental data without further parameterization (Tables 2.1, 2.2; Supplementary Tables S.2.1, S.2.2, Figure S.2.1), predicts that **2** will have a ferromagnetically coupled dipolar ground state and an antiferromagnetically coupled dipolar excited state. Scaling the experimentally derived data by values expected for an anisotropic erbium(III), predicts these states to be split by $0.62\ \text{cm}^{-1}$, a value surprisingly consistent with experimentally fit ($D_{eff} = 0.63(4)\ \text{cm}^{-1}$) and calculated data ($0.65\ \text{cm}^{-1}$) given the simplicity of the model (Table 2.5; see Section 2.6.2). This quick and simple calculation becomes an excellent first-order approximation of expected dipolar coupling in such systems with the propensity of saving computational costs and increasing chemical intuition towards synthetic strategies. It also promises predictive capability in far more complex systems where multiple interactions and distances must be accounted for, and highly complex spin structures may emerge.

Further analysis of the transition matrix elements of the ab initio calculated dipole-coupled states offers more insight into the length of relaxation times in the low-temperature regime. Dipolar coupling brings about significantly lower transition probabilities between opposite spin polarizations of the lowest energy dipolar-coupled state:

$$DD_{0,\alpha\alpha} \overset{10^{-15}}{\leftrightarrows} DD_{0,\beta\beta} \quad (Eq. 9)$$

with those of thermally assisted QTM transitions diminished by a further 6 orders of magnitude (Table S.2.4):

$$DD_{1,\alpha\beta} \overset{10^{-21}}{\underset{}{\overset{\longleftarrow}{\longrightarrow}}} DD_{1,\beta\alpha} \;\; (Eq. 10).$$

This dramatic suppression of the QTM relaxation pathway can be equated with the reduction in probability for simultaneously flipping both spins (indicated by icons in Figure 2.8), consequently leading to an increased dipolar attempt time ($\tau_D = 9.2(4) \times 10^3$ s; Table 2.5). The low probability of QTM transitions in **[2]** shuttle magnetic relaxation over the dipole relaxation barrier, a two-step process in which each step can be thought of as roughly analogous to the flip of a single spin. Despite being a two-step, thermally activated process, the low barrier, and lack of alternate pathways leave:

$$DD_{0,\alpha\alpha} \overset{10^{-4}}{\overset{\longleftarrow}{\longrightarrow}} DD_{0,\alpha\beta} \overset{10^{-4}}{\overset{\longleftarrow}{\longrightarrow}} DD_{0,\beta\beta} \;\; (Eq. 11)$$

as the most prominent pathway for low temperature relaxation. This mechanism is consistent with the residual temperature dependence observed in the time-dependent magnetic susceptibility, even at the lowest temperatures (Figure 2.6, bottom). Note that the state $DD_{0,\beta\alpha}$ provides an equivalent intermediate for the two-step pathway of Eq. 11. In such cases of equivalence, the relaxation will be discussed in terms of the majority α to majority β pathway.

To summarize, we consider the dipolar coupling as a perturbation on the crystal field states, splitting them into a tight manifold composed of linear combinations of the single-ion M_J states nearest in energy (Figure 2.1). By this formalism, the splitting of the crystal field (M_J) manifold under the intramolecular dipolar perturbation becomes a consistent and intuitive predictor of the long-timescale relaxation pathway. For **[2]**, Equations 9 (DD_0) and 10 (DD_1) both depict transitions between states differing by two spin-flips. The parallel spatial orientation of the anisotropy axes in relation to each other and the internuclear vector ensures that DD_0 (the bistable ferromagnetic state) is lower in energy than DD_1 (the antiferromagnetic state). Due to the spatial arrangement and high state-purity, both of these transitions have very low probabilities. Alternatively, Equation 11 depicts the preferred two-step, thermally activated transition wherein each step flips a single Ising spin.

The hierarchical approach to perturbation analysis used to understand **2** allows us to tackle the far more complicated relaxation dynamics of **3**. Experimentally, three relaxation processes can be observed and tracked above $T = 11$ K ($\boldsymbol{\Gamma_{3A-C}}$, Figure 2.6, bottom). As observed in **2**, $\boldsymbol{\Gamma_{3A,B}}$ merge and exhibit a secondary regime of Arrhenius behavior at low temperatures. Alternatively, $\boldsymbol{\Gamma_{3C}}$ is offset from $\boldsymbol{\Gamma_{3A,B}}$, exhibiting its own Orbach, Raman, and dipole regions. As with **2**, we can attribute the weakly temperature-dependent region to dipolar coupling and begin our analysis by calculating a dipole energy manifold based on the dipolar interactions between KD_0 of all three ions (Figure 2.8-b). The coupling interaction manifold of **[3]** shows the presence of four different dipole doublets with excited states (DD_{1-3}) above the ground state at energies of 0.22, 1.11, and 2.83 cm^{-1}, respectively (Figure 2.8-b, Table 2.5). DD_0 and DD_1 have the largest moments with $M_Z = \pm 19$ and $\pm\ 21\ \mu_B$, respectively, and represent the net-ferromagnetically coupled states (Eq. 12). DD_2 and DD_3 represent the net-antiferromagnetically coupled states at $M_Z = \pm 8$ and $\pm\ 10\ \mu_B$. The transition matrix elements span a wide range, with the most probable single-step transitions from the ground state corresponding to:

$$DD_{0,\alpha\alpha\alpha} \overset{10^{-3}}{\leftrightarrows} DD_{1,\beta\alpha\alpha}\ (Eq. 12),$$

$$DD_{0,\alpha\alpha\alpha} \overset{10^{-4}}{\leftrightarrows} DD_{2,\alpha\beta\alpha}\ (Eq. 13),$$

and

$$DD_{0,\alpha\alpha\alpha} \overset{10^{-4}}{\overset{\longleftarrow}{\longrightarrow}} DD_{3,\alpha\alpha\beta}\ (Eq. 14)$$

These three processes correspond to single-step, single-flip transitions from the ground dipole doublet to each excited dipole doublet. Interestingly, two of these calculated processes correspond to experimentally observed relaxation processes. When the time scales of $\mathbf{\Gamma_{3A}}$ and $\mathbf{\Gamma_{3B}}$ merge at low temperatures, D_{eff} is fit to give a dipolar barrier of 0.26(5) cm^{-1}. This corresponds well with the calculated energy splitting between DD_0 and DD_1 (Eq. 12) of $\Delta E_{calc} = 0.22\ \mathrm{cm}^{-1}$ (Figure 2.8-b, Table 2.5; also see Associated Supplemental Content, Section 2.6.4). Analogously, the low temperature transition of $\mathbf{\Gamma_{3C}}$ corresponds to the single-flip transition encompassing the whole dipole manifold (Eq. 14). The calculated energy splitting is still consistent between the model and experimental data ($D_{eff} = 2.90(1)\ \mathrm{cm}^{-1}; \Delta E_{calc} = 2.83\ \mathrm{cm}^{-1}$). Once again, our model wherein the energy levels are derived using two simple crystallographic parameters, r and θ, provides a satisfactory prediction of the net coupling type and energy splitting: DD_0, FM; DD_1, FM, $\Delta E_{pred} = 0.41\ \mathrm{cm}^{-1}$; DD_2, AFM, $\Delta E_{pred} = 1.27\ \mathrm{cm}^{-1}$; DD_3, AFM, $\Delta E_{pred} = 2.79\ \mathrm{cm}^{-1}$ (Table 2.5, also see Associates Supplemental Content 2.6.2).

The dipole attempt times for processes $\mathbf{\Gamma_{3A/B}}$ and $\mathbf{\Gamma_{3C}}$ are $\tau_D = 1.5(5) \times 10^2$ and $1.5(0) \times 10^2$ s, respectively, comparatively lower than those observed in **2**. The difference is due in part to the triangular structure of **3**, where two of the interacting spins are near-linear with respect to each other, with the third oriented in a near-orthogonal configuration to the other two. This is clearly evident in the spin configuration between DD_0 and DD_1 (Figure S.2.1), where erbium centers $[\mathbf{3}]_{\boldsymbol{Er_2}}$ and $[\mathbf{3}]_{\boldsymbol{Er_3}}$ have major projections onto their internuclear axis and are coupled ferromagnetically, whereas erbium center $[\mathbf{3}]_{\boldsymbol{Er_1}}$ offers a minimal contribution to net coupling. Furthermore, the dipolar manifold of **[3]** offers two evident pathways to relaxation (Eqs. 12, 14) and the increased mixing of states due to lowered symmetry of dipolar interactions may also play a role in decreased relaxation times.

As in **[2]**, the logic of correlating transition probability with the number of anisotropic spin flips can be carried throughout the entire manifold of **[3]**, with the highest-probability transitions corresponding to single-flip transitions, followed by two-flip transitions, and the lowest-probability transitions corresponding to the three-flip transitions (Table S.2.12):

$$DD_{n,\alpha\alpha\alpha} \overset{10^{-12}}{\underset{\longrightarrow}{\longleftarrow}} DD_{n,\beta\beta\beta}\ (Eq.\,15)$$

The relationship between anisotropic spin flips and transition probability continues to build upon the intuitive model of dipolar relaxation that could be further applied to multinuclear magnetic complexes with strongly anisotropic spins.

2.5 Conclusions

We have targeted systems that highlight dipolar coupling as a driving factor in controlling magnetic relaxation. Beginning with a mononuclear unit of stable magnetic anisotropy, we synthesized a series of erbium(III) single-molecule magnets of increasing nuclearity to investigate the relaxation dynamics of di- and tri-nuclear erbium(III) systems in the high and low temperature regimes. Broadly speaking, the ability to generate and rationalize the low-energy magnetic manifolds as demonstrated for **1–3** points to strongly anisotropic molecular magnetic dipoles as an underexploited approach to fine-tune the design of n-dimensional (n = 0–3) spin structures with unprecedented levels of complexity.

The existence and properties of a ferromagnetic ground state are made possible by tracking the multi-relaxation behavior through resonant interaction with an AC magnetic field across eight orders of magnitude in frequency space. In doing so, two and three concurrent relaxation pathways are uncovered in the high-temperature regime for the di- and trinuclear species, respectively. When fit to a multi-term relaxation model, a second Arrhenius law-regime is revealed at low temperatures, corresponding to the dynamics of the dipole coupled states within the ground Kramers doublet manifold. Calculation of the Kramers doublet structure and dipolar interactions provide a preliminary quantitative basis for rationalizing the relaxation pathways. In correspondence with ab initio calculations, dipolar coupling suppresses QTM relaxation in the low-temperature regime by forcing through-barrier relaxation transitions to take place between the coupled dipole doublet states and is thus the driving factor to elongated relaxation times. The anisotropic states and dipolar mechanism provide an intuitive framework whereby anisotropic single-spin flips are preferential per each step in a transition through the dipole barrier and QTM is suppressed as it requires the simultaneous flip of every spin in the system. Additionally, the type of coupling and approximate dipolar energy splitting can be predicted through a simple calculation involving only two crystallographically-derived physical parameters. We plan to use the predictive nature of design in these anisotropic dipolar manifolds as a basis for a wide array of exciting directions including higher and more complex symmetries, increased dimensionality, and exploration of the intrinsic quantum properties of the dipole manifolds.

2.6 Associated Supplemental Content

2.6.1 Preparative Details

All manipulations were carried out under anaerobic, anhydrous conditions under an atmosphere of dinitrogen in a Vacuum Technology Inc. glovebox. All glassware was dried at 160° C overnight prior to use. Tetrahydrofuran (THF), toluene, benzene, hexane, and pentane were dried on an activated alumina column and stored over a 1:1 mixture of 3 and 4 Å molecular sieves for at least two days before use. Dimethoxyethane (DME, Sigma Aldrich) was degassed using freeze-pump-thaw cycles prior to use and stored over a 1:1 mixture of 3 and 4 Å molecular sieves for at least two days before use. Erbium triiodide (Alfa Aesar), trimethylaluminum (TMA, Sigma Aldrich), triisopropylsilyl trifluoromethanesulfonate (Acros Organics), 1,3,5,7-cyclooctatetraene (Acros Organics), and *n*-butyllithium (Acros Organics) were used as received. Potassium tert-butoxide (Sigma Aldrich) was sublimed before use. Dipotassium cyclooctatetraenide[a] (K_2COT) and benzyl potassium[b] (KBn) were prepared by previously reported methods. CHN elemental analyses were performed by Midwest Microlab, Indianapolis, IN.

Synthesis of 5,8-bis(triisopropylsilyl)cycloocta-1,3,6-triene

To a −30° C stirring solution of K_2COT (0.5422 g, 2.974 mmol, ∼40 mL DME) was added drop-wise a diluted −30° C solution of triisopropylsilyl trifluoromethanesulfonate (2.400 mL, 8.922 mmol, 3 eq, ∼10 mL DME). The reaction mixture was allowed to react at −30° C over the course of 48 h, during which time it progressed from a clear vivid yellow to a clear eggshell

---

[a] Meihaus, K. R.; Long, J. R. *J Am Chem Soc* **2013**, *135*, 17952.

[b] Hilgar, J. D.; Bernbeck, M. G.; Flores, B. S.; Rinehart, J. D. *Chem Sci* **2018**, *9*, 7204.

colored solution. After the 48-hour reaction period, the reaction mixture was allowed to warm to room temperature, taken out of the glovebox, opened to air, and quenched onto ice. The product was extracted into ~100 mL of hexane and washed with five portions of deionized water (~500 mL total). The organic layer was dried over $MgSO_4$, filtered, and solvent removed *in vacuo* to yield a pale-yellow oil. The product was dissolved in warm MeOH (~200 mL) and crystallized at −20° C over the course of 24 h to afford colorless crystals of 5,8-bis(triisopropylsilyl)cycloocta-1,3,6-triene (0.8213 g, 66.2%).

^{1}H NMR ($CDCl_3$, 500 MHz): δ ppm 6.10 (d, J = 9.0 Hz, 2H), 5.64 (s, 2H), 5.45 (t, J = 8.4 Hz, 2H), 2.78 (d, J = 7.5 Hz, 2H), 1.20 (m, J = 14.2, 7.1 Hz, 6H), 1.07 (dd, J = 7.3, 2.9 Hz, 36H).

Synthesis of (1), (η^8-1,4-bis(triisopropylsilyl)cyclooctatetraenyl)-iodobis-(tetrahydrofuran)-erbium

To a −30° C stirring solution of 5,8-bis(triisopropylsilyl)cycloocta-1,3,6-triene (0.4410 g, 1.058 mmol, ~5 mL THF) was added drop-wise a freshly-prepared −30° C solution of KBn (0.2618 g, 2.010 mmol, 1.9 eq, ~5 mL THF). The reaction mixture was allowed to warm to room temperature over the course of 1 h, after which time it took on a clear, yellow appearance. Meanwhile, a suspension of erbium triiodide (0.6377 g, 1.164 mmol, 1.1 eq, ~7 mL THF) was prepared and stirred at 50° C for 30 min Both mixtures were cooled to −30° C and the *in situ* dipotassium 1,4-bis(triisopropylsilyl)cyclooctatetraenide (referred to as K_2TiPS_2COT) solution was added quickly to the stirring suspension of erbium triiodide. The metallation was allowed to proceed over the course of 48 hours, after which time it took on a light peach-pink color. Excess ErI_3 and KI were removed via centrifugation and the supernatant was dried *in vacuo*. The resulting peach-pink residue was washed with pentane, dried *in vacuo,* and redissolved in a minimum ~7 mL portion of THF and passed through a glass filter. A room-temperature vapor diffusion of pentane into this solution yielded pink needles of **1** (0.4759 g, Yield: 52.6%) suitable for X-ray diffraction. FTIR analysis: 2934 cm^{-1} (*vw*), 2860 cm^{-1} (*vw*), 1457 cm^{-1} (*vw*), 1011 cm^{-1} (*vw*), 865 cm^{-1} (*w*), 639 cm^{-1} (*w*). CHN analysis (calculated, found) for [$C_{36}H_{64}IErO_2Si_2$]: C (47.75, 47.60); H (7.54, 7.51); N (0.00, 0.00).

Synthesis of (2), bis(η_2-iodo)-bis((η^8-1,4-bis(triisopropylsilyl)cyclooctatetraenyl) tetrahydrofuran-erbium)

To a −30˚ C stirring solution of 5,8-bis(triisopropylsilyl)cycloocta-1,3,6-triene (0.3509 g, 0.8418 mmol, ~5 mL THF) was added drop-wise a freshly-prepared −30˚ C solution of KBn (0.2083 g, 1.600 mmol, 1.9 eq, ~5 mL THF). The reaction mixture was allowed to warm to room temperature over the course of an hour, after which time it took on a clear, yellow appearance. Meanwhile, a suspension of erbium triiodide (0.5074 g, 0.9260 mmol, 1.1 eq, ~7 mL THF) was prepared and stirred at 50˚ C for 30 min. Both mixtures were cooled to −30˚ C and the *in situ* K_2TiPS_2COT solution was added quickly to the stirring suspension of erbium triiodide. The metallation was allowed to proceed over the course of 48 h, after which time it took on a light peach-pink color. Excess ErI_3 and KI were removed via centrifugation and the supernatant was dried *in vacuo*. The resulting peach-pink residue was washed with pentane, dried *in vacuo*, and redissolved in a ~10 mL portion of benzene. This solution was stirred at 40˚ C for 15 min and filtered through a glass fiber while warm. Cold pentane was layered on the benzene solution, from which pink-orange X-ray quality crystals of **2** were grown over the course of two d (0.2919 g, Yield: 44.1%). FTIR analysis: 2936 cm^{-1} (*w*), 2859 cm^{-1} (*w*), 1458 cm^{-1} (*w*), 1003 cm^{-1} (*w*), 878 cm^{-1} (*m*), 633 cm^{-1} (*m*). CHN analysis (calculated, found) for [$C_{60}H_{112}I_2Er_2O_2Si_4$]: C (46.01, 45.68); H (7.21, 7.53); N (0.00, 0.00).

Synthesis of (3), (μ_2-iodo)-bis(μ_3-iodo)-tris(η^8-1,4-bis(triisopropylsilyl)cyclooctatetraenyl-erbium)

To a −30˚ C stirring solution of **1** (0.3783 g, 0.4423 mmol, ∼10 mL toluene) was added drop-wise a −30˚ C solution of TMA in toluene (1.769 mL, 2 M, 8 eq). The reaction took on a cloudy, orange appearance within 10 min, and was allowed to react overnight at room temperature after which time it took on an orange-yellow, nearly clear appearance. Insoluble byproducts were removed via filtration through a glass microfiber filter and the filtrate was thoroughly dried *in vacuo* to yield a viscous orange oil. The resulting oil was washed repeatedly with pentane until solids appeared on drying, which were redissolved in a ∼4 mL portion of hexane, and passed through a glass filter. Orange X-ray quality crystals were grown from the concentrated hexane solution at −30˚ C over the course of 4 d (0.0888 g, Yield: 28.2%). FTIR analysis: 2935 cm^{-1} (*m*), 2860 cm^{-1} (*m*), 1459 cm^{-1} (*w*), 1025 cm^{-1} (*w*), 880 cm^{-1} (*m*), 745 cm^{-1} (*w*), 646 cm^{-1} (*s*), 576 cm^{-1} (*m*). CHN analysis (calculated, found) for [$C_{78}H_{144}I_3Er_3Si_6$]: C (43.92, 43.93); H (6.81, 7.18); N (0.00, 0.00).

2.6.2 Example Calculations of Predicted Energies Based on Structural Parameters

Sample Calculation for (2):

State	Angle	Degrees	Radians	Radius	References
DD_0	$\theta_{\alpha,12}$	(-)144.53	(-)2.52	$r_{12} = 4.81$	Figure 2.3 Tables 2.1, 2.3
	$\theta_{\alpha,12}$	(-)144.53	(-)2.52		
DD_1	$\theta_{\alpha,12}$	(-)144.53	(-)2.52		
	$\theta_{\beta,12}$	(+)35.47	(+)0.62		

Note: It is important to properly note direction of angular projection with sign (cw: (-), ccw: (+)).

All energy predictions are scaled by a value of approximately 0.43297 cm^{-1}/T, which accounts for the prefactor of $\frac{\mu_0\mu_{Bohr}^2}{4\pi}$. Furthermore, the energy predictions are scaled by the expected g_Z value for an anisotropic erbium center in the 15/2 ground state (~17.9), while accounting for the pseudo-spin formalism, $\tilde{s} = \frac{1}{2}$.

Energy Prediction of DD_0:

$E_{dip} = -\frac{1}{r^3}[3\cos\theta_1\cos\theta_2 - \cos(\Delta\theta)]$ (Equation 8 in the main text)

$$E_{DD_0} = -\frac{(0.43297)\left(\frac{17.9}{2}\right)^2}{(4.81)^3}[3\cos(-2.52)\cos(-2.52) - \cos(-2.52 + 2.52)]$$

$$E_{DD_0} = -0.31 \text{ cm}^{-1}$$

Note: (-) sign of state predicts FM-coupled state

Energy Prediction of DD_1:

$$E_{DD_1} = -\frac{(0.43297)\left(\frac{17.9}{2}\right)^2}{(4.81)^3}[3\cos(-2.52)\cos(+0.62) - \cos(-2.52 - 0.62)]$$

$$E_{DD_0} = +0.31 \text{ cm}^{-1}$$

Note: (+) sign of state predicts AFM-coupled state

State	**Predicted Coupling** (based on sign)	**Scaled Energy**	**ΔE**
E_{DD_0}	FM	-0.31	0.62 cm^{-1}
E_{DD_1}	AFM	+0.31	

Sample Calculation for (3):

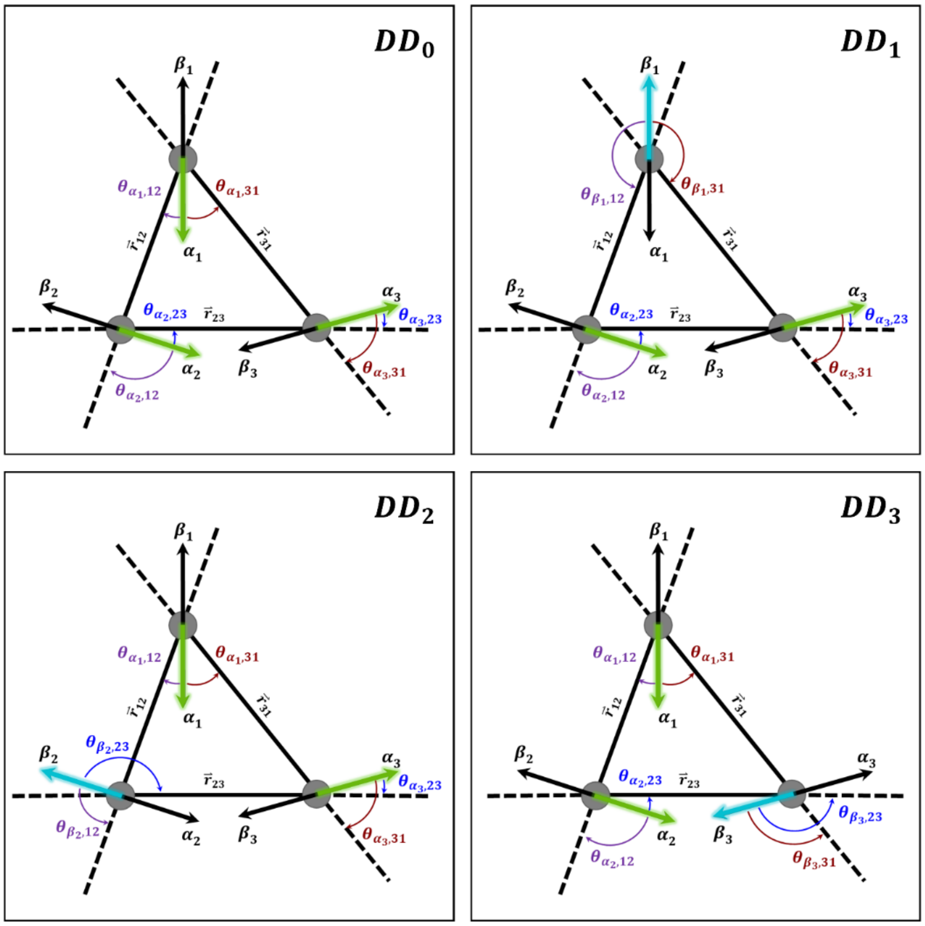

Supplemental Figure 2.1: Simplified graphic of crystal structure of **3**, demonstrating angular projection of the Er-COT vector ($\vec{\boldsymbol{r}}_{\perp,\mathbf{n}}$) onto the internuclear axis ($\vec{\boldsymbol{r}}$) between magnetic centers (gray) making up the ground ($\boldsymbol{DD_0}$) and excited ($\boldsymbol{DD_1}$, $\boldsymbol{DD_2}$, $\boldsymbol{DD_3}$) dipole doublet states. The terms $\boldsymbol{\alpha_{n_i}}$ and $\boldsymbol{\beta_{n_i}}$ represent the spin polarization of the single-ion Kramers wavefunctions as orthogonal basis elements located on Er center n_i. Angles $\boldsymbol{\theta_{\alpha_{n_i},\vec{r}_{n_in_j}}}$ and $\boldsymbol{\theta_{\beta_{n_i},\vec{r}_{n_in_j}}}$ represent the angle between $\boldsymbol{\alpha_{n_i}}$ and $\vec{\boldsymbol{r}}_{n_in_j}$ as tabulated below. Parameters are denoted with subscripts corresponding to their respective erbium centers and the internuclear axis the moment is being projected onto. Sets are color-coded by projection onto $\vec{\boldsymbol{r}}_{\mathbf{12}}$ (purple), $\vec{\boldsymbol{r}}_{\mathbf{23}}$ (blue), and $\vec{\boldsymbol{r}}_{\mathbf{31}}$ (red).

Supplemental Table 2.1: Selected distances (Å) for **3** and averages between both fragments in the unit cell. $\vec{\boldsymbol{r}}_{\perp}$ represents the distance between the COT centroid and erbium, $\vec{\boldsymbol{r}}$ is the internuclear distance between the two erbium centers. Parameters are denoted with subscripts corresponding to their respective erbium centers.

	Fragment 1	**Fragment 2**	**Averages**
$\vec{\boldsymbol{r}}_{\perp,\mathbf{1}}$	1.6853(4)	1.6895(4)	1.6874(4)
$\vec{\boldsymbol{r}}_{\perp,\mathbf{2}}$	1.7169(5)	1.7126(3)	1.7148(4)
$\vec{\boldsymbol{r}}_{\perp,\mathbf{3}}$	1.6885(5)	1.6842(5)	1.6864(5)
$\vec{\boldsymbol{r}}_{\mathbf{12}}$	3.8950(6)	3.8386(6)	3.8668(6)
$\vec{\boldsymbol{r}}_{\mathbf{23}}$	4.2056(7)	4.2111(6)	4.2084(7)
$\vec{\boldsymbol{r}}_{\mathbf{13}}$	4.6240(6)	4.6927(6)	4.6584(6)

Supplemental Table 2.2: Tabulated angles, $\boldsymbol{\theta_\alpha}$ and $\boldsymbol{\theta_\beta}$, of the projection of moment represented by the Er-COT vector ($\vec{\boldsymbol{r}}_{\perp,\mathbf{n}}$) onto the internuclear axis ($\vec{\boldsymbol{r}}$) between magnetic centers making up the ground and excited dipole doublets of **3**.

$\boldsymbol{DD_0}$	**Fragment 1**	**Fragment 2**	**Averages**
$\theta_{\alpha_1,12}$	11.08(2)	11.66(2)	11.37(2)
$\theta_{\alpha_2,12}$	98.058(17)	97.623(15)	97.841(16)
$\theta_{\alpha_2,23}$	12.45(2)	11.422(19)	11.94(20)
$\theta_{\alpha_3,23}$	3.492(18)	2.17(2)	2.83(2)
$\theta_{\alpha_3,31}$	53.895(18)	52.494(18)	53.195(18)
$\theta_{\alpha_1,31}$	47.41(2)	46.47(2)	46.49(2)
$\boldsymbol{DD_1}$	**Fragment 1**	**Fragment 2**	**Averages**
$\theta_{\beta_1,12}$	168.92(2)	168.34(2)	168.68(2)
$\theta_{\alpha_2,12}$	98.058(17)	97.623(15)	97.841(16)
$\theta_{\alpha_2,23}$	12.45(2)	11.422(19)	11.94(20)
$\theta_{\alpha_3,23}$	3.492(18)	2.17(2)	2.83(2)
$\theta_{\alpha_3,31}$	53.895(18)	52.494(18)	53.195(18)
$\theta_{\beta_1,31}$	132.56(2)	133.53(2)	133.06(2)
$\boldsymbol{DD_2}$	**Fragment 1**	**Fragment 2**	**Averages**
$\theta_{\alpha_1,12}$	11.08(2)	11.66(2)	11.37(2)
$\theta_{\beta_2,12}$	81.942(17)	82.377(15)	82.160(16)
$\theta_{\beta_2,23}$	167.55(2)	168.578(19)	168.06(20)
$\theta_{\alpha_3,23}$	3.492(18)	2.17(2)	2.83(2)
$\theta_{\alpha_3,31}$	53.895(18)	52.494(18)	53.195(18)
$\theta_{\alpha_1,31}$	47.41(2)	46.47(2)	46.49(2)

Supplemental Table 2.2: (Continued)

$\boldsymbol{DD_3}$	**Fragment 1**	**Fragment 2**	**Averages**
$\theta_{\alpha_1,12}$	11.08(2)	11.66(2)	11.37(2)
$\theta_{\alpha_2,12}$	98.058(17)	97.623(15)	97.841(16)
$\theta_{\alpha_2,23}$	12.45(2)	11.422(19)	11.94(20)
$\theta_{\beta_3,23}$	176.508(18)	177.83(2)	177.17(19)
$\theta_{\beta_3,31}$	126.105(18)	127.506(18)	126.805(18)
$\theta_{\alpha_1,31}$	47.41(2)	46.47(2)	46.49(2)

Sample Calculation of **3**:

State	Angle	Degrees	Radians	Radii	Reference
DD_0	$\boldsymbol{\theta_{\alpha_1,12}}$	(-)11.37	(-)0.20	$r_{12} = 3.87$ $r_{23} = 4.21$ $r_{31} = 4.66$	Figure S.2.1, Tables S.2.1, S.2.2
	$\boldsymbol{\theta_{\alpha_2,12}}$	(-)97.84	(-)1.71		
	$\boldsymbol{\theta_{\alpha_2,23}}$	(+)11.94	(+)0.21		
	$\boldsymbol{\theta_{\alpha_3,23}}$	(-)2.83	(-)0.05		
	$\boldsymbol{\theta_{\alpha_3,31}}$	(-)53.20	(-)0.93		
	$\boldsymbol{\theta_{\alpha_1,31}}$	(+)46.49	(+)0.82		

Note: It is important to properly note direction of angular projection with sign (*cw*: (-), *ccw*: (+))

We utilize the same method of predicting the energies and then scaling them as in **(2)**.

Energy Prediction of $\boldsymbol{DD_0}$:

$$E_{DD_0}^{12} = -\frac{(0.43297)\left(\frac{17.9}{2}\right)^2}{(3.87)^3}\left[3\cos(-0.20)\cos(-1.71) - \cos(-0.20 + 1.71)\right]$$

$$E_{DD_0}^{12} = +0.277\ \mathrm{cm}^{-1}$$

(+) ➞ AFM Component

Continuing for the other two pair-wise interactions:

$$E_{DD_0}^{23} = -\frac{(0.43297)\left(\frac{17.9}{2}\right)^2}{(4.21)^3}\left[3\cos(+0.21)\cos(-0.05) - \cos(+0.21 + 0.05)\right]$$

$$E_{DD_0}^{23} = -0.913\ \mathrm{cm}^{-1}$$

(−) → FM Component

$$E_{DD_0}^{31} = -\frac{(0.43297)\left(\frac{17.9}{2}\right)^2}{(4.66)^3}[3\cos(-0.93)\cos(+0.82) - \cos(-0.93+0.82)]$$

$$E_{DD_0}^{31} = -0.481 \text{ cm}^{-1}$$

(−) → FM Component

$$E_{DD_0}^{total} = E_{DD_0}^{12} + E_{DD_0}^{23} + E_{DD_0}^{31}$$

$$E_{DD_0}^{total} = -1.117 \text{ cm}^{-1}$$

(−) → FM Net State

Iterating analogous pair-wise calculations for states $DD_1 - DD_3$ with angles from Table S.2.2, and scaling as above to give the resultant predicted energies and couplings:

State	**Predicted Energy** (scaled)	**Predicted Coupling** (based on sign)	**Predicted Energy Splittings**
$E_{DD_0}^{total}$	-1.12	FM	0.00 cm^{-1}
$E_{DD_1}^{total}$	-0.71	FM	0.41 cm^{-1}
$E_{DD_2}^{total}$	$+0.16$	AFM	1.27 cm^{-1}
$E_{DD_3}^{total}$	$+1.67$	AFM	2.79 cm^{-1}

2.6.3 Sample Characterization

Crystallographic Methods

Single crystal diffraction data for **1** were collected at 200 K, and for **2**, and **3** at 100 K on a Bruker κ Diffractometer using a Mo(Kα) radiation source and an Apex II Area Detector. The structures were solved using direct methods via the SHELX routine[c] and refined using full-matrix least-squares procedures with the SHELXL routine. Olex^2 was used as a graphical front end during refinement.[d] Hydrogens were modeled using a riding model for all positions. The *PLATON* SQUEEZE algorithm[e] was utilized to remove disordered solvent (THF) from the cavities of the structure. Supplementary crystallographic data can be accessed from the Cambridge Crystallographic Data Center via deposition numbers: 2083100 (**1**), 2083099 (**2**), 2083101 (**3**).

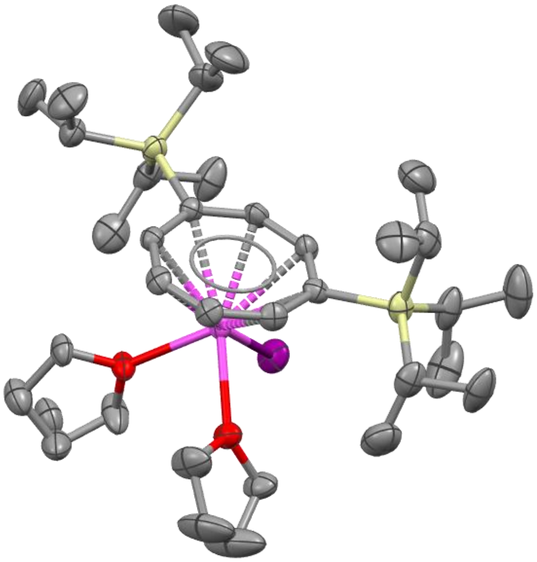

Supplemental Figure 2.2: Crystal structure of **1**, showing thermal ellipsoids at 50% probability. Atoms are colored by element type: gray (carbon), yellow (silicon), red (oxygen), purple (iodine), pink (erbium). Hydrogen atoms have been omitted for clarity. Selected distances and angles: $\vec{r}_{\mathrm{Er-COT}}$ = 1.7694(2) Å; $\vec{r}_{\mathrm{Er-I}}$ = 3.0241(3) Å; $\theta_{COT-Er-I}$ = 131.852(10) °.

---

[c] Sheldrick, G. M. *Acta Crystallogr A* **2015**, *71*, 3.

[d] Dolomanov, O. V.; Bourhis, L. J.; Gildea, R. J.; Howard, J. A. K.; Puschmann, H. *J Appl Crystallogr* **2009**, *42*, 339.

[e] Spek, A. L. *Acta Crystallographica Section C Structural Chemistry* **2015**, *71*, 9.

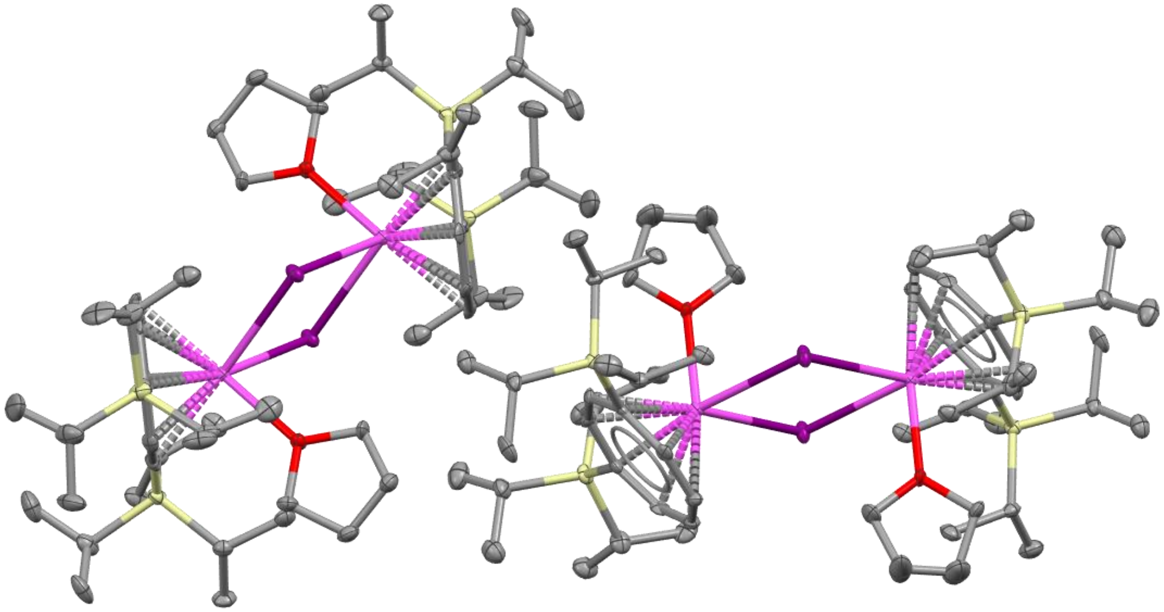

Supplemental Figure 2.3: Crystal structure of **2**, showing thermal ellipsoids at 50% probability. Atoms are colored by element type: gray (carbon), yellow (silicon), red (oxygen), purple (iodine), pink (erbium). Hydrogen atoms have been omitted for clarity.

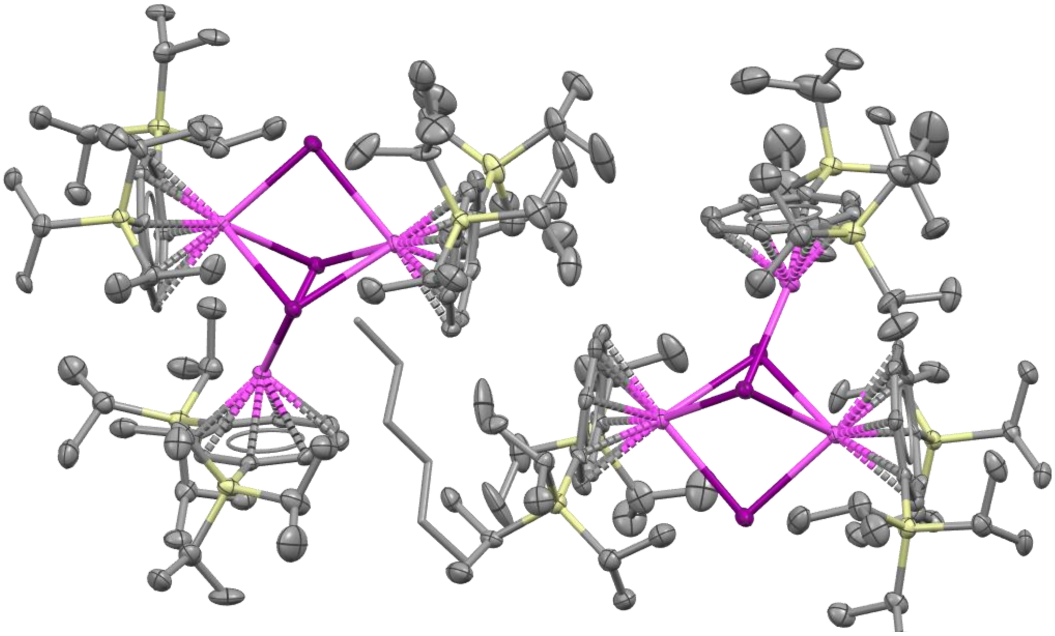

Supplemental Figure 2.4: Crystal structure of **3**, showing thermal ellipsoids at 50% probability. Atoms are colored by element type: gray (carbon), yellow (silicon), purple (iodine), pink (erbium). Hydrogen atoms have been omitted for clarity. Outer sphere solvent (hexane) is present in the lattice, represented without thermal ellipsoids for clarity.

Magnetometry Methods

Magnetic data were collected under DC and VSM scan modes using a Quantum Design MPMS3 SQUID Magnetometer with equipped AC susceptibility attachment. Crystal samples were finely crushed and loaded in custom quartz tubes (D&G Glassblowing Inc.), layered with eicosane wax, and subsequently flame-sealed under static vacuum. Eicosane wax was melted within the sealed sample to abate sample torquing and to facilitate thermal conductivity. Diamagnetic corrections for the samples and eicosane wax were calculated using Pascal's constants[f] and subtracted from all static moment data. Thermal magnetic susceptibilities were collected in DC scan mode under a 100 Oe applied field. Isothermal magnetization data were collected in VSM mode between −7 to 7 T at a 50 Oe sec^{-} sweep rate. Short and long-timescale AC data were fit to a Debye (Cole-Cole relaxation) model for **1** (n = 1), and an expanded Debye model[g] for **2** (n = 2) and **3** (n = 3), following Equation S.2.1.

$$\chi_{\mathrm{AC}}(\omega) = \chi_{S,tot} + \sum_{n} \frac{\Delta\chi_n}{1+(i\omega\tau_n)^{1-\alpha_n}} \qquad \textit{(Eq. S.2.1)}$$

Equation S.2.1: Modified Debye (Cole-Cole) relaxation model, where n is the number of processes, $\chi_{S,tot}$ is the sum of the adiabatic susceptibilities of the relaxing species, $\Delta\chi$ is the difference between the adiabatic and isothermal limits of the susceptibility, ω is the angular frequency, τ is the relaxation time, and α accounts for a distribution of relaxation times about τ.

Details related to the collection and analysis of long-timescale magnetic data are discussed in previous work.[h] MPMS 3 data parsing, fitting, and plotting was performed with our

---

[f] Bain, G. A.; Berry, J. F. *J Chem Educ* **2008**, *85*, 532.

[g] Guo, Y.-N.; Xu, G.-F.; Wernsdorfer, W.; Ungur, L.; Guo, Y.; Tang, J.; Zhang, H.-J.; Chibotaru, L. F.; Powell, A. K. *J Am Chem Soc* **2011**, *133*, 11948; Ho, L. T. A.; Chibotaru, L. F. *Phys Rev B* **2016**, *94*.

[h] Hilgar, J. D.; Butts, A. K.; Rinehart, J. D. *Phys Chem Chem Phys* **2019**, *21*, 22302.

MATLAB package, *Super*. This object-oriented code package and all applicable documentation is available at *https://github.com/RinehartGroup/super-matlab* under the MIT License.

Magnetic Data of Compound 1

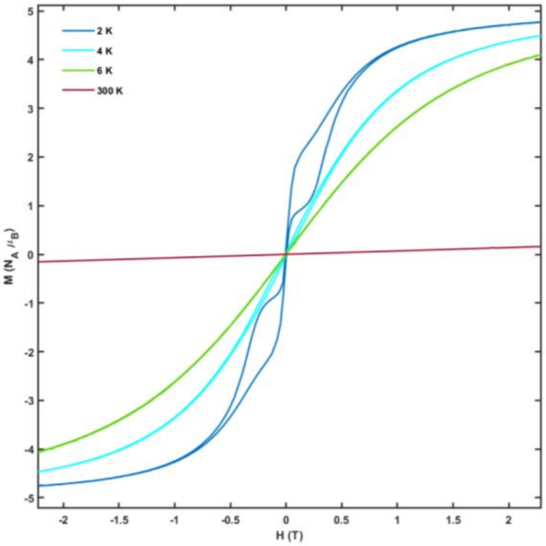

Supplemental Figure 2.5: Isothermal magnetization of 1 at T = 2, 4, 6, and 300 K collected between H= 7 to 7 T at a constant sweep rate of 50 Oe sec^{-1}.

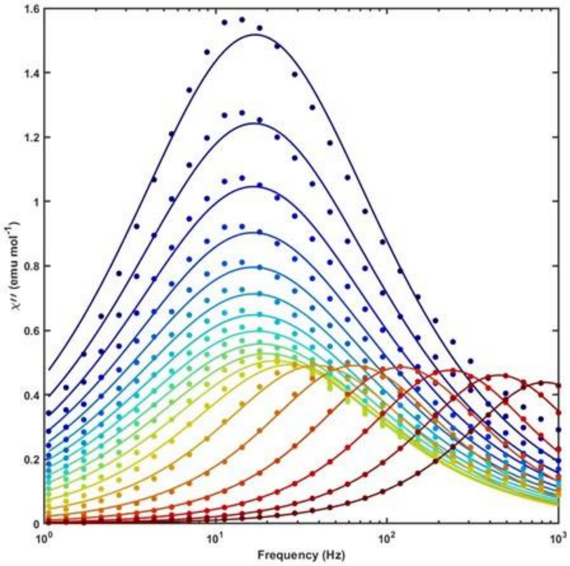

Supplemental Figure 2.6: AC out-of-phase susceptibility (χ'') of **1** collected between *T* = 2 - 10.5 K (blue - red). Dots represent data and lines are fit to a generalized Debye model.

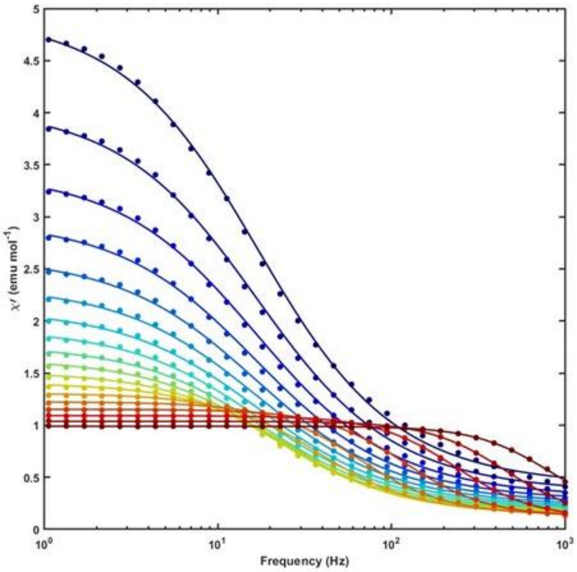

Supplemental Figure 2.7: AC in-phase susceptibility (χ'') of **1** collected between *T* = 2 - 10.5 K (blue - red). Dots represent data and lines are fit to a generalized Debye model.

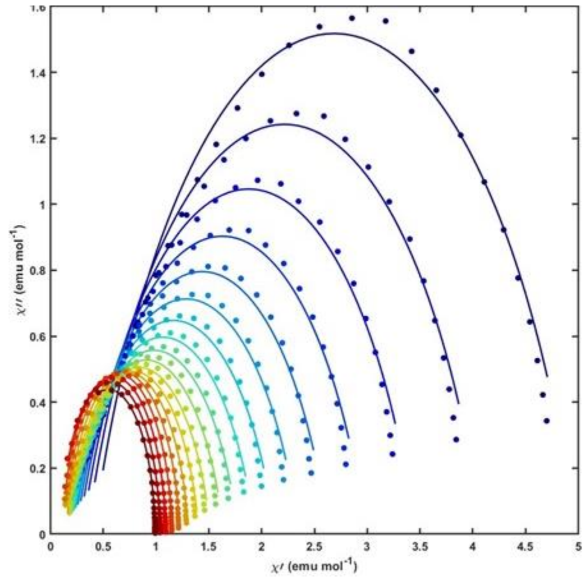

Supplemental Figure 2.8: Cole-cole plot of **1** collected between *T* = 2 - 10.5 K (blue - red). Dots represent data and lines are fit to a generalized Debye model.

Supplemental Table 2.3: Model fit values for standard AC data collected for **1** between T = 2 - 10.5 K.

T	τ_1	$\tau_{1,\ error,\ LB}$	$\tau_{1,\ error,\ UB}$	α_1	$\alpha_{1,\ error,\ LB}$	$\alpha_{1,\ error,\ UB}$	χ_{T1}	$\chi_{T1,\ error,\ LB}$	$\chi_{T1,\ error,\ UB}$	χ_S	$\chi_{S,\ error,\ LB}$	$\chi_{S,\ error,\ UB}$
2.0	9.37E-03	8.96E-03	9.78E-03	0.253	0.233	0.272	4.971	4.897	5.045	0.407	0.355	0.458
2.5	9.50E-03	9.08E-03	9.91E-03	0.254	0.234	0.273	4.088	4.026	4.149	0.345	0.303	0.387
3.0	9.57E-03	9.14E-03	1.00E-02	0.254	0.235	0.274	3.454	3.401	3.507	0.299	0.263	0.335
3.5	9.63E-03	9.20E-03	1.01E-02	0.254	0.234	0.274	2.988	2.942	3.034	0.266	0.234	0.297
4.0	9.63E-03	9.19E-03	1.01E-02	0.253	0.233	0.273	2.634	2.593	2.675	0.240	0.212	0.267
4.5	9.54E-03	9.11E-03	9.97E-03	0.250	0.230	0.270	2.354	2.318	2.390	0.218	0.194	0.243
5.0	9.39E-03	8.97E-03	9.82E-03	0.246	0.225	0.266	2.127	2.095	2.160	0.203	0.180	0.225
5.5	9.09E-03	8.69E-03	9.49E-03	0.237	0.217	0.257	1.939	1.910	1.967	0.190	0.170	0.211
6.0	8.65E-03	8.27E-03	9.02E-03	0.224	0.204	0.245	1.779	1.753	1.805	0.180	0.161	0.199
6.5	8.04E-03	7.70E-03	8.38E-03	0.207	0.187	0.227	1.641	1.618	1.664			
7.0	7.14E-03	6.85E-03	7.43E-03	0.183	0.162	0.203	1.517	1.497	1.537			
7.5	5.83E-03	5.63E-03	6.04E-03	0.149	0.130	0.167	1.408	1.392	1.423			
8.0	4.13E-03	4.01E-03	4.24E-03	0.106	0.090	0.121	1.309	1.298	1.320			
8.5	2.48E-03	2.43E-03	2.52E-03	0.067	0.056	0.078	1.225	1.218	1.231			
9.0	1.33E-03	1.31E-03	1.34E-03	0.039	0.033	0.046	1.153	1.150	1.156			
9.5	6.80E-04	6.76E-04	6.84E-04	0.023	0.019	0.027	1.091	1.090	1.093			
10.0	3.54E-04	3.51E-04	3.56E-04	0.011	0.007	0.015	1.037	1.036	1.038			
10.5	1.92E-04	1.89E-04	1.95E-04	0.003	-0.003	0.010	0.990	0.988	0.991			

Supplemental Table 2.3: Model fit values for standard AC data collected for **1** between T = 2 - 10.5 K.(Continued)

6.5	0.172	0.154	0.189
7.0	0.165	0.149	0.181
7.5	0.158	0.143	0.172
8.0	0.148	0.136	0.160
8.5	0.134	0.125	0.143
9.0	0.118	0.113	0.124
9.5	0.104	0.100	0.108
10.0	0.100	0.095	0.105
10.5	0.108	0.096	0.120

Magnetic Data of Compound 2

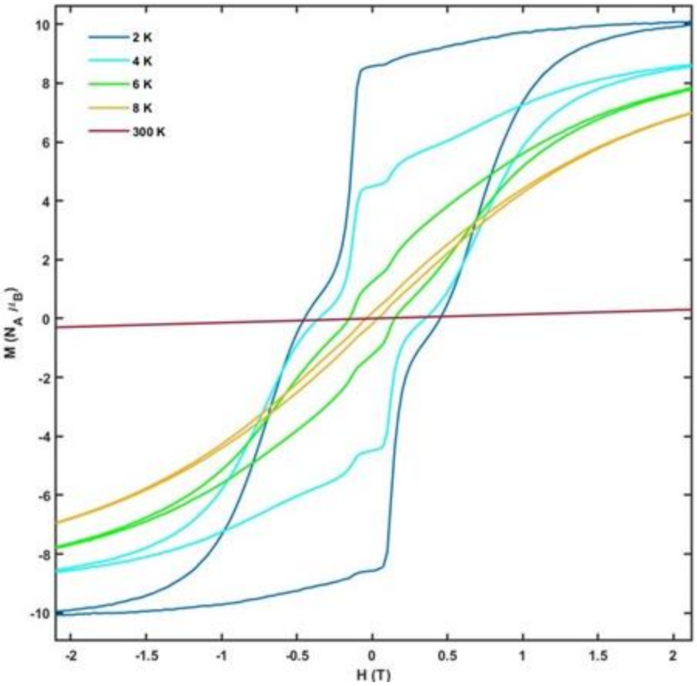

Supplemental Figure 2.9: Isothermal magnetization of **2** at 2, 4, 6, 8, and 300 K collected between −7 to 7 T at a constant 50 Oe sec^{-1} sweep rate.

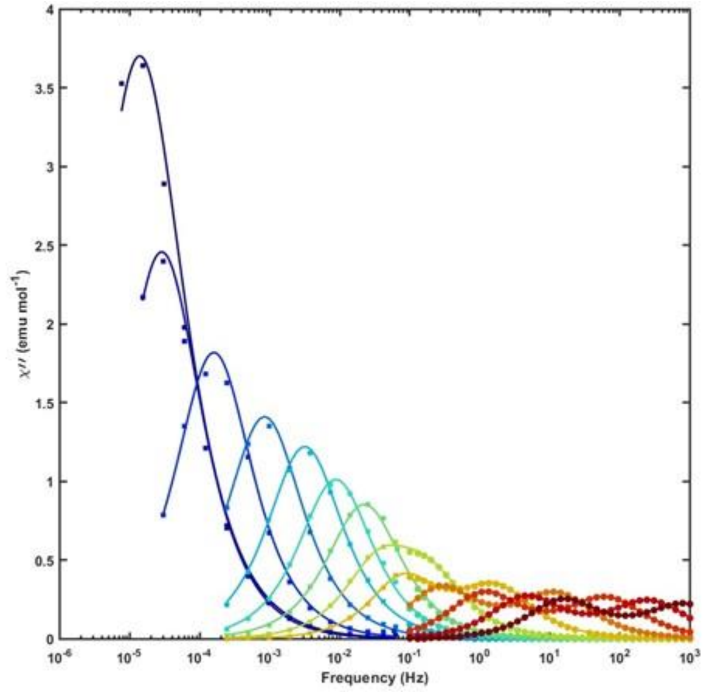

Supplemental Figure 2.10: AC out-of-phase susceptibility of **2** collected between *T* = 2 - 14 K (blue - red). Data points are susceptibilities measured via standard AC measurements (circles) and extracted from Fourier analysis of VSM data (squares). Lines represent fits to an extended Debye model.

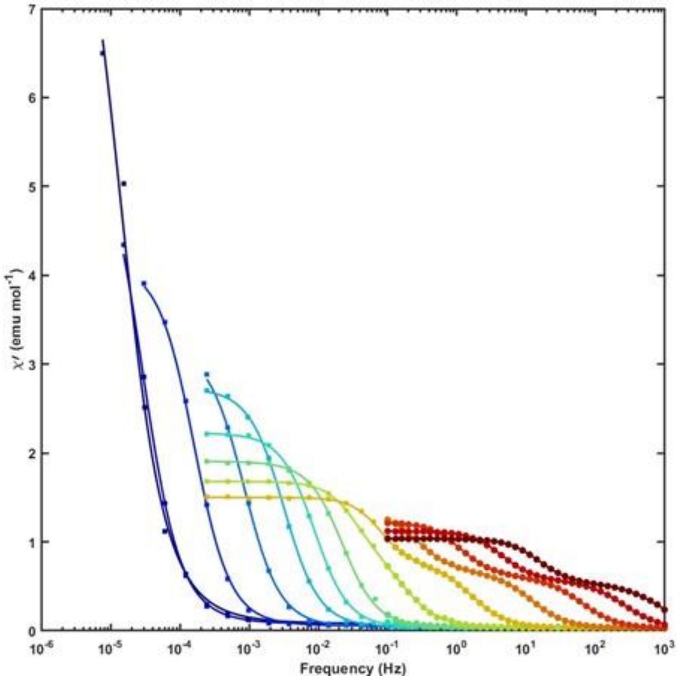

Supplemental Figure 2.11: AC in-phase magnetic susceptibility of **2** collected between *T* = 2 - 14 K (blue - red). Data points are susceptibilities measured via standard AC measurements (circles) and extracted from Fourier analysis of VSM data (squares). Lines represent fits to an extended Debye model.

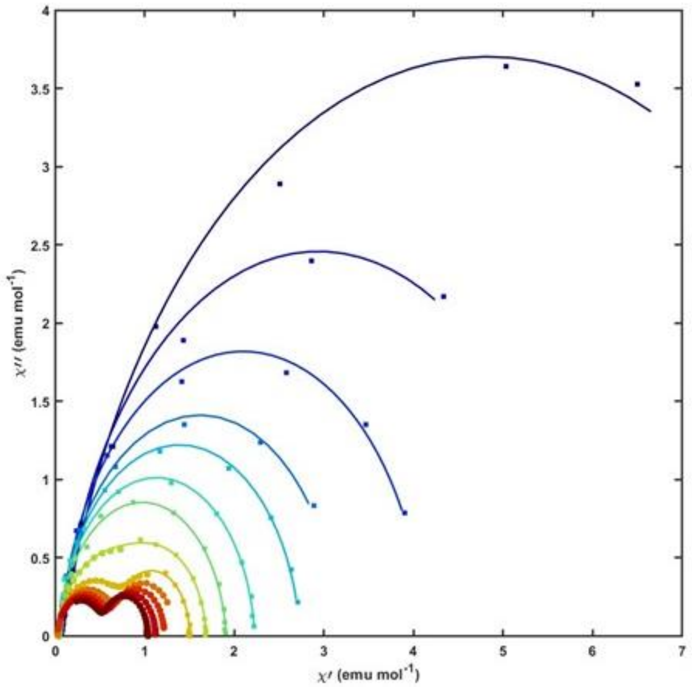

Supplemental Figure 2.12: Cole-cole plot of **2** collected between *T* = 2 - 14 K (blue - red). Data points are susceptibilities measured via standard AC measurements (circles) and extracted from Fourier analysis of VSM data (squares). Lines represent fits to an extended Debye model.

Supplemental Table 2.4: Model fit values and error bounds for AC data collected for **2** between *T* = 1.8 - 14 K. Values of T are in Kelvin, τ in seconds, and χ in emu mol^{-1}.

T	τ_1	$\tau_{1,\ error,\ LB}$	$\tau_{1,\ error,\ UB}$	α_1	$\alpha_{1,\ error,\ LB}$	$\alpha_{1,\ error,\ UB}$	χ_{T1}	$\chi_{T1,\ error,\ LB}$	$\chi_{T1,\ error,\ UB}$
1.8	1.27E+04	1.05E+04	1.49E+04	0.143	0.084	0.201	10.88	9.80	11.95
1.9	1.24E+04	1.06E+04	1.42E+04	0.161	0.113	0.209	10.09	9.26	10.91
2.0	1.15E+04	9.98E+03	1.29E+04	0.157	0.113	0.201	9.58	8.89	10.27
2.1	1.06E+04	8.92E+03	1.23E+04	0.097	0.031	0.163	8.34	7.53	9.16
2.2	1.01E+04	8.83E+03	1.14E+04	0.133	0.085	0.182	7.95	7.37	8.53
2.6	7.24E+03	6.43E+03	8.06E+03	0.099	0.058	0.140	5.80	5.39	6.22
3.0	5.56E+03	5.23E+03	5.89E+03	0.096	0.072	0.121	5.80	5.58	6.01
3.4	2.97E+03	2.76E+03	3.18E+03	0.088	0.058	0.118	5.03	4.80	5.26
4.0	1.00E+03	9.67E+02	1.03E+03	0.074	0.056	0.092	4.14	4.07	4.22

Supplemental Table 2.4: Model fit values and error bounds for AC data collected for **2** between *T* = 1.8 - 14 K. (Continued)

5.0	1.89E+02	1.86E+02	1.91E+02	0.069	0.063	0.075	3.19	3.17	3.21
6.0	5.02E+01	4.98E+01	5.06E+01	0.062	0.058	0.066	2.73	2.72	2.74
7.0	1.82E+01	1.80E+01	1.84E+01	0.049	0.044	0.054	2.23	2.22	2.24
8.0	7.13E+00	7.04E+00	7.22E+00	0.057	0.051	0.063	1.91	1.90	1.92
9.0	8.84E-01	7.95E-01	9.72E-01	0.074	0.056	0.093	0.85	0.76	0.95
10.0	9.74E-02	9.48E-02	1.00E-01	0.073	0.062	0.085	0.76	0.74	0.77
11.0	1.36E-02	1.34E-02	1.37E-02	0.077	0.071	0.084	0.67	0.66	0.67
12.0	2.58E-03	2.55E-03	2.62E-03	0.089	0.082	0.097	0.61	0.61	0.62
13.0	6.22E-04	6.14E-04	6.30E-04	0.094	0.085	0.103	0.57	0.56	0.57
14.0	1.89E-04	1.83E-04	1.95E-04	0.105	0.088	0.122	0.53	0.53	0.54

T	τ_2	$\tau_{2, error, LB}$	$\tau_{2, error, UB}$	α_2	$\alpha_{2, error, LB}$	$\alpha_{2, error, UB}$	χ_{T2}	$\chi_{T2, error, LB}$	$\chi_{T2, error, UB}$
9.0	4.59E+00	4.22E+00	4.97E+00	0.012	-0.014	0.039	0.86	0.76	0.96
10.0	2.00E+00	1.96E+00	2.05E+00	0.000	-0.013	0.013	0.78	0.76	0.79
11.0	5.74E-01	5.68E-01	5.81E-01	0.045	0.035	0.055	0.71	0.70	0.72
12.0	1.37E-01	1.35E-01	1.38E-01	0.034	0.027	0.041	0.63	0.62	0.64
13.0	3.47E-02	3.44E-02	3.51E-02	0.032	0.026	0.038	0.57	0.56	0.58
14.0	1.02E-02	1.01E-02	1.03E-02	0.027	0.022	0.033	0.53	0.51	0.54

T	χ_S	$\chi_{S, error, LB}$	$\chi_{S, error, UB}$
1.8	1.24E-01	-9.32E-03	2.58E-01
1.9	8.71E-02	-1.55E-02	1.90E-01
2.0	8.18E-02	-1.62E-02	1.80E-01
2.1	1.23E-01	-4.45E-03	2.50E-01
2.2	1.05E-01	1.52E-02	1.95E-01
2.6	8.59E-02	3.60E-02	1.36E-01
3.0	7.63E-02	4.24E-02	1.10E-01
3.4	7.10E-02	3.44E-02	1.08E-01

Supplemental Table 2.4: Model fit values and error bounds for AC data collected for **2** between *T* = 1.8 - 14 K. (Continued)

4.0	5.30E-02	2.61E-02	7.98E-02
5.0	4.16E-02	3.88E-02	4.45E-02
6.0	3.94E-02	3.73E-02	4.15E-02
7.0	3.73E-02	3.47E-02	3.98E-02
8.0	3.72E-02	3.41E-02	4.02E-02
9.0	3.46E-02	3.22E-02	3.70E-02
10.0	3.10E-02	2.84E-02	3.35E-02
11.0	2.81E-02	2.64E-02	2.97E-02
12.0	2.25E-02	1.99E-02	2.51E-02
13.0	1.74E-02	1.29E-02	2.18E-02
14.0	2.29E-02	1.04E-02	3.56E-02

Magnetic Data of Compound 3

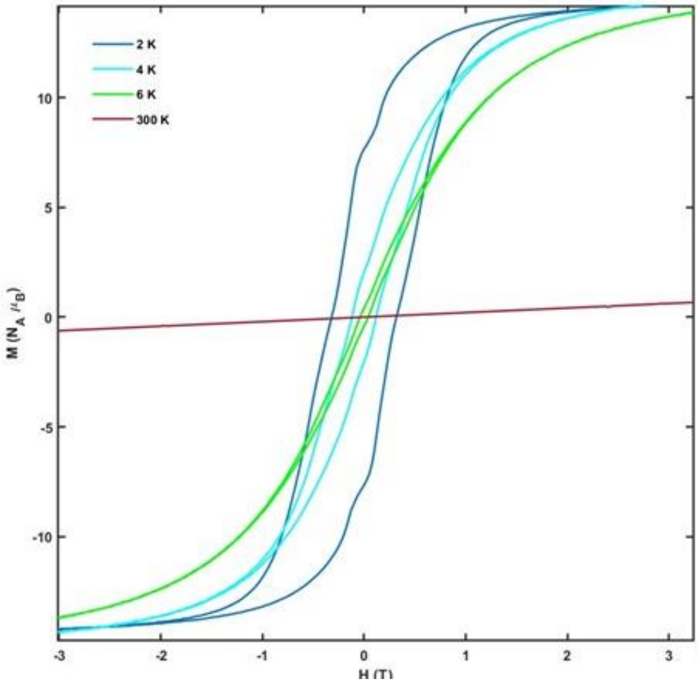

Supplemental Figure 2.13 Isothermal magnetization of **3** at 2, 4, 6, and 300 K collected between −7 to 7 T at a constant 50 Oe sec^{-1} sweep rate.

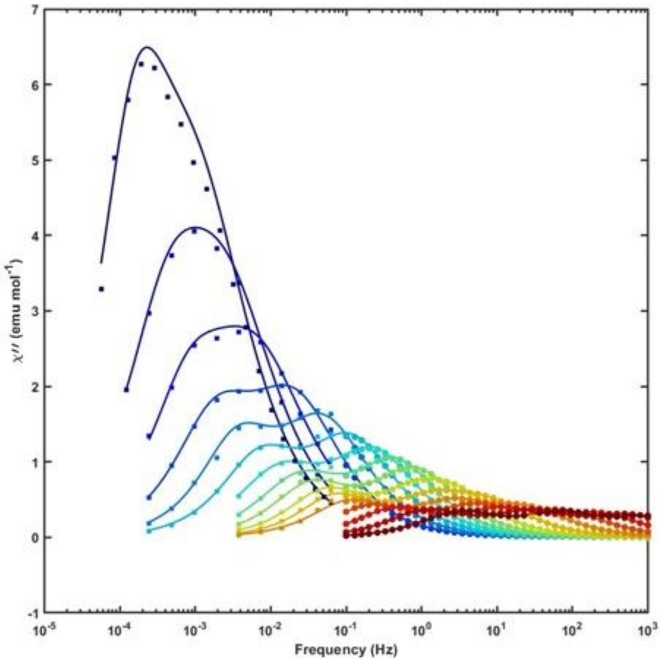

Supplemental Figure 2.14: AC out-of-phase susceptibility of **3** collected between $T = 2$ - 17 K (blue - red). Data points are susceptibilities measured via standard AC measurements (circles) and extracted from Fourier analysis of VSM data (squares). Lines represent fits to an extended Debye model.

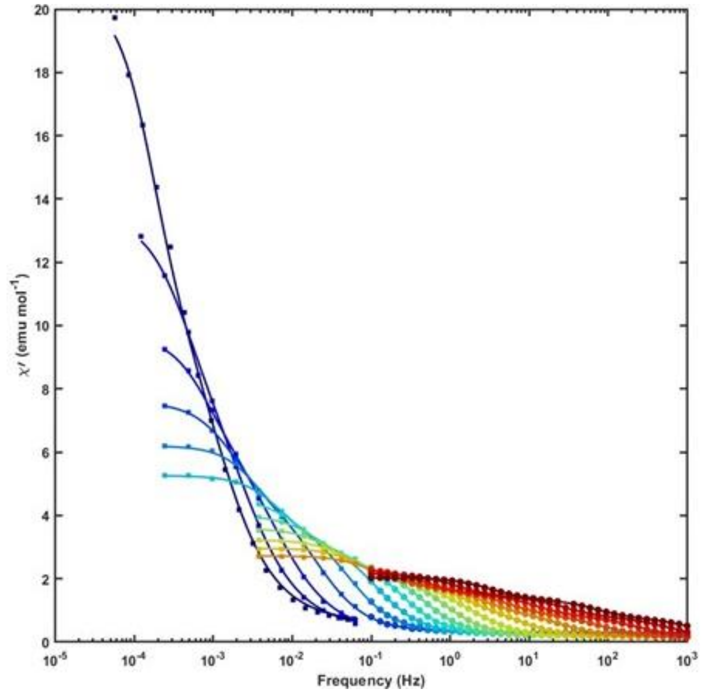

Supplemental Figure 2.15: AC in-phase susceptibility of **3** collected between $T = 2$ - 17 K (blue - red). Data points are susceptibilities measured via standard AC measurements (circles) and extracted from Fourier analysis of VSM data (squares). Lines represent fits to an extended Debye model.

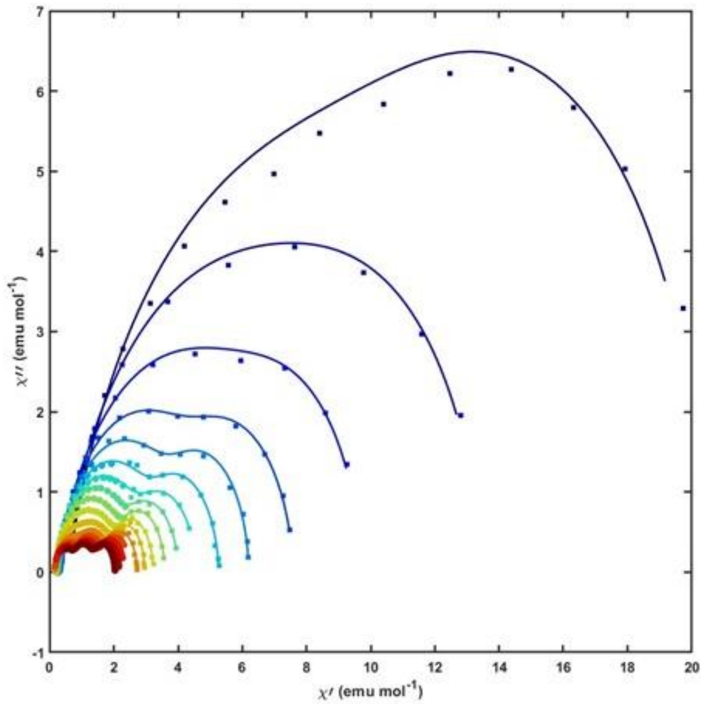

Supplemental Figure 2.16: Cole-cole plot of **3** collected between T = 2 - 17 K (blue - red). Data points are susceptibilities measured via standard AC measurements (circles) and extracted from Fourier analysis of VSM data (squares). Lines represent fits to an extended Debye model.

Supplemental Table 2.5: Model fit values for AC data collected for **3** between T = 1.8 - 17 K. Values of T are in Kelvin, τ in seconds, and χ in emu mol^{-1}.

T	τ_1	$\tau_{1,\ error,\ LB}$	$\tau_{1,\ error,\ UB}$	α_1	$\alpha_{1,\ error,\ LB}$	$\alpha_{1,\ error,\ UB}$	χ_{T1}	$\chi_{T1,\ error,\ LB}$	$\chi_{T1,\ error,\ UB}$
1.8	1.84E+02	4.46E+01	3.24E+02	0.216	0.105	0.326	13.30	6.12	20.48
1.9	1.63E+02	6.09E+01	2.65E+02	0.213	0.123	0.303	12.45	6.81	18.10
2.0	1.40E+02	5.56E+01	2.24E+02	0.214	0.124	0.304	11.81	6.75	16.87
2.1	1.32E+02	5.25E+01	2.11E+02	0.218	0.133	0.303	11.57	6.60	16.54
2.2	1.17E+02	3.44E+01	2.00E+02	0.215	0.116	0.314	10.91	5.21	16.61
2.6	9.01E+01	3.02E+01	1.50E+02	0.221	0.139	0.302	9.90	4.30	15.50
3.0	6.38E+01	2.96E+01	9.81E+01	0.215	0.145	0.284	8.79	4.84	12.75
3.5	3.52E+01	7.22E+00	6.32E+01	0.211	0.095	0.327	6.29	1.28	11.30
4.0	2.51E+01	1.44E+01	3.58E+01	0.216	0.133	0.299	6.69	4.54	8.84
4.5	1.22E+01	8.49E+00	1.59E+01	0.186	0.089	0.282	5.22	3.88	6.56

Supplemental Table 2.5: Model fit values for AC data collected for **3** between *T* = 1.8 - 17 K. (Continued)

5.0	7.45E+00	7.05E+00	7.86E+00	0.144	0.133	0.155	4.49	4.30	4.68
6.0	3.09E+00	2.94E+00	3.24E+00	0.128	0.116	0.140	3.83	3.70	3.95
7.0	1.36E+00	1.31E+00	1.41E+00	0.114	0.103	0.124	3.19	3.10	3.27
8.0	6.67E-01	6.48E-01	6.85E-01	0.102	0.094	0.110	2.73	2.66	2.79
9.0	3.40E-01	3.30E-01	3.50E-01	0.080	0.070	0.090	2.34	2.29	2.40
10.0	1.93E-01	1.89E-01	1.97E-01	0.099	0.090	0.107	2.21	2.18	2.24
11.0	5.80E-02	4.68E-02	6.93E-02	0.068	0.044	0.093	1.27	0.92	1.62
12.0	1.90E-02	1.57E-02	2.22E-02	0.079	0.041	0.116	0.97	0.76	1.18
13.0	6.00E-03	5.36E-03	6.64E-03	0.090	0.058	0.123	0.90	0.81	0.99
14.0	2.01E-03	1.96E-03	2.06E-03	0.100	0.090	0.110	0.87	0.85	0.89
15.0	7.05E-04	6.90E-04	7.19E-04	0.099	0.086	0.111	0.82	0.81	0.83
16.0	2.77E-04	2.69E-04	2.84E-04	0.062	0.035	0.088	0.75	0.73	0.77
17.0	1.52E-04	1.42E-04	1.61E-04	0.000	-0.067	0.067	0.72	0.68	0.75

T	τ_2	$\tau_{2, error, LB}$	$\tau_{2, error, UB}$	α_2	$\alpha_{2, error, LB}$	$\alpha_{2, error, UB}$	χ_{T2}	$\chi_{T2, error, LB}$	$\chi_{T2, error, UB}$
1.8	1.37E+03	9.74E+02	1.78E+03	0.000	-0.241	0.241	10.51	2.36	18.66
1.9	1.12E+03	8.46E+02	1.40E+03	0.000	-0.175	0.175	9.85	3.67	16.03
2.0	9.77E+02	7.44E+02	1.21E+03	0.000	-0.161	0.161	9.29	3.79	14.78
2.1	8.72E+02	6.56E+02	1.09E+03	0.003	-0.156	0.161	8.51	3.20	13.81
2.2	7.54E+02	5.19E+02	9.88E+02	0.018	-0.158	0.195	8.26	2.21	14.32
2.6	5.47E+02	2.87E+02	8.07E+02	0.080	-0.128	0.288	6.30	0.31	12.28
3.0	3.78E+02	2.30E+02	5.27E+02	0.064	-0.110	0.237	5.11	0.92	9.30
3.5	2.16E+02	7.18E+01	3.61E+02	0.149	-0.028	0.326	5.26	-0.09	10.61
4.0	1.96E+02	1.33E+02	2.60E+02	0.036	-0.140	0.212	3.28	0.89	5.67
4.5	1.23E+02	9.14E+01	1.55E+02	0.084	-0.012	0.180	3.69	2.11	5.27
5.0	8.85E+01	8.35E+01	9.35E+01	0.071	0.044	0.098	3.41	3.19	3.63
6.0	4.47E+01	4.24E+01	4.69E+01	0.020	-0.008	0.048	2.64	2.50	2.78
7.0	2.25E+01	2.15E+01	2.36E+01	0.049	0.026	0.073	2.32	2.22	2.41

Supplemental Table 2.5: Model fit values for AC data collected for **3** between *T* = 1.8 - 17 K. (Continued)

8.0	1.24E+01	1.19E+01	1.28E+01	0.088	0.061	0.115	2.07	1.98	2.16
9.0	6.68E+00	6.42E+00	6.94E+00	0.087	0.062	0.113	1.89	1.81	1.96
10.0	4.69E+00	4.55E+00	4.82E+00	0.045	0.025	0.065	1.56	1.52	1.61
11.0	2.09E-01	1.65E-01	2.52E-01	0.000	-0.109	0.109	0.92	0.52	1.32
12.0	1.17E-01	1.01E-01	1.34E-01	0.080	0.002	0.157	1.14	0.88	1.40
13.0	6.40E-02	5.93E-02	6.88E-02	0.078	0.024	0.132	1.04	0.91	1.16
14.0	3.22E-02	3.16E-02	3.27E-02	0.052	0.037	0.067	0.91	0.89	0.94
15.0	1.39E-02	1.37E-02	1.41E-02	0.045	0.032	0.059	0.84	0.81	0.86
16.0	5.59E-03	5.46E-03	5.71E-03	0.071	0.053	0.088	0.85	0.81	0.88
17.0	2.22E-03	2.14E-03	2.31E-03	0.052	0.025	0.079	0.87	0.80	0.94

T	τ_3	$\tau_{3, error, LB}$	$\tau_{3, error, UB}$	α_3	$\alpha_{3, error, LB}$	$\alpha_{3, error, UB}$	χ_{T3}	$\chi_{T3, error, LB}$	$\chi_{T3, error, UB}$
11.0	3.03E+00	2.89E+00	3.17E+00	0.032	0.010	0.054	1.39	1.32	1.46
12.0	2.26E+00	2.16E+00	2.35E+00	0.000	-0.025	0.025	1.18	1.12	1.25
13.0	1.47E+00	1.41E+00	1.53E+00	0.037	0.014	0.061	1.10	1.06	1.15
14.0	7.58E-01	7.48E-01	7.68E-01	0.047	0.034	0.059	1.00	0.98	1.02
15.0	3.50E-01	3.46E-01	3.54E-01	0.055	0.046	0.063	0.94	0.93	0.96
16.0	1.39E-01	1.37E-01	1.41E-01	0.044	0.035	0.052	0.89	0.87	0.90
17.0	5.01E-02	4.90E-02	5.11E-02	0.057	0.048	0.067	0.95	0.92	0.98

T	χ_S	$\chi_{S, error, LB}$	$\chi_{S, error, UB}$
1.8	6.13E-01	2.56E-01	9.71E-01
1.9	5.57E-01	2.84E-01	8.31E-01
2.0	5.70E-01	3.03E-01	8.36E-01
2.1	5.43E-01	2.95E-01	7.91E-01
2.2	5.39E-01	2.65E-01	8.12E-01
2.6	4.58E-01	2.50E-01	6.65E-01
3.0	3.87E-01	2.20E-01	5.53E-01
3.4	3.37E-01	1.22E-01	5.52E-01

Supplemental Table 2.5: Model fit values for AC data collected for **3** between T = 1.8 - 17 K. (Continued)

4.0	2.27E-01	2.01E-02	4.33E-01
5.0	2.40E-01	-2.65E-03	4.82E-01
6.0	2.98E-01	2.91E-01	3.04E-01
7.0	2.64E-01	2.56E-01	2.71E-01
8.0	2.37E-01	2.30E-01	2.43E-01
9.0	2.16E-01	2.12E-01	2.21E-01
10.0	2.01E-01	1.96E-01	2.06E-01
11.0	1.84E-01	1.79E-01	1.88E-01
12.0	1.78E-01	1.74E-01	1.82E-01
13.0	1.67E-01	1.61E-01	1.72E-01
14.0	1.57E-01	1.50E-01	1.65E-01
15.0	1.49E-01	1.46E-01	1.52E-01
16.0	1.41E-01	1.36E-01	1.47E-01
17.0	1.62E-01	1.48E-01	1.76E-01

Relaxation Fitting Methods

Temperature and τ data of **1** were fit to a multi-term relaxation model shown in Equation S.2.2. Temperature and τ data of **2** and **3** were fit to a multi-term relaxation model shown in Equation S.2.3. These equations are non-linear, multi-variable regression models encompassing a sampling space of many magnitudes. As such, it is possible to converge on multiple solutions of such a problem that would offer reasonable fits to the data. A data sample pool was generated by iteratively fitting the relaxation data to the relaxation model 50 times per relaxation process, while holding all bounds and parameters constant. A statistical analysis was concluded on the generated sample space to demonstrate validity and variability in the model. Merging processes Γ_{2A} & Γ_{2B}, and Γ_{3A} & Γ_{3B} were analyzed simultaneously in a 100-fit sample space.

$$\tau^{-1} = \tau_0^{-1} exp\left(\frac{-U_{eff}}{k_B T}\right) + CT^n + QTM \qquad \textit{(Eq. S.2.2)}$$

Equation S.2.2: Multi-term relaxation mechanism equation accounting for Orbach, Raman, and QTM relaxation processes, where τ is the fitted relaxation time, τ_0 is the attempt time, U_{eff} is the effective barrier, k_B is the Boltzmann constant, T is the temperature, C is the Raman relaxation coefficient, n is the Raman exponent, and QTM is the quantum tunneling of magnetization term.

$$\tau^{-1} = \tau_0^{-1} exp\left(\frac{-U_{eff}}{k_B T}\right) + CT^n + \tau_D^{-1} exp\left(\frac{-D_{eff}}{k_B T}\right) \qquad \textit{(Eq. S.2.3)}$$

Equation S.2.3: Multi-term relaxation mechanism equation accounting for Orbach, Raman, and dipolar processes, where τ is the fitted relaxation time, τ_0 is the attempt time, U_{eff} is the effective barrier, k_B is the Boltzmann constant, T is the temperature, C is the Raman relaxation coefficient, n is the Raman exponent, τ_D is the dipole attempt time, and D_{eff} is the dipole effective barrier.

2.6.4 Computational Details

All calculations were carried out at the CASSCF level using the OpenMolcas computational package.[i] Input atom coordinates were taken from crystallographic data and used without further geometry optimization. Calculations on **1** were concluded with triisopropyl groups and with triisopropyl groups removed and replaced with hydrogen atoms, **[1]**, whose positions were placed with the standard riding model to demonstrate similarity in results. Triisopropyl groups in **2** and **3** were substituted with hydrogen atoms whose positions were placed with the standard riding model due to disorder present on the groups as well as to save

---

[i] Aquilante, F.; Autschbach, J.; Baiardi, A.; Battaglia, S.; Borin, V. A.; Chibotaru, L. F.; Conti, I.; De Vico, L.; Delcey, M.; Fdez. Galván, I.; Ferré, N.; Freitag, L.; Garavelli, M.; Gong, X.; Knecht, S.; Larsson, E. D.; Lindh, R.; Lundberg, M.; Malmqvist, P. Å.; Nenov, A.; Norell, J.; Odelius, M.; Olivucci, M.; Pedersen, T. B.; Pedraza-González, L.; Phung, Q. M.; Pierloot, K.; Reiher, M.; Schapiro, I.; Segarra-Martí, J.; Segatta, F.; Seijo, L.; Sen, S.; Sergentu, D.-C.; Stein, C. J.; Ungur, L.; Vacher, M.; Valentini, A.; Veryazov, V. *The Journal of Chemical Physics* **2020**, *152*, 214117.; Fdez. Galván, I.; Vacher, M.; Alavi, A.; Angeli, C.; Aquilante, F.; Autschbach, J.; Bao, J. J.; Bokarev, S. I.; Bogdanov, N. A.; Carlson, R. K.; Chibotaru, L. F.; Creutzberg, J.; Dattani, N.; Delcey, M. G.; Dong, S. S.; Dreuw, A.; Freitag, L.; Frutos, L. M.; Gagliardi, L.; Gendron, F.; Giussani, A.; González, L.; Grell, G.; Guo, M.; Hoyer, C. E.; Johansson, M.; Keller, S.; Knecht, S.; Kovačević, G.; Källman, E.; Li Manni, G.; Lundberg, M.; Ma, Y.; Mai, S.; Malhado, J. P.; Malmqvist, P. Å.; Marquetand, P.; Mewes, S. A.; Norell, J.; Olivucci, M.; Oppel, M.; Phung, Q. M.; Pierloot, K.; Plasser, F.; Reiher, M.; Sand, A. M.; Schapiro, I.; Sharma, P.; Stein, C. J.; Sørensen, L. K.; Truhlar, D. G.; Ugandi, M.; Ungur, L.; Valentini, A.; Vancoillie, S.; Veryazov, V.; Weser, O.; Wesołowski, T. A.; Widmark, P.-O.; Wouters, S.; Zech, A.; Zobel, J. P.; Lindh, R. *Journal of Chemical Theory and Computation* **2019**, *15*, 5925.

disk space and reduce calculation cost; these are hereafter referred to as **[2]** and **[3]**. Due to the presence of multiple fragments in the unit cells for both **2** and **3**, calculations were completed individually on each fragment and averaged out across the fragments in the unit cell. Cant angles (θ_{cant}) demonstrating offset between the main magnetic axes and the Er-COT vector were carried out following the procedure discussed in our previous work.[j]

Basis functions of the ANO-RCC type were generated with the SEWARD module. The quality of a specific atomic basis function was determined by the atom's connectivity to the Er^{3+} ion (**Er**: ANO-RCC-VTZP; **atoms bound to Er**: ANO-RCC-VDZP; **all other atoms**: ANO-RCC-VDZ). Two-electron integrals were Cholesky decomposed (10^{-6} cutoff). A 7-orbital, 11-electron active space (CAS(11,7)) was selected for the CASSCF calculation, which was carried out using the RASSCF module. In this space, all 35 configuration-interaction (CI) roots of spin multiplicity 4 and all 112 CI roots of spin multiplicity 2 were included. The RASSI module was used to calculate spin-orbit matrix elements between CAS output wavefunctions. The SINGLE_ANISO module of OpenMolcas was used to calculate relevant magnetic properties based on these multiconfigurational SCF results.

The POLY_ANISO module[k] was utilized to determine exactly the dipolar interaction in **[2]** and **[3]**, utilizing the aforementioned SINGLE_ANISO results. Compound **[2]** was modeled as a single center with inversion symmetry. Each erbium(III) center in **[3]** was modeled separately by the fragmentation model for polynuclear compounds, substituting the remaining two centers for diamagnetic yttrium(III) counterparts.

---

[j] Bernbeck, M. G.; Hilgar, J. D.; Rinehart, J. D. *Polyhedron* **2020**, *175*.

[k] Chibotaru, L. F.; Ungur, L.; Soncini, A. *Angewandte Chemie International Edition* **2008**, *47*, 4126.

Supplemental Table 2.6: Selected average magnetic moment matrix elements between the J = 15⁄2 multiplets of **1** and **[1]**.

	1 $\lVert T_{ij} \rVert$		
KD (n)	$KD_{n,\alpha} \overset{\leftarrow}{\rightarrow} KD_{n,\beta}$	$KD_{n,\alpha} \overset{\leftarrow}{\rightarrow} KD_{n+1,\alpha}$	$KD_{n,\alpha} \overset{\leftarrow}{\rightarrow} KD_{n+1,\beta}$
0	2.64E-03	1.58E+00	8.64E-03
1	2.63E-02	3.66E-01	4.47E-01
2	3.15E+00	2.99E+00	4.56E-01
3	9.36E-01	2.02E+00	7.02E-01
4	5.04E-01	1.52E+00	6.82E-01
5	4.70E-01	1.93E+00	4.98E-01
6	3.91E-01	2.14E+00	2.76E-01
7	1.36E-01	--	--
	[1] $\lVert T_{ij} \rVert$		
KD (n)	$KD_{n,\alpha} \overset{\leftarrow}{\rightarrow} KD_{n,\beta}$	$KD_{n,\alpha} \overset{\leftarrow}{\rightarrow} KD_{n+1,\alpha}$	$KD_{n,\alpha} \overset{\leftarrow}{\rightarrow} KD_{n+1,\beta}$
0	2.13E-03	1.57E+00	6.57E-03
1	1.55E-02	2.22E-01	4.52E-01
2	3.10E+00	2.92E+00	5.35E-01
3	1.04E+00	1.93E+00	7.08E-01
4	3.94E-01	1.55E+00	7.23E-01
5	5.25E-01	2.03E+00	5.12E-01
6	4.39E-01	1.94E+00	3.60E-01
7	1.85E-01	--	--

Supplemental Table 2.7: Selected average magnetic moment matrix elements between the J = 15⁄2 multiplets of **2** and **[2]**.

	[2], Average $\lVert T_{ij} \rVert$		
KD (n)	$KD_{n,\alpha} \overset{\leftarrow}{\rightarrow} KD_{n,\beta}$	$KD_{n,\alpha} \overset{\leftarrow}{\rightarrow} KD_{n+1,\alpha}$	$KD_{n,\alpha} \overset{\leftarrow}{\rightarrow} KD_{n+1,\beta}$
0	6.40E-05	1.55E+00	2.24E-04
1	4.97E-04	1.66E-01	7.31E-02
2	3.18E+00	2.84E+00	1.60E-01
3	2.63E-01	1.07E+00	1.57E-01
4	8.49E-02	1.76E+00	4.33E-02
5	1.23E-01	2.23E+00	9.56E-02

Supplemental Table 2.7: Selected average magnetic moment matrix elements between the J = 15⁄2 multiplets of **2** and **[2]**. (Continued)

6	5.81E-02	9.06E-01	8.07E-02
7	1.13E-02	--	--
	[2], Fragment 1 $\lVert T_{ij} \rVert$		
KD (n)	$KD_{n,\alpha} \leftrightarrows KD_{n,\beta}$	$KD_{n,\alpha} \leftrightarrows KD_{n+1,\alpha}$	$KD_{n,\alpha} \leftrightarrows KD_{n+1,\beta}$
0	7.61E-05	1.55E+00	2.17E-04
1	4.61E-04	1.57E-01	6.19E-02
2	3.19E+00	2.97E+00	2.45E-01
3	4.05E-01	1.11E+00	1.83E-01
4	6.02E-02	1.46E+00	3.00E-02
5	9.52E-02	2.29E+00	8.51E-02
6	5.17E-02	9.32E-01	6.36E-02
7	8.79E-03	--	--
	[2], Fragment 2 $\lVert T_{ij} \rVert$		
KD (n)	$KD_{n,\alpha} \leftrightarrows KD_{n,\beta}$	$KD_{n,\alpha} \leftrightarrows KD_{n+1,\alpha}$	$KD_{n,\alpha} \leftrightarrows KD_{n+1,\beta}$
0	5.19E-05	1.55E+00	2.31E-04
1	5.32E-04	1.76E-01	8.44E-02
2	3.16E+00	2.72E+00	7.52E-02
3	1.21E-01	1.02E+00	1.32E-01
4	1.10E-01	2.06E+00	5.66E-02
5	1.52E-01	2.17E+00	1.06E-01
6	6.45E-02	8.79E-01	9.78E-02
7	1.38E-02	--	--

Supplemental Table 2.8: *J* = 15⁄2 manifold spectrum of **[2]** and averages between both fragments.

	[2], Fragment 1		**[2], Fragment 2**		**[2], Average**	
KD (*n*)	M$_z$ (μ_B)	E (cm^{-1})	M$_z$ (μ_B)	E (cm^{-1})	M$_z$ (μ_B)	E (cm^{-1})
0	8.95	0.00	8.96	0.00	8.96	0.00
1	7.75	96.01	7.75	95.25	7.75	95.63
2	0.61	190.39	0.62	197.42	0.62	193.91
3	2.41	238.14	3.27	241.76	2.84	239.95
4	5.84	252.43	5.19	256.02	5.52	254.22
5	3.51	309.04	3.54	311.78	3.52	310.41
6	6.91	349.17	7.18	355.99	7.04	352.58
7	8.27	411.29	8.30	417.70	8.28	414.49

Supplemental Table 2.9: *g*-values and calculated cant angles of **[2]** and averages between both fragments.

g	**[2], Fragment 1**	**[2], Fragment 2**	**[2], Average**
gX	0.000202	0.000126	0.000164
gY	0.000254	0.000185	0.000220
gZ	17.906892	17.919106	17.912999
θ_{cant}	1.57°	1.28°	1.43°

Supplemental Table 2.10: Dipole manifold spectrum of **[2]** and averages between both fragments.

	[2], Fragment 1		**[2], Fragment 2**		**[2], Average**	
DD (*n*)	M$_z$ (μ_B)	E (cm^{-1})	M$_z$ (μ_B)	E (cm^{-1})	M$_z$ (μ_B)	E (cm^{-1})
0	0.00	17.91	0.00	17.92	0.00	17.91
1	0.65	0.00	0.66	0.00	0.65	0.00

Supplemental Table 2.11: Selected average magnetic moment matrix elements between the dipole doublets of **[2]** and averages between both fragments. Transitions in the “Averages” column are highlighted with respect to number of spin flips per transition (as discussed in the main text) with red (one), blue (two).

Transition	**[2], Average** $\|T_{ij}\|$	**[2], Fragment 1** $\|T_{ij}\|$	**[2], Fragment 2** $\|T_{ij}\|$
$DD_{0,\alpha\alpha} \overset{\|T_{ij}\|}{\underset{\longrightarrow}{\longleftarrow}} DD_{0,\beta\beta}$	1.43E-15	1.39E-15	1.46E-15
$DD_{0,\alpha\alpha} \overset{\|T_{ij}\|}{\underset{\longrightarrow}{\longleftarrow}} DD_{1,\alpha\beta}$	1.13E-04	1.34E-04	9.29E-05
$DD_{0,\alpha\alpha} \overset{\|T_{ij}\|}{\underset{\longrightarrow}{\longleftarrow}} DD_{1,\beta\alpha}$	1.14E-04	1.36E-04	9.28E-05
$DD_{1,\alpha\alpha} \overset{\|T_{ij}\|}{\underset{\longrightarrow}{\longleftarrow}} DD_{1,\beta\beta}$	8.47E-21	9.31E-21	7.62E-21

Supplemental Table 2.12: $J = 15/2$ manifold spectrum of **[3]** and averages between both fragments.

Fragment 1	**[3], Er-1**		**[3], Er-2**		**[3], Er-3**	
KD (*n*)	M$_z$ (μ_B)	E (cm^{-1})	M$_z$ (μ_B)	E (cm^{-1})	M$_z$ (μ_B)	E (cm^{-1})
0	8.97	0.00	8.95	0.00	8.98	0.00
1	7.75	97.99	7.68	80.96	7.77	96.47
2	6.28	236.43	5.54	172.98	5.40	243.72
3	4.75	257.52	3.85	212.68	4.70	255.42
4	3.90	296.97	4.45	248.76	0.69	293.34
5	4.39	337.88	3.56	292.50	3.04	349.60
6	4.72	379.41	5.13	323.69	5.67	363.93
7	5.82	404.42	6.22	347.77	5.97	395.06
Fragment 2	**[3], Er-1**		**[3], Er-2**		**[3], Er-3**	
KD (*n*)	M$_z$ (μ_B)	E (cm^{-1})	M$_z$ (μ_B)	E (cm^{-1})	M$_z$ (μ_B)	E (cm^{-1})
0	8.98	0.00	8.95	0.00	8.99	0.00
1	7.77	99.93	7.67	80.69	7.78	92.95
2	6.07	239.18	5.40	170.81	4.45	240.96
3	5.22	259.64	3.81	211.85	4.84	255.70
4	3.12	293.74	4.50	249.71	0.47	292.05
5	4.38	338.42	3.43	293.53	3.53	350.53
6	4.86	373.13	5.20	324.59	5.83	367.09
7	6.16	402.50	6.21	347.89	6.11	398.09
Average	**[3], Er-1, Avg**		**[3], Er-2, Avg**		**[3], Er-3, Avg**	
KD (*n*)	M$_z$ (μ_B)	E (cm^{-1})	M$_z$ (μ_B)	E (cm^{-1})	M$_z$ (μ_B)	E (cm^{-1})
0	8.98	0.00	8.95	0.00	8.98	0.00
1	7.76	98.96	7.68	80.82	7.77	94.71
2	6.18	237.81	5.47	171.90	4.93	242.34
3	4.98	258.58	3.83	212.27	4.77	255.56
4	3.51	295.36	4.47	249.23	0.58	292.69
5	4.38	338.15	3.50	293.02	3.28	350.07
6	4.79	376.27	5.17	324.14	5.75	365.51
7	5.99	403.46	6.22	347.83	6.04	396.57

Supplemental Table 2.13: *g*-values and calculated cant angles of **[3]** and averages between both fragments.

Fragment 1	**[3], Er-1**	**[3], Er-2**	**[3], Er-3**
gX	0.001174	0.000755	0.000789
gY	0.001384	0.001074	0.000981
gZ	17.946448	17.898482	17.961393
θ_{cant}	3.53°	6.60°	2.47°
Fragment 2	**[3], Er-1**	**[3], Er-2**	**[3], Er-3**
gX	0.000644	0.001428	0.000204
gY	0.000758	0.002025	0.000249
gZ	17.969535	17.907571	17.970761
θ_{cant}	3.35°	6.41°	2.82°
Average	**[3], Er-1, Avg**	**[3], Er-2, Avg**	**[3], Er-3, Avg**
gX	0.000909	0.001091	0.000496
gY	0.001071	0.001550	0.000615
gZ	17.957992	17.903027	17.966077
θ_{cant}	3.44°	6.51°	2.65°

Supplemental Table 2.14: Dipole manifold spectrum of **[3]** and averages between both fragments.

	[3], Fragment 1		**[3], Fragment 2**		**[3], Average**	
DD (*n*)	M_z (μ_B)	E (cm^{-1})	M_z (μ_B)	E (cm^{-1})	M_z (μ_B)	E (cm^{-1})
0	18.63	0.00	18.98	0.00	18.81	0.00
1	21.34	0.24	21.06	0.20	21.20	0.22
2	8.18	1.12	8.40	1.10	8.29	1.11
3	9.79	2.84	9.59	2.82	9.69	2.83

Supplemental Table 2.15: Selected average magnetic moment matrix elements between the dipole doublets of [3] and averages between both fragments. This table can be read in a cross-wise fashion, with the intersection of states corresponding to the magnetic moment matrix element for the transition between those states. For example:

$$DD_{0,\alpha\alpha\alpha} \overset{2.14\ x\ 10^{-4}}{\overset{\longleftarrow}{\longrightarrow}} DD_{3,\alpha\alpha\beta}$$

Some redundant transitions are not shown, as it is implied that such transitions are identical:

$$DD_{0,\alpha\alpha\alpha} \overset{2.14\ x\ 10^{-4}}{\overset{\longleftarrow}{\longrightarrow}} DD_{3,\alpha\alpha\beta} \equiv DD_{0,\beta\beta\beta} \overset{2.14\ x\ 10^{-4}}{\overset{\longleftarrow}{\longrightarrow}} DD_{3,\beta\beta\alpha}$$

Transitions in the “Averages” table are highlighted with respect to number of spin flips per transition (as discussed in the main text) with red (one), green (two), and blue (three).

[3], Averages $\|T_{ij}\|$

DD_n		0	1	2	3	1	2	3
	State	$\beta\beta\beta$	$\alpha\beta\beta$	$\beta\alpha\beta$	$\beta\beta\alpha$	$\beta\alpha\alpha$	$\alpha\beta\alpha$	$\alpha\alpha\beta$
0	$\alpha\alpha\alpha$	6.22E-12	7.57E-08	3.22E-08	6.30E-08	1.02E-03	8.19E-04	2.14E-04
1	$\beta\alpha\alpha$	7.57E-08	6.46E-12	2.33E-04	5.91E-04	N/A	1.04E-07	3.12E-08
2	$\alpha\beta\alpha$	3.22E-08	2.33E-04	2.99E-12	4.68E-04	1.04E-07	N/A	1.64E-08
3	$\alpha\alpha\beta$	6.30E-08	5.91E-04	4.68E-04	2.08E-12	3.12E-08	1.64E-08	N/A

[3], Fragment 1 $\|T_{ij}\|$

DD_n		0	1	2	3	1	2	3
	State	$\beta\beta\beta$	$\alpha\beta\beta$	$\beta\alpha\beta$	$\beta\beta\alpha$	$\beta\alpha\alpha$	$\alpha\beta\alpha$	$\alpha\alpha\beta$
0	$\alpha\alpha\alpha$	8.89E-12	9.67E-08	5.49E-08	5.71E-08	1.22E-03	5.44E-04	3.41E-04
1	$\beta\alpha\alpha$	9.67E-08	8.86E-12	3.72E-04	4.08E-04	N/A	8.85E-08	5.32E-08
2	$\alpha\beta\alpha$	5.49E-08	3.72E-04	4.83E-12	6.03E-04	8.85E-08	N/A	2.16E-08
3	$\alpha\alpha\beta$	5.71E-08	4.08E-04	6.03E-04	3.32E-12	5.32E-08	2.16E-08	N/A

[3], Fragment 2 $\|T_{ij}\|$

DD_n		0	1	2	3	1	2	3
	State	$\beta\beta\beta$	$\alpha\beta\beta$	$\beta\alpha\beta$	$\beta\beta\alpha$	$\beta\alpha\alpha$	$\alpha\beta\alpha$	$\alpha\alpha\beta$
0	$\alpha\alpha\alpha$	3.55E-12	5.46E-08	9.60E-09	6.89E-08	8.30E-04	1.09E-03	8.71E-05

Supplemental Table 2.15: Selected average magnetic moment matrix elements between the dipole doublets of [3] and averages between both fragments. (Continued)

1	$\beta\alpha\alpha$	5.46E-08	4.06E-12	9.46E-05	7.73E-04	N/A	1.19E-07	9.23E-09
2	$\alpha\beta\alpha$	9.60E-09	9.46E-05	1.15E-12	3.32E-04	1.19E-07	N/A	1.12E-08
3	$\alpha\alpha\beta$	6.89E-08	7.73E-04	3.32E-04	8.42E-13	9.23E-09	1.12E-08	N/A

2.6 Acknowledgements

Chapter 2 is directly adapted from material as it appears in the Journal of the American Chemical Society: Orlova, A.P., Hilgar, J.D., Bernbeck, M.G., Gembicky, M., Rinehart, J.D., “Intuitive Control of Low-Energy Magnetic Excitations via Directed Dipolar Interactions in a Series of Er(III)-Based Complexes,” *J. Amer. Chem. Soc.* **2022**. 144 (25), 11316. The dissertation author was the primary researcher and author of this paper.

2.7 References

1. Rinehart, J. D.; Long, J. R. "Exploiting single-ion anisotropy in the design of f-element single-molecule magnets" *Chem Sci* **2011**, *2*, 2078.

2. Woodruff, D. N.; Winpenny, R. E. P.; Layfield, R. A. "Lanthanide Single-Molecule Magnets" *Chemical Reviews* **2013**, *113*, 5110.

3. Jackson, C. E.; Moseley, I. P.; Martinez, R.; Sung, S.; Zadrozny, J. M. "A reaction-coordinate perspective of magnetic relaxation" *Chemical Society Reviews* **2021**, *50*, 6684.

4. Christou, G.; Gatteschi, D.; Hendrickson, D. N.; Sessoli, R. "Single-Molecule Magnets" *MRS Bulletin* **2000**, *25*, 66.

5. Guo, F. S.; Day, B. M.; Chen, Y. C.; Tong, M. L.; Mansikkamaki, A.; Layfield, R. A. "Magnetic hysteresis up to 80 kelvin in a dysprosium metallocene single-molecule magnet" *Science* **2018**, *362*, 1400.

6. Ding, Y.-S.; Yu, K.-X.; Reta, D.; Ortu, F.; Winpenny, R. E. P.; Zheng, Y.-Z.; Chilton, N. F. "Field- and temperature-dependent quantum tunnelling of the magnetisation in a large barrier single-molecule magnet" *Nature Communications* **2018**, *9*, 3134.

7. Gómez-Coca, S.; Urtizberea, A.; Cremades, E.; Alonso, P. J.; Camón, A.; Ruiz, E.; Luis, F. "Origin of slow magnetic relaxation in Kramers ions with non-uniaxial anisotropy" *Nature Communications* **2014**, *5*, 4300.

8. Lunghi, A.; Totti, F.; Sanvito, S.; Sessoli, R. "Intra-molecular origin of the spin-phonon coupling in slow-relaxing molecular magnets" *Chem Sci* **2017**, *8*, 6051.

9. Moseley, D. H.; Stavretis, S. E.; Zhu, Z.; Guo, M.; Brown, C. M.; Ozerov, M.; Cheng, Y.; Daemen, L. L.; Richardson, R.; Knight, G.; Thirunavukkuarasu, K.; Ramirez-Cuesta, A. J.; Tang, J.; Xue, Z.-L. "Inter-Kramers Transitions and Spin–Phonon Couplings in a Lanthanide-Based Single-Molecule Magnet" *Inorganic Chemistry* **2020**, *59*, 5218.

10. Liu, J.-L.; Chen, Y.-C.; Tong, M.-L. "Symmetry strategies for high performance lanthanide-based single-molecule magnets" *Chemical Society Reviews* **2018**, *47*, 2431.

11. Bernbeck, M. G.; Hilgar, J. D.; Rinehart, J. D. "Probing axial anisotropy in dinuclear alkoxide-bridged Er-COT single-molecule magnets" *Polyhedron* **2020**, *175*, 114206.

12. Hilgar, J. D.; Bernbeck, M. G.; Flores, B. S.; Rinehart, J. D. "Metal-ligand pair anisotropy in a series of mononuclear Er-COT complexes" *Chem Sci* **2018**, *9*, 7204.

13. Hilgar, J. D.; Bernbeck, M. G.; Rinehart, J. D. "Million-fold Relaxation Time Enhancement across a Series of Phosphino-Supported Erbium Single-Molecule Magnets" *J Am Chem Soc* **2019**, *141*, 1913.

14. Hilgar, J. D.; Butts, A. K.; Rinehart, J. D. "A method for extending AC susceptometry to long-timescale magnetic relaxation" *Phys Chem Chem Phys* **2019**, *21*, 22302.

15. Hilgar, J. D.; Flores, B. S.; Rinehart, J. D. "Ferromagnetic coupling in a chloride-bridged erbium single-molecule magnet" *Chem Commun* **2017**, *53*, 7322.

16. Meng, Y.-S.; Yang, M.-W.; Xu, L.; Xiong, J.; Hu, J.-Y.; Liu, T.; Wang, B.-W.; Gao, S. "Design principle of half-sandwich type erbium single-ion magnets through crystal field engineering: a combined magnetic and electronic structure study" *Dalton Transactions* **2019**, *48*, 10407.

17. Lu, G.; Liu, Y.; Deng, W.; Huang, G.-Z.; Chen, Y.-C.; Liu, J.-L.; Ni, Z.-P.; Giansiracusa, M.; Chilton, N. F.; Tong, M.-L. "A perfect triangular dysprosium single-molecule magnet with virtually antiparallel Ising-like anisotropy" *Inorganic Chemistry Frontiers* **2020**, *7*, 2941.

18. Trambitas, A. G.; Yang, J. Y.; Melcher, D.; Daniliuc, C. G.; Jones, P. G.; Xie, Z. W.; Tamm, M. "Synthesis and Structure of Rare-Earth-Metal Dicarbollide Complexes with an Imidazolin-2-iminato Ligand Featuring Very Short Metal-Nitrogen Bonds" *Organometallics* **2011**, *30*, 1122.

19. Cendrowski-Guillaume, S. M.; Le Gland, G.; Nierlich, M.; Ephritikhine, M. "Lanthanide Borohydrides as Precursors to Organometallic Compounds. Mono(cyclooctatetraenyl) Neodymium Complexes" *Organometallics* **2000**, *19*, 5654.

20. Mashima, K.; Shibahara, T.; Nakayama, Y.; Nakamura, A. "Mononuclear η8-cyclooctatetraenyl(thiolato)samarium(III) complexes (η8-C8H8)Sm(SR)(hmpa)2 (R=2,4,6-triisopropylphenyl and 2-pyridyl; HMPA=hexamethylphosphoric triamide) derived from metallic samarium, diaryl disulfide, and 1,3,5,7-cyclooctatetraene in the" *Journal of Organometallic Chemistry* **1998**, *559*, 197.

21. Hodgson, K. O.; Raymond, K. N. "Dimeric .pi.-cyclooctatetraene dianion complex of cerium(III). Crystal and molecular structure of [Ce(C8H8)Cl.20C4H8]2" *Inorganic Chemistry* **1972**, *11*, 171.

22. Hilgar, J. D.; Bernbeck, M. G.; Flores, B. S.; Rinehart, J. D. "Metal–ligand pair anisotropy in a series of mononuclear Er–COT complexes" *Chem Sci* **2018**, *9*, 7204.

23. Wayda, A. L.; Mukerji, I.; Dye, J. L.; Rogers, R. D. "Divalent lanthanoid synthesis in liquid ammonia. 2. The synthesis and x-ray crystal structure of (C8H8)Yb(C5H5N)3.1/2C5H5N" *Organometallics* **1987**, *6*, 1328.

24. Mashima, K.; Fukumoto, H.; Nakayama, Y.; Tani, K.; Nakamura, A. "Cationic monocyclooctatetraenyl-lanthanoid complexes derived from metallic lanthanoid: crystal structures of [Sm(η8−C8H8)(hmpa)3]I and [Sm(η8−C8H8)(hmpa)3][Sm(η8−C8H8)2] (HMPA = hexamethylphosphoric triamide)" *Polyhedron* **1998**, *17*, 1065.

25. Edelmann, A.; Lorenz, V.; Hrib, C. G.; Hilfert, L.; Blaurock, S.; Edelmann, F. T. "Steric Effects in Lanthanide Sandwich Complexes Containing Bulky Cyclooctatetraenyl Ligands" *Organometallics* **2013**, *32*, 1435.

26. Meermann, C.; Ohno, K.; Törnroos, K. W.; Mashima, K.; Anwander, R. "Rare-Earth Metal Bis(dimethylsilyl)amide Complexes Supported by Cyclooctatetraenyl Ligands" *European Journal of Inorganic Chemistry* **2009**, *2009*, 76.

27. Roesky, P. W.; Gamer, M. T.; Marinos, N. "Yttrium and Lanthanide Diphosphanylamides: Syntheses and Structures of Complexes with one{(Ph2P)2N}− ligand in the Coordination Sphere" *Chemistry - A European Journal* **2004**, *10*, 3537.

28. Harriman, K. L. M.; Korobkov, I.; Murugesu, M. "From a Piano Stool to a Sandwich: A Stepwise Route for Improving the Slow Magnetic Relaxation Properties of Thulium" *Organometallics* **2017**, *36*, 4515.

29. Visseaux, M.; Nief, F.; Ricard, L. "Synthesis of mixed phospholyl/cyclooctatetraenyl–lanthanide complexes. Crystal and molecular structure of (cyclooctatetraenyl)[3,4-dimethyl-2,5-bis(trimethylsilyl)-phospholyl](tetrahydrofuran)neodymium" *Journal of Organometallic Chemistry* **2002**, *647*, 139.

30. Kahn, O. *Molecular Magnetism*; VCH Publishers, Inc., 1993.

31. Gatteschi, D.; Sessoli, R.; Villain, J. "Molecular Nanomagnets" *Mesoscopic Phys Nano* **2006**, 1, 71.

32. Guo, Y.-N.; Xu, G.-F.; Gamez, P.; Zhao, L.; Lin, S.-Y.; Deng, R.; Tang, J.; Zhang, H.-J. "Two-Step Relaxation in a Linear Tetranuclear Dysprosium(III) Aggregate Showing Single-Molecule Magnet Behavior" *J Am Chem Soc* **2010**, *132*, 8538.

33. Guo, Y.-N.; Xu, G.-F.; Wernsdorfer, W.; Ungur, L.; Guo, Y.; Tang, J.; Zhang, H.-J.; Chibotaru, L. F.; Powell, A. K. "Strong Axiality and Ising Exchange Interaction Suppress Zero-Field Tunneling of Magnetization of an Asymmetric Dy2 Single-Molecule Magnet" *J Am Chem Soc* **2011**, *133*, 11948.

34. Ho, L. T. A.; Chibotaru, L. F. "Multiple relaxation times in single-molecule magnets" *Phys Rev B* **2016**, *94*, 104422.

35. Fdez. Galván, I.; Vacher, M.; Alavi, A.; Angeli, C.; Aquilante, F.; Autschbach, J.; Bao, J. J.; Bokarev, S. I.; Bogdanov, N. A.; Carlson, R. K.; Chibotaru, L. F.; Creutzberg, J.; Dattani, N.; Delcey, M. G.; Dong, S. S.; Dreuw, A.; Freitag, L.; Frutos, L. M.; Gagliardi, L.; Gendron, F.; Giussani, A.; González, L.; Grell, G.; Guo, M.; Hoyer, C. E.; Johansson, M.; Keller, S.; Knecht, S.; Kovačević, G.; Källman, E.; Li Manni, G.; Lundberg, M.; Ma, Y.; Mai, S.; Malhado, J. P.; Malmqvist, P. Å.; Marquetand, P.; Mewes, S. A.; Norell, J.; Olivucci, M.; Oppel, M.; Phung, Q. M.; Pierloot, K.; Plasser, F.; Reiher, M.; Sand, A. M.; Schapiro, I.; Sharma, P.; Stein, C. J.; Sørensen, L. K.; Truhlar, D. G.; Ugandi, M.; Ungur, L.; Valentini, A.; Vancoillie, S.; Veryazov, V.; Weser, O.; Wesołowski, T. A.; Widmark, P.-O.; Wouters, S.; Zech, A.; Zobel, J. P.; Lindh, R. "OpenMolcas: From Source Code to Insight" *Journal of Chemical Theory and Computation* **2019**, *15*, 5925.

36. Aquilante, F.; Autschbach, J.; Baiardi, A.; Battaglia, S.; Borin, V. A.; Chibotaru, L. F.; Conti, I.; De Vico, L.; Delcey, M.; Fdez. Galván, I.; Ferré, N.; Freitag, L.; Garavelli, M.; Gong, X.; Knecht, S.; Larsson, E. D.; Lindh, R.; Lundberg, M.; Malmqvist, P. Å.; Nenov, A.; Norell, J.; Odelius, M.; Olivucci, M.; Pedersen, T. B.; Pedraza-González, L.; Phung, Q. M.; Pierloot, K.; Reiher, M.; Schapiro, I.; Segarra-Martí, J.; Segatta, F.; Seijo, L.; Sen, S.; Sergentu, D.-C.; Stein, C. J.; Ungur, L.; Vacher, M.; Valentini, A.; Veryazov, V. "Modern quantum chemistry with [Open]Molcas" *The Journal of Chemical Physics* **2020**, *152*, 214117.

37. Chibotaru, L. F.; Ungur, L.; Soncini, A. "The Origin of Nonmagnetic Kramers Doublets in the Ground State of Dysprosium Triangles: Evidence for a Toroidal Magnetic Moment" *Angewandte Chemie International Edition* **2008**, *47*, 4126.

38. Liebschner, D.; Afonine, P. V.; Urzhumtsev, A. G.; Adams, P. D. "Implementation of the riding hydrogen model in CCTBX to support the next generation of X-ray and neutron joint refinement in Phenix" *Method Enzymol* **2020**, *634*, 177.

39. Sheldrick, G. M.; Schneider, T. R. "SHELXL: High-resolution refinement" *Macromolecular Crystallography, Pt B* **1997**, *277*, 319.

40. Le Roy, J. J.; Korobkov, I.; Murugesu, M. "A sandwich complex with axial symmetry for harnessing the anisotropy in a prolate erbium(iii) ion" *Chem. Commun.* **2014**, *50*, 1602.

41. Le Roy, J. J.; Ungur, L.; Korobkov, I.; Chibotaru, L. F.; Murugesu, M. "Coupling Strategies to Enhance Single-Molecule Magnet Properties of Erbium–Cyclooctatetraenyl Complexes" *J Am Chem Soc* **2014**, *136*, 8003.

42. Ungur, L.; Thewissen, M.; Costes, J.-P.; Wernsdorfer, W.; Chibotaru, L. F. "Interplay of Strongly Anisotropic Metal Ions in Magnetic Blocking of Complexes" *Inorganic Chemistry* **2013**, *52*, 6328.

43. Lin, P. H.; Korobkov, I.; Wernsdorfer, W.; Ungur, L.; Chibotaru, L. F.; Murugesu, M. "A Rare mu(4)-O Centred Dy-4 Tetrahedron with Coordination-Induced Local Chirality and Single-Molecule Magnet Behaviour" *European Journal of Inorganic Chemistry* **2011**, 1535.

44. Demir, S.; Gonzalez, M. I.; Darago, L. E.; Evans, W. J.; Long, J. R. "Giant coercivity and high magnetic blocking temperatures for N2 3− radical-bridged dilanthanide complexes upon ligand dissociation" *Nature Communications* **2017**, *8*, 2144.

45. Mavragani, N.; Errulat, D.; Gálico, D. A.; Kitos, A. A.; Mansikkamäki, A.; Murugesu, M. "Radical-Bridged Ln 4 Metallocene Complexes with Strong Magnetic Coupling and a Large Coercive Field" *Angewandte Chemie International Edition* **2021**, *60*, 24206.

46. Rinehart, J. D.; Fang, M.; Evans, W. J.; Long, J. R. "Strong exchange and magnetic blocking in N23−-radical-bridged lanthanide complexes" *Nature Chemistry* **2011**, *3*, 538.

47. Rinehart, J. D.; Fang, M.; Evans, W. J.; Long, J. R. "A N23–Radical-Bridged Terbium Complex Exhibiting Magnetic Hysteresis at 14 K" *J Am Chem Soc* **2011**, *133*, 14236.

48. Coey, J. M. D. *Magnetism and Magnetic Materials*; Cambridge University Press: Cambridge, 2010.

49. Dolai, M.; Moreno-Pineda, E.; Wernsdorfer, W.; Ali, M.; Ghosh, A. "Exchange-Bias Quantum Tunneling of the Magnetization in a Dysprosium Dimer" *The Journal of Physical Chemistry A* **2021**, *125*, 8230.

50. Ghosh, T.; Marbey, J.; Wernsdorfer, W.; Hill, S.; Abboud, K. A.; Christou, G. "Exchange-biased quantum tunnelling of magnetization in a [Mn3]2 dimer of single-molecule magnets with rare ferromagnetic inter-Mn3 coupling" *Phys Chem Chem Phys* **2021**, *23*, 8854.

51. Han, T.; Giansiracusa, M. J.; Li, Z. H.; Ding, Y. S.; Chilton, N. F.; Winpenny, R. E. P.; Zheng, Y. Z. "Exchange-Biasing in a Dinuclear Dysprosium(III) Single-Molecule Magnet with a

Large Energy Barrier for Magnetisation Reversal" *Chemistry – A European Journal* **2020**, *26*, 6773.

Chapter 3 Molecular Network Approach to Anisotropic Ising Lattices: Parsing Magnetization Dynamics in Er^{3+} Systems with 0-3 Dimensional Spin Interactivity

We present a wide-ranging interrogation of the border between single-molecule and solid-state magnetism through a study erbium-based Ising-type magnetic compounds with fixed magnetic unit, using three different charge-balancing cations as the means to modulate the crystal packing environment. Properties rooted in the isolated spin Hamiltonian remain fixed, yet a careful observation of the dynamics reveals the breakdown of this approximation in a number of interesting ways. First, differences in crystal packing lead to a striking three-orders of magnitude suppression in magnetic relaxation rates indicating a rich interplay between intermolecular interactions governed by the anisotropic Ising lattice stabilization and localized slow magnetic relaxation driven by the spin-forbidden nature of quantum tunneling of the f-electron-based magnetization. By means of diverse and rigorous physical methods, including temperature-dependent x-ray crystallography, field, temperature, and time-dependent magnetometry, and the application of a new magnetization fitting technique to quantify the magnetic susceptibility peakshape, we are able to construct a more nuanced view of the role non-zero-dimensional interactions can play in what are predominantly considered zero-dimensional magnetic materials. Specifically, we use low field susceptibility and virgin-curve analysis to isolate a metamagnetic spin-flip transitions in each system with a field strength corresponding to the expected strength of the internal dipole-dipole lattice. This behavior is vital to a complete interpretation of the dynamics, and likely common for systems of such high anisotropy. This collective interactivity opens a new realm of possibility for molecular magnetic materials where their unprecedented, localized anisotropy is the determining factor in building higher dimensionality.

3.1 Introduction

Design of functional magnetic materials has been a longstanding endeavor in the realm of materials science. While magnetic behavior is often associated with the ordering behavior of bulk materials, current technological trends in miniaturization, spin-based electronics, and the harnessing of quantum information have expanded the scope of possibility of what can constitute a functional material to a far broader range of time, size, and interaction strength. The field of single-molecule magnetism has revealed the inherent molecular level magnetism possible through careful synthetic design of molecules.[1-5] Over the last 40 years, effects of quantization, exchange coupling, and spatial anisotropy on the time, temperature, and field dependence of spin polarization under both equilibrium and non-equilibrium conditions have all been targeted for study. Single-molecule magnets (SMMs)[6-10] possess remarkable properties, such as a time-dependent spin memory effect similar to a superparamagnet, except acting via quantized states. This ability to retain and modulate spin at the molecular level with chemically tailored property control has generated substantial interest of a fundamental as well as applied nature in alternative information storage mechanisms, quantum computing, and molecular spintronics, among other promising applications.[11-16] One of the largest challenges to SMM implementation is the poor translation from behavior of SMMs in isolation to SMMs interacting with each other or other external degrees of freedom. In actuality, all SMMs are intrinsically dependent on their environment and any application must recognize, and ideally leverage, this crucial point.

To continue to advance SMMs within a functional materials context, it becomes imperative to explore the profoundly complex connection between single-molecule properties and their surrounding environment. This includes the connection between the spin system and vibronic degrees of freedom,[17-21] coupling to external electromagnetic radiation,[22-26] as well as coupling to the internal magnetic fields generated by the arrangement of SMM magnetic moments. The potential for local magnetic moments to influence the global magnetic dynamics have not gone unnoticed,[27-29] largely in solid-state literature of metallic, ionic, and covalent solids, where discourse on correlated interactions is imperative due to their strength. In molecular solids, correlated interactions are far less discussed, yet on the energy scale of magnetization dynamics, they can play an important role, especially in samples with small crystallites and under non-equilibrium conditions. SMMs containing a single lanthanide ion designed to induce maximum axial anisotropy (often a Dy^{3+}/Er^{3+} ion with ground state $|J = 15/2, m_J = \pm 15/2\rangle$) possess some of the largest and most anisotropic angular momenta possible on a per-ion basis. Although nearly always modeled as a population of isolated SMMs, the relative simplicity of their Ising-like moment and symmetry restricted intermolecular dipole-dipole interaction offers a unique opportunity to scrutinize them for evidence of the effects of local correlation. In this work, we approach this challenge through examination of three different crystal lattice configurations of the same anionic single-ion SMM $[ErCOT_2]^-$ by means of field, temperature, and time-dependent magnetometry and temperature-dependent x-ray crystallography. New quantitative insight is garnered from field dependent magnetization using a fitting technique with parameters that are interpreted in terms of localized and intermolecular contributions induced by the dipole-dipole interactions relevant to the molecular crystalline arrangement. Additionally, this work characterizes the nature and consequences of a metamagnetic spin-flip transition that marks the separation between the correlated ground state that maximally internalizes local fields versus the aligned excited state generated by external applied fields. By delving into the connections between single-molecule magnetism and solid-state magnetism, we seek to uncover the promising avenues for harnessing molecular building blocks to engineer materials with tailored magnetic properties that take advantage of spatial dimensionality.

3.2 Experimental & Crystallographic Details

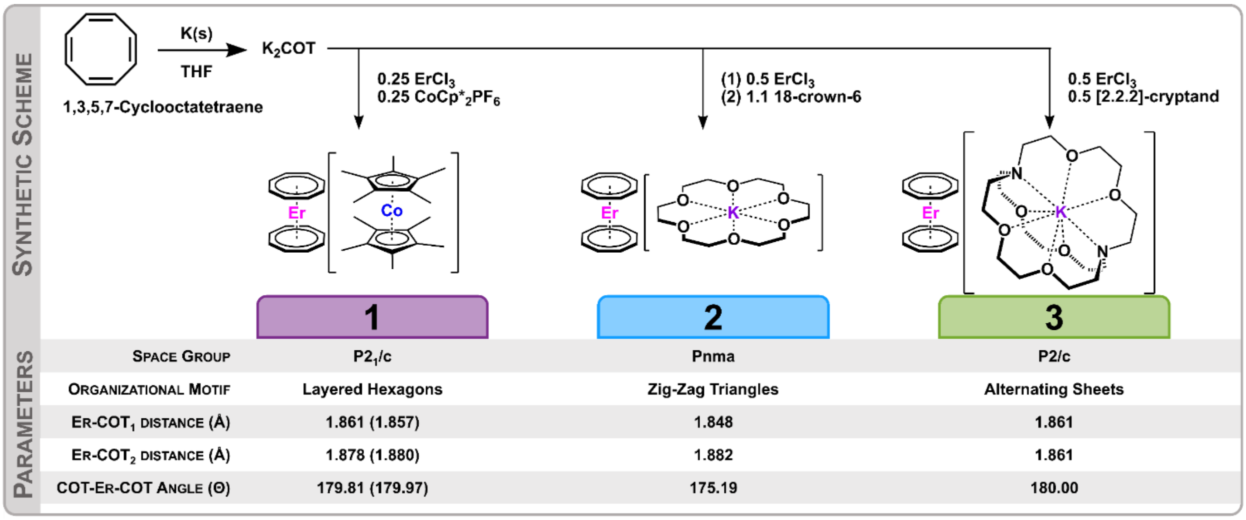

	1	2	3
Space Group	$P2_1/c$	Pnma	P2/c
Organizational Motif	Layered Hexagons	Zig-Zag Triangles	Alternating Sheets
Er-COT$_1$ distance (Å)	1.861 (1.857)	1.848	1.861
Er-COT$_2$ distance (Å)	1.878 (1.880)	1.882	1.861
COT-Er-COT Angle (Θ)	179.81 (179.97)	175.19	180.00

Figure 3.1: Synthetic scheme and selected crystallographic parameters of **1**, **2**, and **3**.

A series of three magnetic molecules was synthesized in which the magnetic unit is held constant, while the charge-balancing cation is varied. The lanthanocene magnetic unit $[ErCOT_2]^-$ (bis(cyclooctatetraenyl)-erbium), was chosen due to its well-studied[10,27,30-38] crystal field structure, highly axial ground state anisotropy, and well-defined SMM behavior. The axial single-ion anisotropy provides a nearly-ideal magnetic building unit for construction of anisotropic Ising-type[39] lattices. Furthermore, the driving factor determining the single-ion anisotropy is the local crystal field environment, meaning that the molecular anisotropy axis, well-approximated by the structural COT-Er-COT vector, can be treated as a local Ising spin axis, reliably tethering spin-space to a concrete cartesian direction. Charge-balancing cations chosen for this study were selected to drive differences in the crystal packing and orientations of magnetic units with respect to one another within the crystal lattice. As such, we synthesized near-linearly stacked bis(pentamethylcyclopentadienyl)-cobalt(III) bis(cyclooctatetraenyl)-erbium(III) (**1**, $[\mathrm{CoCp^{*}_2}][\mathrm{ErCOT_2}]$), previously studied K(18-crown-6) bis(cyclooctatetraenyl)-erbium(III) (**2**, $[\mathrm{K(18\text{-}C\text{-}6)}][\mathrm{ErCOT_2}]$),[37] and near-orthogonal K([2.2.2]cryptand) bis(cyclooctatetraenyl)-erbium(III) (**3**, $[\mathrm{K(crypt)}][\mathrm{ErCOT_2}]$; Figure 3.1, Synthetic Scheme). As the scope of this work was to analyze these compounds under the lens of dipolar coupling, it was pertinent to conduct a dilution study with a diamagnetic molecular analog containing Y(III), to disrupt the crystalline dipolar network via random insertion of diamagnetic sites. Dilution of the parent erbium(III) compound to form **1-Y**, **2-Y**, and **3-Y** was achieved with a diamagnetic yttrium(III) analog in 5:95 Er:Y molar ratios. Yttrium was chosen due to its similar ionic radii to erbium and its allowance to generate diamagnetic isostructural analogues of the parent erbium compounds.

Single crystal x-ray diffraction data reveal that the $[\mathrm{ErCOT_2}]^{-}$ anionic units are similar across the three compounds of interest, with Er-COT distances within 1.85-1.88 Å. The $\mathrm{COT_1}$-Er-$\mathrm{COT_2}$ angle for **2** shows a slightly greater canting than **1** and **3** due to K-18C6 coordination on one side of the $[\mathrm{ErCOT_2}]^{-}$ unit (Figure 3.1, Parameters). To ascertain the similarity of the magnetic states at the level of the crystal field interactions, CASSCF calculations were performed within the SINGLE_ANISO module of OpenMolcas[40,41] for **1-3**, with and without charge-balancing cations. CASSCF calculations provide consistently anisotropic ground states ($g_z = 17.99$, $g_x = g_y = 0.00$; $\mathrm{KD_0} = \pm 15/2$, 100% pure; $\Delta E_{\mathrm{KD1}} \sim 160\ \mathrm{cm^{-1}}$; Table S.3.4). From these calculations we conclude that the $[\mathrm{ErCOT_2}]^{-}$ anionic unit provides a consistent basis for studying varying intermolecular interactions in crystalline lattices. To further develop this concept, a thorough analysis of the spatial relationship between molecules, and thus their local anisotropy axes, was made via x-ray crystallographic studies.

Compound **1** crystallizes in $P2_1/c$, with two crystallographically distinct $[ErCOT_2]^-$ units in the unit cell (Figure 3.2, A-D). Two analogous buckled hexagonal motifs (Layer A and A′ in Figure 3.2, B) stack down the c-axis of the crystal lattice. The hexagonal motif is buckled down the center of a "boat" hexagonal conformation with $[ErCOT_2]^-$ units in positions 1 – 3 located on slightly elevated Plane I (black circles, red outline), and $[ErCOT_2]^-$ units in positions 4 – 7 on slightly lowered Plane II (white circles, blue outline, Figure 3.2, C). These hexagonal motifs are linked side-on (positions 4 & 5 to 6 & 7) and head-on (positions 1 to 3) across the ab-plane and stacked down the crystallographic c-axis (Figure 3.2, D). In applying our previous heuristic dipolar coupling approximation,[27] the angles between the following units predict ferromagnetic coupling: 1:2, 2:3, 4:5, 6:7 (center to center and edge to edge), with antiferromagnetic coupling predicted to arise from all other interactions: 1:4, 1:6, 2:4, 2:6, 2:5, 2:7, 3:5, 3:7 (center to edge). Importantly, the lattice configuration of **1** obtains a near-colinear head-to-head interlayer stacking of the $ErCOT_2$ units, spaced by the $[CoCp^*_2]^+$ charge-balancing cation, generating a pseudo-1D linear wire throughout the crystal lattice. This stacking interaction occurs by plane: Plane I, Layer A stacks to Plane I′, Layer A′, positions 1 to 2′, 2 to 3′, 3 to 1′. Correspondingly, positions 4 – 7 on Plane II stack with Plane II′ (4:5′, 5:4′, 6:7′, 7:6′; the 4:5′ stacking interaction is highlighted in yellow in Figure 3.2**,** D). All interlayer interactions (head-on, as in 4:5′, and side-on, as in 4:4′) are predicted to be ferromagnetically coupled. This complex interleaving of molecular forms yields ferromagnetically coupled planes down the c-axis, complemented by intralayer antiferromagnetic interactions (*vide infra*). The simultaneous presence of hexagonal motifs and antiferromagnetic coupling is accompanied by the intraplanar buckling which serves to alleviate magnetic spin-frustration on the triangular motifs within the hexagons. While certainly not the only force

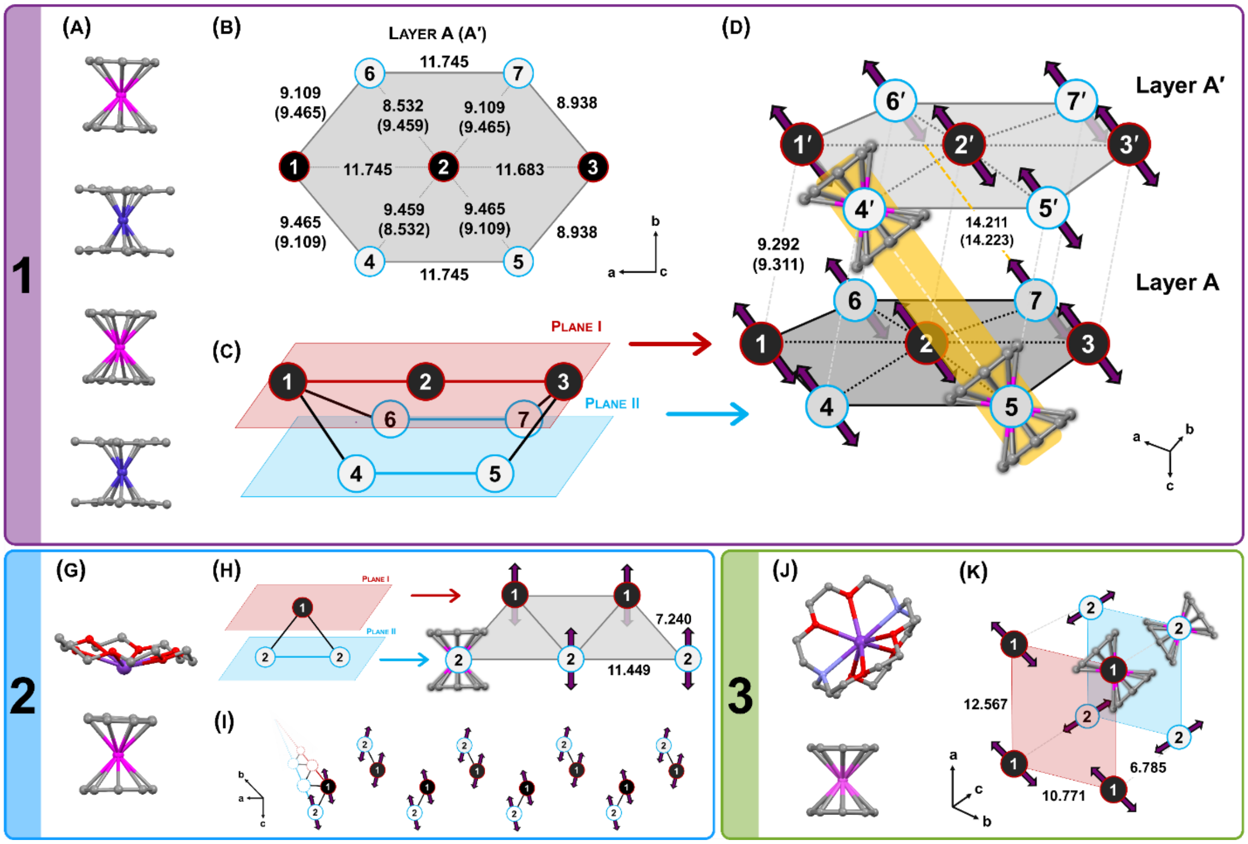

Figure 3.2: Solid-state structures of unit cells and organizational lattice motifs of **1** (Box 1), **2** (Box 2), and **3** (Box 3). Spheres in unit cells represent erbium (pink), cobalt (blue), and carbon (gray), oxygen (red), potassium (purple), nitrogen (light blue); hydrogen atoms have been omitted for clarity. All distances listed in angstroms. Black and white circles represent magnetic units, corresponding to planes depicted in figures. Two-sided arrows demonstrate approximate anisotropy axes of magnetic units. (A) Unit cell of **1**. (B) Structural parameters of two hexagonal motifs within **1**. (C) Exaggerated buckled-hexagonal motif of **1**. Parallelograms depict planes I (red) and II (blue), upon which lie magnetic units 1 – 3 (black circles, red outline) and 4 – 7 (white circles, blue outline), respectively. (D) Two stacked layers of the hexagonal organizational motif of **1**, demonstrating inter-layer stacking interactions, highlighted in yellow. (G) Unit cell of **2**. (H) Zig-zag triangular organizational motif of **2**. (I) Lattice organization of **2**, demonstrating canting between triangular zig-zag motifs within the crystal. (J) Unit cell of **3**. (K) Alternating sheets organizational motif of **3.**

involved, the structure's alignment to allow favorable Ising interactions indicates an unusually large level of structural stabilization based on the spin system.

Compound **2** crystallizes in Pnma with one crystallographically distinct $[ErCOT_2]^-$ unit within the unit cell, in two symmetry-related obtuse isosceles triangular "zig-zag" motifs traveling down the b-axis (Figure 3.2, G-I). As in **1**, there are two planes upon which $[ErCOT_2]^-$ anionic units are positioned, one slightly elevated over the other. The anisotropy axes of the individual units are nearly parallel to one another, resulting in a near-90-degree angle of projection onto their internuclear axis (Figure 3.2, H, I). Based on the mutual dipolar interaction of their large angular momenta, this spatial arrangement results in a minimization of the antiferromagnetic coupling energy. The two crystallographically generated zig-zag motifs created by this interaction are canted with respect to one another (Figure 3.2**,** I; depicted as 1, 2 and 1′, 2′, respectively) and traverse the b-axis.

Compound **3** crystallizes in P2/c, with sheets of $[ErCOT_2]^-$ anionic units oriented in one direction across the ab-plane (Figure 3.2**,** J, K). The sheets traverse down the c-axis, alternating between two nearly orthogonal orientations of the $[ErCOT_2]^-$ anionic units.

Intrigued by the relationship between the anisotropy axes and the crystallographic arrangement, we completed a temperature-dependent crystallographic analysis on **1** to garner insight into the important modes of structural relaxation and look for correlations to our magnetostructural parameterization (*vide supra*). In brief, a crystal of approximately 0.03 x 0.05 x 0.06 mm was identified and mounted on a Bruker ApexII-Ultra CCD with microfocus rotating anode using a Mo(Kα) radiation source. Full collections were completed at seven temperatures from 200 to 80 K and all structures were solved using direct methods via the SHELX routine and refined with SHELXL.[42] At 200 K the structure of **1** solved in space group $P2_1/m$ with one crystallographically distinct $[CoCp^*_2][ErCOT_2]$ unit in the unit cell. There is only one hexagonal motif with added symmetry generated by the mirror plane. At 80 K, the structure solves into $P2_1/c$ with the two analogous hexagonal motifs, as previously discussed. The structural changes of the hexagonal motifs were tracked by comparing the 200 K, $P2_1/m$ (hot) and 80 K, $P2_1/c$ (cold)

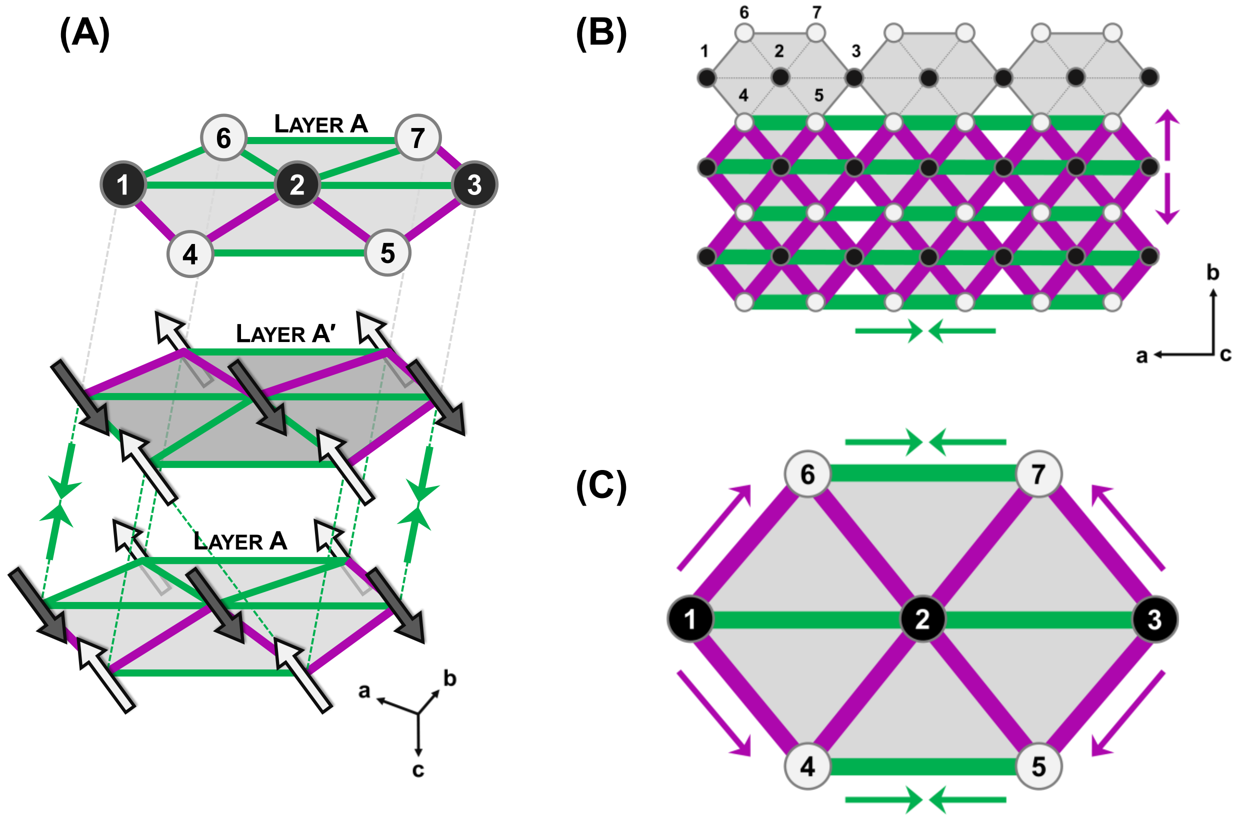

Figure 3.3: Crystallographically derived structural expansions (purple) and contractions (green) in **1** upon cooling from 200 K, $P2_1/m$ to 80 K, $P2_1/c$. (A) Layer-by-layer structural changes. Arrows demonstrate energy minimizing spin configuration within the local Ising axis framework. Structural changes upon cooling, in extended lattice overlay of hexagonal motifs (B) and combined across the lattice to be shown on one representative hexagonal motif (C).

structures (Figure 3.3**,** A-C, green: contractions; purple, expansions). The structural expansions upon cooling accompany relaxation of the spin frustration within the lattice, while also resulting in an increase in the distance between ferromagnetically coupled sheets. In Layer A, we see expansion on one side of the hexagon away from the central positions. Conversely, in Layer A′, the expansion occurs on the other side of the hexagon. In looking at the lattice (Figure 3.3**,** A-C) we see a general expansion outward from the center positions, balanced by a contraction along the lengths of the hexagons, and a contraction in the stacking between layers A and A′ (Figure 3.3**,** A). Although it is not possible from the current evidence to say definitively that the symmetry lowering is the result of "freezing out" a spin-phonon coupling, it is consistent with both the structural evidence and the small energies organizing the molecular lattice. These temperature-dependent structural changes serve as clues towards building a more complex and nuanced model of their behavior in the context of their environment. The SMM model is effective at explaining a broad range of magnetic behavior from the perspective of an isolated spin system, but the strong and often highly directional properties of SMMs can have interesting effects on the relatively flat energy landscape of the molecular crystalline environment that warrant closer study. Observing the range of closely related organizational motifs, their interconversion as a function of temperature, and their telling relationship with the anisotropy axes, we turned to a full characterization of the magnetic behavioral differences between **1**, **2**, and **3**.

3.3 Results & Discussion

To investigate the effects of crystal lattice organization on the magnetic properties of our compounds, we collected static magnetic isothermal magnetization data and dynamic magnetic data via standard magnetometry techniques. Representative isothermal sweeps of magnetization versus magnetic field are shown in Figure 3.4, left, collected at $T = 2$ K. All compounds saturate near 5 μ_B. Compounds **1** and **2** both display open hysteresis (60 Oe s^{-1}), with coercive fields of H_c = 2.4 and 1.7 T. Compound **3** displays a waist-restricted hysteresis loop with no evidence of coercive field. Arrhenius relaxation plots of τ versus temperature and corresponding fits of **1**, **2**, and **3** are shown in Figure 3.4, right. As observed previously,[27] the low temperature relaxation regime is characterized by an Arrhenius-linear processes characterized by a weak temperature dependence and highly impeded transition rates. The phenomenological model for this process uses τ_D to describe the attempt time and D_{eff}, the barrier (analogous to the high-temperature τ_0 and U_{eff}). Interestingly, this fitting model is effective despite the difference in magnetic structure

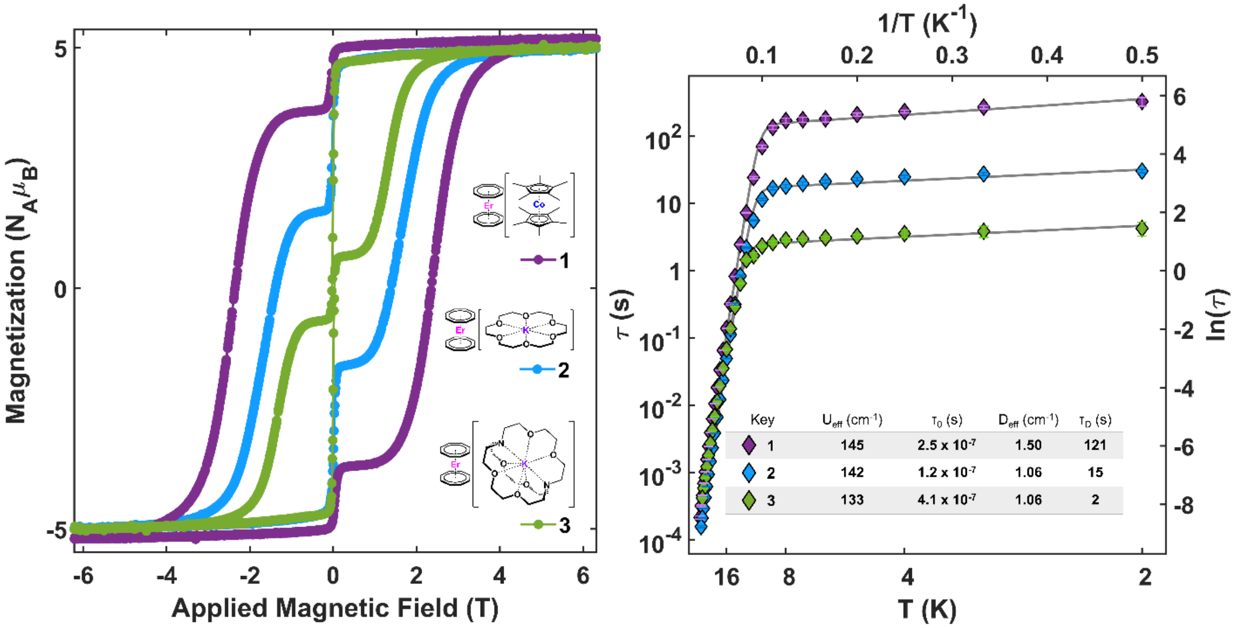

Key	U_{eff} (cm^{-1})	τ_0 (s)	D_{eff} (cm^{-1})	τ_D (s)
◆ 1	145	2.5×10^{-7}	1.50	121
◆ 2	142	1.2×10^{-7}	1.06	15
◆ 3	133	4.1×10^{-7}	1.06	2

Figure 3.4: (left) Isothermal magnetization of **1**, **2**, and **3** (purple, blue, and green circles, respectively; lines are guides for the eye)**.** Data were collected at T = 2 K, at a 60 Oe s^{-1} magnetic field sweep rate. (right) Arrhenius plots of relaxation times versus temperature for **1**, **2**, and **3** (purple, blue, and green diamonds, respectively). Error bars within diamond markers demonstrate upper and lower error limits of τ values. Gray lines are fits to a multi-term relaxation model. Inset table shows fit parameters.

compared to other systems where it has been found effective. When employed previously in the study of locally dipole-dipole coupled molecules, both τ_D and D_{eff} corresponded well to the expected behavior induced by coupling of local, highly anisotropic Ising states. In the current system, however, the interpretation is far more complex as the Ising dipoles couple in three dimensions. Fitting of the experimental data, followed by the extraction of these parameters allow us to see the stark differences in relaxation dynamics in the cold-temperature regime below 10 K, corresponding well to the differences seen in isothermal magnetization data. Experimental data falling within the Orbach regime (high-temperature) are consistent between compounds and corresponds well to the CASSCF calculated energy splitting between the ground state Kramers doublet (KD_0) and the first excited state Kramers doublet (KD_1, 160 cm^{-1}, Table S.3.4). However, within the low-temperature regime, we see a three-order of magnitude difference in dipolar attempt

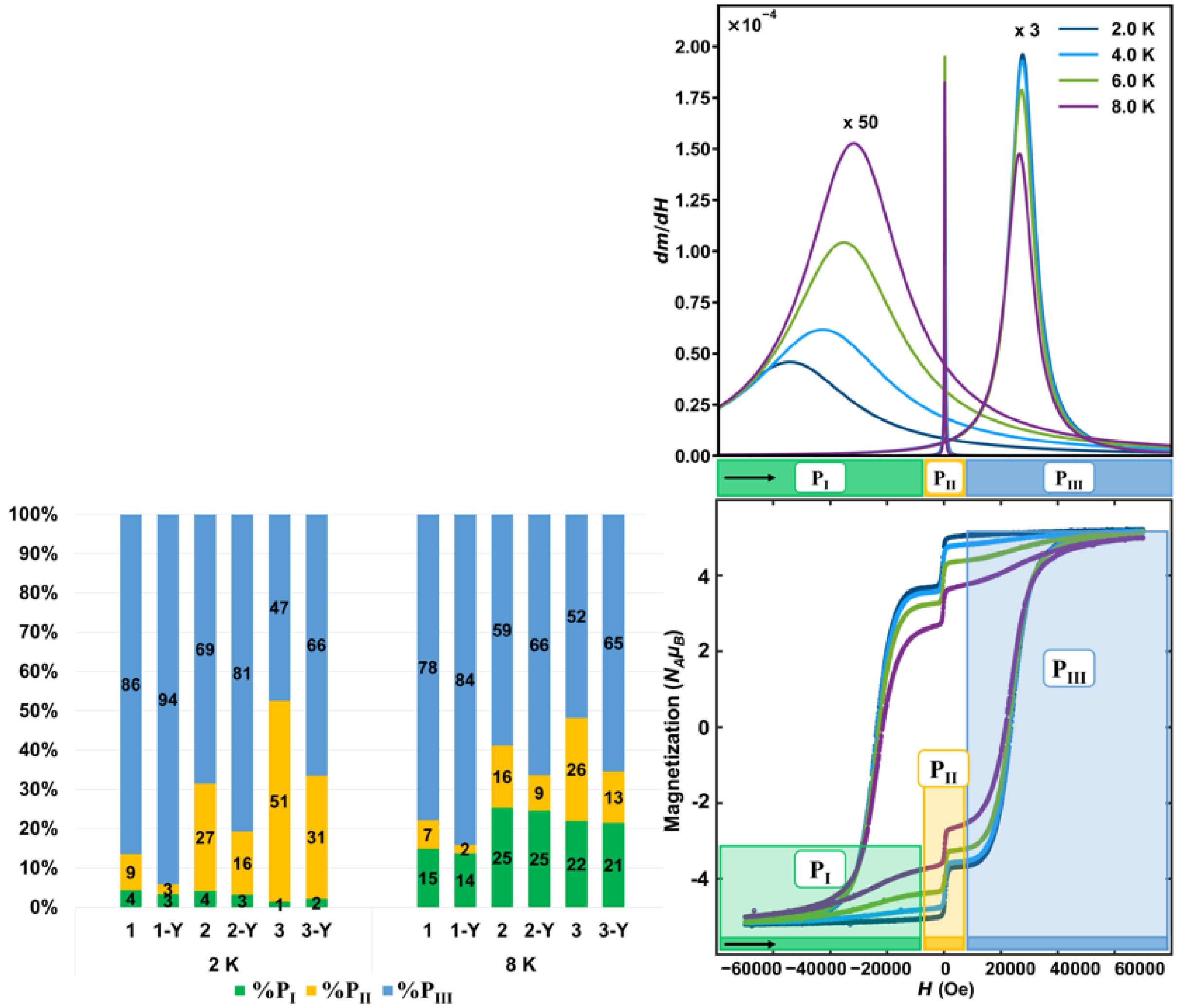

Figure 3.5: (left) Percent contribution of $\mathbf{P_I}$ (green), $\mathbf{P_{II}}$ (yellow), and $\mathbf{P_{III}}$ (blue) for compounds **1**, **2**, **3**, and their diluted analogues, **1-Y**, **2-Y**, and **3-Y** from modified Cauchy distribution fits of magnetization isotherms at 2 and 8 K. (right) Modified Cauchy fits to reverse sweep of isothermal magnetization loops collected at T = 2, 4, 6, 8 K for **1** at a constant sweep rate of 60 Oe s^{-1}. $\mathbf{P_I}$ (green), $\mathbf{P_{II}}$ (yellow), and $\mathbf{P_{III}}$ (blue) correspond to processes (peaks) observed from fitting the data. $\mathbf{P_I}$ and $\mathbf{P_{III}}$ are magnified by x50 and x3, respectively. Black arrow designates direction of sweeping field.

time, $\tau_{D,}$ at 2 K, varying between 121, 15, and 2 seconds for **1**, **2**, and **3**, respectively (Figure 3.4, right, inset). A work published recently notes a similar relationship in the low-temperature regime on a series of modified $[ErCOT_2]^-$ substituted compounds,[38] attributing the differences to a dipolar interaction.

Upon seeing these initial differences in magnetic behavior, we were curious to quantify them further. As such, we collected isothermal magnetization hysteresis loops at T = 2, 4, 6, and 8

K for **1**, **2**, **3** and their diluted analogues, **1-Y**, **2-Y**, and **3-Y**, and fit them using a Cauchy statistical distribution model (Figure 3.5; also see Associated Supplemental Content, Section 3.6.3). The Cauchy distribution can be used to model a wide variety of statistical behaviors arising from quantum mechanical systems, and, specifically, the Cauchy probability density function (PDF) yields the Lorentzian peak shape consistent with a homogeneous distribution. We've recently reported on the use of this statistical distribution with regards to magnetization quantification in nanoparticles[43], and extend it to molecular systems in this work. Utilizing *multi_Cauchy,*[44] an open-source software package, data were fit to a combination of three unique Cauchy cumulative distribution functions (CDF). To better illustrate the temperature dependency and subtle variations in peaks, the fit parameters were applied to analytical forms of the PDF formulation of the Cauchy distribution and plotted. This technique allows us to quantify, track, and compare (de)magnetization processes occurring across all compounds in a model-agnostic manner. We are able to extract and quantify parameters from the fits, such as: $\mathbf{H_P}$ (the field at which a transition takes place), $\boldsymbol{\gamma}$ (broadness of the peak; half width, half max), and percent contribution of the process ($P_n \ / \ \sum P_I + P_{II} + P_{III}$). All compounds, including their diluted counterparts show the presence of three (de)magnetization events: $\mathbf{P_I}$, $\mathbf{P_{II}}$, and $\mathbf{P_{III}}$. Figure 3.5 shows fits to the reverse sweeps of magnetization isotherms of **1** in which these three (de)magnetization processes are evident: $\mathbf{P_I}$ (green, broad, ~ -40 kOe), $\mathbf{P_{II}}$ (yellow, sharp, ~ 0 Oe), and $\mathbf{P_{III}}$ (blue, broad, ~ 24 kOe). By quantifying the sample magnetization in terms of its change with respect to field, we can more clearly delineate the importance of the spin, lattice, and bath as the system approaches and at equilibrium. As temperature is increased from 2 to 8 K, $\mathbf{P_I}$ increases in percent contribution and decreases in magnitude of $\mathbf{H_P}$. $\mathbf{P_{II}}$ and $\mathbf{P_{III}}$ both decrease in percent contribution and $\mathbf{H_{P_{III}}}$ magnitude decreases as well. The trend in temperature-dependence follows for all compounds, concentrated and dilute, except for **3**, $\mathbf{P_{III}}$, which increases in percent contribution and $\mathbf{H_P}$ with increasing temperature (Figure 3.5). Curiously, the percent contribution of the weakest contribution, $\mathbf{P_{I}}$**,** appears to be nearly unchanged, regardless of dilution. Quantification of **P** gives us a more concrete, albeit empirical, way to discuss time, temperature, and field dependence within the blocked regime where a model generated from non-interacting SMMs may fail. The most commonly discussed manifestation of this failure is the zero-field avalanche effect observed when the momentum of dipole flips can induce the flips of nearby spins in a self-propagating manner that drastically accelerates the approach to equilibrium of the entire sample. Modeling or predicting this effect or any other inter-SMM relaxation dynamics (e.g. spin glass formation, spin clustering dynamics, or manifestations of magnetic order) is complex and the behavior often goes unnoticed, or its effects conflated with the slow-relaxation dynamics of an SMM. With this technique, we are able to quantify $\mathbf{P_{II}}$, the drop(rise) near zero field that is typically attributed to QTM processes or magnetic avalanche,[37,45,46] and see that the diluted counterparts show decreased percent contribution in $\mathbf{P_{II}}$, as seen in many past works,[37,47-49] with increased sharpness, as evidenced by the low $\boldsymbol{\gamma}$ parameters (e.g. $\mathbf{P_{II}}$ at 2 K: $\boldsymbol{\gamma}_{\mathbf{1}}$ = 195, 9.2% contribution versus $\boldsymbol{\gamma}_{\mathbf{1\text{-}Y}}$ = 9, 2.6% contribution, also see Associated Content, Section 3.6.3).

Furthermore, when we subjected our samples to an applied field for ZFC and FC susceptibility measurements, we discovered that many of the complex and often undiscussed variations in behavior observed for SMMs could be correlated to susceptibility processes defined in terms of $\mathbf{P_{I\text{-}III}}$ (Figure 3.6-A; see Associated Content, Section 3.6.3). The overlay of concentrated **1** and dilute **1-Y** susceptibility plots show a combination of expected and unexpected behavior for an SMM (Figure 3.6-A, colored and black and white circles, respectively). The data collected at a field of 1000 Oe is indicative of standard SMM behavior. A low temperature

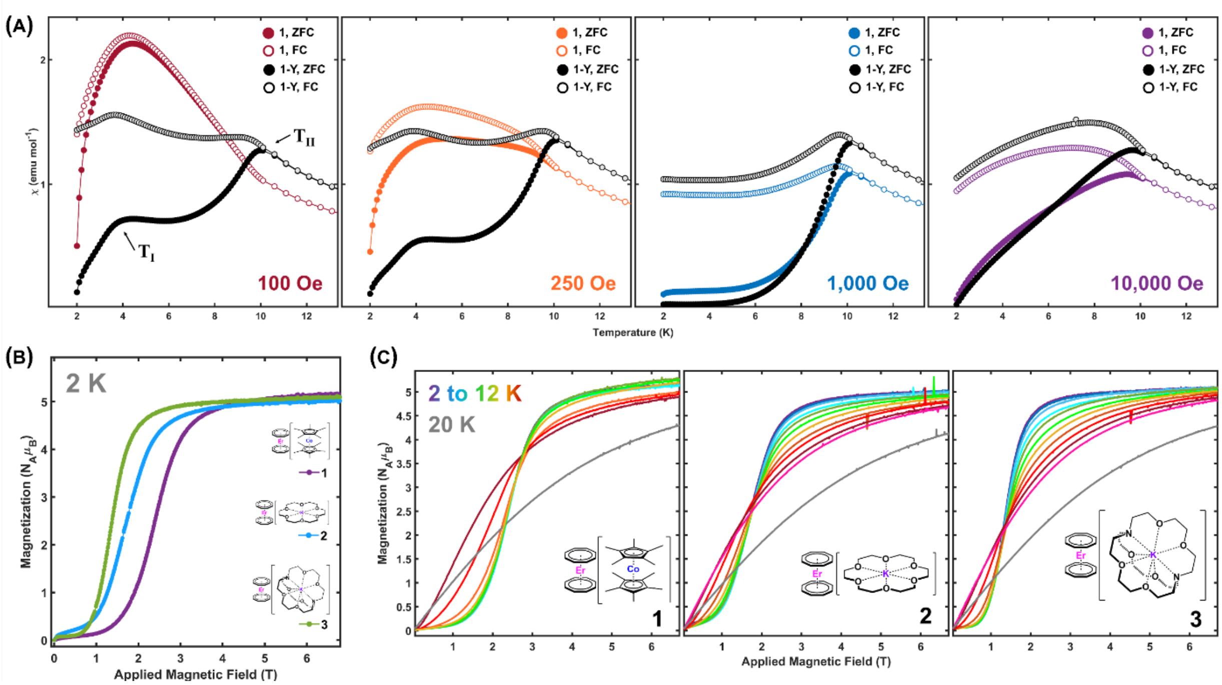

Figure 3.6: (A) ZFC (filled markers) and FC (open markers) susceptibility data for **1** (colored circles) and **1-Y** (black and white circles) under varied applied fields. **T$_{\mathbf{I}}$** and **T$_{\mathbf{II}}$** are susceptibility transition event temperatures, as discussed in the text. Lines are guides for the eye. (B) Isothermal virgin magnetization curves collected at applied fields of H = 0 – 7 T at T = 2 K for **1** (purple), **2** (blue), and **3** (green) at a constant sweep rate of 60 Oe s^{-1} using vibrating sample magnetometry VSM. (C) Isothermal virgin magnetization curves collected at applied fields of H = 0 – 7 T at T = 2 – 12 (purple to red), 20 K (gray) for **1**, **2**, and **3** at a constant sweep rate of 60 Oe s^{-1} in VSM mode. Note that low temperature curves are overlapping in **1**.

“blocked” region exists under zero-field cooled (ZFC) conditions where the SMM is unable to respond to the field. The sample is unable to establish the new equilibrium condition as determined by the applied field until the temperature is raised enough to overcome the barrier to magnetic relaxation. When the system is cooled under an applied field (field-cooled, FC) the magnetization immediately responds because the equilibrium condition was in place as the system cooled. The temperature marked **T$_{\mathbf{II}}$** is consistent with the expected convergence for the ZFC/FC behavior of **1** given its relaxation dynamics. Deviations from this behavior at both higher and lower fields are drastic and indicative of more complex behavior involved outside of the 1000 Oe measurement. The important information about deviations from ideal SMM behavior can be summarized as such:

for all samples in all magnetic fields, the diluted sample conforms to SMM behavior better than the corresponding concentrated sample. The deviation from ideal behavior occurs at high and very low applied magnetic fields. The bifurcation between ZFC and FC susceptibility curves for **1** is minimal at low field, leading to a broad, highly susceptible feature, **T_I** ~ 4 K. With increasing field towards 1000 Oe, eventually only a small shoulder remains at **T_I**. This surprising dramatically field-dependent behavior yielding two maxima in magnetic susceptibility is seen consistently in all our samples with similar trends in behavior between concentrated and diluted species (see Associated Supplemental Content, Section 3.6.2, Magnetometry Methods). These trends suggested that **1-3** could all display collective spin interactions of varying magnitudes. This behavior is perhaps most striking in **1** where a net cooperative interaction results in the large broad enhancement of susceptibility over the entire low temperature range. This interaction can be suppressed by a relatively weak applied field at all but the lowest temperatures. It can also be weakened by generating defects in the dipolar lattice through magnetic dilution.

It is worth noting that additional complexity in the coupling and relaxation behavior of SMMs arising from their crystalline arrangement may be far more common than reported, especially for single-ion systems where axial anisotropy plays such a key role. Revealing this behavior, however, requires non-standard measurements and analysis for SMMs such as study of the demagnetization curvature, virgin curve analysis, and low field susceptibility measurements. The precedence for long-range coupling of highly anisotropic spin centers has a rich history of study in the solid-state physics magnetism community where the presence of multiple susceptibility peaks is used to detect potential spin-flop, spin-flip, or metamagnetic phase transitions.[50-59] Given the many intrinsic similarities between molecular crystals of lanthanide single-ion SMMs and solid state anisotropy-driven magnetic materials, the isothermal virgin magnetization curves from $H = 0 – 7$ T at $T = 2 – 12$, 20 K (Figure 3.6, B, C; Supplemental Figures 3.15, 3.23, 3.34) were collected. These data, in connection with the high degree of anisotropy of the $[ErCOT_2]^-$ anionic dipolar spin network, confirm the presence of a metamagnetic spin-flip transition in all our compounds below their 10 K blocking temperature. This is especially evident in the lower temperature curves (Figure 3.6-B, 2 K data) where we maintain a minimal magnetization of the AFM coupled ground state, followed by an abrupt magnetization event with small change in applied field. The spin-flip transition takes place at 2.4, 1.7, and 1.3 T for **1**, **2**, and **3**, respectively, and brings all samples to their collective fully magnetized FM coupled state. Interestingly, this metamagnetic spin-flip transition corresponds with the field at which $\mathbf{P_{III}}$ occurs ($\boldsymbol{H_{P_{III}}}$) at 2 K. The spin-flip transition is observed in **1-3**, yet each species displays aspects unique to its magnetostructural arrangement. In **1**, the overlap of curves between 2 – 8 K show that the metamagnetic spin-flip transition is nearly temperature-independent with a sudden change in magnetization curvature, whereas both **2** and **3** show a far smoother transition over the entire temperature range.

Let us summarize the findings of this work prior to analysis and comparison between molecular properties preserved versus modified in the solid-state. The following are consistent across all compounds and can be attributed to inherent characteristics of the $[ErCOT_2]^-$ anisotropic unit: magnetization saturation (M_{sat}~5 μ_B), the presence of a near-zero-field drop in magnetization ($\mathbf{P_{II}}$), high-temperature relaxation dynamics driven by an Orbach barrier originating from the local crystal field (~160 cm^{-1}), a spin-flip transition resulting from competition between the intermolecular magnetic dipole network and the applied magnetic field. Characteristics that differ across the three compounds and thus should be discussed as effects modified by solid-state arrangement are: the coercive field (H_c), the intensity of the near-zero-field magnetization drop (percent contribution of $\mathbf{P_{II}}$), the low-temperature relaxation dynamics (below 10 K), the field-dependency of the spin-flip transition, and the temperatures of the phase transitions.

The high-temperature relaxation dynamics are consistent across all compounds due to the same Orbach barrier imposed by the $[ErCOT_2]^-$ unit. This has been discussed thoroughly in SMM literature and will not be discussed in this work.[6-8,60] The saturation magnetization is consistent across all our compounds, which again signifies that this feature can be attributed to preserved single-ion behavior. The cascading event near zero field, $\mathbf{P_{II}}$, (Figure 3.5; also see Section 3.6.3) is present in all compounds, and its percent contribution towards demagnetization is decreased in the diluted counterparts. This also has precedence in the literature and can be attributed to self-propagating relaxation in the QTM regime falling under the category of magnetic avalanche effects.[37,45-49,61] In keeping with theory and previous observation, the relative percentage of the sample that relaxes via QTM ($\mathbf{P_{II}}$) can be minimized through magnetic dilution. In dilute spin systems, local dipole fluctuations are limited which inhibits further nucleation and growth of spin clusters. The spin-flip transition associated with metamagnetism, often described in solid state systems such as $DyPO_4$, $FeCl_2$, and others[62-65], as well as heavy fermion systems[66-69] occurs in electronic structures where an AFM ground state responds to a small change in applied field to yield a dramatic increase in magnetization to become a spin-polarized FM-type state. The characteristics necessary for metamagnetic spin-flip transitions are strong anisotropy and competing interactions within sublattices.[64,70-72] Compounds **1**-**3** are composed of highly anisotropic, Ising-type magnetic units, all of which have distinct crystallographic organizational motifs (Figure 3.2) defining the low-lying magnetic structure. In that light, the presence of a metamagnetic phase transition is entirely unsurprising, and yet uncommon for single-molecular magnetic systems.

The collection of virgin isothermal magnetization curves offers an interesting corroboration of the spin-flip transition in all three of our compounds. This transition happens at applied fields of H = 2.4, 1.7, and 1.3 T for **1**-**3**, respectively, implying that the crystal lattice organizational motifs are responsible for the changes and that the 3D, ferro- and antiferromagnetic stabilization proffered by **1** leads to the strongest resistance to the spin flip transition. By contrast, the nearly orthogonal arrangement dominating the lattice of **3** is more easily broken by the external field. This behavioral trend corresponds well to the transitions in magnetization we tracked from the full isothermal magnetization loops (Figure 3.5) and the coercive fields of the compounds and demonstrates that the starting ground state of all our compounds is, as we predicted through crystallographic analysis, dominated by AFM-coupling. There is one stark difference across the series of compounds: the applied field necessary to enable the spin-flip transition. If a greater field is needed to propagate a transition, this speaks for the coupling strength in the ground state, prior to any application of field. This means that the internal fields generated within the organizational structures of **1**, **2**, and **3** differ in their propensity of coupling, enabling the elongation of relaxation times we see in the Arrhenius plots (Figure 3.4, right). This is likely evidenced by the alignment of anisotropy vectors within the organizational motifs in the synthesized crystal domains. All anisotropy vectors of **1** point in the same direction, whereas the anisotropy vectors of **2** and **3** offer less synergistic organization. Saturation magnetization values demonstrate that these differences are overcome by a large applied magnetic field for each of the compounds. This implies that the nuances of magnetic behavior are driven by the initial ground state of the coupled crystalline system. While these data can shed further light on what is or is not a magnetic effect of truly magnetic origin, this question is somewhat specious as the existence of the SMM distinct from its environment is both theoretically and practically tenuous. More importantly, a better understanding of the interplay between molecular and intermolecular effects expands the potential materials toolbox and application space open for potential synthetic control by molecular magnetochemists.

Now let us further examine the curious features of the two susceptibility peaks in our data coupled with the transitions seen in isothermal magnetization hysteresis loops. The presence of multiple susceptibility peaks and field-dependent susceptibility events have been discussed in solid-state literature for CeGe[50], lanthanide-containing double perovskites[52], Gd/TbAuAl_4Ge_2[53], and others[50,51,54-59]. Most works discuss these kinds of anomalous events as magnetic phase transitions with long-range ordering and potential presence of spin rearrangement or polarizability. Consistently, these multiple peaks are assigned as Neel-temperatures and attributed to phase transitions occurring within the compound. While the FC/ZFC susceptibility behavior of **1-Y** (Figure 3.6, **T_I** and **T_{II}**) involves the local slow relaxation dynamics of the SMM, the presence of phase transition behavior is viable and, in some cases, a likely effect as well. The structural changes we tracked during our temperature-dependent crystallographic study (Figure 3.2, 3.3) show that symmetry lowering in the lattice can change the energy of the dipolar-coupling. While all complexes and their diluted counterparts display the effects we study, the particulars vary widely, indicating that the nuances are characteristic of solid-state organizational structures within the materials and may change based on small differences in dilution ratios, or in the formation of domain structures[73] within the crystals. The concentrated analogues, **1** – **3**, see significant broadening of the same susceptibility peaks, especially at lower applied fields. This implies that intermolecular or interlayer interactions between the magnetic unit decreases the resolution with which we can resolve these events by modulating the interaction of states biased by applied field.

Finally, we hypothesize that the transitions we see in DC susceptibility, $\mathbf{T_I}$ and $\mathbf{T_{II}}$, are related to, and can inform the processes we track in isothermal magnetization ($\mathbf{P_I}$, $\mathbf{P_{II}}$, and $\mathbf{P_{III}}$, Figure 3.5). $\mathbf{T_I}$ is strongly influenced by even small fields, similar to $\mathbf{P_{II}}$, the near-zero transition seen in isothermal magnetization loops. $\mathbf{T_I}$ becomes a probe into low-field nuances around $\mathbf{P_{II}}$, showing how the long-range stabilizing effect of the dipolar lattice homogenizes the internal field and restricts the rate of QTM.

3.4 Conclusions

We've presented a series of three $ErCOT_2$ compounds and their diluted analogues in which we've held the magnetic unit constant and modified the organizational motifs of the crystal lattice through judicious choice of charge-balancing cation. These compounds vary dramatically in their low-temperature relaxation behavior, attributable to dipolar interactions functioning within the organizational motifs of the crystal lattice. In some cases, it is possible to differentiate between effects arising from inherent single-ion properties and those arising from collective interactions, but often the effects are interrelated, coupled, or synergistic in ways that make such distinctions counterproductive. We've shown the surprising presence of structural changes indicative of coupling between the lattice and spin and a freezing out a symmetry-lowered mode, evidenced by a temperature dependent crystallographic analysis.

The collection of data in this work extends measurements common to molecular magnetochemists to characterize multidimensional magnetic interactions, a process which could yield a wealth of new insight from the already extensive catalog of high anisotropy crystalline synthetic materials. Low-field magnetic analysis shows how insight into factors such as the impact of intermolecular interactions on spin-phonon coupling, magnetostructural rearrangements, and relaxation dynamics can be revealed. Additionally, the discussion of solid-state-like effects and behaviors on SMM systems is nearly absent from the literature and the field. To our knowledge, our work on the $[ErCOT_2]^-$ magnetic unit is the first to describe the effects of metamagnetism on a crystalline lattice of SMMs. The $[ErCOT_2]^-$ magnetic system serves as an ideal candidate for the study of anisotropic Ising systems due to the presence of the real-space tethering of the local anisotropy axes and their use in interpreting the complex interrelation of localized and delocalized effects occurring in magnetic molecular crystals. As a means of quantifying our discussion without narrowing its scope, we've extended our isothermal magnetization fitting technique (Cauchy CDF) to molecular-based systems to facilitate comparison between (de)magnetization processes between any system with non-linear magnetization vs. field. This provides a quantitative basis for the development of theory and comparison to existing models for SMM-based systems. We hope this work encourages practicing magnetochemists to analyze magnetic behaviors at varied applied fields and to dig deeper into solid-state-like attributes that present viable pathways to the development of molecular spin based technologies.

3.5 Methods

All magnetic data collection was completed on crushed microcrystalline samples layered with eicosane in custom quartz tubes sealed under vacuum on an MPMS3 SQUID. Isothermal magnetization data were collected in VSM mode at varied temperatures at a magnetic field sweep rate of $dH/dt = 60$ Oe/s. To quantify the magnetization curves for comparative analysis, fits to a modified Cauchy distribution were carried out following a previously published protocol with the *multi_Cauchy* software package.[43,44] Dynamic magnetic properties were probed via standard AC susceptibility techniques with an extended frequency space ($1000 - 10^{-5}$ Hz) analyzed by a previously described waveform technique.[27,33] AC susceptibility and waveform data were fit to a Debye model and the corresponding relaxation data were fit to a multi-term relaxation equation including an Orbach and Dipolar relaxation term (Equation S.3.1). Temperature-dependent magnetic susceptibility data were collected as zero-field cooled (ZFC) and field-cooled (FC) susceptibility data in DC mode at biasing fields of H = 100, 250, 500, 750, 1,000, 10,000, and 40,000 Oe. ZFC data were collected by first cooling the sample to T = 2 K without an applied biasing field, then applying the biasing field of choice to the cooled sample and collecting data as the temperature was incremented up to T = 300 K. FC data were collected in sequence, with the application of external biasing field of choice during the initial cooling step. Virgin magnetization curves were collected in VSM mode at varied temperatures at a magnetic field sweep rate of dH/dt = 60 Oe/s. Details of the crystallographic temperature study, synthetic methodologies relating to the dilution studies, as well as computational and fitting methods are discussed further in the Associated Supplemental Content.

3.6 Associated Supplemental Content

3.6.1 Preparative Details

All manipulations were conducted under anaerobic, anhydrous conditions under an atmosphere of N_2 in a Vacuum Technology Inc. glovebox. All glassware was dried at 160 °C overnight prior to use. Tetrahydrofuran (THF) and pentane were dried on an activated alumina column and stored over a 1:1 mixture of 3 and 4 Å molecular sieves for at least two days before use. Erbium trichloride (Alfa Aesar), yttrium trichloride (Alfa Aesar), 1,3,5,7-cyclooctatetraene (Acros Organics), bis(η^5-pentamethylcyclopentadienyl)cobalt(II) hexafluorophosphate ($[CoCp^*_2][PF_6]$) (Sigma Aldrich, Strem), 1,4,7,10,13,16-hexaoxacyclooctadecane (18-crown-6) (Alfa Aesar), and 4,7,13,16,21,24-hexaoxa-1,10-diazabicyclo[8.8.8]hexacosane ([2.2.2]cryptand)

(VWR) were all used as received. CHN elemental analyses were performed by Midwest Microlab, Indianapolis, IN, U.S.A.

Synthesis of Dipotassium cyclooctatetraenide, K_2COT

An excess of potassium metal was washed several times with THF until the resulting solution was clear with a slight blue tint. To the clean potassium was added ca. 15 mL THF and the container was placed in the freezer (-30°C) to cool. Meanwhile, 1 mL COT was diluted in ca. 5 mL THF. This solution was also placed in the freezer to cool. After about 30 minutes, a slow, dropwise addition of the COT solution to the potassium in THF was performed. The color of the reaction mixture was observed to change from amber-yellow to dark brown. The reaction mixture was left in the freezer for 24 hours, after which time the dark brown solution was collected and centrifuged. The clear, dark brown supernatant was collected and concentrated *in vacuo*. This solution was returned to the freezer and large, light brown crystals grew within 24 hours. These crystals were dried *in vacuo* and washed with pentane. After crushing, the off-white micro-crystalline powder was used in further reactions.

Synthesis of Potassium bis(η^8-cyclooctatetraenyl)erbium(III), $K[Er(COT)_2]$

Synthesis was adapted from previous methods.[1] K_2COT (2 eq., 0.4267 g) was dissolved in ca. 8 mL THF and cooled in a -30°C freezer. In a separate vial, $ErCl_3$ (1 eq., 0.3202 g) was placed in ca. 2-3 mL THF and stirred, resulting in a pink slurry. The cold K_2COT was added slowly, dropwise to the stirring $ErCl_3$ slurry, resulting in a cloudy, yellow mixture. This mixture was left to react for 24-48 hours at -30°C, at which point it was centrifuged yielding a clear yellow

---

[1] Meihaus, K. R.; Long, J. R. "Magnetic Blocking at 10 K and a Dipolar-Mediated Avalanche in Salts of the Bis(eta(8)-cyclooctatetraenide) Complex [Er(COT)(2)](-)" *J Am Chem Soc* **2013**, *135*, 17952.

supernatant and yellow pellet. The supernatant was collected, and the thick yellow pellet was extracted three times with ca. 5 mL THF. All fractions were combined into one vial and solvent was removed *in vacuo*, yielding a yellow microcrystalline powder. This was washed with several portions of pentane, dried, and used in downstream synthesis (0.4080 g, Yield: 84 %).

Synthesis of Compound 1, [CoCp*$_2$][Er(COT)$_2$]

To a stirring suspension of $ErCl_3$ (0.1052 g, 0.3845 mmol) and [CoCp*$_2$][PF_6] (0.1815 g, 0.3826 mmol) in ca. 4 mL THF was added dropwise a cooled solution of K_2COT (0.2788 g, 1.529 mmol, ca. 8 mL THF). The reaction mixture immediately took on a dark-brown color and was allowed to stir at room temperature for 24 hours. After this period, insoluble impurities were removed *via* centrifugation, followed by filtration through a glass filter. The clear, brown supernatant was concentrated *in vacuo* and crystallized in the freezer (-30 °C). After 48 hours, small, violet crystals of X-ray diffraction quality had grown (0.0692 g, Yield: 25.6%). CHN analysis (calculated, found) for [$ErCoC_{36}H_{46}$]: C (61.34, 60.68); H (6.58, 6.65); N (0.00, 0.00).

Synthesis of Compound 2, [K-(18-crown-6)][Er(COT)$_2$]

Synthesis was adapted from previous reported methods.[1] 1.1 equivalents of 18-crown-6 (0.1242 g) and 1 equivalent of K[Er(COT)$_2$] (0.1773 g) were dissolved separately in ca. 5 mL of THF each and cooled in a -30 °C freezer. The 18-crown-6 solution was then added to the K[Er(COT)$_2$] solution, dropwise with stirring. The yellow solution gradually became cloudier over the course of 5 min and was allowed to react for 24-48 hours. The reaction mixture was then centrifuged, resulting in a clear yellow supernatant and yellow pellet. The supernatant was concentrated *in vacuo* and then left undisturbed at room temperature for ~3 hours, at which point crystals began to form and the solution was transferred to a -30°C freezer to continue crystallization. The pellet was resuspended in THF and stirred at 48°C for 24 hours. The resulting mixture was centrifuged and concentrated following the aforementioned procedure and moved to the freezer to crystallize. Together, both solutions yielded 0.0339 g (19.1% yield) of X-ray quality yellow block crystals, the unit cell parameters of which matched those previously reported for this compound (1001174).[1]

Synthesis of Compound 3, K([2.2.2]cryptand)[Er(COT)$_2$]

To a stirring suspension of $ErCl_3$ (0.0379 g, 0.1385 mmol, ca. 2 mL THF) was added dropwise a chilled solution of K_2COT (0.0505 g, 0.2770 mmol, ca. 3 mL THF). The murky, yellow reaction mixture was stirred in the freezer (-30 °C) for 24 h. Then, to a stirring solution of chilled K(2.2.2)cryptand (0.0521 g, 0.1383 mmol, ca. 2 mL THF) was added the original reaction mixture. A color change from yellow to orange was observed on addition. This reaction mixture was allowed to react in the freezer at -30°C for 24 hours. Insoluble impurities were removed *via* centrifugation and the vivid yellow-green supernatant was collected. Vivid yellow needle X-ray quality crystals were grown over the course of 4 days *via* pentane-THF vapor diffusion carried out in the freezer (-30 °C) (0.0482 g, Yield: 44.0%). CHN analysis (calculated, found) for $ErKC_{34}H_{52}N_2O_6$: C (51.62, 51.49); H (6.62, 6.79); N (3.54, 3.62).

Details of Dilution Study

Magnetic dilutions of **1**, **2** and **3** were prepared following the corresponding procedures for their undiluted parent compound, with the utilization of yttrium as the diamagnetic counterpart to erbium. Reactions were carried out using a 1:19 molar ratio of $ErCl_3$ to YCl_3 to produce a 5% molar dilution with respect to erbium. Diluted magnetic measurements were scaled to expected magnetization saturation values based on the parent concentrated compounds to yield resulting molar ratios:

- The dilute reaction of **1** yielded a molar percent ratio of Er:Y of 5.6:94.1 and a mass percent ratio of 10.0:90.0.
- The dilute reaction of **2** yielded a molar percent ratio of Er:Y of 4.8:95.2 and a mass percent ratio of 8.6:91.4.
- The dilute reaction of **3** yielded a molar percent ratio of Er:Y of 6.4:93.6 and a mass percent ratio of 11.5:88.6.

3.6.2 Sample Characterization

Crystallographic Methods

Single crystal diffraction data for **1** were collected on a Bruker Apex II-Ultra CCD with microfocus rotating anode using a Mo(Kα) radiation source. The structures were solved using direct methods via the SHELX routine and refined using full-matrix least-squares procedures with the SHELXL routine.[m] Olex^2 was used as a graphical front end during refinement.[n] Hydrogens

---

[m] Sheldrick, G. M. "Structure determination revisited" *Acta Crystallogr A* **2015**, *71*, S9; Sheldrick, G. M. "SHELXT - Integrated space-group and crystal-structure determination" *Acta Crystallogr A* **2015**, *71*, 3; Sheldrick, G. M. "Crystal structure refinement with SHELXL" *Acta Crystallogr C* **2015**, *71*, 3.

[n] Dolomanov, O. V.; Bourhis, L. J.; Gildea, R. J.; Howard, J. A. K.; Puschmann, H. "OLEX2: a complete structure solution, refinement and analysis program" *J Appl Crystallogr* **2009**, *42*, 339.

were modeled using a riding model for all positions. Supplementary crystallographic data for structures collected and solved at 80 K and 200 K can be accessed from the Cambridge Crystallographic Data Center via deposition numbers: 2256231 (**1, 80 K**, Figure S.3.1) and 2267662 (**1, 200 K,** Figure S.3.2).

Single crystal diffraction data for **3** were collected at 200 K on a Bruker κ Diffractometer using a Mo(Kα) radiation source and an Apex II area detector (Figure S.3.3). The structures were solved using direct methods via the SHELX routine and refined using full-matrix least-squares procedures with the SHELXL routine. Olex[2] was used as a graphical front end during refinement. Hydrogens were modeled using a riding model for all positions. Supplementary crystallographic data can be accessed from the Cambridge Crystallographic Data Center via deposition number: 2256233.

A unit cell collection of **2** at 200 K was completed on the aforementioned instruments and compared to previously published sources[1] as a means to characterize this compound. Unit cell parameters matched the expected compound; CCDC deposition number: 1001174.

In addition, the diamagnetic yttrium analogue of **1** was synthesized: **$[CoCp^{*}_2][YCOT_2]$**, with single crystal diffraction data collected at 200 K on a Bruker κ Diffractometer using a Mo(Kα) radiation source and an Apex II area detector. The structures were solved using direct methods via the SHELX routine and refined using full-matrix least-squares procedures with the SHELXL routine. Olex[2] was used as a graphical front end during refinement. Hydrogens were modeled using a riding model for all positions. Supplementary crystallographic data can be accessed from the Cambridge Crystallographic Data Center via deposition number: 2256232.

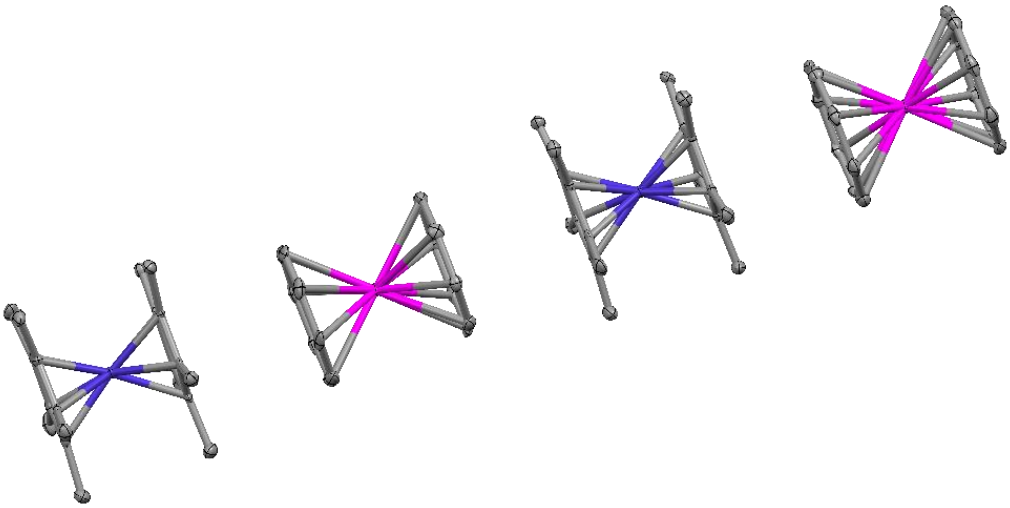

Supplemental Figure 3.1: Crystal structure of **1**, 80 K, showing thermal ellipsoids at 50% probability. Atoms are colored by element type: gray (carbon), blue (cobalt), pink (erbium). Hydrogen atoms have been omitted for clarity.

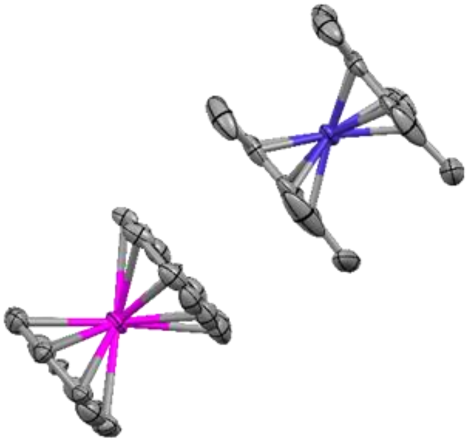

Supplemental Figure 3.2: Crystal structure of **1**, 200 K, showing thermal ellipsoids at 50% probability. Atoms are colored by element type: gray (carbon), blue (cobalt), pink (erbium). Hydrogen atoms have been omitted for clarity.

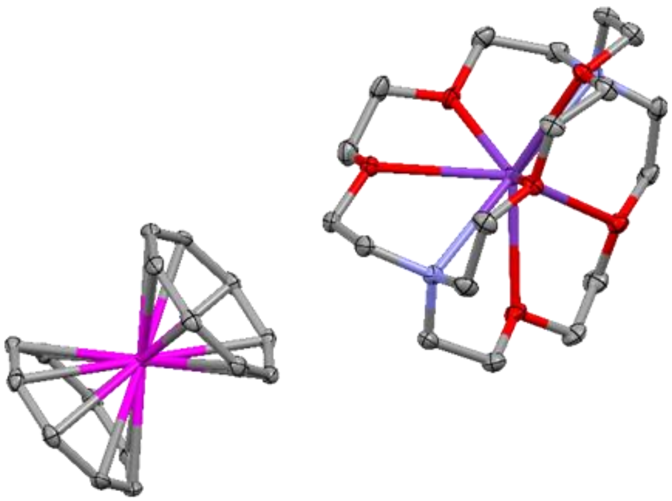

Supplemental Figure 3.3: Crystal structure of **3**, showing thermal ellipsoids at 50% probability. Atoms are colored by element type: gray (carbon), light blue (nitrogen), pink (erbium), red (oxygen), purple (potassium). Hydrogen atoms have been omitted for clarity.

Magnetometry Methods

Magnetic data were collected under DC and VSM scan modes using a Quantum Design MPMS3 SQUID Magnetometer with equipped AC susceptibility attachment. Crystal samples were finely crushed and loaded in custom quartz tubes (D&G Glassblowing Inc.), layered with eicosane wax, and subsequently flame-sealed under static vacuum. Eicosane wax was melted within the sealed sample to abate sample torquing and to facilitate thermal conductivity. Diamagnetic corrections for the samples and eicosane wax were calculated using Pascal's constants[o] and subtracted from all static moment data. Thermal magnetic susceptibilities were collected as ZFC and FC data in DC scan mode under applied fields of H = 100, 250, 500, 750, 1,000, 10,000, and 40,000 Oe. Isothermal magnetization data were collected in VSM mode between −7 to 7 T at a 60 Oe sec^{-} sweep rate for full hysteresis loops and virgin curves.

---

[o] Bain, G. A.; Berry, J. F. "Diamagnetic corrections and Pascal's constants" *J Chem Educ* **2008**, *85*, 532.

Short and long-timescale AC data were fit to a Debye (Cole-Cole relaxation) model. Details related to the collection and analysis of long-timescale magnetic data are discussed in our previous works.[p] Temperature and τ data were fit to a multi-term relaxation model shown in Equation S.3.1. MPMS 3 data parsing, fitting, and plotting was performed with our MATLAB package, *Super*. This object-oriented code package and all applicable documentation is available at *https://github.com/RinehartGroup/super-matlab* under the MIT License.[q]

$$\tau^{-1} = \tau_0^{-1} exp\left(\frac{-U_{eff}}{k_B T}\right) + \tau_D^{-1} exp\left(\frac{-D_{eff}}{k_B T}\right) \qquad \textit{(Eq. S.3.1)}$$

Equation S.3.1. Multi-term relaxation mechanism equation accounting for Orbach and dipolar processes, where τ is the fitted relaxation time, τ_0 is the attempt time, U_{eff} is the effective barrier, k_B is the Boltzmann constant, T is the temperature, τ_D is the dipole attempt time, and D_{eff} is the dipole effective barrier.

---

[p] Hilgar, J. D.; Butts, A. K.; Rinehart, J. D. "A method for extending AC susceptometry to long-timescale magnetic relaxation" *Phys Chem Chem Phys* 2019, *21*, 22302; Orlova, A. P.; Hilgar, J. D.; Bernbeck, M. G.; Gembicky, M.; Rinehart, J. D. "Intuitive Control of Low-Energy Magnetic Excitations via Directed Dipolar Interactions in a Series of Er(III)-Based Complexes" *J Am Chem Soc* **2022**, *144*, 11316.

[q] Hilgar, J. D., Orlova, A.P., Bernbeck, M.G. 2022.

Magnetic Data of Compounds 1 & 1-Y

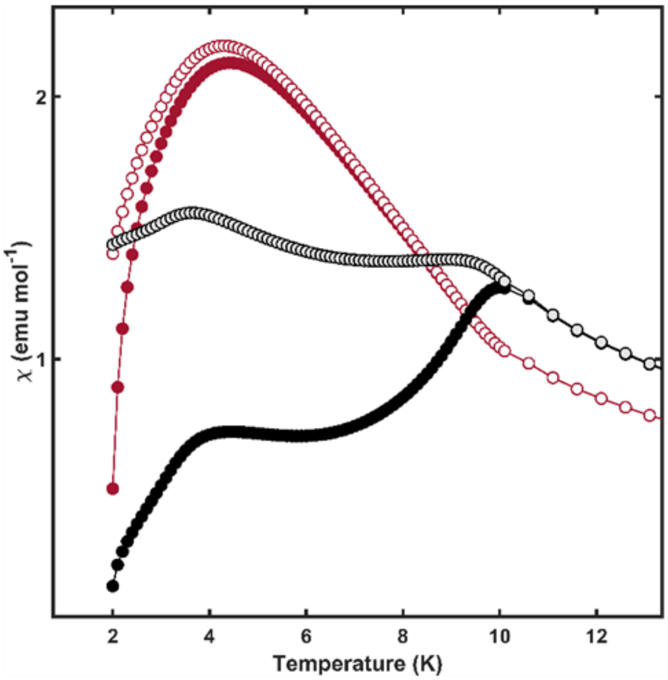

Supplemental Figure 3.4: DC susceptibility data for **1** (colored circles) and **1-Y** (black and white circles) under H = 100 Oe applied field. ZFC data is represented by filled markers, FC by open markers.

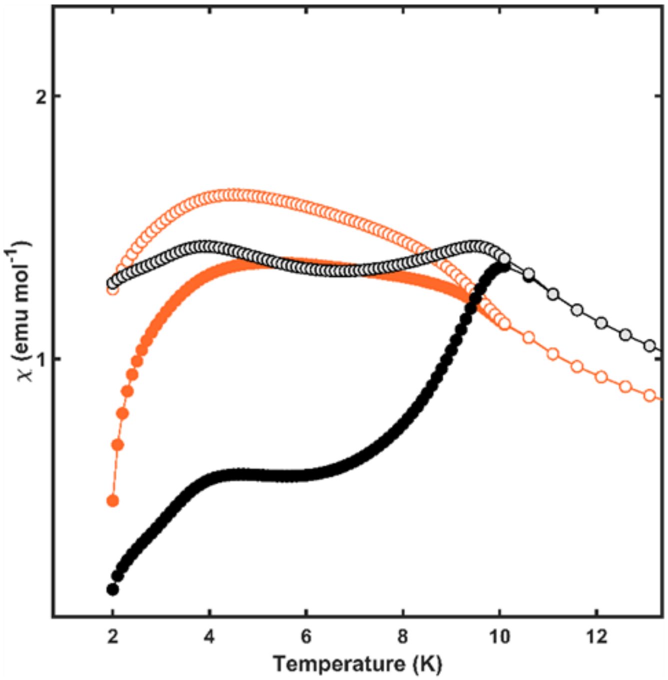

Supplemental Figure 3.5: DC susceptibility data for **1** (colored circles) and **1-Y** (black and white circles) under H = 250 Oe applied field. ZFC data is represented by filled markers, FC by open markers.

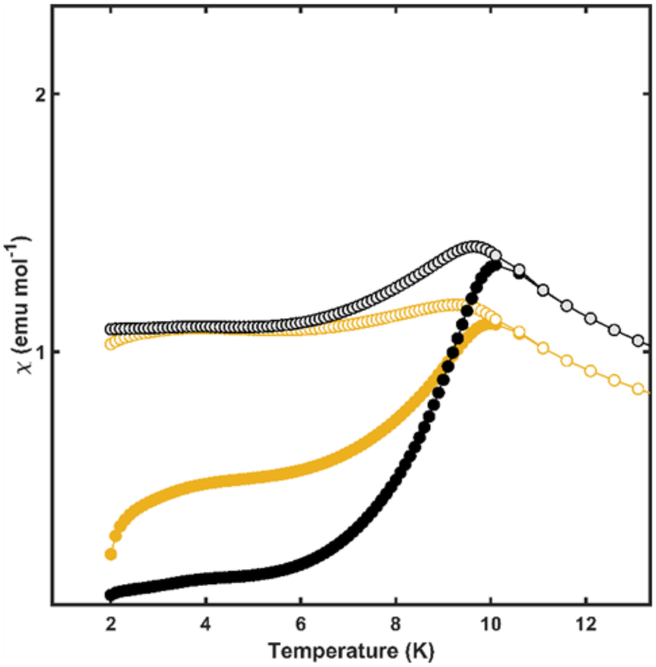

Supplemental Figure 3.6: DC susceptibility data for **1** (colored circles) and **1-Y** (black and white circles) under H = 500 Oe applied field. ZFC data is represented by filled markers, FC by open markers.

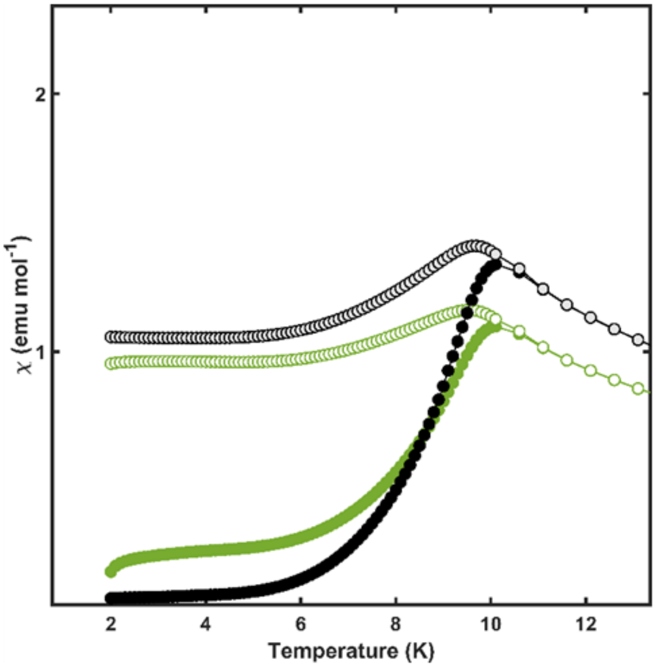

Supplemental Figure 3.7: DC susceptibility data for **1** (colored circles) and **1-Y** (black and white circles) under H = 750 Oe applied field. ZFC data is represented by filled markers, FC by open markers.

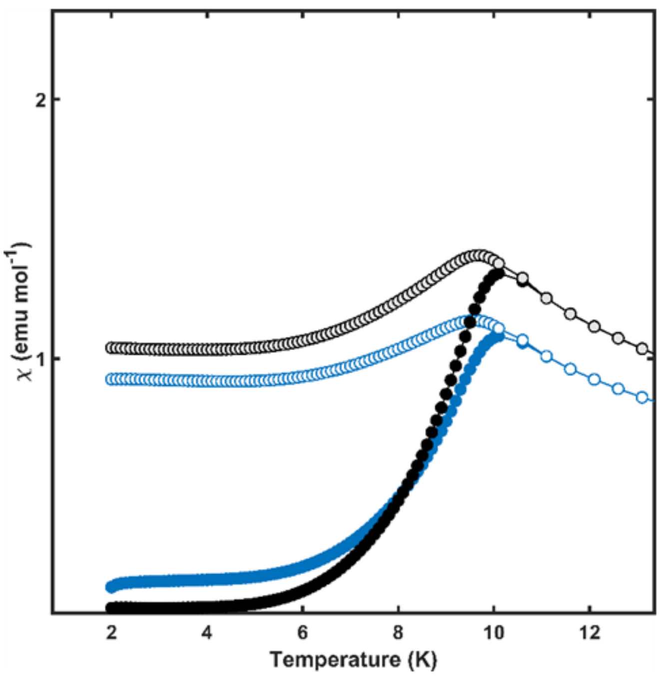

Supplemental Figure 3.8: DC susceptibility data for **1** (colored circles) and **1-Y** (black and white circles) under H = 1000 Oe applied field. ZFC data is represented by filled markers, FC by open markers.

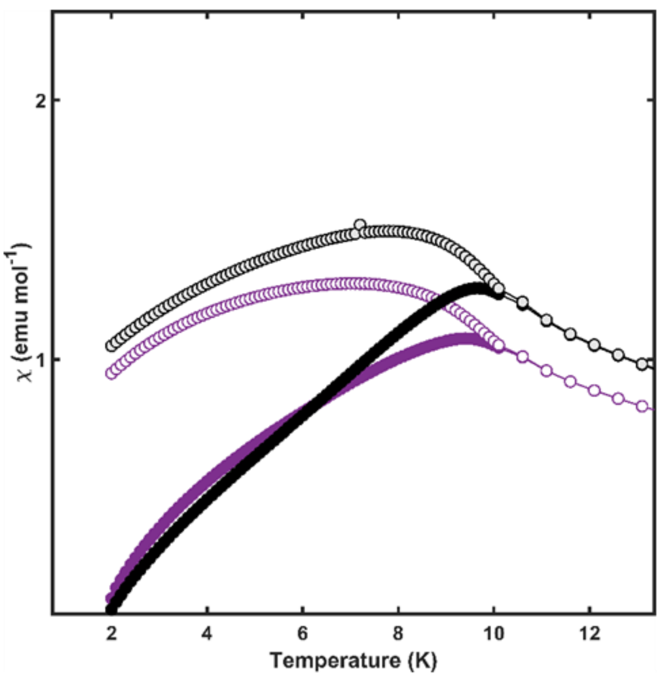

Supplemental Figure 3.9: DC susceptibility data for **1** (colored circles) and **1-Y** (black and white circles) under H = 10,000 Oe applied field. ZFC data is represented by filled markers, FC by open markers.

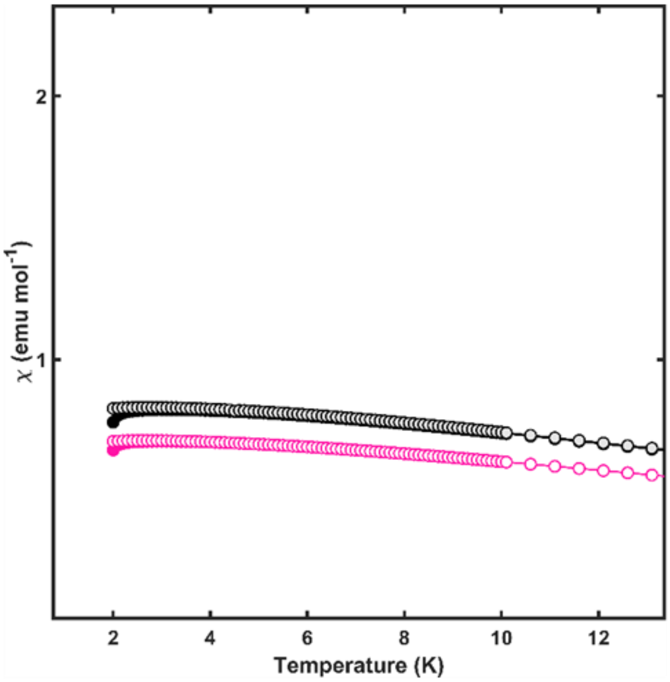

Supplemental Figure 3.10: DC susceptibility data for **1** (colored circles) and **1-Y** (black and white circles) under H = 40,000 Oe applied field. ZFC data is represented by filled markers, FC by open markers.

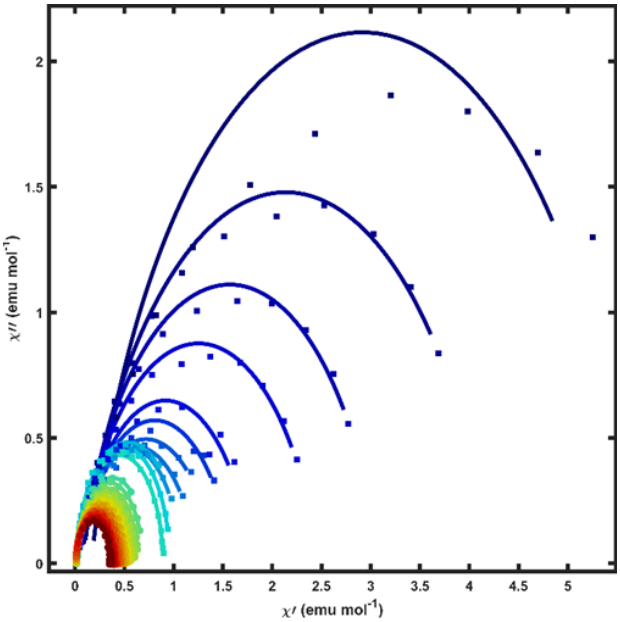

Supplemental Figure 3.11: Cole-cole plot of **1** collected between *T* = 2 - 29 K (blue - red). Data points are susceptibilities measured via standard AC measurements (circles) and extracted from Fourier analysis of VSM data (squares). Lines represent fits to a generalized Debye model.

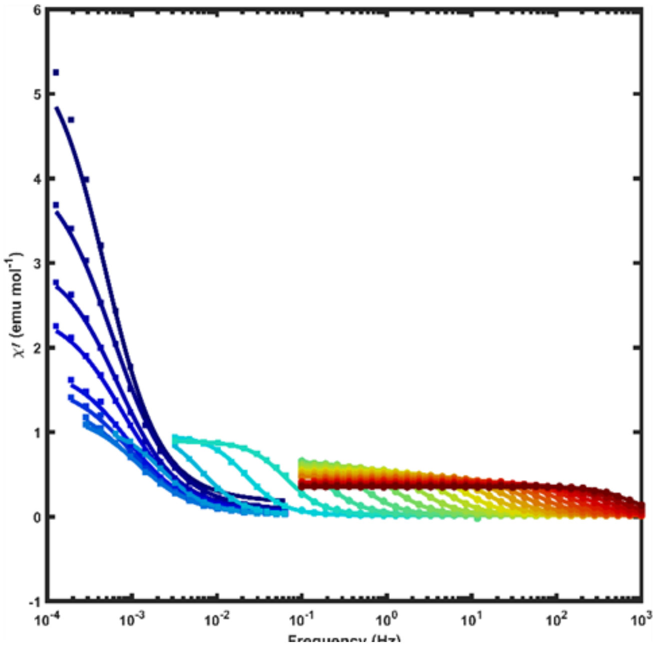

Supplemental Figure 3.12: AC in-phase susceptibility (χ') of **1** collected between *T* = 2 - 29 K (blue - red). Data points are susceptibilities measured via standard AC measurements (circles) and extracted from Fourier analysis of VSM data (squares). Lines represent fits to a generalized Debye model.

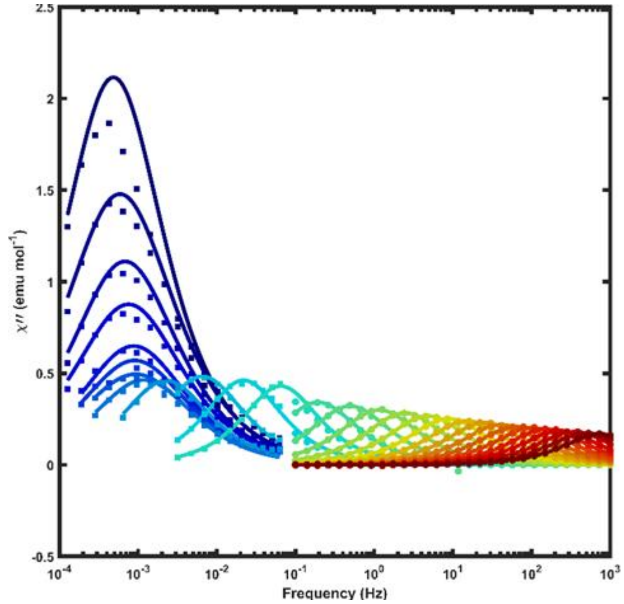

Supplemental Figure 3.13: AC out-of-phase susceptibility (χ'') of **1** collected between *T* = 2 - 29 K (blue - red). Data points are susceptibilities measured via standard AC measurements (circles) and extracted from Fourier analysis of VSM data (squares). Lines represent fits to a generalized Debye model.

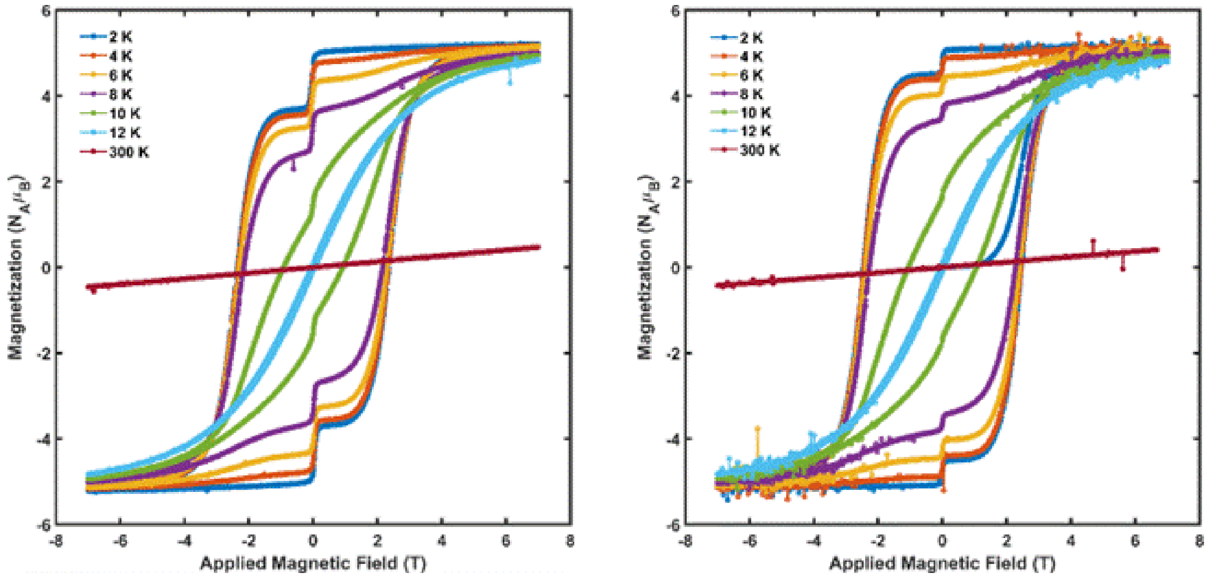

Supplemental Figure 3.14: Isothermal magnetization of **1** (left) and **1-Y** (right) at *T* = 2, 4, 6, 8, 10, 12, and 300 K collected between $H = -7$ to 7 T at a constant sweep rate of 60 Oe sec^{-1}. Markers are data points from VSM mode collection, lines through the data are guides for the eye.

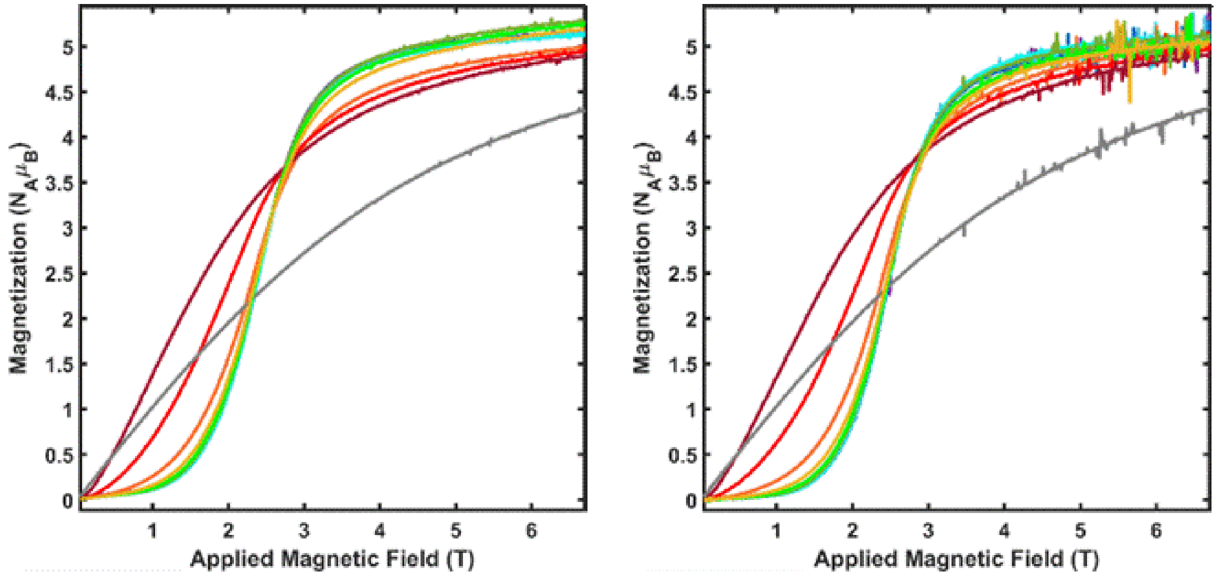

Supplemental Figure 3.15: Virgin isothermal magnetization of **1** (left) and **1-Y** (right) at *T* = 2 – 12 K (purple to blue to red) and 20 K (gray), collected in VSM mode between $H = 0$ to 7 T at a constant sweep rate of 60 Oe sec^{-1}.

Supplemental Table 3.1: Model fit values for AC and waveform data collected for 1 between T = 2 - 29 K.

T	τ_1	$\tau_{1, error, LB}$	$\tau_{1, error, UB}$	α_1	$\alpha_{1, error, LB}$	$\alpha_{1, error, UB}$	χ_T	$\chi_{T, error, LB}$	$\chi_{T, error, UB}$	χ_S	$\chi_{S, error, LB}$	$\chi_{S, error, UB}$
2	328.34	279.83	376.86	0.17	0.10	0.23	5.67	5.24	6.10	0.16	0.03	0.29
3	270.99	255.80	286.17	0.21	0.19	0.23	4.21	4.10	4.33	0.06	0.02	0.10
4	233.67	222.08	245.26	0.20	0.17	0.22	3.09	3.01	3.16	0.05	0.02	0.08
5	210.79	199.92	221.65	0.21	0.18	0.23	2.47	2.41	2.53	0.03	0.01	0.06
6	181.58	162.26	200.90	0.19	0.15	0.24	1.80	1.71	1.89	0.03	0.00	0.07
7	176.17	161.72	190.63	0.20	0.17	0.24	1.59	1.53	1.66	0.02	0.00	0.04
8	171.70	156.68	186.71	0.22	0.19	0.25	1.43	1.36	1.49	0.01	0.00	0.03
9	135.20	125.84	144.55	0.17	0.14	0.20	1.23	1.19	1.28	0.02	0.00	0.04
10	70.30	66.33	74.28	0.08	0.05	0.12	1.08	1.04	1.11	0.03	0.01	0.04
11	24.31	23.30	25.32	0.06	0.03	0.08	1.07	1.04	1.10	0.01	0.00	0.02
12	7.29	7.17	7.41	0.01	0.00	0.02	0.96	0.95	0.97	0.02	0.01	0.02
13	2.46	2.41	2.51	0.01	0.00	0.02	0.89	0.88	0.90	0.02	0.02	0.02
14	0.83	0.82	0.83	0.04	0.03	0.04	0.74	0.73	0.74	0.01	0.01	0.02
15	0.32	0.31	0.33	0.03	0.01	0.05	0.69	0.67	0.70	0.01	0.01	0.02
16	0.14	0.14	0.14	0.03	0.03	0.04	0.64	0.64	0.65	0.01	0.01	0.01
17	0.07	0.07	0.07	0.03	0.03	0.03	0.61	0.61	0.61	0.01	0.01	0.01
18	0.03	0.03	0.03	0.03	0.02	0.03	0.57	0.57	0.57	0.01	0.01	0.01
19	0.02	0.02	0.02	0.03	0.03	0.03	0.54	0.54	0.54	0.01	0.01	0.01
20	0.01	0.01	0.01	0.03	0.03	0.03	0.51	0.51	0.52	0.01	0.01	0.01
21	0.01	0.01	0.01	0.02	0.02	0.03	0.49	0.49	0.49	0.01	0.01	0.01
22	0.00	0.00	0.00	0.02	0.02	0.03	0.47	0.47	0.47	0.01	0.01	0.01
23	0.00	0.00	0.00	0.03	0.02	0.03	0.45	0.45	0.45	0.01	0.01	0.01
24	0.00	0.00	0.00	0.02	0.01	0.03	0.43	0.43	0.43	0.01	0.01	0.01
25	0.00	0.00	0.00	0.02	0.01	0.03	0.41	0.41	0.41	0.01	0.01	0.01
26	0.00	0.00	0.00	0.02	0.01	0.03	0.40	0.39	0.40	0.01	0.01	0.01
27	0.00	0.00	0.00	0.02	0.00	0.03	0.38	0.38	0.38	0.01	0.00	0.02
28	0.00	0.00	0.00	0.00	-0.01	0.02	0.37	0.37	0.37	0.02	0.01	0.03
29	0.00	0.00	0.00	0.00	-0.02	0.02	0.36	0.35	0.36	0.02	0.00	0.03

Magnetic Data of Compounds 2 & 2-Y

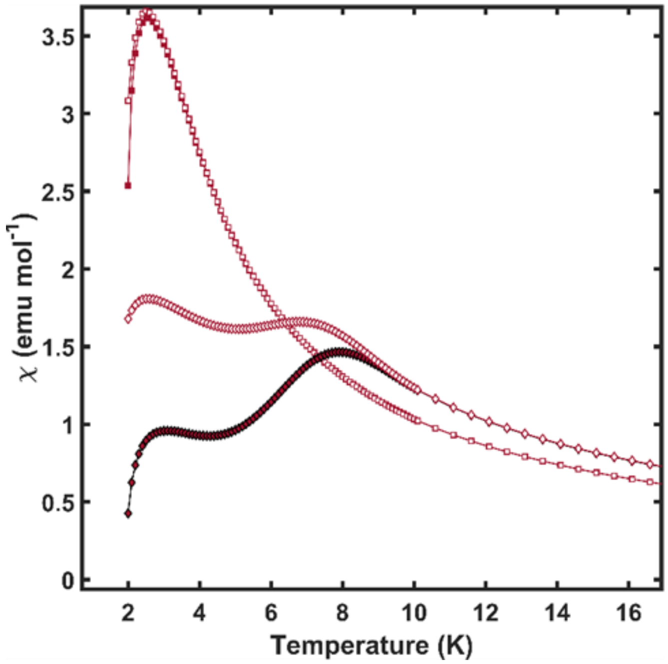

Supplemental Figure 3.16: DC susceptibility data for **2** (squares) and **2-Y** (diamonds) under H = 100 Oe applied field. ZFC data is represented by filled markers, FC by open markers.

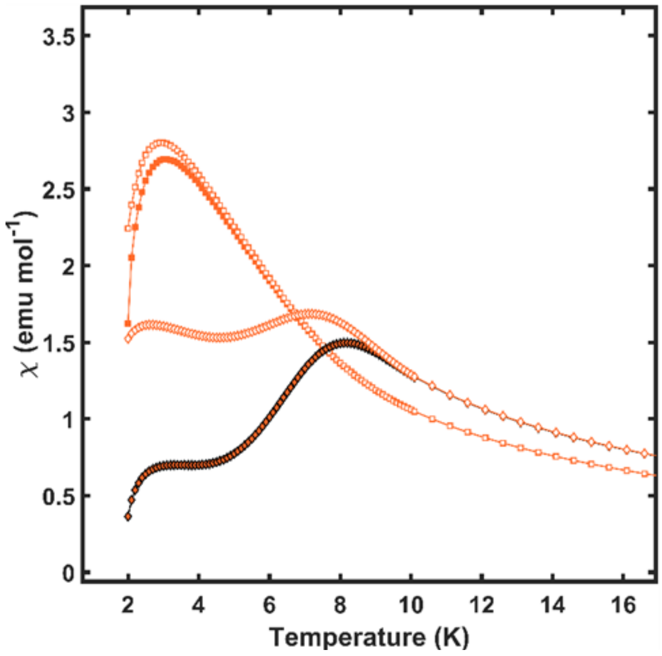

Supplemental Figure 3.17: DC susceptibility data for **2** (squares) and **2-Y** (diamonds) under H = 250 Oe applied field. ZFC data is represented by filled markers, FC by open markers.

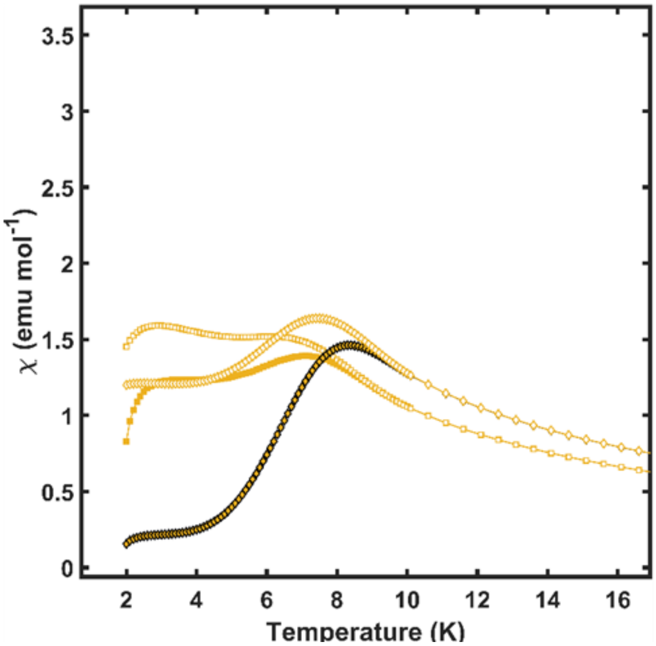

Supplemental Figure 3.18: DC susceptibility data for **2** (squares) and **2-Y** (diamonds) under H = 500 Oe applied field. ZFC data is represented by filled markers, FC by open markers.

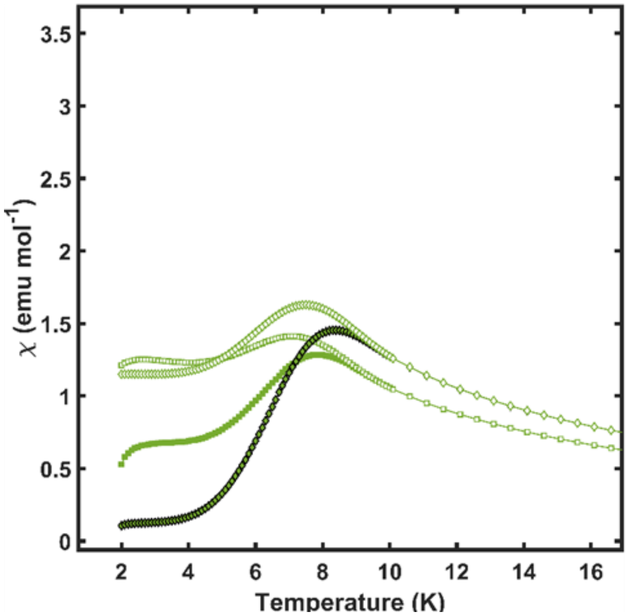

Supplemental Figure 3.19: DC susceptibility data for **2** (squares) and **2-Y** (diamonds) under H = 750 Oe applied field. ZFC data is represented by filled markers, FC by open markers.

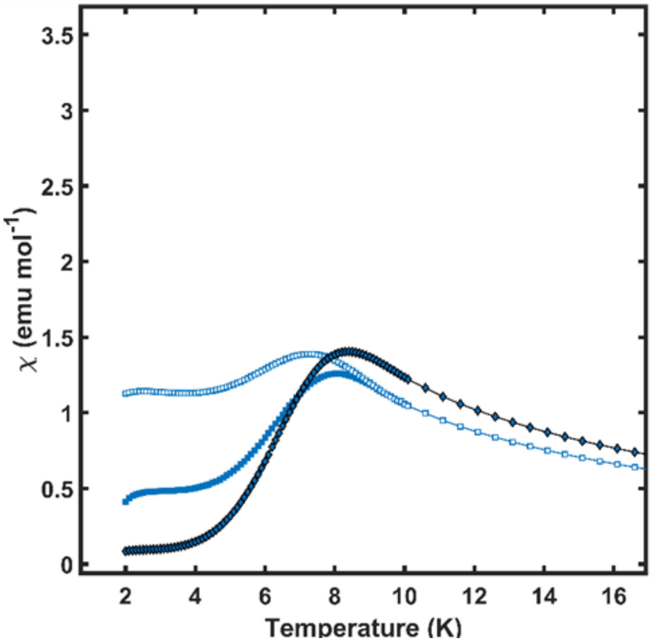

Supplemental Figure 3.20: DC susceptibility data for **2** (squares) and **2-Y** (diamonds) under H = 1,000 Oe applied field. ZFC data is represented by filled markers, FC by open markers.

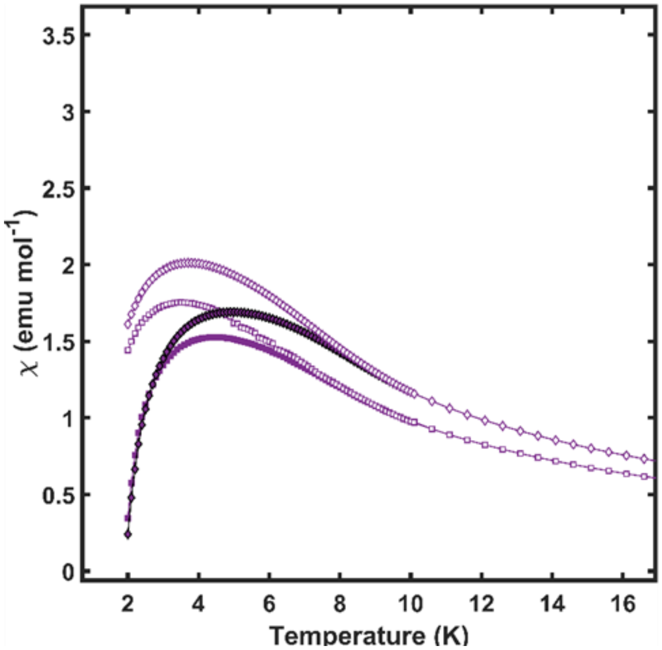

Supplemental Figure 3.21: DC susceptibility data for **2** (squares) and **2-Y** (diamonds) under H = 10,000 Oe applied field. ZFC data is represented by filled markers, FC by open markers.

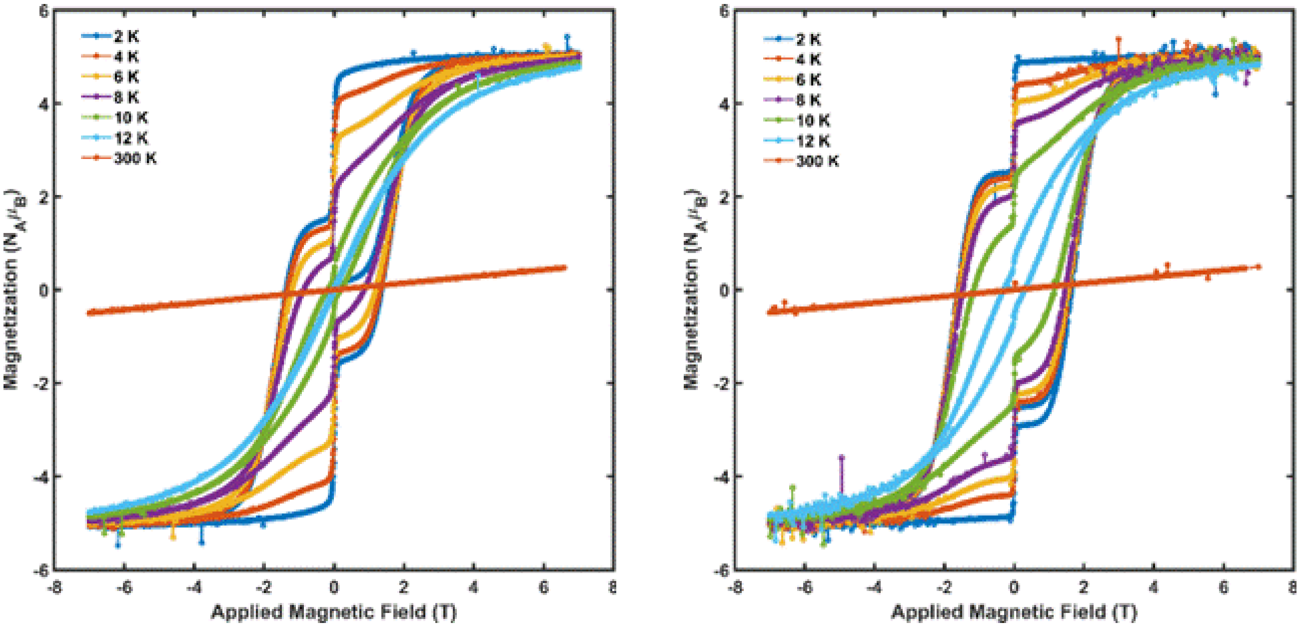

Supplemental Figure 3.22: Isothermal magnetization of **2** (left) and **2-Y** (right) at *T* = 2, 4, 6, 8, 10, 12, and 300 K collected between $H = -7$ to 7 T at a constant sweep rate of 60 Oe sec^{-1}. Markers are data points from VSM mode collection, lines through the data are guides for the eye.

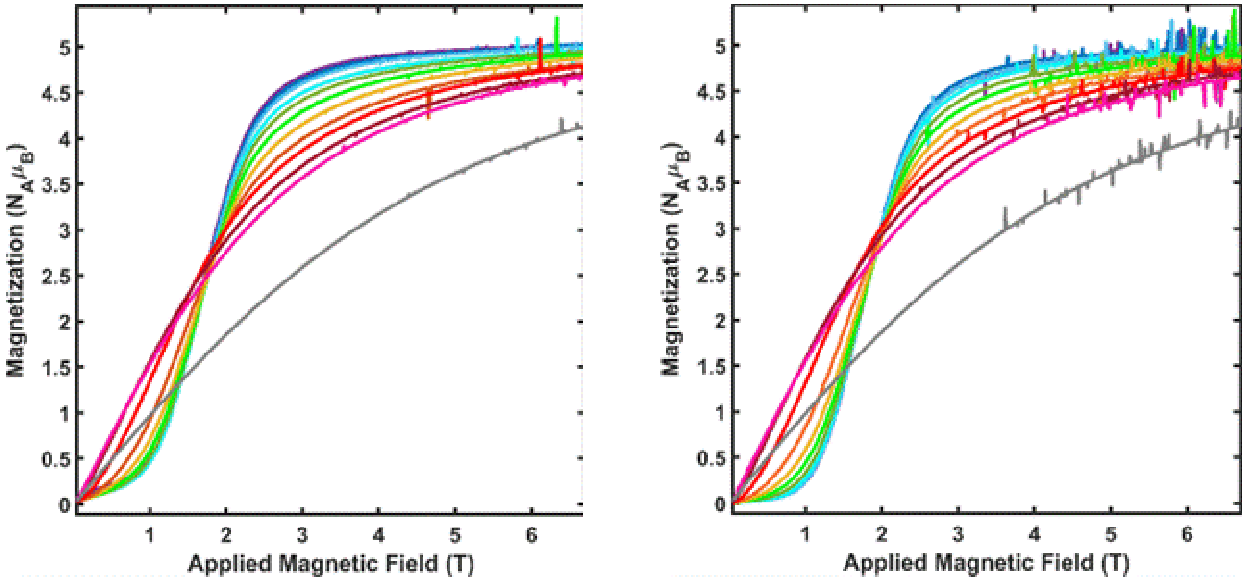

Supplemental Figure 3.23: Virgin isothermal magnetization of **2** (left) and **2-Y** (right) at *T* = 2 – 12 K (purple to blue to red) and 20 K (gray), collected in VSM mode between $H = 0$ to 7 T at a constant sweep rate of 60 Oe sec^{-1}.

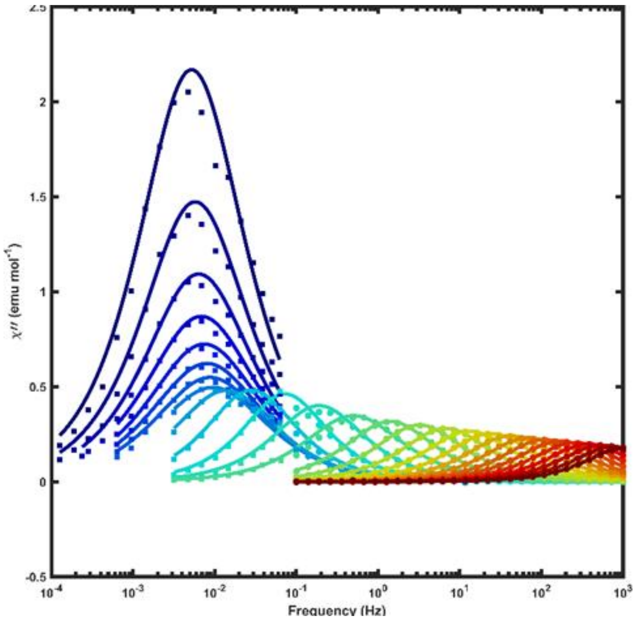

Supplemental Figure 3.24: AC out-of-phase susceptibility (χ'') of **2** collected between *T* = 2 - 28 K (blue - red). Data points are susceptibilities measured via standard AC measurements (circles) and extracted from Fourier analysis of VSM data (squares). Lines represent fits to a generalized Debye model.

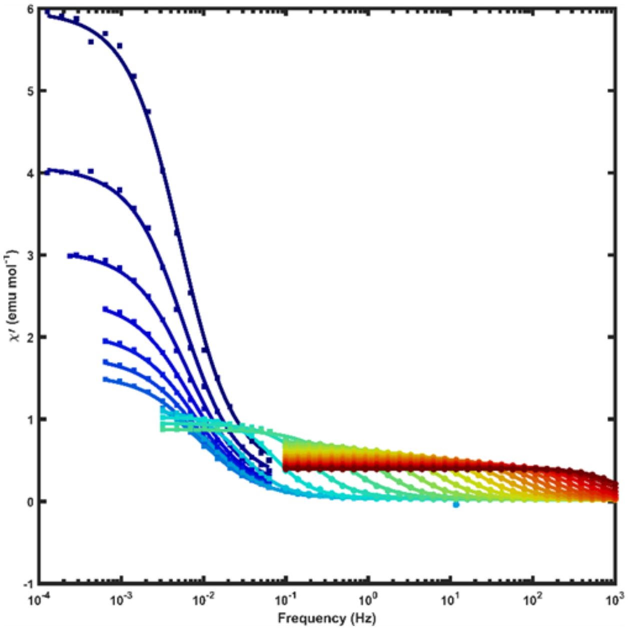

Supplemental Figure 3.25: AC in-phase susceptibility (χ') of **2** collected between *T* = 2 - 28 K (blue - red). Data points are susceptibilities measured via standard AC measurements (circles) and extracted from Fourier analysis of VSM data (squares). Lines represent fits to a generalized Debye model.

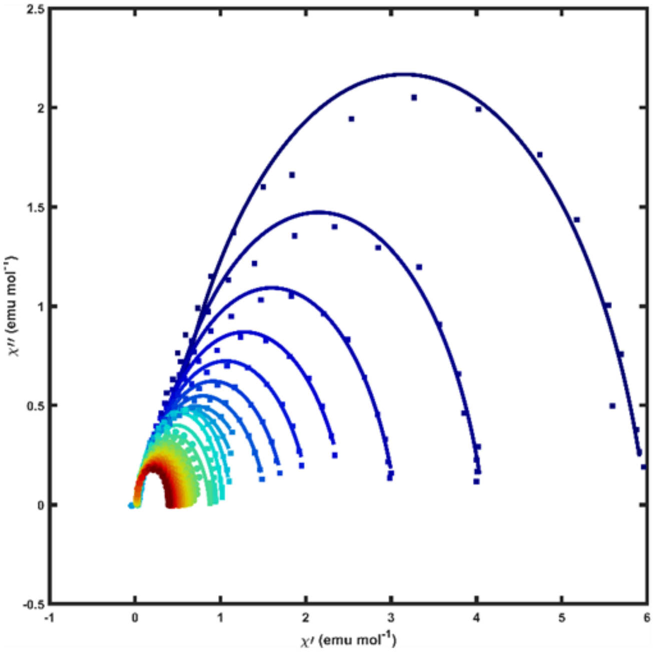

Supplemental Figure 3.26: Cole-cole plot of **2** collected between *T* = 2 - 28 K (blue - red). Data points are susceptibilities measured via standard AC measurements (circles) and extracted from Fourier analysis of VSM data (squares). Lines represent fits to a generalized Debye model.

Supplemental Table 3.2: Model fit values for AC and waveform data collected for **2** between T = 2 - 28 K.

T	τ_1	$\tau_{1,\ error,\ LB}$	$\tau_{1,\ error,\ UB}$	α_1	$\alpha_{1,\ error,\ LB}$	$\alpha_{1,\ error,\ UB}$	χ_T	$\chi_{T,\ error,\ LB}$	$\chi_{T,\ error,\ UB}$	χ_S	$\chi_{S,\ error,\ LB}$	$\chi_{S,\ error,\ UB}$
2	30.43	28.66	32.20	0.17	0.14	0.20	5.99	5.88	6.09	0.32	0.19	0.45
3	27.50	26.02	28.98	0.17	0.14	0.20	4.09	4.02	4.15	0.22	0.13	0.30
4	24.95	23.71	26.19	0.18	0.16	0.21	3.06	3.02	3.11	0.14	0.08	0.20
5	23.13	21.86	24.40	0.20	0.17	0.23	2.47	2.42	2.53	0.09	0.04	0.14
6	21.31	20.11	22.51	0.20	0.17	0.23	2.06	2.02	2.11	0.07	0.02	0.12
7	19.79	18.61	20.97	0.20	0.17	0.24	1.78	1.74	1.82	0.05	0.01	0.10
8	18.12	17.04	19.21	0.20	0.17	0.23	1.55	1.52	1.59	0.04	0.00	0.08
9	16.78	15.82	17.73	0.21	0.19	0.23	1.41	1.37	1.45	0.03	0.03	0.04
10	11.54	11.05	12.02	0.15	0.13	0.17	1.25	1.22	1.28	0.03	0.03	0.04
11	5.60	5.49	5.70	0.08	0.07	0.09	1.12	1.11	1.13	0.03	0.03	0.04
12	2.19	2.14	2.24	0.05	0.03	0.06	1.03	1.02	1.04	0.03	0.03	0.04
13	0.84	0.81	0.87	0.09	0.07	0.11	0.95	0.94	0.96	0.03	0.02	0.03
14	0.32	0.31	0.33	0.13	0.11	0.15	0.88	0.87	0.89	0.02	0.01	0.03
15	0.11	0.11	0.11	0.08	0.07	0.08	0.74	0.74	0.74	0.02	0.02	0.02
16	0.05	0.05	0.05	0.07	0.07	0.08	0.69	0.69	0.69	0.02	0.02	0.02
17	0.02	0.02	0.02	0.07	0.07	0.08	0.65	0.65	0.65	0.02	0.02	0.02
18	0.01	0.01	0.01	0.07	0.07	0.07	0.61	0.61	0.62	0.02	0.02	0.02
19	0.01	0.01	0.01	0.07	0.06	0.07	0.58	0.58	0.58	0.02	0.02	0.02
20	0.00	0.00	0.00	0.07	0.06	0.07	0.55	0.55	0.55	0.02	0.02	0.02
21	0.00	0.00	0.00	0.06	0.06	0.07	0.53	0.53	0.53	0.02	0.02	0.02
22	0.00	0.00	0.00	0.05	0.05	0.06	0.50	0.50	0.50	0.02	0.02	0.02
23	0.00	0.00	0.00	0.05	0.05	0.06	0.48	0.48	0.48	0.02	0.02	0.02
24	0.00	0.00	0.00	0.04	0.04	0.05	0.46	0.46	0.46	0.02	0.02	0.02
25	0.00	0.00	0.00	0.03	0.03	0.04	0.44	0.44	0.44	0.02	0.02	0.03
26	0.00	0.00	0.00	0.03	0.02	0.03	0.43	0.43	0.43	0.03	0.02	0.03
27	0.00	0.00	0.00	0.01	0.00	0.02	0.41	0.41	0.41	0.03	0.03	0.04
28	0.00	0.00	0.00	0.00	-0.01	0.01	0.40	0.40	0.40	0.04	0.03	0.05

Magnetic Data of Compounds 3 & 3-Y

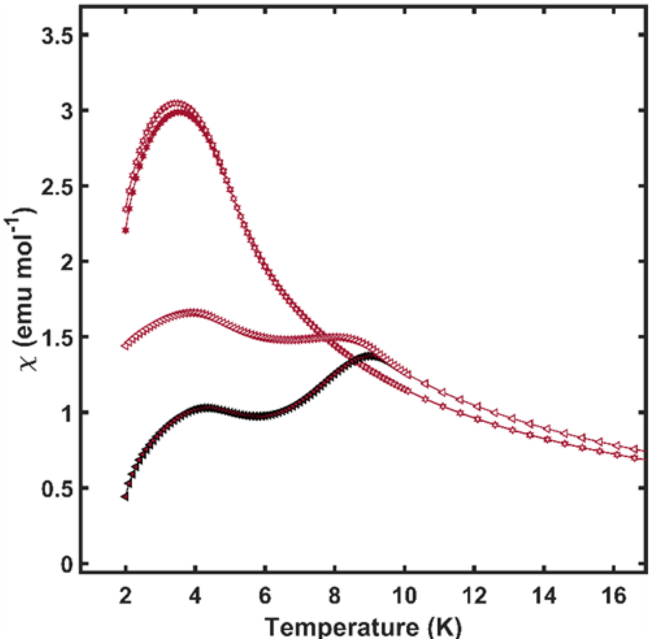

Supplemental Figure 3.27: DC susceptibility data for **3** (stars) and **3-Y** (triangles) under H = 100 Oe applied field. ZFC data is represented by filled markers, FC by open markers.

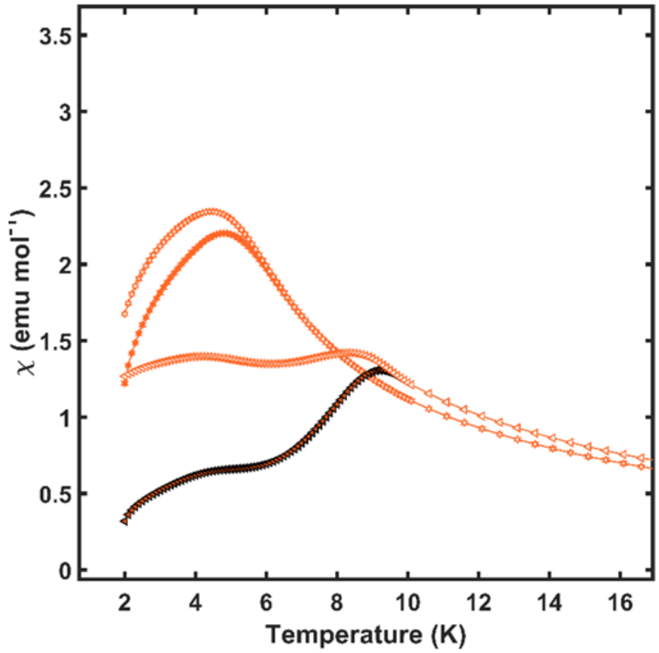

Supplemental Figure 3.28: DC susceptibility data for **3** (stars) and **3-Y** (triangles) under H = 250 Oe applied field. ZFC data is represented by filled markers, FC by open markers.

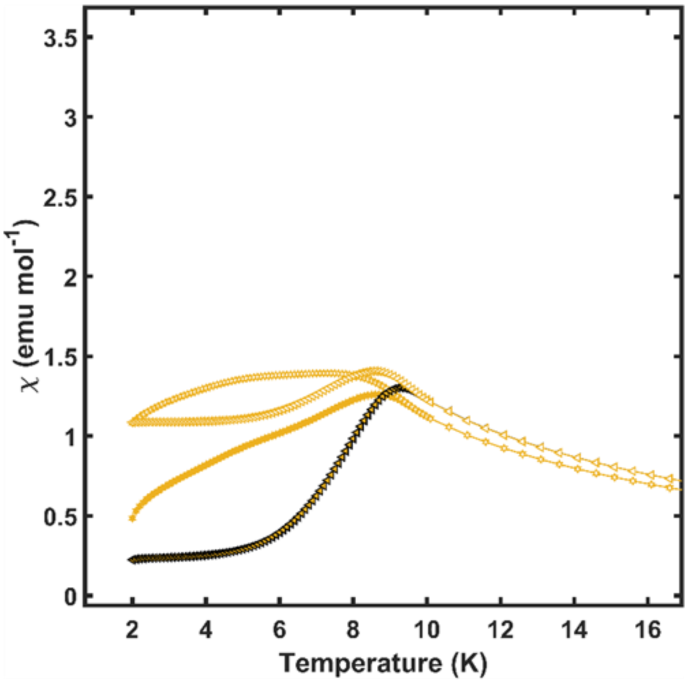

Supplemental Figure 3.29: DC susceptibility data for **3** (stars) and **3-Y** (triangles) under H = 500 Oe applied field. ZFC data is represented by filled markers, FC by open markers.

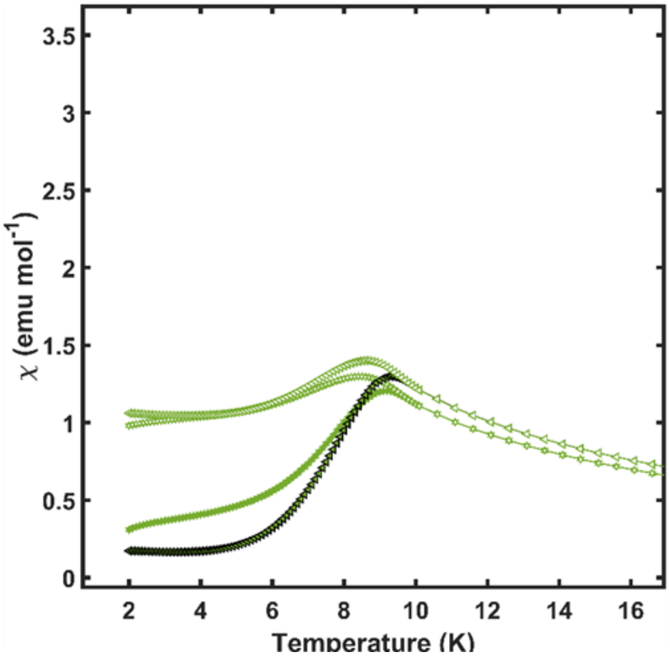

Supplemental Figure 3.30: DC susceptibility data for **3** (stars) and **3-Y** (triangles) under H = 750 Oe applied field. ZFC data is represented by filled markers, FC by open markers.

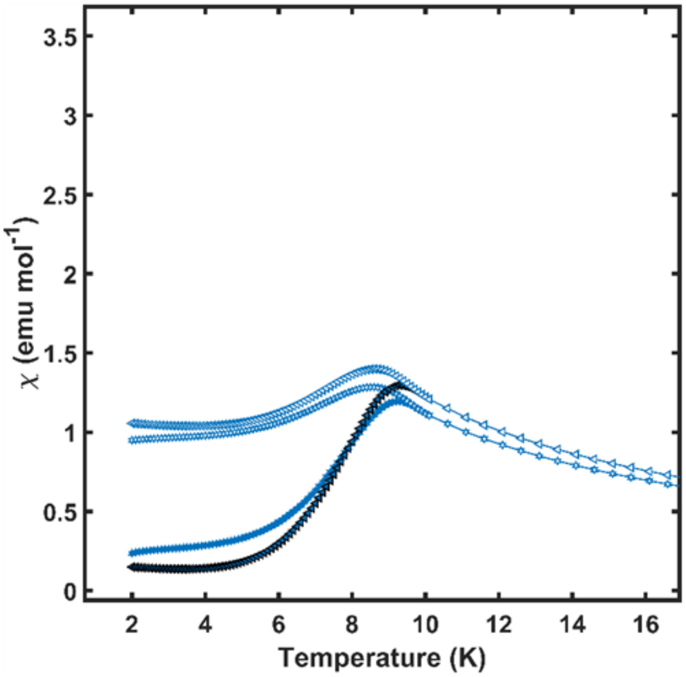

Supplemental Figure 3.31: DC susceptibility data for **3** (stars) and **3-Y** (triangles) under H = 1,000 Oe applied field. ZFC data is represented by filled markers, FC by open markers.

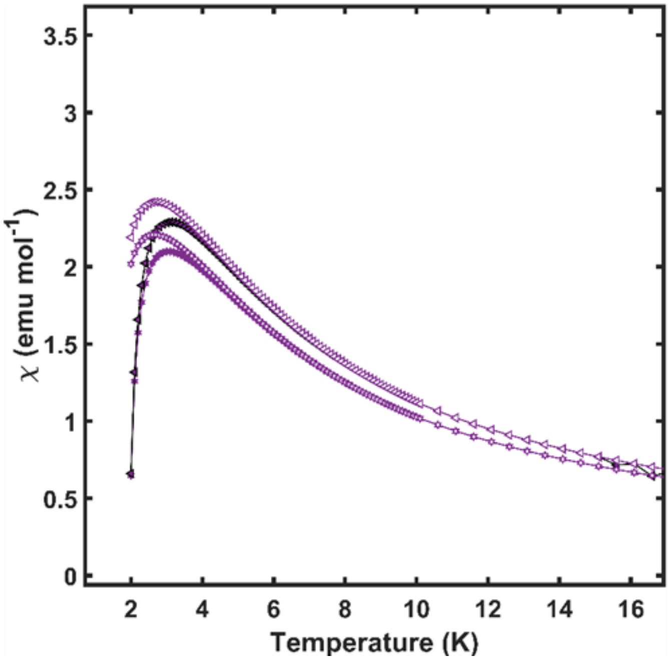

Supplemental Figure 3.32: DC susceptibility data for **3** (stars) and **3-Y** (triangles) under H = 10,000 Oe applied field. ZFC data is represented by filled markers, FC by open markers.

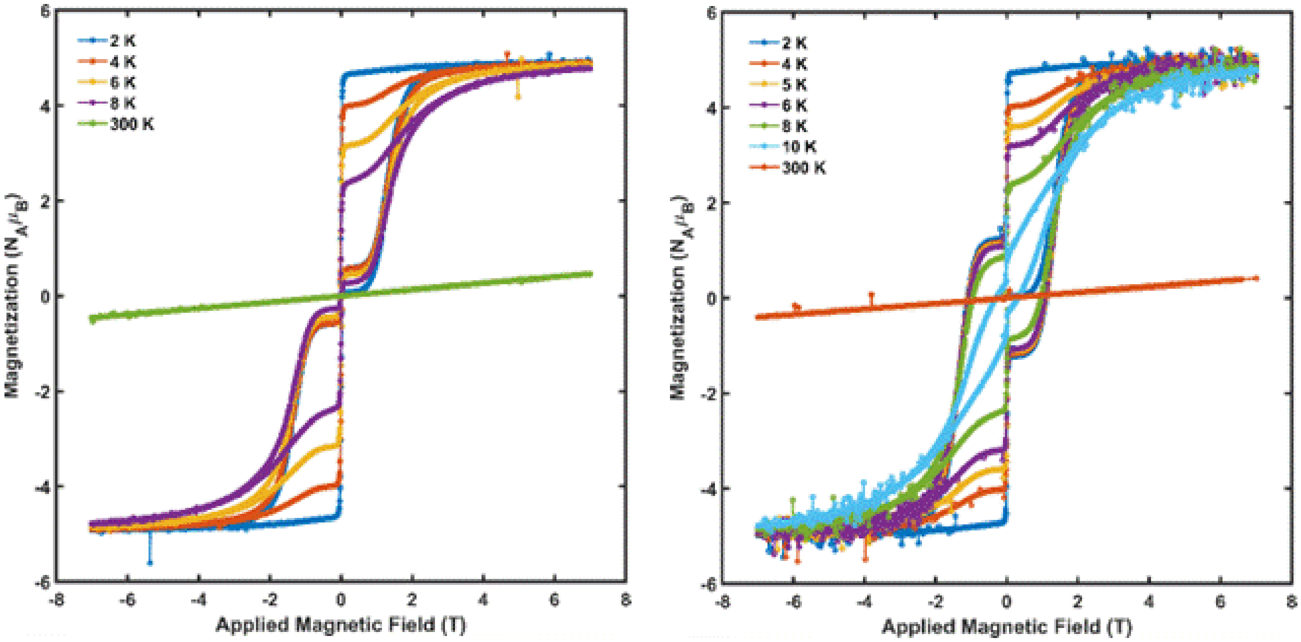

Supplemental Figure 3.33: Isothermal magnetization of **3** (left) and **3-Y** (right) at T = 2, 4, 6, 8, 10, 12, and 300 K collected between $H = -7$ to 7 T at a constant sweep rate of 60 Oe sec^{-1}. Markers are data points from VSM mode collection, lines through the data are guides for the eye.

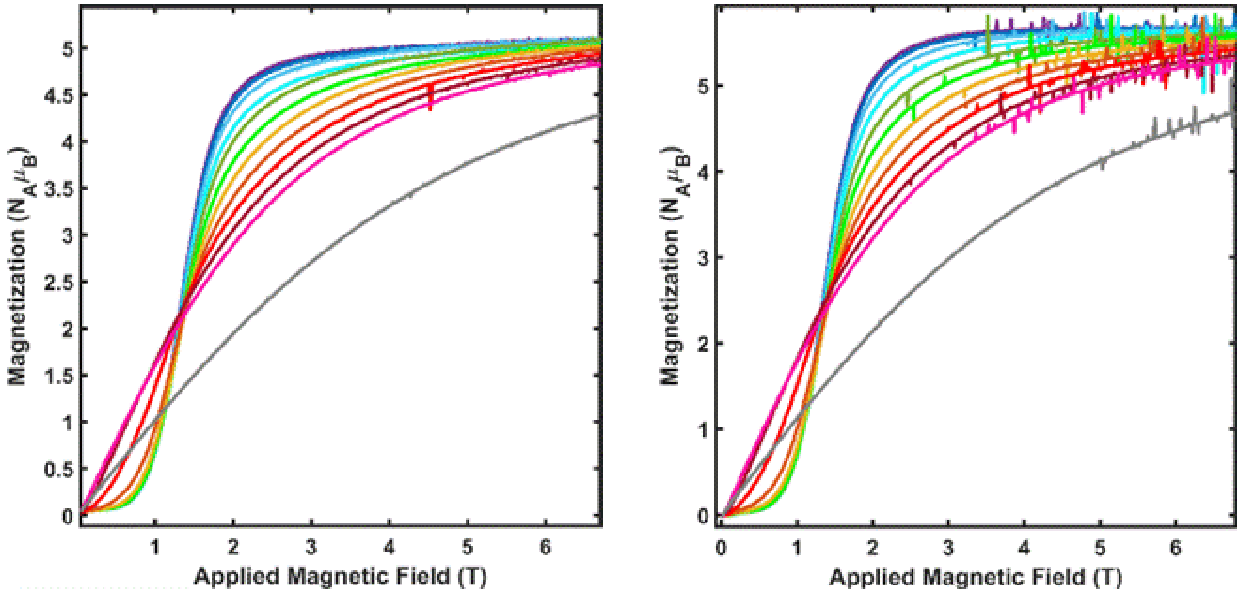

Supplemental Figure 3.34: Virgin isothermal magnetization of **3** (left) and **3-Y** (right) at T = 2 – 12 K (purple to blue to red) and 20 K (gray), collected in VSM mode between $H = 0$ to 7 T at a constant sweep rate of 60 Oe sec^{-1}.

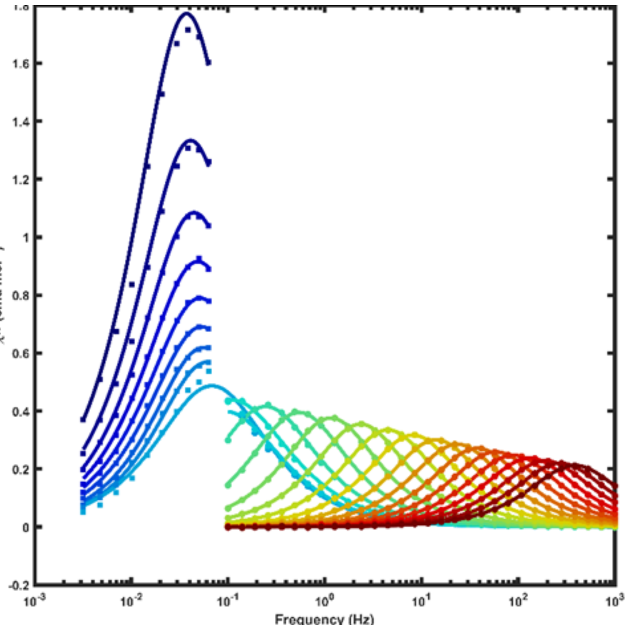

Supplemental Figure 3.35: AC out-of-phase susceptibility (χ'') of **3** collected between T = 2 - 27 K (blue - red). Data points are susceptibilities measured via standard AC measurements (circles) and extracted from Fourier analysis of VSM data (squares). Lines represent fits to a generalized Debye model.

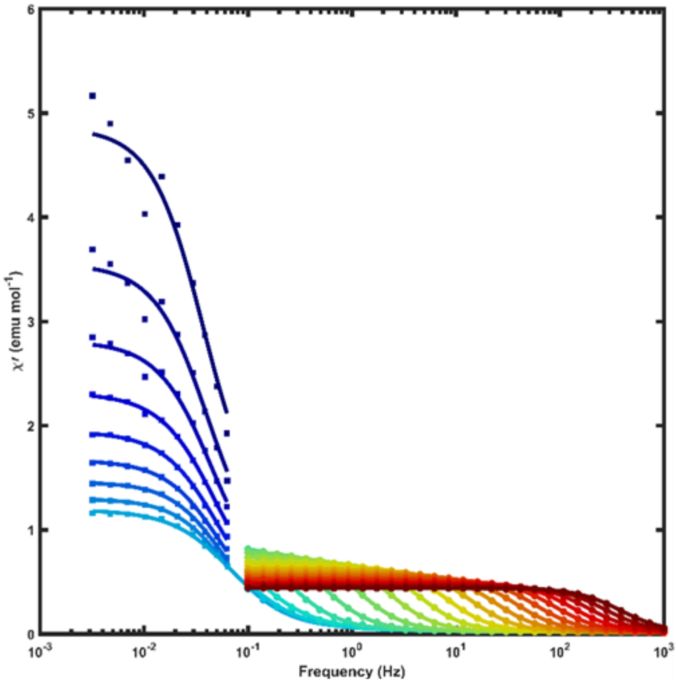

Supplemental Figure 3.36: AC in-phase susceptibility (χ') of **3** collected between T = 2 - 27 K (blue - red). Data points are susceptibilities measured via standard AC measurements (circles) and extracted from Fourier analysis of VSM data (squares). Lines represent fits to a generalized Debye model.

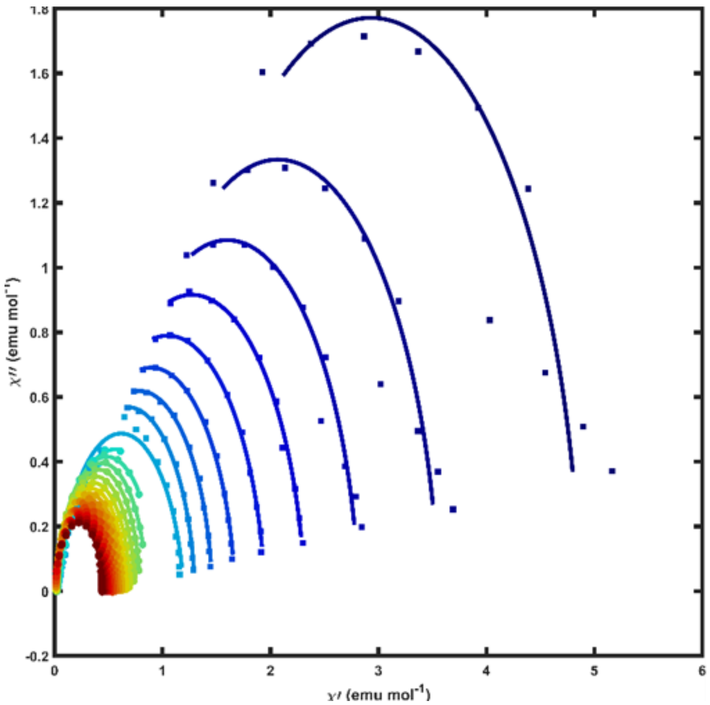

Supplemental Figure 3.37: Cole-cole plot of **3** collected between *T* = 2 - 27 K (blue - red). Data points are susceptibilities measured via standard AC measurements (circles) and extracted from Fourier analysis of VSM data (squares). Lines represent fits to a generalized Debye model.

Supplemental Table 3.3: Model fit values for AC and waveform data collected for **3** between T = 2 - 27 K.

T	τ_1	$\tau_{1,\ error,\ LB}$	$\tau_{1,\ error,\ UB}$	α_1	$\alpha_{1,\ error,\ LB}$	$\alpha_{1,\ error,\ UB}$	χ_T	$\chi_{T,\ error,\ LB}$	$\chi_{T,\ error,\ UB}$	χ_S	$\chi_{S,\ error,\ LB}$	$\chi_{S,\ error,\ UB}$
2	4.26	3.27	5.25	0.06	-0.08	0.19	4.87	4.62	5.12	1.00	0.31	1.68
3	3.87	3.13	4.60	0.07	-0.03	0.17	3.56	3.42	3.70	0.58	0.16	1.00
4	3.57	3.12	4.02	0.07	0.01	0.14	2.82	2.75	2.88	0.38	0.16	0.61
5	3.26	3.09	3.44	0.09	0.06	0.11	2.32	2.30	2.34	0.22	0.14	0.30
6	3.09	2.92	3.26	0.09	0.06	0.11	1.95	1.93	1.97	0.15	0.07	0.22
7	2.99	2.79	3.18	0.08	0.05	0.10	1.67	1.66	1.69	0.12	0.04	0.19
8	2.87	2.70	3.05	0.05	0.03	0.08	1.46	1.45	1.47	0.11	0.05	0.17
9	2.62	2.46	2.77	0.06	0.04	0.08	1.30	1.29	1.31	0.05	0.00	0.11
10	2.34	2.26	2.41	0.11	0.09	0.13	1.20	1.18	1.21	0.04	0.03	0.04
11	1.67	1.49	1.86	0.11	0.08	0.14	0.98	0.91	1.05	0.03	0.03	0.03
12	1.45	1.38	1.51	0.13	0.11	0.14	1.10	1.07	1.13	0.03	0.02	0.03
13	0.65	0.64	0.66	0.06	0.05	0.07	0.94	0.93	0.95	0.03	0.02	0.03
14	0.29	0.29	0.29	0.03	0.02	0.03	0.85	0.85	0.85	0.02	0.02	0.02
15	0.14	0.14	0.14	0.01	0.01	0.02	0.79	0.79	0.79	0.02	0.02	0.02
16	0.07	0.07	0.07	0.01	0.01	0.01	0.74	0.74	0.74	0.02	0.02	0.02
17	0.04	0.04	0.04	0.01	0.00	0.01	0.70	0.69	0.70	0.02	0.02	0.02
18	0.02	0.02	0.02	0.00	0.00	0.01	0.66	0.66	0.66	0.02	0.02	0.02
19	0.01	0.01	0.01	0.00	0.00	0.01	0.62	0.62	0.62	0.02	0.02	0.02
20	0.01	0.01	0.01	0.00	0.00	0.01	0.59	0.59	0.59	0.02	0.02	0.02
21	0.00	0.00	0.00	0.01	0.00	0.01	0.56	0.56	0.56	0.02	0.02	0.02
22	0.00	0.00	0.00	0.01	0.00	0.01	0.54	0.54	0.54	0.01	0.01	0.02
23	0.00	0.00	0.00	0.01	0.00	0.01	0.52	0.51	0.52	0.01	0.01	0.02
24	0.00	0.00	0.00	0.01	0.00	0.01	0.49	0.49	0.49	0.01	0.01	0.02
25	0.00	0.00	0.00	0.01	0.00	0.01	0.47	0.47	0.48	0.01	0.01	0.02
26	0.00	0.00	0.00	0.00	0.00	0.01	0.46	0.46	0.46	0.02	0.01	0.02
27	0.00	0.00	0.00	0.00	-0.01	0.01	0.44	0.44	0.44	0.01	0.01	0.02

Computational Methods

All calculations were carried out at the CASSCF level using the OpenMolcas computational package.[r] Input atom coordinates were taken from crystallographic data and used without further geometry optimization. Basis functions of the ANO-RCC type were generated with the SEWARD module. The quality of a specific atomic basis function was determined by the atom's connectivity to the Er^{3+} ion (**Er**: ANO-RCC-VTZP; **atoms bound to Er**: ANO-RCC-VDZP; **all other atoms**: ANO-RCC-VDZ). Two-electron integrals were Cholesky decomposed (10^{-6} cutoff). A 7-orbital, 11-electron active space (CAS(11,7)) was selected for the CASSCF calculation, which was carried out using the RASSCF module. In this space, all 35 configuration-interaction (CI) roots of spin multiplicity 4 and all 112 CI roots of spin multiplicity 2 were included. The RASSI module was used to calculate spin-orbit matrix elements between CAS output wavefunctions. The SINGLE_ANISO module of OpenMolcas was used to calculate relevant magnetic properties based on these multiconfigurational SCF results.

---

[r] Aquilante, F.; Autschbach, J.; Baiardi, A.; Battaglia, S.; Borin, V. A.; Chibotaru, L. F.; Conti, I.; De Vico, L.; Delcey, M.; Galvan, I. F.; Ferre, N.; Freitag, L.; Garavelli, M.; Gong, X. J.; Knecht, S.; Larsson, E. D.; Lindh, R.; Lundberg, M.; Malmqvist, P. A.; Nenov, A.; Norell, J.; Odelius, M.; Olivucci, M.; Pedersen, T. B.; Pedraza-Gonzalez, L.; Phung, Q. M.; Pierloot, K.; Reiher, M.; Schapiro, I.; Segarra-Marti, J.; Segatta, F.; Seijo, L.; Sen, S.; Sergentu, D. C.; Stein, C. J.; Ungur, L.; Vacher, M.; Valentini, A.; Veryazov, V. "Modern quantum chemistry with [Open]Molcas" *J Chem Phys* **2020**, *152*.; Galvan, I. F.; Vacher, M.; Alavi, A.; Angeli, C.; Aquilante, F.; Autschbach, J.; Bao, J. J.; Bokarev, S. I.; Bogdanov, N. A.; Carlson, R. K.; Chibotaru, L. F.; Creutzberg, J.; Dattani, N.; Delcey, M. G.; Dong, S. J. S.; Dreuw, A.; Freitag, L.; Frutos, L. M.; Gagliardi, L.; Gendron, F.; Giussani, A.; Gonzalez, L.; Grell, G.; Guo, M. Y.; Hoyer, C. E.; Johansson, M.; Keller, S.; Knecht, S.; Kovacevic, G.; Kallman, E.; Li Manni, G.; Lundberg, M.; Ma, Y. J.; Mai, S.; Malhado, J. P.; Malmqvist, P. A.; Marquetand, P.; Mewes, S. A.; Norell, J.; Olivucci, M.; Oppel, M.; Phung, Q. M.; Pierloot, K.; Plasser, F.; Reiher, M.; Sand, A. M.; Schapiro, I.; Sharma, P.; Stein, C. J.; Sorensen, L. K.; Truhlar, D. G.; Ugandi, M.; Ungur, L.; Valentini, A.; Vancoillie, S.; Veryazov, V.; Weser, O.; Wesolowski, T. A.; Widmark, P. O.; Wouters, S.; Zech, A.; Zobel, J. P.; Lindh, R. "OpenMolcas: From Source Code to Insight" *Journal of Chemical Theory and Computation* **2019**, *15*, 5925.

Supplemental Table 3.4: CASSCF parameters of **1**, **2**, and **3** calculated with and without charge-balancing cation. Strikethrough implies calculation completed without charge-balancing cation.

Compound	**KD$_0$, % pure, E (cm^{-1})**	**KD$_1$, % pure, E (cm^{-1})**	**g$_x$**	**g$_y$**	**g$_z$**
[CoCp$^*_2$][ErCOT$_2$]	±15/2, 100, 0	±13/2, 99.8, 157	0.00000859424658	0.00001044867142	17.99084348335763
~~[CoCp$^*_2$]~~[ErCOT$_2$]	±15/2, 100, 0	±13/2, 100, 158	0.00000180716311	0.00000188556934	17.99196343874752
[K-18C6][ErCOT$_2$]	±15/2, 100, 0	±13/2, 99.8, 163	0.00000641824794	0.00000844882880	17.99661106484002
~~[K-18C6]~~[ErCOT$_2$]	±15/2, 99.9, 0	±13/2, 99.9, 164	0.00000678649985	0.00000890859666	17.99420531284822
[K-k222][ErCOT$_2$]	±15/2, 100, 0	±13/2, 99.9, 157	0.00000306657380	0.00000517739152	17.99399046042119
~~[K-k222]~~[ErCOT$_2$]	±15/2, 100, 0	±13/2, 100, 158	0.00000596522543	0.00000668636035	17.99423191521609

3.6.3 Curve Fitting & Analysis

Overview:

A quantitative peak fitting analysis of isothermal magnetization curves involved fitting the data to a modified Cauchy Distribution. This fitting process parameterized the magnetization curves to enable a comparative analysis.[s] The modified Cauchy Distribution fits allow for deconvolution of multiple magnetic phases and/or transitions, providing insights into each magnetic transition through statistical values. Parameters such as peak width, intensity, location, and percentage based on the area under the curve are reported. Notably, this analysis condenses the magnetization curve into its gamma parameter, representing the half-width at half-maximum of the peak. Conclusions about the nature of the process occurring at that magnetic field can be drawn based on these statistical values.

Methods:

For each sample, magnetization curves were normalized to the maximum magnetization at 2 K. For all samples and temperatures, three inflection points (peaks) were detected. The data were fit to a combination of three unique Cauchy cumulative distribution functions (CDF), Equation S.3.2. To better illustrate the temperature dependency and subtle variations in peaks, the fit parameters were applied to the probability density function (PDF) formulation of the Cauchy distribution and plotted utilizing open-access software *multi_Cauchy*.[t] The *multi_Cauchy* code package and all applicable documentation is available at https://doi.org/10.5281/zenodo.8299498, under the MIT license.

---

[s] Kirkpatrick, K. M.; Zhou, B. H.; Bunting, P. C.; Rinehart, J. D. "Quantifying superparamagnetic signatures in nanoparticle magnetite: a generalized approach for physically meaningful statistics and synthesis diagnostics" *Chem Sci* **2023.**

[t] Bunting, P. C.; Rinehart, J. D.; v0.2.0 ed. Zenodo, 2023.

$$M(H;\ H_P,\gamma\ ) = \frac{2M_S}{\pi} arctan\left(\frac{H-H_P}{\gamma}\right)\ \ (Eq.\ S.3.2)$$

Equation S.3.2. Modified Cauchy distribution function (CDF), where *H* is the applied field, H_P is the field at which a particular demagnetization (peak) maximum occurs, γ is the broadness parameter, and M_S is the saturation magnetization.

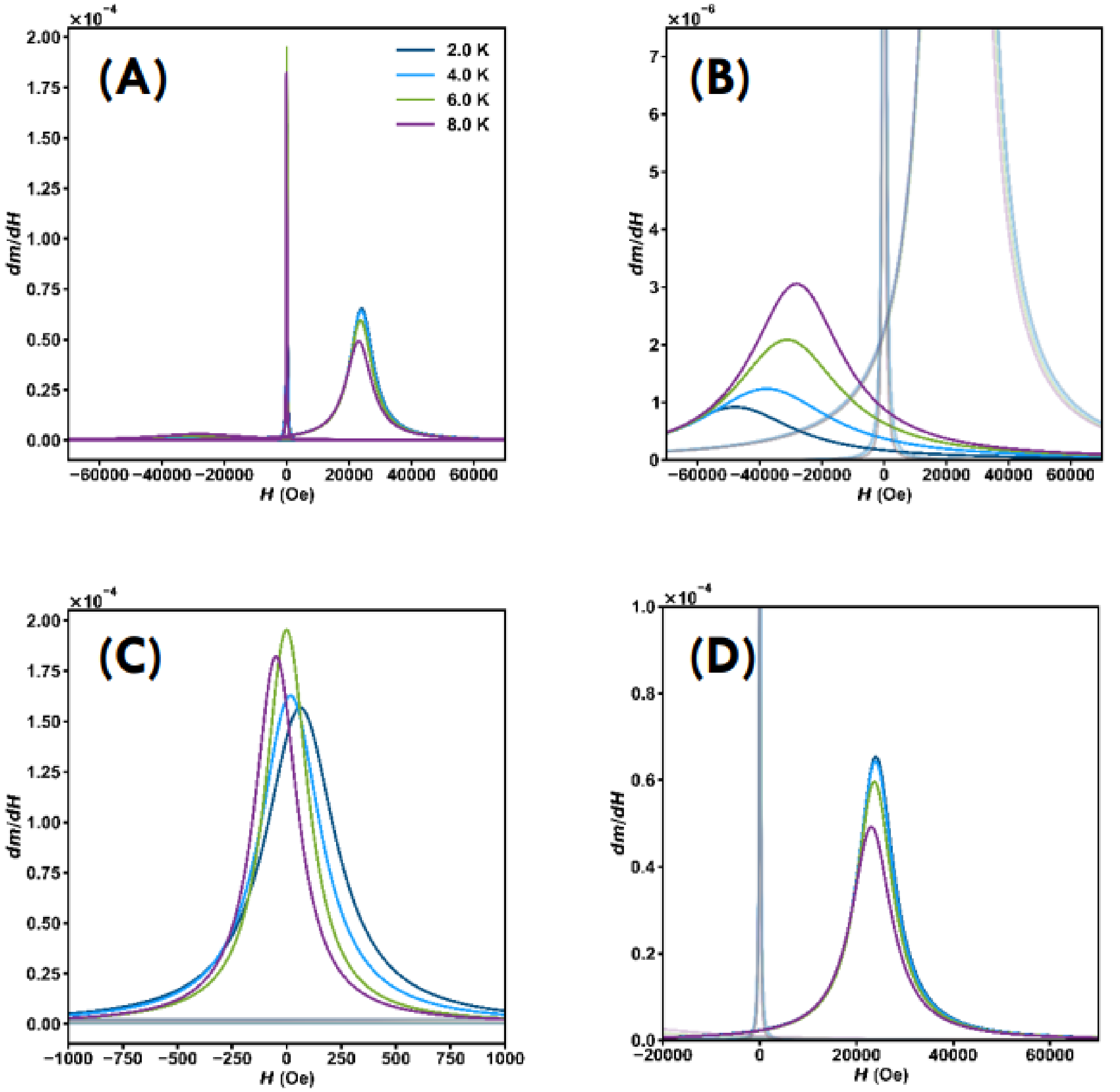

Supplemental Figure 3.38: Cauchy fits of isothermal magnetization loops collected at T = 2, 4, 6, and 8 K of **1**. (a) Fits of all three processes. (b) Zoom of process 1. (c) Zoom of process 2. (d) Zoom of process 3.

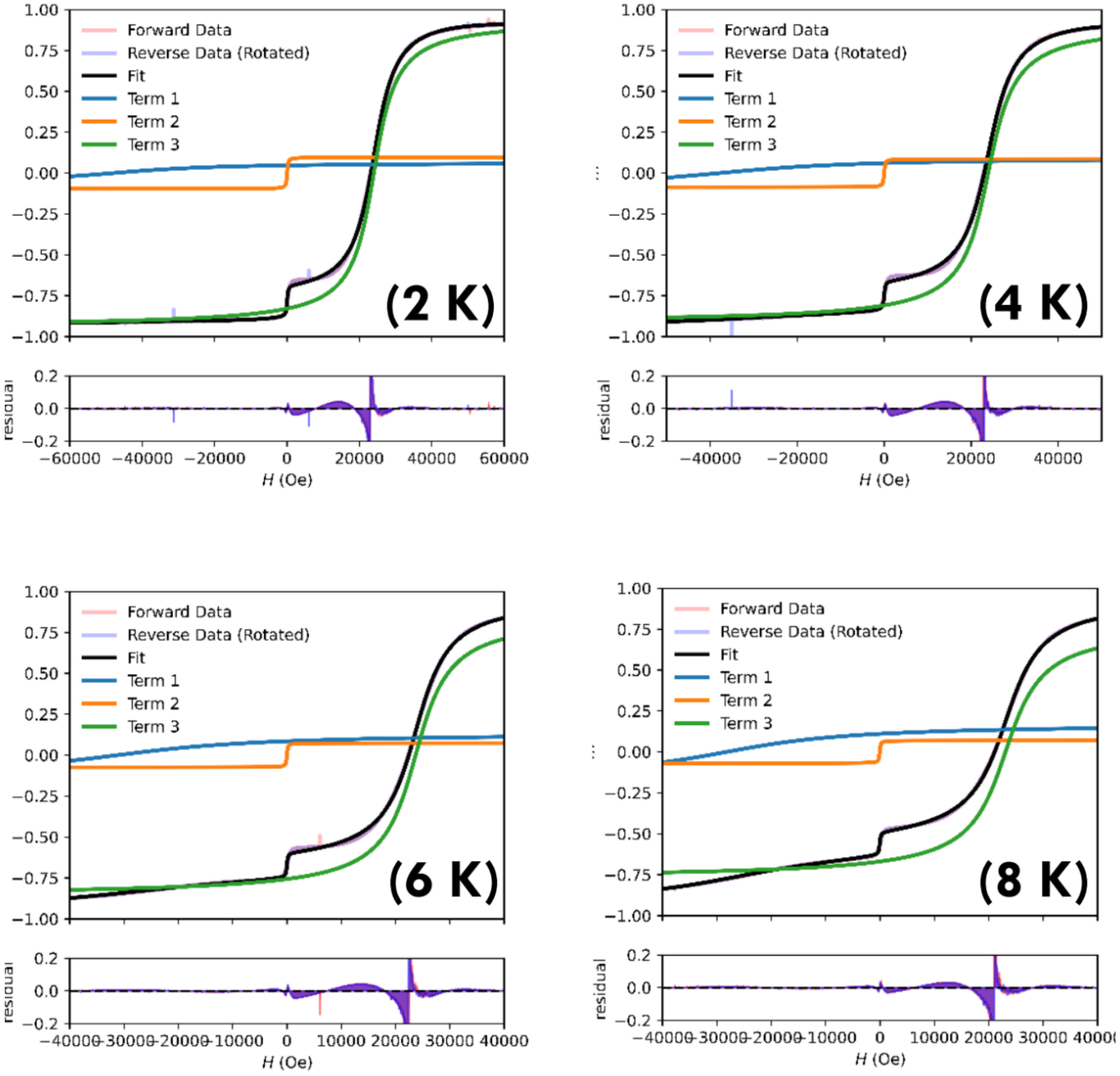

Supplemental Figure 3.39: Cauchy fits of isothermal magnetization loops collected at T = 2, 4, 6, and 8 K of **1**, showing contributions of each term (process). Residuals are demonstrated below each graph.

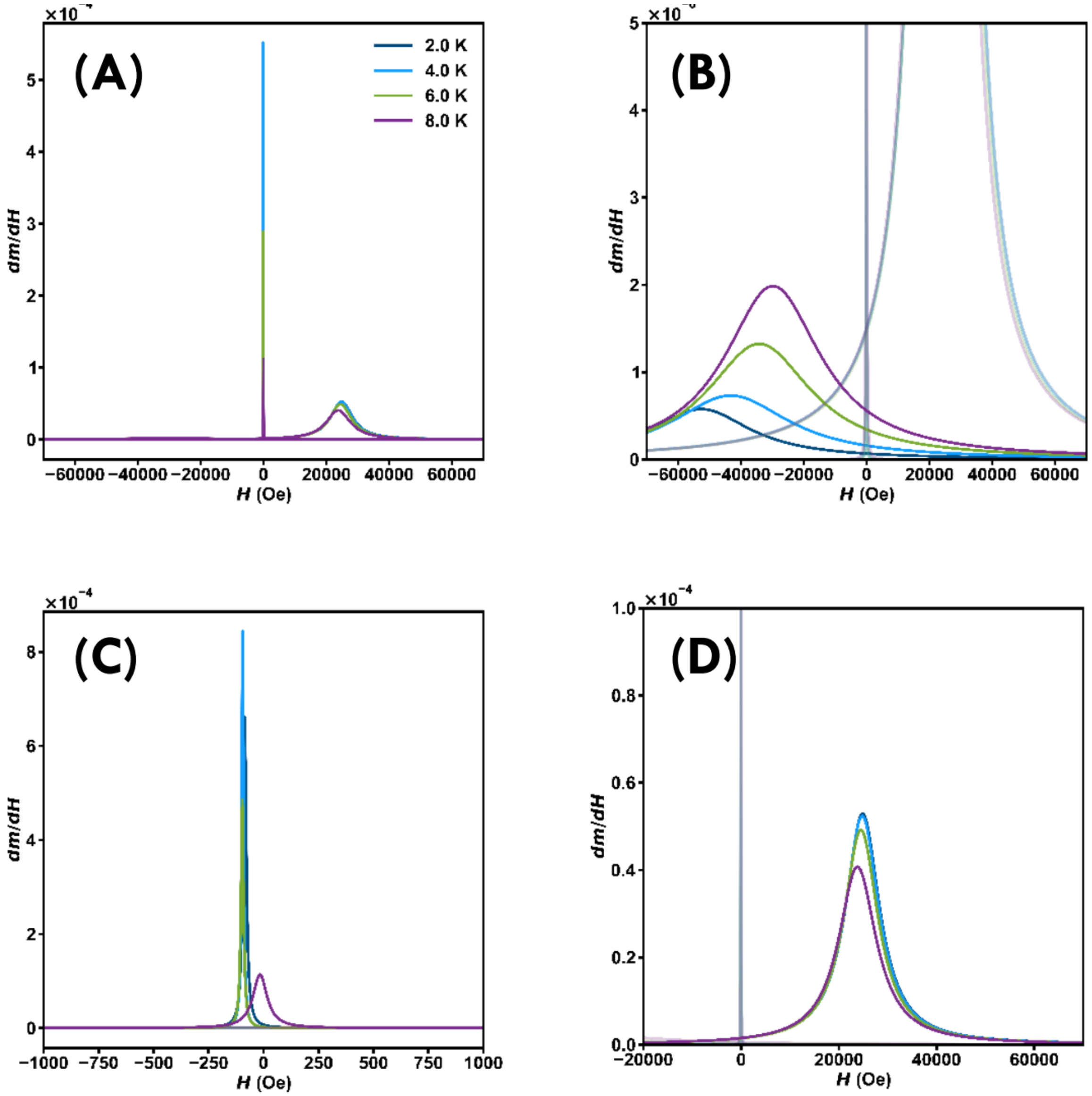

Supplemental Figure 3.40: Cauchy fits of isothermal magnetization loops collected at *T* = 2, 4, 6, and 8 K of **1-Y**. (a) Fits of all three processes. (b) Zoom of process 1. (c) Zoom of process 2. (d) Zoom of process 3.

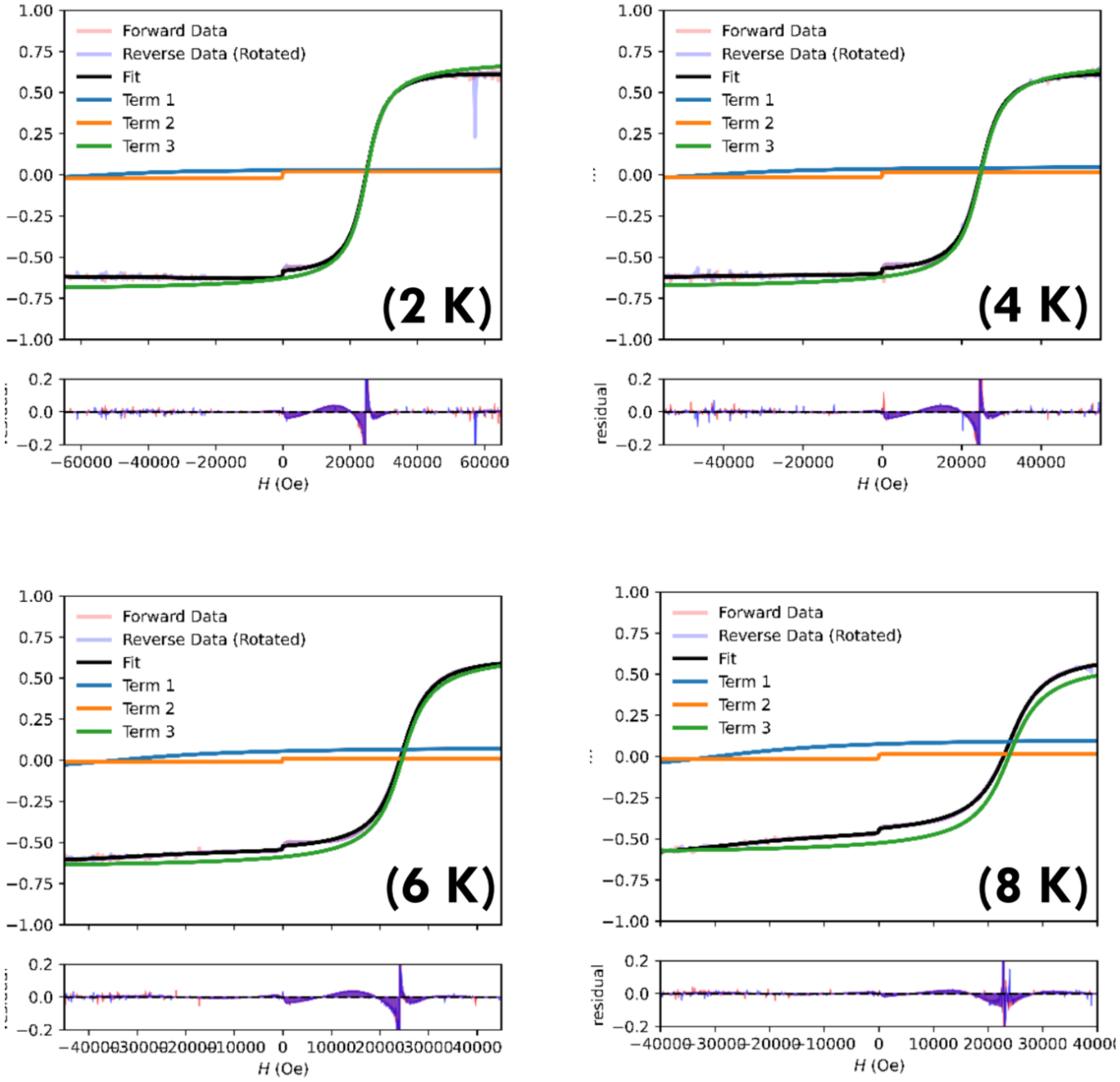

Supplemental Figure 3.41: Cauchy fits of isothermal magnetization loops collected at T = 2, 4, 6, and 8 K of **1-Y**, showing contributions of each term (process). Residuals are demonstrated below each graph.

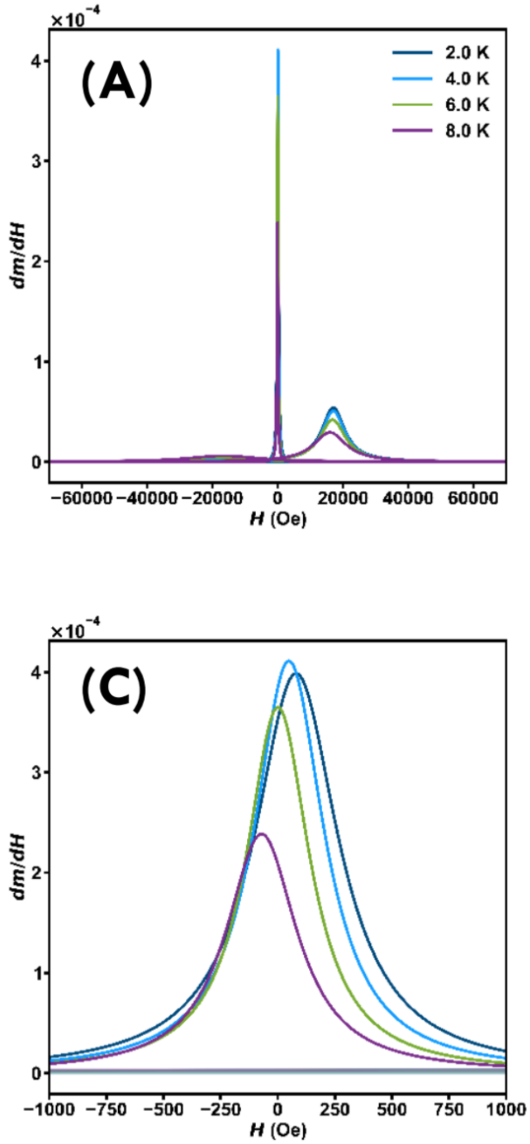

Supplemental Figure 3.42: Cauchy fits of isothermal magnetization loops collected at *T* = 2, 4, 6, and 8 K of **2**. (a) Fits of all three processes. (b) Zoom of process 1. (c) Zoom of process 2. (d) Zoom of process 3.

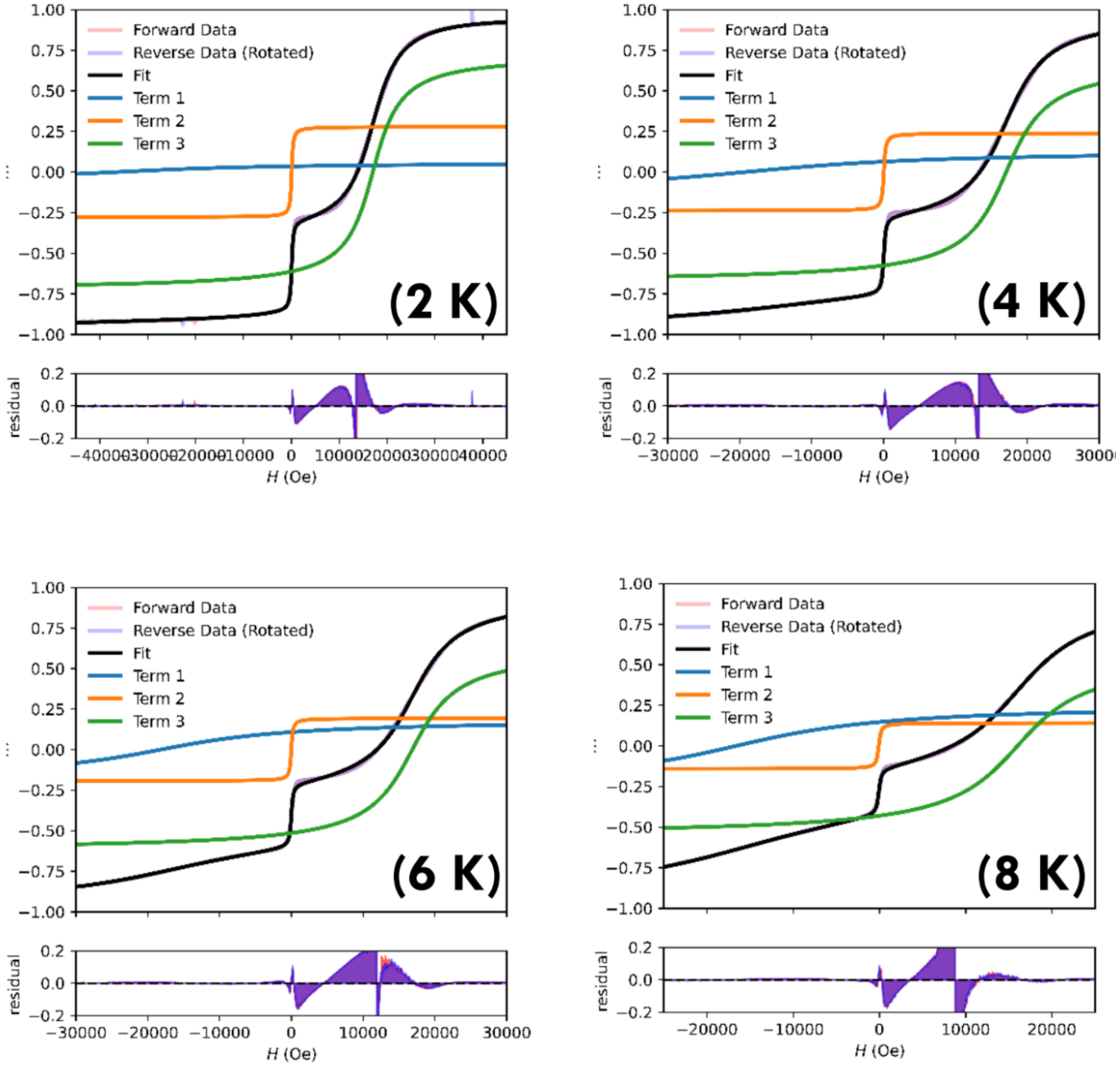

Supplemental Figure 3.43: Cauchy fits of isothermal magnetization loops collected at T = 2, 4, 6, and 8 K of **2**, showing contributions of each term (process). Residuals are demonstrated below each graph.

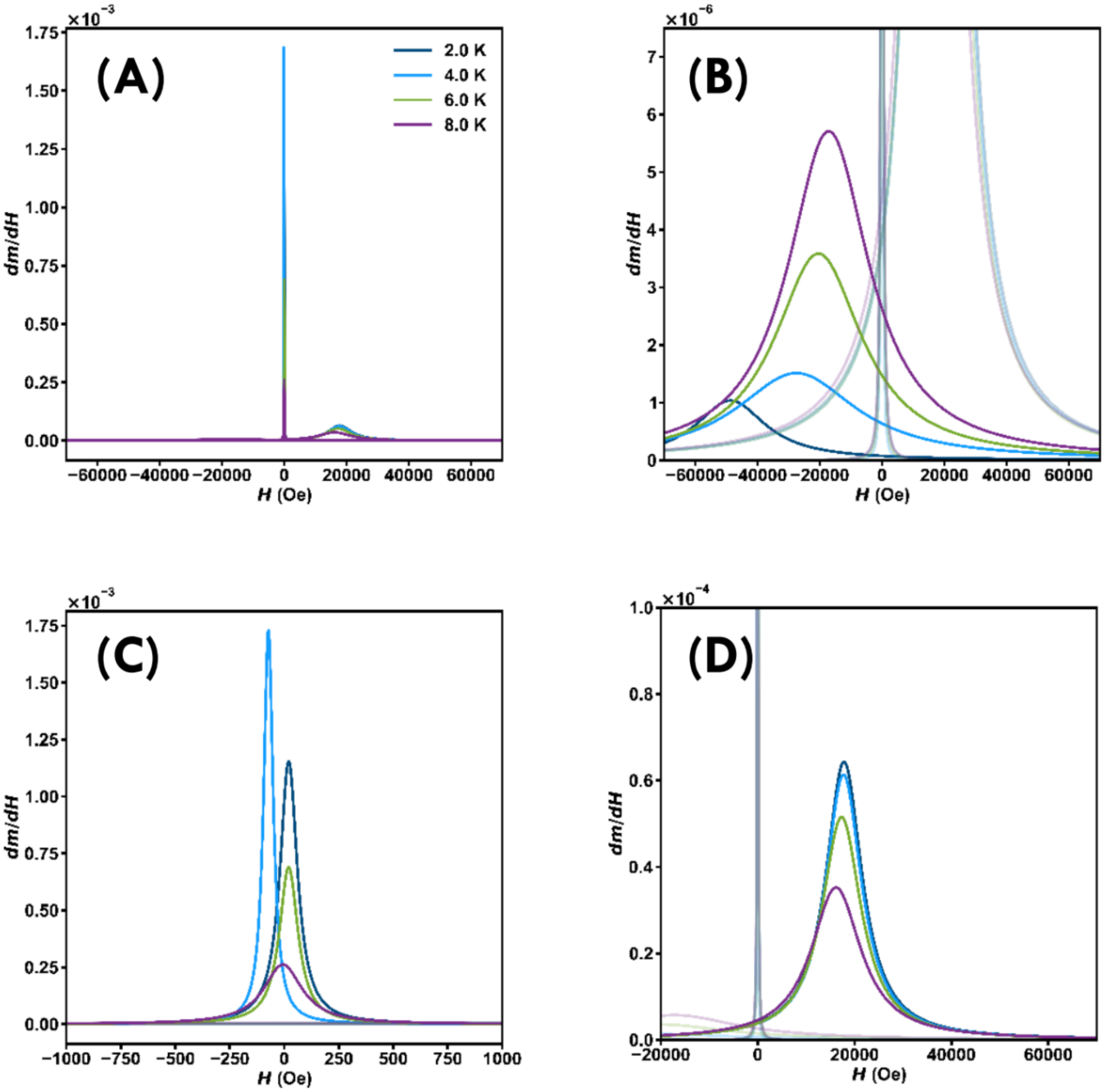

Supplemental Figure 3.44: Cauchy fits of isothermal magnetization loops collected at T = 2, 4, 6, and 8 K of **2-Y**. (a) Fits of all three processes. (b) Zoom of process 1. (c) Zoom of process 2. (d) Zoom of process 3.

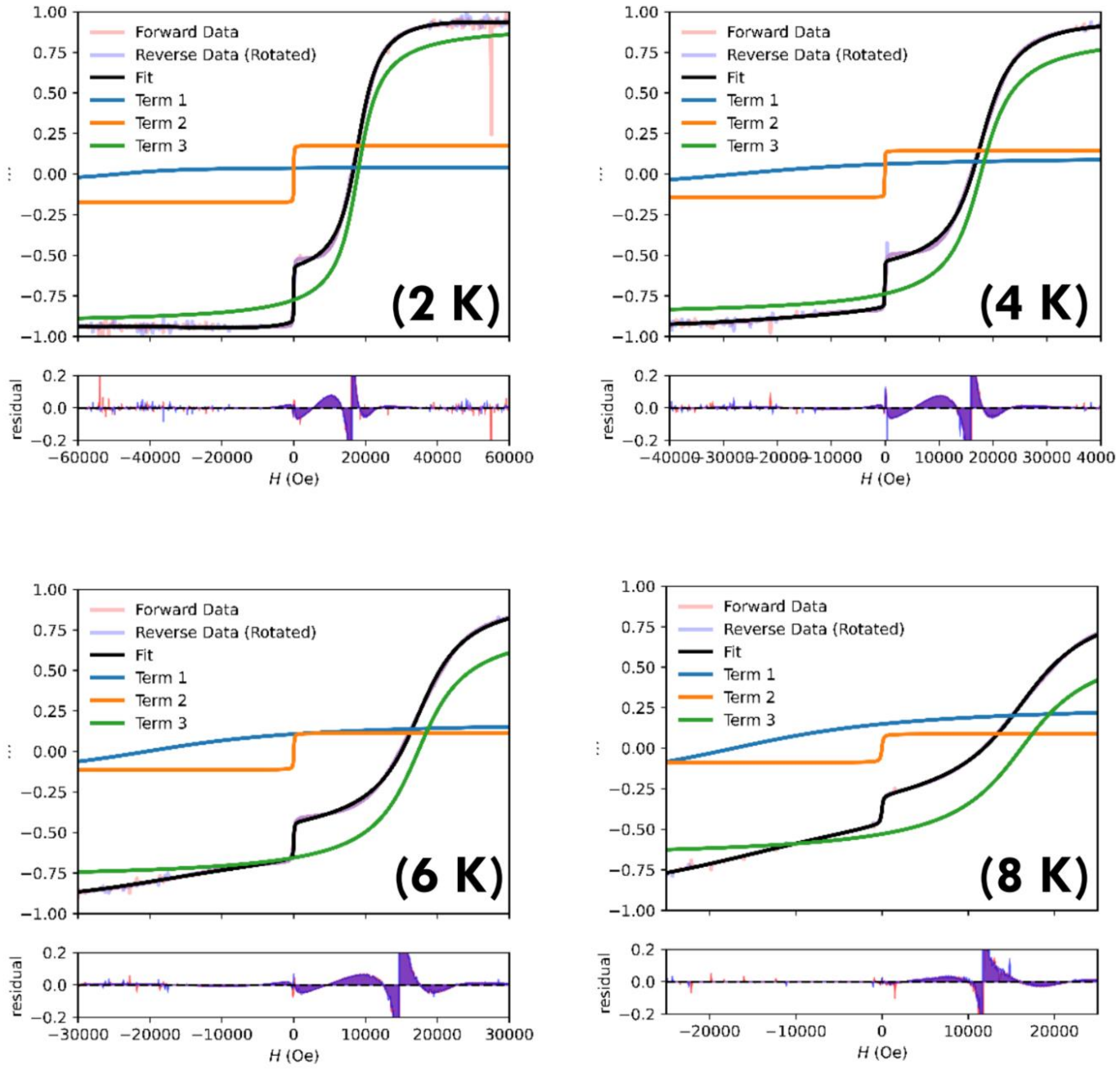

Supplemental Figure 3.45: Cauchy fits of isothermal magnetization loops collected at T = 2, 4, 6, and 8 K of **2-Y**, showing contributions of each term (process). Residuals are demonstrated below each graph.

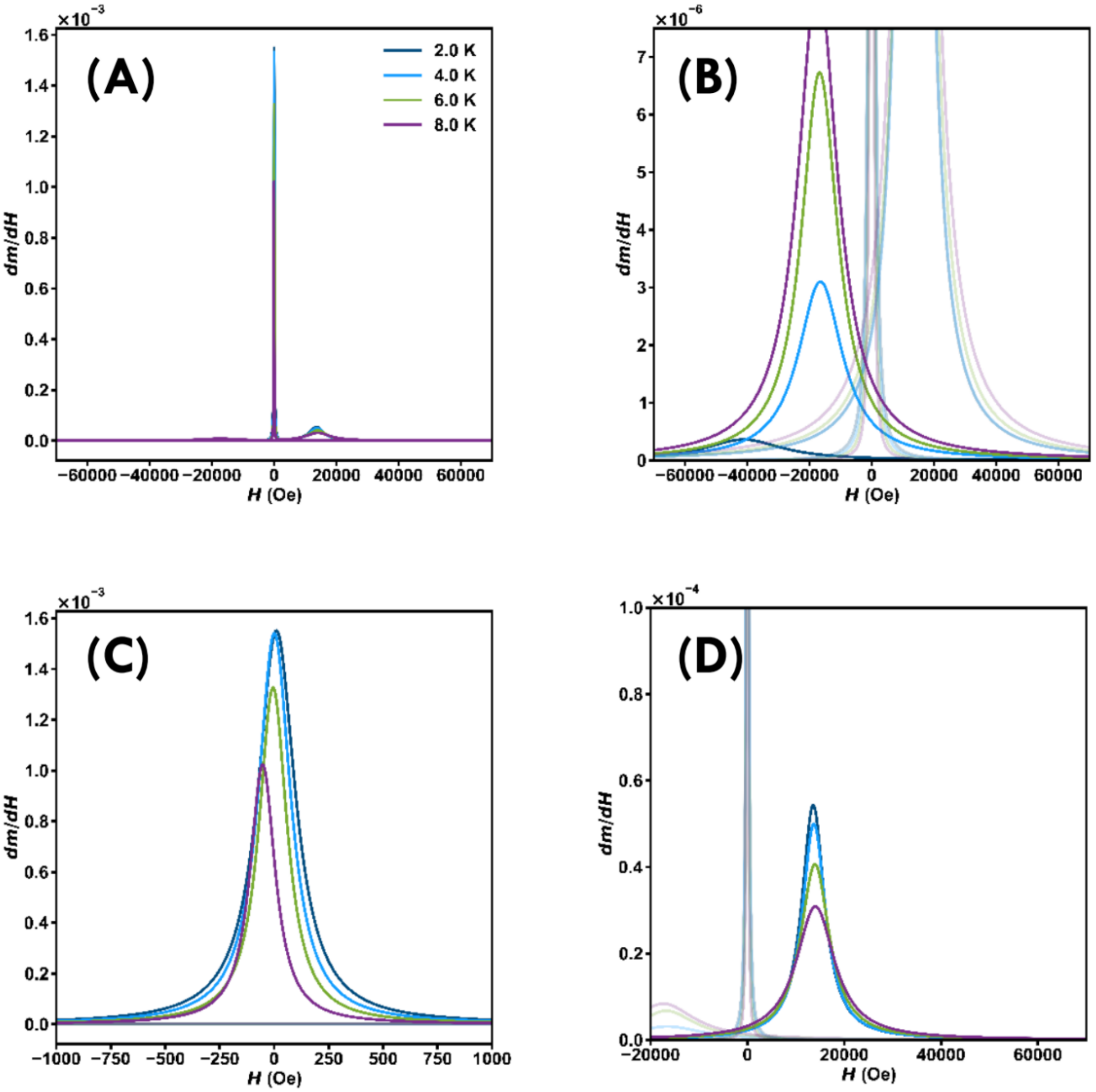

Supplemental Figure 3.46: Cauchy fits of isothermal magnetization loops collected at *T* = 2, 4, 6, and 8 K of **3**. (a) Fits of all three processes. (b) Zoom of process 1. (c) Zoom of process 2. (d) Zoom of process 3.

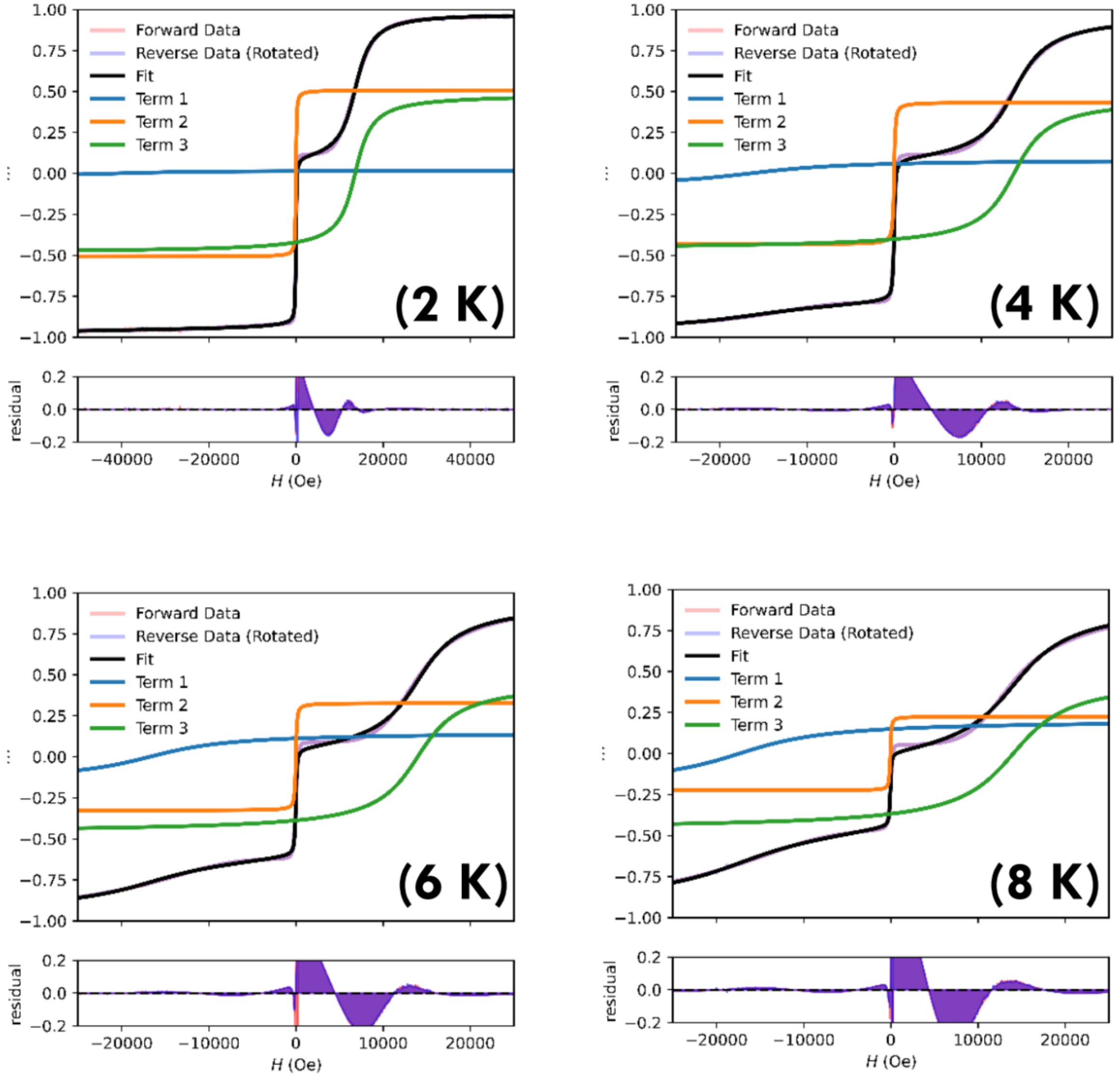

Supplemental Figure 3.47: Cauchy fits of isothermal magnetization loops collected at T = 2, 4, 6, and 8 K of **3**, showing contributions of each term (process). Residuals are demonstrated below each graph.

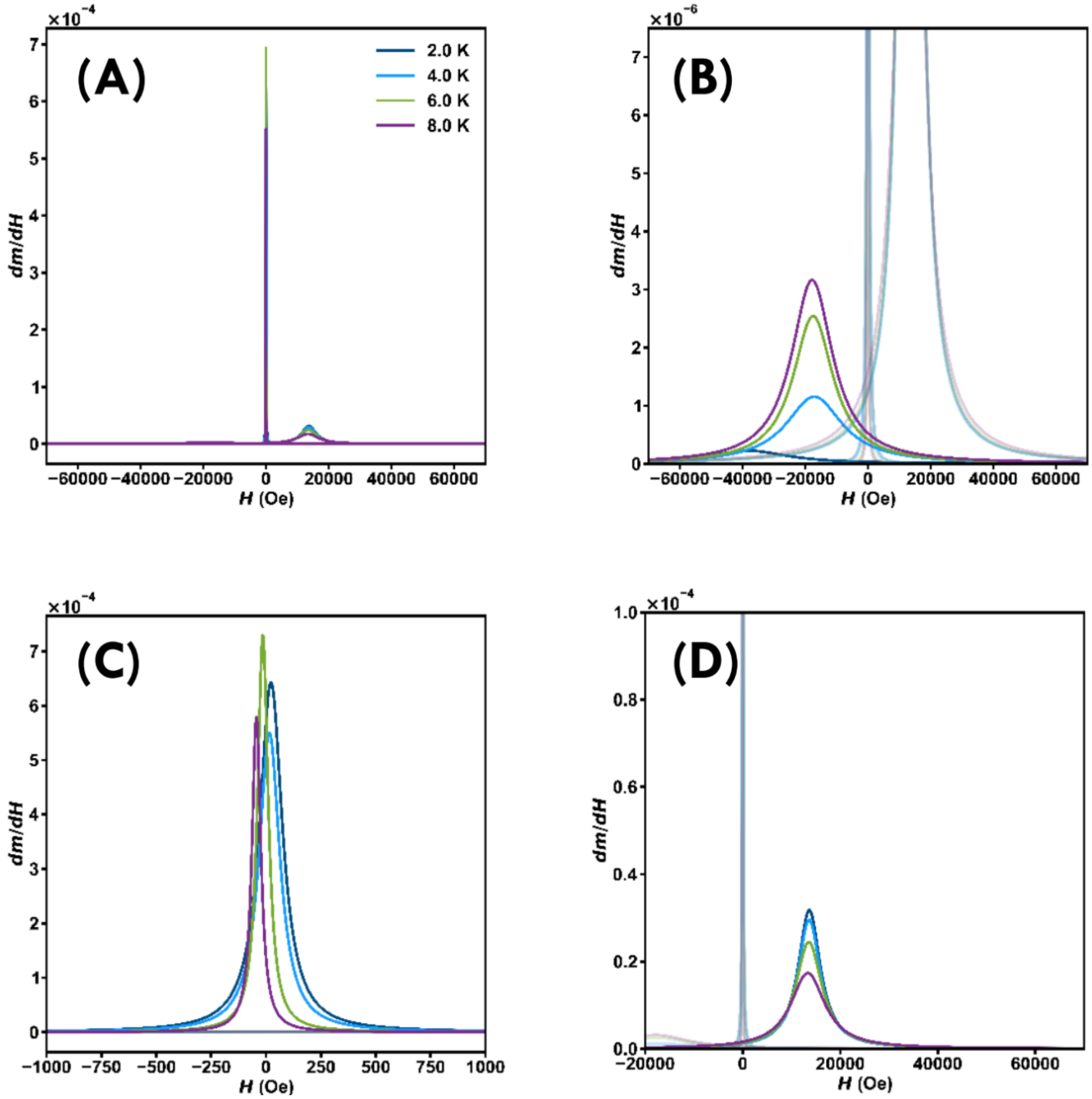

Supplemental Figure 3.48: Cauchy fits of isothermal magnetization loops collected at *T* = 2, 4, 6, and 8 K of **3-Y**. (a) Fits of all three processes. (b) Zoom of process 1. (c) Zoom of process 2. (d) Zoom of process 3.

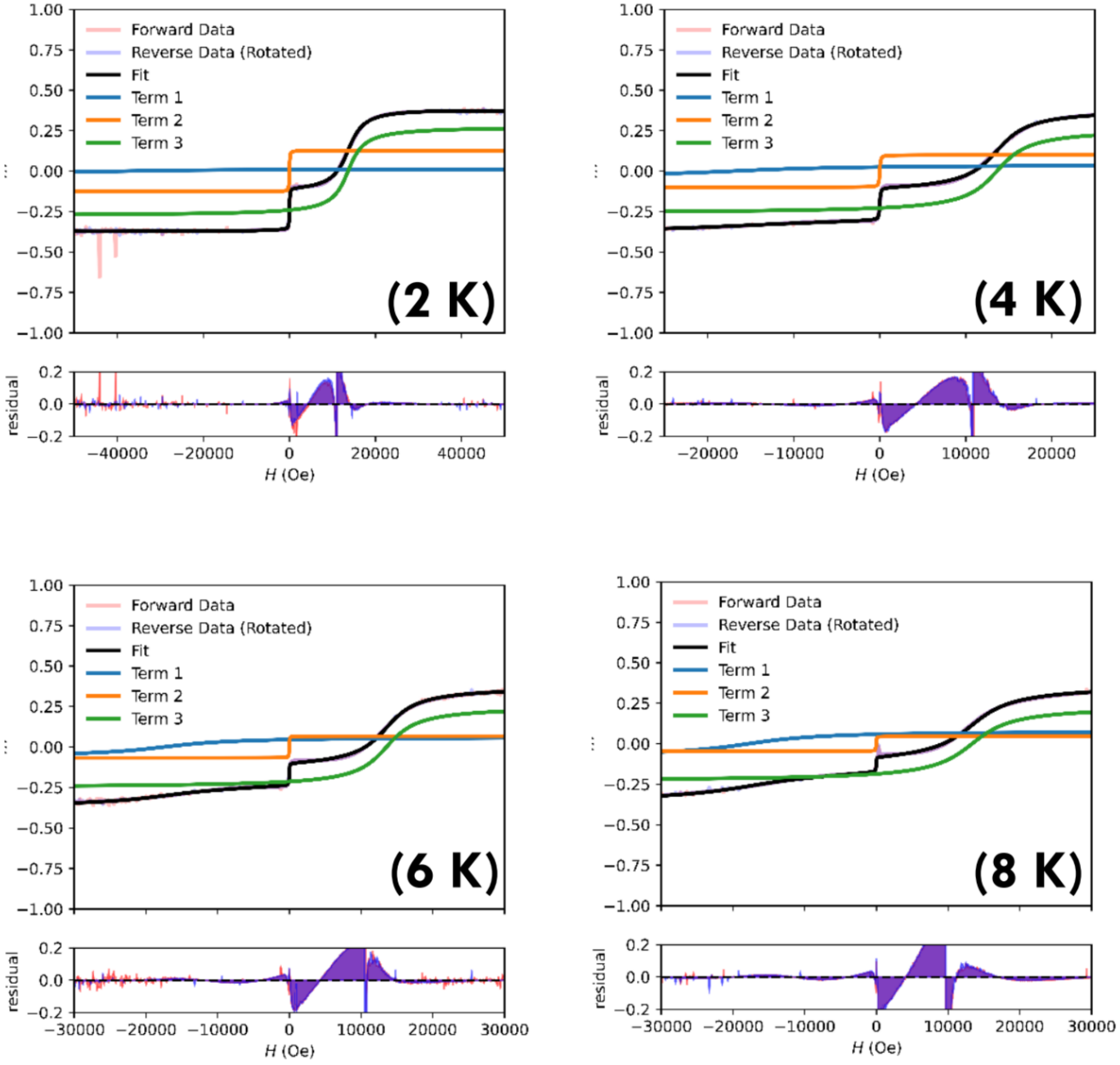

Supplemental Figure 3.49: Cauchy fits of isothermal magnetization loops collected at T = 2, 4, 6, and 8 K of **3-Y**, showing contributions of each term (process). Residuals are demonstrated below each graph.

Supplemental Table 3.5: Fit parameters arising from Cauchy fitments completed on **1**.

Temp. (K)	M_S Peak 1	M_S error Peak 1	M_S Peak 2	M_S error Peak 2	M_S Peak 3	M_S error Peak 3	H_P Peak 1	H_P error Peak 1	H_P Peak 2	H_P error Peak 2	H_P Peak 3	H_P error Peak 3
2	0.065	0.001	0.096	0.000	0.943	0.001	-47841	550	62	11	24004	7
4	0.096	0.002	0.086	0.001	0.919	0.002	-37779	409	17	11	23923	7
6	0.136	0.002	0.074	0.001	0.862	0.001	-31173	226	-1	13	23694	7
8	0.173	0.001	0.069	0.000	0.775	0.001	-28147	101	-49	9	23075	6
Temp. (K)	γ Peak 1	γ error Peak 1	γ Peak 2	γ error Peak 2	γ Peak 3	γ error Peak 3	Max Height Peak 1	Max Height Peak 2	Max Height Peak 3	Percent Contrib. Peak 1	Percent Contrib. Peak 2	Percent Contrib. Peak 3
2	22697	691	195	12	4592	15	9.17E-07	1.57E-04	6.54E-05	4.3	9.2	86.5
4	24882	612	168	13	4548	16	1.23E-06	1.63E-04	6.43E-05	6.7	8.3	85.0
6	20748	304	120	12	4609	15	2.09E-06	1.95E-04	5.95E-05	10.6	7.4	82.1
8	18001	127	120	10	5018	12	3.05E-06	1.82E-04	4.92E-05	14.9	7.3	77.9

Supplemental Table 3.6: Fit parameters arising from Cauchy fitments completed on **1-Y**.

Temp. (K)	M_S Peak 1	M_S error Peak 1	M_S Peak 2	M_S error Peak 2	M_S Peak 3	M_S error Peak 3	H_P Peak 1	H_P error Peak 1	H_P Peak 2	H_P error Peak 2	H_P Peak 3	H_P error Peak 3
2	0.035	0.002	0.019	0.000	0.705	0.002	-52587	1159	-86	12	24849	11
4	0.052	0.001	0.014	0.000	0.695	0.001	-43261	580	-95	4	24770	8
6	0.084	0.002	0.011	0.000	0.661	0.002	-34162	357	-97	9	24502	10
8	0.116	0.001	0.014	0.000	0.600	0.001	-29836	130	-16	13	23796	6
Temp. (K)	γ Peak 1	γ error Peak 1	γ Peak 2	γ error Peak 2	γ Peak 3	γ error Peak 3	Max Height Peak 1	Max Height Peak 2	Max Height Peak 3	Percent Contrib. Peak 1	Percent Contrib. Peak 2	Percent Contrib. Peak 3
2	19119	1272	9	19	4246	23	5.76E-07	5.01E-04	5.29E-05	3.3	2.6	94.1
4	22810	786	5	0	4226	17	7.32E-07	5.52E-04	5.24E-05	5.2	1.8	92.9
6	20212	511	7	18	4279	21	1.32E-06	2.89E-04	4.91E-05	9.2	1.4	89.4
8	18669	171	39	18	4687	13	1.99E-06	1.12E-04	4.07E-05	13.8	2.1	84.2

Supplemental Table 3.7: Fit parameters arising from Cauchy fitments completed on **2**.

Temp. (K)	M_S Peak 1	M_S error Peak 1	M_S Peak 2	M_S error Peak 2	M_S Peak 3	M_S error Peak 3	H_P Peak 1	H_P error Peak 1	H_P Peak 2	H_P error Peak 2	H_P Peak 3	H_P error Peak 3
2	0.058	0.002	0.278	0.001	0.726	0.001	-36199	725	81	4	17031	10
4	0.133	0.003	0.239	0.001	0.682	0.002	-19156	435	49	4	17066	10
6	0.185	0.002	0.193	0.001	0.623	0.001	-18204	134	1	4	16846	10
8	0.259	0.001	0.142	0.000	0.558	0.001	-16592	55	-71	3	16006	8
Temp. (K)	γ Peak 1	γ error Peak 1	γ Peak 2	γ error Peak 2	γ Peak 3	γ error Peak 3	Max Height Peak 1	Max Height Peak 2	Max Height Peak 3	Percent Contrib. Peak 1	Percent Contrib. Peak 2	Percent Contrib. Peak 3
2	25118	1047	222	5	4272	19	7.31E-07	3.99E-04	5.41E-05	4.1	27.3	68.5
4	20472	442	185	5	4276	19	2.07E-06	4.11E-04	5.08E-05	10.7	23.9	65.4
6	14031	147	168	5	4716	18	4.21E-06	3.64E-04	4.20E-05	16.9	20.3	62.7
8	13422	62	189	4	6030	15	6.15E-06	2.38E-04	2.94E-05	25.3	15.8	58.9

Supplemental Table 3.8: Fit parameters arising from Cauchy fitments completed on **2-Y**.

Temp. (K)	M_S Peak 1	M_S error Peak 1	M_S Peak 2	M_S error Peak 2	M_S Peak 3	M_S error Peak 3	H_P Peak 1	H_P error Peak 1	H_P Peak 2	H_P error Peak 2	H_P Peak 3	H_P error Peak 3
2	0.045	0.002	0.175	0.001	0.923	0.004	-48635	1004	21	7	17808	20
4	0.112	0.003	0.143	0.001	0.878	0.002	-27547	628	-73	10	17707	12
6	0.192	0.002	0.112	0.001	0.796	0.002	-20456	229	20	5	17311	12
8	0.284	0.002	0.088	0.001	0.692	0.002	-17161	135	-6	10	16170	14
Temp. (K)	γ Peak 1	γ error Peak 1	γ Peak 2	γ error Peak 2	γ Peak 3	γ error Peak 3	Max Height Peak 1	Max Height Peak 2	Max Height Peak 3	Percent Contrib. Peak 1	Percent Contrib. Peak 2	Percent Contrib. Peak 3
2	13669	1228	48	10	4568	39	1.04E-06	1.15E-03	6.43E-05	3.2	16.0	80.8
4	23508	781	26	7	4555	24	1.51E-06	1.68E-03	6.13E-05	8.0	13.4	78.6
6	17046	248	52	7	4919	23	3.58E-06	6.89E-04	5.15E-05	15.6	10.9	73.6
8	15832	139	108	11	6257	27	5.71E-06	2.61E-04	3.52E-05	24.6	9.0	66.4

Supplemental Table 3.9: Fit parameters arising from Cauchy fitments completed on **3**.

Temp. (K)	M_S Peak 1	M_S error Peak 1	M_S Peak 2	M_S error Peak 2	M_S Peak 3	M_S error Peak 3	H_P Peak 1	H_P error Peak 1	H_P Peak 2	H_P error Peak 2	H_P Peak 3	H_P error Peak 3
2	0.017	0.001	0.508	0.001	0.484	0.001	-41179	996	11	1	13591	10
4	0.084	0.001	0.434	0.001	0.464	0.001	-16506	172	1	1	13742	11
6	0.150	0.001	0.327	0.001	0.463	0.001	-16752	91	-5	2	13959	16
8	0.204	0.002	0.225	0.001	0.466	0.002	-17335	82	-53	4	14043	23

Temp. (K)	γ Peak 1	γ error Peak 1	γ Peak 2	γ error Peak 2	γ Peak 3	γ error Peak 3	Max Height Peak 1	Max Height Peak 2	Max Height Peak 3	Percent Contrib. Peak 1	Percent Contrib. Peak 2	Percent Contrib. Peak 3
2	15273	1404	104	2	2834	18	3.61E-07	1.55E-03	5.43E-05	1.4	51.2	47.4
4	8667	215	90	2	2957	17	3.10E-06	1.53E-03	5.00E-05	8.0	45.0	46.9
6	7111	124	78	3	3626	25	6.73E-06	1.33E-03	4.06E-05	15.3	35.8	48.9
8	7737	114	70	4	4800	39	8.38E-06	1.02E-03	3.09E-05	22.0	26.2	51.8

Supplemental Table 3.10: Fit parameters arising from Cauchy fitments completed on **3-Y**.

Temp. (K)	M_S Peak 1	M_S error Peak 1	M_S Peak 2	M_S error Peak 2	M_S Peak 3	M_S error Peak 3	H_P Peak 1	H_P error Peak 1	H_P Peak 2	H_P error Peak 2	H_P Peak 3	H_P error Peak 3
2	0.011	0.001	0.127	0.000	0.276	0.001	-38235	1564	23	4	13651	18
4	0.040	0.001	0.099	0.000	0.262	0.001	-17144	310	16	3	13621	12
6	0.062	0.001	0.067	0.001	0.252	0.001	-17505	223	-14	4	13543	25
8	0.079	0.001	0.044	0.000	0.232	0.001	-17815	128	-44	4	13345	25

Temp. (K)	γ Peak 1	γ error Peak 1	γ Peak 2	γ error Peak 2	γ Peak 3	γ error Peak 3	Max Height Peak 1	Max Height Peak 2	Max Height Peak 3	Percent Contrib. Peak 1	Percent Contrib. Peak 2	Percent Contrib. Peak 3
2	15588	2238	63	5	2767	29	2.25E-07	6.42E-04	3.18E-05	2.2	31.3	66.5
4	10943	359	58	4	2830	19	1.15E-06	5.45E-04	2.95E-05	9.1	25.5	65.4
6	7731	297	29	6	3280	41	2.54E-06	6.94E-04	2.44E-05	15.5	18.3	66.2
8	7971	171	24	5	4260	41	3.16E-06	5.52E-04	1.73E-05	21.5	13.0	65.5

3.7 Acknowledgements

Chapter 3 is directly adapted from material as it appears in the Journal of the American Chemical Society: Orlova, A.P., Varley, M.S., Bernbeck, M.G., Kirkpatrick, K.M., Bunting, P.C., Gembicky, M., Rinehart, J.D., "Molecular Network Approach to Anisotropic Ising Lattices: Parsing Magnetization Dynamics in Erbium Systems with 0-3 Dimensional Spin Interactivity," *J. Amer. Chem. Soc.* **2023**. 145 (40), 22265. The dissertation author was the primary researcher and author of this paper.

3.8 References

(1) Goodwin, C. A. P.; Ortu, F.; Reta, D.; Chilton, N. F.; Mills, D. P. "Molecular magnetic hysteresis at 60 kelvin in dysprosocenium" *Nature* **2017**, *548*, 439.

(2) Gould, C. A.; McClain, K. R.; Reta, D.; Kragskow, J. G. C.; Marchiori, D. A.; Lachman, E.; Choi, E. S.; Analytis, J. G.; Britt, R. D.; Chilton, N. F.; Harvey, B. G.; Long, J. R. "Ultrahard magnetism from mixed-valence dilanthanide complexes with metal-metal bonding" *Science* **2022**, *375*, 198.

(3) Guo, F. S.; Day, B. M.; Chen, Y. C.; Tong, M. L.; Mansikkamaki, A.; Layfield, R. A. "Magnetic hysteresis up to 80 kelvin in a dysprosium metallocene single-molecule magnet" *Science* **2018**, *362*, 1400.

(4) Ishikawa, N. "Single molecule magnet with single lanthanide ion" *Polyhedron* **2007**, *26*, 2147.

(5) Mertes, K. M.; Suzuki, Y.; Sarachik, M. P.; Myasoedov, Y.; Shtrikman, H.; Zeldov, E.; Rumberger, E. M.; Hendrickson, D. N.; Christou, G. "Mn12-acetate: a prototypical single molecule magnet" *Solid State Communications* **2003**, *127*, 131.

(6) Christou, G.; Gatteschi, D.; Hendrickson, D. N.; Sessoli, R. "Single-Molecule Magnets" *MRS Bulletin* **2000**, *25*, 66.

(7) Woodruff, D. N.; Winpenny, R. E. P.; Layfield, R. A. "Lanthanide Single-Molecule Magnets" *Chemical Reviews* **2013**, *113*, 5110.

(8) Chen, Y.-C.; Tong, M.-L. "Single-molecule magnets beyond a single lanthanide ion: the art of coupling" *Chem Sci* **2022**, *13*, 8716.

(9) Jiang, S.-D.; Wang, B.-W.; Sun, H.-L.; Wang, Z.-M.; Gao, S. "An Organometallic Single-Ion Magnet" *J Am Chem Soc* **2011**, *133*, 4730.

(10) Ungur, L.; Le Roy, J. J.; Korobkov, I.; Murugesu, M.; Chibotaru, L. F. "Fine-tuning the Local Symmetry to Attain Record Blocking Temperature and Magnetic Remanence in a Single-Ion Magnet**" *Angew Chem Int Edit* **2014**, *53*, 4413.

(11) Bogani, L.; Wernsdorfer, W. "Molecular spintronics using single-molecule magnets" *Nat Mater* **2008**, *7*, 179.

(12) Ganzhorn, M.; Wernsdorfer, W. "Molecular Quantum Spintronics Using Single-Molecule Magnets" *Nanosci Technol* **2014**, 319.

(13) Hymas, K.; Soncini, A. "Molecular spintronics using single-molecule magnets under irradiation" *Phys Rev B* **2019**, *99*.

(14) Jenkins, M.; Hummer, T.; Martinez-Perez, M. J.; Garcia-Ripoll, J.; Zueco, D.; Luis, F. "Coupling single-molecule magnets to quantum circuits" *New J Phys* **2013**, *15*.

(15) Natterer, F. D.; Yang, K.; Paul, W.; Willke, P.; Choi, T. Y.; Greber, T.; Heinrich, A. J.; Lutz, C. P. "Reading and writing single-atom magnets" *Nature* **2017**, *543*, 226.

(16) Wang, Y. C.; Hu, Z. X.; Sanders, B. C.; Kais, S. "Qudits and High-Dimensional Quantum Computing" *Front Phys-Lausanne* **2020**, *8*.

(17) Briganti, M.; Santanni, F.; Tesi, L.; Totti, F.; Sessoli, R.; Lunghi, A. "A Complete Ab Initio View of Orbach and Raman Spin-Lattice Relaxation in a Dysprosium Coordination Compound" *J Am Chem Soc* **2021**, *143*, 13633.

(18) Kragskow, J. G. C.; Marbey, J.; Buch, C. D.; Nehrkorn, J.; Ozerov, M.; Piligkos, S.; Hill, S.; Chilton, N. F. "Analysis of vibronic coupling in a 4f molecular magnet with FIRMS" *Nature Communications* **2022**, *13*.

(19) Kragskow, J. G. C.; Mattioni, A.; Staab, J. K.; Reta, D.; Skelton, J. M.; Chilton, N. F. "Spin-phonon coupling and magnetic relaxation in single-molecule magnets" *Chemical Society Reviews* **2023**, *52*, 4567.

(20) Lunghi, A.; Totti, F.; Sanvito, S.; Sessoli, R. "Intra-molecular origin of the spin-phonon coupling in slow-relaxing molecular magnets" *Chem Sci* **2017**, *8*, 6051.

(21) Santanni, F.; Albino, A.; Atzori, M.; Ranieri, D.; Salvadori, E.; Chiesa, M.; Lunghi, A.; Bencini, A.; Sorace, L.; Totti, F.; Sessoli, R. "Probing Vibrational Symmetry Effects and Nuclear Spin Economy Principles in Molecular Spin Qubits" *Inorganic Chemistry* **2021**, *60*, 140.

(22) Dubroca, T.; Wang, X. L.; Mentink-Vigier, F.; Trociewitz, B.; Starck, M.; Parker, D.; Sherwin, M. S.; Hill, S.; Krzystek, J. "Terahertz EPR spectroscopy using a 36-tesla high-homogeneity series-connected hybrid magnet" *J Magn Reson* **2023**, *353*.

(23) Ghosh, S.; Datta, S.; Friend, L.; Cardona-Serra, S.; Gaita-Arino, A.; Coronado, E.; Hill, S. "Multi-frequency EPR studies of a mononuclear holmium single-molecule magnet based on the polyoxometalate [Ho-III(W5O18)(2)](9-)" *Dalton Transactions* **2012**, *41*, 13697.

(24) Hill, S.; Perenboom, J. A. A. J.; Dalal, N. S.; Hathaway, T.; Stalcup, T.; Brooks, J. S. "High-sensitivity electron paramagnetic resonance of Mn-12-acetate" *Phys Rev Lett* **1998**, *80*, 2453.

(25) Park, K.; Novotny, M. A.; Dalal, N. S.; Hill, S.; Rikvold, P. A. "Role of dipolar and exchange interactions in the positions and widths of EPR transitions for the single-molecule magnets Fe-8 and Mn-12" *Phys Rev B* **2002**, *66*.

(26) Park, K.; Novotny, M. A.; Dalal, N. S.; Hill, S.; Rikvold, P. A. "Effects of D-strain, g-strain, and dipolar interactions on EPR linewidths of the molecular magnets Fe-8 and Mn-12" *Phys Rev B* **2002**, *65*.

(27) Orlova, A. P.; Hilgar, J. D.; Bernbeck, M. G.; Gembicky, M.; Rinehart, J. D. "Intuitive Control of Low-Energy Magnetic Excitations via Directed Dipolar Interactions in a Series of Er(III)-Based Complexes" *J Am Chem Soc* **2022**, *144*, 11316.

(28) Lu, G.; Liu, Y.; Deng, W.; Huang, G.-Z.; Chen, Y.-C.; Liu, J.-L.; Ni, Z.-P.; Giansiracusa, M.; Chilton, N. F.; Tong, M.-L. "A perfect triangular dysprosium single-molecule magnet with virtually antiparallel Ising-like anisotropy" *Inorganic Chemistry Frontiers* **2020**, *7*, 2941.

(29) Krylov, D.; Velkos, G.; Chen, C. H.; Buchner, B.; Kostanyan, A.; Greber, T.; Avdoshenko, S. M.; Popov, A. A. "Magnetic hysteresis and strong ferromagnetic coupling of sulfur-bridged Dy ions in clusterfullerene Dy2S@C-82" *Inorganic Chemistry Frontiers* **2020**, *7*, 3521.

(30) Bernbeck, M. G.; Hilgar, J. D.; Rinehart, J. D. "Probing axial anisotropy in dinuclear alkoxide-bridged Er-COT single-molecule magnets" *Polyhedron* **2020**, *175*.

(31) Hilgar, J. D.; Bernbeck, M. G.; Flores, B. S.; Rinehart, J. D. "Metal-ligand pair anisotropy in a series of mononuclear Er-COT complexes" *Chem Sci* **2018**, *9*, 7204.

(32) Hilgar, J. D.; Bernbeck, M. G.; Rinehart, J. D. "Million-fold Relaxation Time Enhancement across a Series of Phosphino-Supported Erbium Single-Molecule Magnets" *J Am Chem Soc* **2019**, *141*, 1913.

(33) Hilgar, J. D.; Butts, A. K.; Rinehart, J. D. "A method for extending AC susceptometry to long-timescale magnetic relaxation" *Phys Chem Chem Phys* **2019**, *21*, 22302.

(34) Hilgar, J. D.; Flores, B. S.; Rinehart, J. D. "Ferromagnetic coupling in a chloride-bridged erbium single-molecule magnet" *Chem Commun* **2017**, *53*, 7322.

(35) Le Roy, J. J.; Korobkov, I.; Murugesu, M. "A sandwich complex with axial symmetry for harnessing the anisotropy in a prolate erbium(III) ion" *Chem Commun* **2014**, *50*, 1602.

(36) Le Roy, J. J.; Ungur, L.; Korobkov, I.; Chibotaru, L. F.; Murugesu, M. "Coupling Strategies to Enhance Single-Molecule Magnet Properties of Erbium-Cyclooctatetraenyl Complexes" *J Am Chem Soc* **2014**, *136*, 8003.

(37) Meihaus, K. R.; Long, J. R. "Magnetic Blocking at 10 K and a Dipolar-Mediated Avalanche in Salts of the Bis(eta(8)-cyclooctatetraenide) Complex [Er(COT)(2)](-)" *J Am Chem Soc* **2013**, *135*, 17952.

(38) Xue, T. J.; Ding, Y. S.; Reta, D.; Chen, Q. W.; Zhu, X. F.; Zheng, Z. P. "Closely Related Organometallic Er(III) Single-Molecule Magnets with Sizably Different Relaxation Times of Quantum Tunneling of Magnetization" *Cryst Growth Des* **2022**.

(39) Ising, E. "Beitrag zur Theorie des Ferromagnetismus" *Zeitschrift für Physik* **1925**, *31*, 253.

(40) Fdez. Galván, I.; Vacher, M.; Alavi, A.; Angeli, C.; Aquilante, F.; Autschbach, J.; Bao, J. J.; Bokarev, S. I.; Bogdanov, N. A.; Carlson, R. K.; Chibotaru, L. F.; Creutzberg, J.; Dattani, N.; Delcey, M. G.; Dong, S. S.; Dreuw, A.; Freitag, L.; Frutos, L. M.; Gagliardi, L.; Gendron, F.; Giussani, A.; González, L.; Grell, G.; Guo, M.; Hoyer, C. E.; Johansson, M.; Keller, S.; Knecht, S.; Kovačević, G.; Källman, E.; Li Manni, G.; Lundberg, M.; Ma, Y.; Mai, S.; Malhado, J. P.; Malmqvist, P. Å.; Marquetand, P.; Mewes, S. A.; Norell, J.; Olivucci, M.; Oppel, M.; Phung, Q. M.; Pierloot, K.; Plasser, F.; Reiher, M.; Sand, A. M.; Schapiro, I.; Sharma, P.; Stein, C. J.; Sørensen, L. K.; Truhlar, D. G.; Ugandi, M.; Ungur, L.; Valentini, A.; Vancoillie, S.; Veryazov, V.; Weser, O.; Wesołowski, T. A.; Widmark, P.-O.; Wouters, S.; Zech, A.; Zobel, J. P.; Lindh, R. "OpenMolcas: From Source Code to Insight" *Journal of Chemical Theory and Computation* **2019**, *15*, 5925.

(41) Aquilante, F.; Autschbach, J.; Baiardi, A.; Battaglia, S.; Borin, V. A.; Chibotaru, L. F.; Conti, I.; De Vico, L.; Delcey, M.; Fdez. Galván, I.; Ferré, N.; Freitag, L.; Garavelli, M.; Gong, X.; Knecht, S.; Larsson, E. D.; Lindh, R.; Lundberg, M.; Malmqvist, P. Å.; Nenov, A.; Norell, J.; Odelius, M.; Olivucci, M.; Pedersen, T. B.; Pedraza-González, L.; Phung, Q. M.; Pierloot, K.; Reiher, M.; Schapiro, I.; Segarra-Martí, J.; Segatta, F.; Seijo, L.; Sen, S.; Sergentu, D.-C.; Stein, C. J.; Ungur, L.; Vacher, M.; Valentini, A.; Veryazov, V. "Modern quantum chemistry with [Open]Molcas" *The Journal of Chemical Physics* **2020**, *152*, 214117.

(42) Sheldrick, G. M.; Schneider, T. R. "SHELXL: High-resolution refinement" *Macromolecular Crystallography, Pt B* **1997**, *277*, 319.

(43) Kirkpatrick, K. M.; Zhou, B. H.; Bunting, P.; Rinehart, J. D. "Quantifying superparamagnetic signatures in nanoparticle magnetite: A generalized approach for physically meaningful statistics and synthesis diagnostics" *Chem Sci* **2023**.

(44) Bunting, P. R., Jeffrey; v0.2.0 ed. Zenodo, 2023.

(45) McHugh, S.; Wen, B.; Ma, X.; Sarachik, M. P.; Myasoedov, Y.; Zeldov, E.; Bagai, R.; Christou, G. "Tuning magnetic avalanches in the molecular magnet Mn-12-acetate" *Phys Rev B* **2009**, *79*.

(46) Sarachik, M. P. "Magnetic Avalanches in Molecular Magnets" *Nanosci Technol* **2014**, 113.

(47) Habib, F.; Lin, P. H.; Long, J.; Korobkov, I.; Wernsdorfer, W.; Murugesu, M. "The Use of Magnetic Dilution To Elucidate the Slow Magnetic Relaxation Effects of a Dy-2 Single-Molecule Magnet" *J Am Chem Soc* **2011**, *133*, 8830.

(48) Garanin, D. A. "Dipolar-controlled spin tunneling and relaxation in molecular magnets" *Eur Phys J B* **2012**, *85*.

(49) Ding, Y. S.; Yu, K. X.; Reta, D.; Ortu, F.; Winpenny, R. E. P.; Zheng, Y. Z.; Chilton, N. F. "Field- and temperature-dependent quantum tunnelling of the magnetisation in a large barrier single-molecule magnet" *Nature Communications* **2018**, *9*.

(50) Singh, K.; Mukherjee, K. "Possibility of a new order parameter driven by multipolar moment and Fermi surface evolution in CeGe" *Scientific Reports* **2019**, *9*.

(51) Taniguchi, T.; Hattori, K.; Yoshida, M.; Takeda, H.; Nakamura, S.; Sakakibara, T.; Tsujimoto, M.; Sakai, A.; Matsumoto, Y.; Nakatsuji, S.; Takigawa, M. "Field-Induced Switching of Ferro-Quadrupole Order Parameter in PrTi2Al20" *Journal of the Physical Society of Japan* **2019**, *88*, 084707.

(52) Gemmill, W. R.; Smith, M. D.; Prozorov, R.; Loye, H. C. Z. "Crystal growth and magnetic properties of lanthanide-containing osmium double perovskites, Ln(2)NaOsO(6) (Ln = La, Pr, Nd)" *Inorganic Chemistry* **2005**, *44*, 2639.

(53) Feng, K. K.; Leahy, I. A.; Oladehin, O.; Wei, K. Y.; Lee, M. H. Y.; Baumbach, R. "Magnetic ordering in GdAuAl4Ge2 and TbAuAl4Ge2: Layered compounds with triangular lanthanide nets" *J Magn Magn Mater* **2022**, *564*.

(54) Feng, H. L.; Yamaura, K.; Tjeng, L. H.; Jansen, M. "The role of nonmagnetic d(0) vs. d(10) B-type cations on the magnetic exchange interactions in osmium double perovskites" *J Solid State Chem* **2016**, *243*, 119.

(55) Maharaj, A. V.; Rosenberg, E. W.; Hristov, A. T.; Berg, E.; Fernandes, R. M.; Fisher, I. R.; Kivelson, S. A. "Transverse fields to tune an Ising-nematic quantum phase transition" *P Natl Acad Sci USA* **2017**, *114*, 13430.

(56) Martynov, S. N. "Single-Ion Weak Antiferromagnetism and Spin-Flop Transition in a Two-Sublattice Ferromagnet" *Phys Solid State+* **2020**, *62*, 1165.

(57) Pakhira, S.; Mazumdar, C.; Basu, A.; Ranganathan, R.; Bhowmik, R. N.; Satpati, B. "Unusual bidirectional frequency dependence of dynamical susceptibility in hexagonal intermetallic Pr2Ni0.95Si2.95" *Scientific Reports* **2018**, *8*.

(58) Sarli, N.; Keskin, M. "Two distinct magnetic susceptibility peaks and magnetic reversal events in a cylindrical core/shell spin-1 Ising nanowire" *Solid State Communications* **2012**, *152*, 354.

(59) Shen, Y.; Liu, C. L.; Qin, Y. Y.; Shen, S. D.; Li, Y. D.; Bewley, R.; Schneidewind, A.; Chen, G.; Zhao, J. "Intertwined dipolar and multipolar order in the triangular-lattice magnet TmMgGaO4" *Nature Communications* **2019**, *10*.

(60) Castro-Alvarez, A.; Gil, Y.; Llanos, L.; Aravena, D. "High performance single-molecule magnets, Orbach or Raman relaxation suppression?" *Inorganic Chemistry Frontiers* **2020**, *7*, 2478.

(61) Ding, Y.-S.; Yu, K.-X.; Reta, D.; Ortu, F.; Winpenny, R. E. P.; Zheng, Y.-Z.; Chilton, N. F. "Field- and temperature-dependent quantum tunnelling of the magnetisation in a large barrier single-molecule magnet" *Nature Communications* **2018**, *9*.

(62) Dillon, J. F.; Chen, E. Y.; Giordano, N.; Wolf, W. P. "Time-Reversed Antiferromagnetic States in Dysprosium Aluminum Garnet" *Phys Rev Lett* **1974**, *33*, 98.

(63) Mitsek, A. I.; Kolmakova, N. P.; Sirota, D. I. "Metamagnetism of 2-Sublattice Uniaxial Anti-Ferromagnets" *Phys Status Solidi A* **1981**, *65*, 503.

(64) Stryjewski, E.; Giordano, N. "Metamagnetism" *Adv Phys* **1977**, *26*, 487.

(65) Oh, D. G.; Kim, J. H.; Kim, M. K.; Jeong, K. W.; Shin, H. J.; Hong, J. M.; Kim, J. S.; Moon, K.; Lee, N. R.; Choi, Y. J. "Spin-flip-driven anomalous Hall effect and anisotropic magnetoresistance in a layered Ising antiferromagnet" *Scientific Reports* **2023**, *13*.

(66) Leclercq, B.; Kabbour, H.; Damay, F.; Colin, C. V.; Pautrat, A.; Arevalo-Lopez, A. M.; Mentre, O. "Metamagnetic Transitions versus Magnetocrystalline Anisotropy in Two Cobalt Arsenates with 1D Co2+ Chains" *Inorganic Chemistry* **2019**, *58*, 12609.

(67) Aoki, D.; Knafo, W.; Sheikin, I. "Heavy fermions in a high magnetic field" *Cr Phys* **2013**, *14*, 53.

(68) Hirose, Y.; Toda, M.; Yoshiuchi, S.; Yasui, S.; Sugiyama, K.; Honda, F.; Hagiwara, M.; Kindo, K.; Settai, R.; Onuki, Y. "Metamagnetic Transition in Heavy Fermion Compounds YbT2Zn20 (T:Co, Rh, Ir)" *J Phys Conf Ser* **2011**, *273*.

(69) Miyake, A.; Shimizu, Y.; Sato, Y. J.; Li, D.; Nakamura, A.; Homma, Y.; Honda, F.; Flouquet, J.; Tokunaga, M.; Aoki, D. "Metamagnetic Transition in Heavy Fermion Superconductor UTe2" *Journal of the Physical Society of Japan* **2019**, *88*.

(70) Gorter, C. J.; Vanpeskitinbergen, T. "Transitions and Phase Diagrams in an Orthorhombic Antiferromagnetic Crystal" *Physica* **1956**, *22*, 273.

(71) Neel, L. "Metamagnetisme Et Proprietes Magnetiques De Mn Au2" *Cr Hebd Acad Sci* **1956**, *242*, 1549.

(72) Landau, L. "On the Theory of Phase Transitions" *Ukr J Phys* **2008**, *53*, 25.

(73) Franke, K. J. A.; Ophus, C.; Schmid, A. K.; Marrows, C. H. "Switching between Magnetic Bloch and Neel Domain Walls with Anisotropy Modulations" *Phys Rev Lett* **2021**, *127*.

Chapter 4 Designing Quantum Spaces of Higher Dimensionality from a Tetranuclear Erbium-Based Single-Molecule Magnet

The spin relaxation of an Er^{3+} tetranuclear single-molecule magnet, **$[Er(hdcCOT)I]_4$**, (hdcCOT = hexahydrodicyclopentacyclooctatetraenide dianion), is modeled as a near-tetrahedral arrangement of Ising-type spins. Combining evidence from single-crystal X-ray diffraction, magnetometry, and computational techniques, the slow spin relaxation is interpreted as a consequence of symmetry restrictions imposed on quantum tunneling within the cluster core. The union of spin and spatial symmetries describe a ground state spin-spin coupled manifold wherein 16 eigenvectors generate the 3D quantum spin-space described by the vertices of a rhombic dodecahedron. Analysis of the experimental findings in this context reveals a correlation between the magnetic transitions and edges connecting cubic and octahedral subsets of the eigenspace convex hull. Additionally, the model is shown to map to a theoretically proposed quantum Cayley network, indicating an underexplored synergy between mathematical descriptions of molecular spin interactions and quantum computing configuration spaces.

4.1 Introduction

Many research efforts in molecular magnetism are pivoting towards exploring and understanding behaviors of molecular magnets in the context of quantum information science, primarily focusing on quantum computation upon molecular qubits.[1-4] A recent National Academies[5] report describes the necessity of chemists to focus on design, synthesis, measurement, and control of molecular quantum systems, prioritizing addressing and controlling multiple electron spins in molecular systems. To realize molecular versatility and scalability in applications such as quantum computing, simulation, and sensing, current mainstays of chemical intuition that rely on symmetry, charge, and bonding must be adapted to the presence of complex electron spin interactions. Recognizing this, molecular magnetism researchers have sought better control over how the choice of magnetic center and coupling methodology[6] determines the interplay between local (1-site) and global (many-site) responses.[7-10] The search to uncover more fundamental spin-structure-property relationships has led to a growing literature of transition metal,[11-16] lanthanide, and mixed-metal systems[17-25] placed into multi-spin architectures of clusters,[26-27] chains,[28-29] or extended frameworks.[30-34] The majority of multinuclear (4 or more centers) lanthanide cluster research has focused on dysprosium ions bridged with oxygen,[26, 35-39] as dysprosium's propensity towards an axially anisotropic ground state allows for straightforward characterization of SMM (single-molecule magnet) behaviors.[7] We set out to utilize similar energetic perturbative design principles for erbium,[8] trapping it in an highly anisotropic ground state environment through crystal-field effects. However, design of a lanthanide-based cluster[26] single-molecule magnet via coupling mononuclear single-molecule magnets rarely improves upon or even retains the slow relaxation dynamics of the solitary ion, often due to mixing of crystal field states via intra-ion coupling. To maximize the mapping of single-ion bases onto the coupled cluster interaction, we minimized the energy perturbation by reducing orbital-based exchange interactions, instead relying on a dipole-coupling of the highly anisotropic spins. To further reduce the free-parameter space, a cluster was synthesized with spatial orientation of the Ising axes that approximates the four three-fold rotation axes of a tetrahedron: **[Er(hdcCOT)I]$_4$**, (hdcCOT = hexahydrodicyclopentacyclooctatetraenide dianion).

To address the complexity of this system, we impose symmetry restrictions on the magnetic dipole-dipole portion of the Hamiltonian through crystallographic relationships between individual Er^{3+}

centers.[40-43] In such systems, the eigenstates of the total angular momentum can be engineered to be highly predictable, controllable by external fields, and resistant to random field fluctuations. Curiously, the Er^{3+} ion has been incorporated into numerous molecular clusters,[37, 44-54] displays high moment and anisotropy,[55-57] yet slow magnetization dynamics are observed in only one instance, and only under induced field.[58] Inspired by pyrochlore structures well-known for spin-ice behavior,[59] theoretical tetrahedral qubit design[60] predicting minimal decoherence, a four-dimensional proposed quantum network with perfect spin transfer,[61] and the potential to implement Ising-type Hamiltonians for quantum computation,[62] we hypothesized that a tetranuclear, tetrahedral molecular analogue would be an interesting subject of study. As such, we present an investigation into the first tetranuclear erbium cluster to exhibit slow magnetic relaxation and SMM behavior, **[Er(hdcCOT)I]$_4$**, and offer insights into the computationally derived, dipole-coupled spin states responsible for its magnetic characteristics.

4.2 Results & Discussion

4.2.1 Synthesis & Magnetism

Synthesis of tetranuclear **[Er(hdcCOT)I]$_4$** proceeds through the addition of K_2[hdcCOT](thf)$_2$ to a suspension of ErI_3 in cold THF in a rigorously air-free environment. This procedure generates the monomeric, Lewis-base adduct, Er[hdcCOT]I(thf)$_2$ as pink-orange crystals. Subsequently, well-dried crystals of the monomer are dissolved in hot toluene and reacted with excess tetramethylaluminum (Al(Me)$_3$) to abstract THF and form the tetranuclear **[Er(hdcCOT)I]$_4$** as red-orange crystals (Figure 4.1, Synthetic Scheme). Single-crystal X-ray diffraction analysis shows that **[Er(hdcCOT)I]$_4$** crystallizes in space group C2/c, with two unique erbium ions within the structure. The full structure is composed of four bridging iodide ions

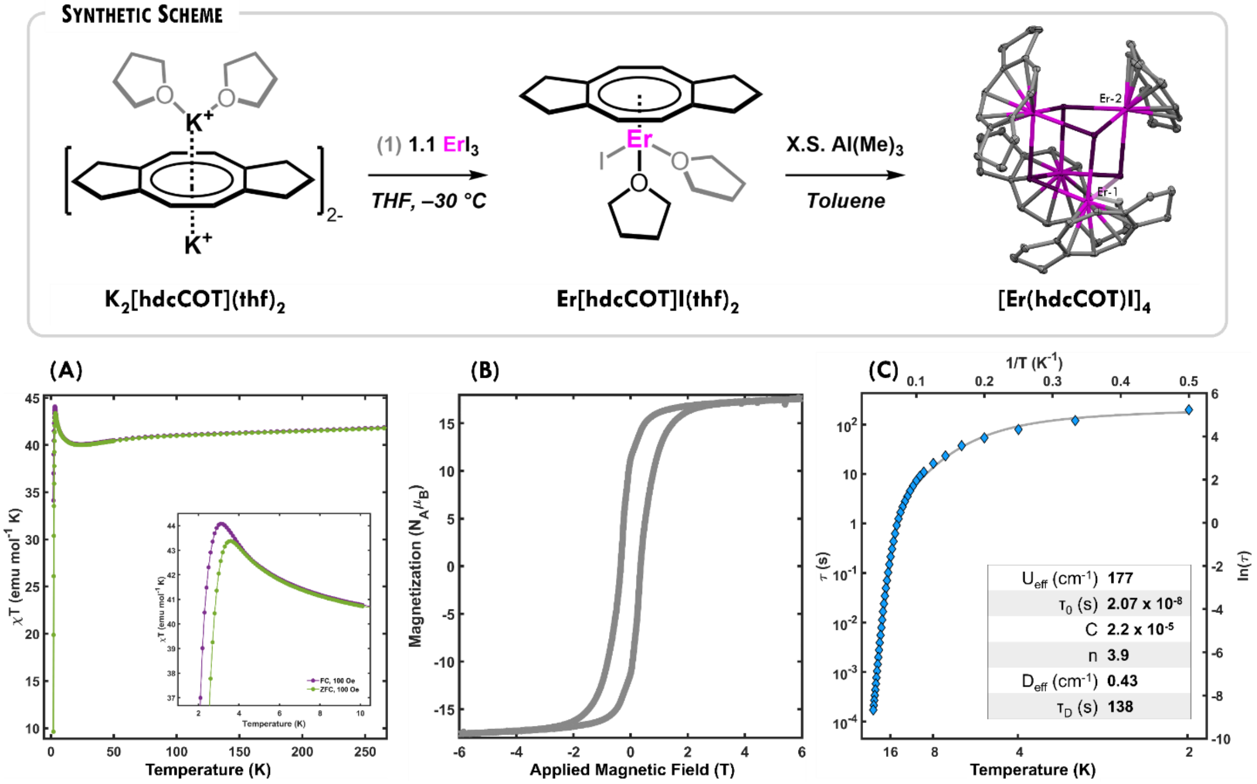

Figure 4.1: Synthetic scheme and x-ray single-crystal structure of **[Er(hdcCOT)I]$_4$**. Ellipsoids in structures represent carbon (gray), iodine (purple), and erbium (pink). Two unique erbium ions within the structure are labeled as Er-1 and Er-2. Hydrogen atoms are omitted for clarity. Magnetic data for **[Er(hdcCOT)I]$_4$**: (A) Thermal magnetic susceptibility between 2 – 300 K, collected in FC (purple) and ZFC (green) modes under an applied field of 100 Oe. (B) Isothermal magnetization at T = 2 K, 60 Oe/s sweep rate. (C) Arrhenius plots of relaxation times versus temperature (blue diamonds; error bars are within markers for upper and lower error limits of τ values). Gray line is a fit to a multiterm relaxation model (Equation S.4.1) with inset table depicting fit parameters.

connecting four erbium centers situated 4.3645(6) - 4.8670(5) Å apart. The Er-hdcCOT units are oriented in a near-tetrahedral environment with respect to the cluster center ($\tau_4 = 0.94$, where $\tau_4 = 1$ is an ideal tetrahedron).[63-65] These units generate the highly anisotropic ground states of each erbium ion, with anisotropy axes directed through each of the hdcCOT centroids. Befitting our previously introduced intuitive model of analysis of anisotropy vectors for such systems,[40] and further corroborated by computational findings in the following section, we are able to see the first spin-structure relationship in this compound: tetrahedral crystallographic arrangement of Er-hdcCOT units generates a tetrahedral spin-space of uncoupled ground Kramers doublets on each erbium ion.

To understand the implications of such a spin-space relationship, we collected static and dynamic data on finely ground microcrystalline samples in an MPMS3 SQUID magnetometer (see Section 4.4.2). Susceptibility data were collected in field-cooled (FC) and zero-field-cooled (ZFC) modes under an applied field of 100 Oe between 2 and 300 K and plotted as the susceptibility-temperature product ($\chi_M T$) vs. temperature (Figure 4.1-A). Both curves depict a dramatic rise in thermal susceptibility as temperature increases from 2 K, reaching maxima at 3.1 and 3.5 K, respectively, followed by a steep decrease at higher temperatures, indicative of ferromagnetic coupling interactions operant at these temperatures. Divergence between the FC and ZFC curves at temperatures below 4.4 K indicates magnetic blocking on the timescale of the measurement. By the superparamagnetic blocking definition of $T(\tau = 100 \text{ s})$, the blocking temperature is ~3 K. Around 25 K, both curves begin to slope upwards, gradually increasing to a room temperature $\chi_M T$ value of 41.79 emu mol^{-1} K. The compound presents open hysteresis at T = 2 K, up to temperatures of ~10 K, saturates near 18 $N_A\mu_B$, and has a coercive field of H_c = 3,500 Oe (0.35 T; Figure 4.1-B).

A combination of standard AC susceptibility and extended frequency space techniques[32, 40, 66-67] were utilized to investigate dynamic magnetic behavior. These data are summarized as curves of the natural log of relaxation times versus inverse temperature in order to emphasize the connection to, and deviation from, Arrhenius behavior (Figure 4.1-C). Using a standard phenomenological model, the data is fit to a combination of basic mechanisms: Orbach, Raman, and dipolar (Equation S.4.1; dipolar term introduced in prior works[32, 40]). At higher temperatures, the relaxation dynamics are consistent with typical SMM Arrhenius behavior, with relaxation through thermal excitation, following the Orbach mechanism. The extracted experimental barrier, U_{eff} = 177 cm^{-1}, is in range with the high-temperature dynamics of other Er-COT compounds and derivatives,[8, 32, 40-42, 66, 68-75] and outperforms its monomeric counterpart[66] (reported U_{eff} = 147 cm^{-1}).

In the context of **[Er(hdcCOT)I]$_4$**, the dipolar term encompasses the weakly temperature dependent processes occurring within the ground spin manifold over the temperature range of 2 – 7 K. In this temperature regime, magnetic relaxation dynamics will be most influenced by small energetic perturbations arising from dipolar coupling interactions between the ground Kramers doublets of each spin center (KD_0, $M_J = \pm 15/2$), and will give rise to 2^n dipole-coupled states, where *n* is the number of spin centers. Within this context, this small perturbation amounts to a fit D_{eff} = 0.43 cm^{-1}. The dipolar attempt time (τ_D = 138 s) and nearly thermal independent behavior are consistent with symmetry restrictions on transitions in a closely spaced manifold of states. Intrigued by the geometric manifestation of the isolated spin spaces, we sought more quantitative corroboration from a computational and theoretical study.

4.2.2 Computational Investigation

To facilitate our computational study, we took an energetically perturbative approach with respect to the electronic structure of the cluster. First, we utilized CASSCF methods with Single_Aniso, RASSI, RASSCF, and SEWARD modules of OpenMolcas[76-78] to gain insight into the spin-orbit coupling present at the single-ion level within each spin center. Then, we utilized the Poly_Aniso module of OpenMolcas to investigate the spin-spin interactions within the cluster and the emergent dipole-coupled quantum space. These calculations were completed on a set of compounds (see Section 4.4.2, Computational Methods) to understand the complex spin structure of the cluster and the consequences of symmetry restrictions on the wavefunction, with the main

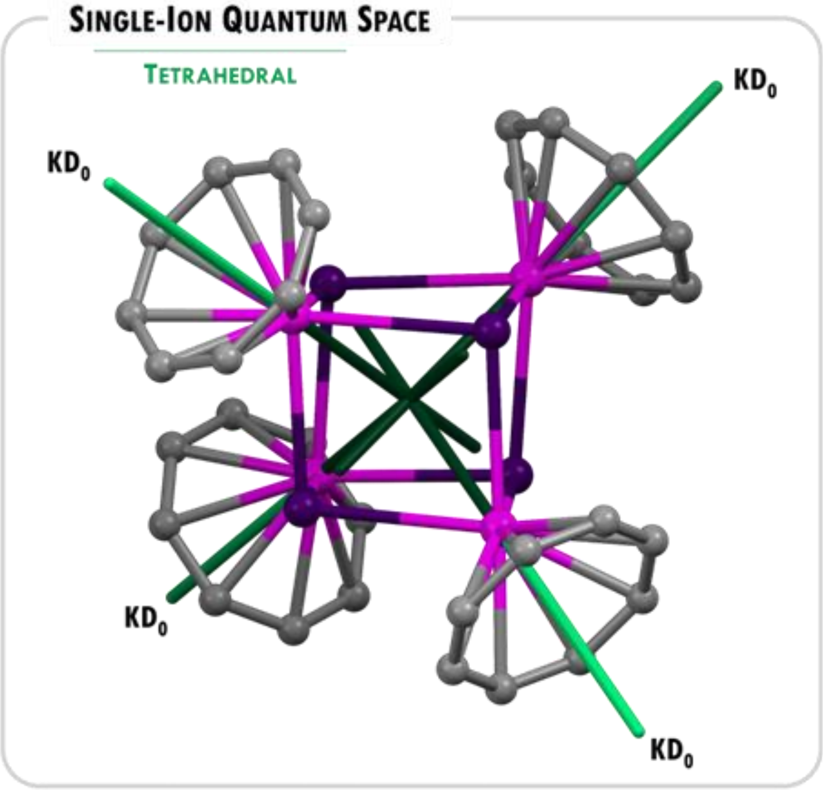

Figure 4.2: Computationally derived tetrahedral single-ion quantum space of **Er-T$_d$** with anisotropy axes arising from each spin center's ground Kramers doublet (KD) represented by green lines.

focus of this work being on two analogues: crystallographic near-tetrahedral **[Er(hdcCOT)I]$_4$**, (τ_4 = 0.94) and **Er-T$_d$**, an idealized model cluster, [ErCOTI]$_4$, with T$_d$ symmetry imposed on the Er-I core using the Largent-Polik-Schmidt algorithm[79-80] (τ_4 = 1; Figure 4.2; see Section 4.4.2, Computational Methods).

Single-ion calculations were completed on crystallographic coordinates of each erbium center in **[Er(hdcCOT)I]$_4$** and **Er-T$_d$** and describe the single-ion energy surface composed of Kramers doublets (KDs) of each magnetic ion. Computations show that single-ion energetics are comparable between crystallographic and idealized structures, with highly anisotropic (g_z = 17.96, $g_{x,y}$ = 0.00), nearly pure M_J = ±15/2 ground states (KD$_0$), and M_J = ±13/2 first excited states (KD$_1$), separated by ~85 cm^{-1} (vide infra; ESI, Section 6). As expected, and seen in prior compounds, the main anisotropy axes of the ground Kramers doublets (KD_0) of each spin center lie along the Er-COT vector (Figure 4.2, shown for **Er-T$_d$** and depicted with green lines). It would be expected that this single-ion electronic profile would be operational at higher temperatures. Interestingly, the experimentally derived barrier (U_{eff} = 177 cm^{-1}) is over twice the energy of the first available excited state, and approaches, but does not reach, the second excited state (KD_2 = 244 cm^{-1}). This is likely due to a high degree of mixing between KD_2 and KD_3, which encompass M_J = ±1/2 and ±11/2 states with ~50% purity. In the idealized tetrahedral cluster, the purity of these states increases substantially (up to 92%), but KD_2 becomes a primarily M_J = ±½ state, making it highly susceptible to facilitate relaxation, even when coupled.

Table 4.1: Computationally derived parameters of dipole-coupled quantum spaces of idealized **Er-T$_d$** and crystallographic **[Er(hdcCOT)I]$_4$**.

	Er-T$_d$		**[Er(hdcCOT)I]$_4$**	
DD_n, n =	Energy (cm^{-1})	Eigenvalue	Energy (cm^{-1})	Eigenvalue
0	0.00	±20.98	0.00	±19.45
1	0.01	±20.67	0.08	±20.11
2	0.02	±20.58	0.52	±22.52
3	1.17	±18.12	1.30	±17.45
4	1.17	±18.08	1.30	±17.45
5	1.18	±17.85	1.36	±18.46
6	1.19	±17.81	1.36	±18.46
7	4.69	±0.23	4.72	±0.80

At lower temperatures, transitions between ground and excited KDs become less thermally accessible, and relaxation dynamics are governed by transitions within intramolecularly coupled ground KDs of each magnetic center.[40] To provide insight into this low-temperature relaxation behavior, we generated a phenomenological model of dipole-dipole exchange between the four highly anisotropic, Ising-type, ground KDs (M_J = ±15/2) of each magnetic center in the cluster(s) through the Poly_Aniso module of OpenMolcas. The outputs of these calculations provide the dipole-coupled energy manifolds of **[Er(hdcCOT)I]$_4$** and **Er-T$_d$**, their eigenvalues, and projections in space. Both compound symmetries yield manifolds composed of sixteen eigenstates, eight doublets (calculated as pseudospin, $\tilde{S}$ = ½, due to the highly axial single-ion states), situated between 0.0 – 4.7 cm^{-1} and referred to as dipole doublets (DD$_{0-7}$; Table 4.1). As hypothesized, further degeneracies and interrelationships between states are evident for both the crystallographic and idealized cluster, with **Er-T$_d$** most clearly elucidating symmetry-induced aspects of the spin structure. The first three multiplets (DD$_{0-2}$) approach a six-fold degeneracy. States DD$_{3,4}$ and DD$_{5,6}$ are each four-fold degenerate, generating two sets of quartets at nearly identical energies. State DD$_7$ is unique in that its eigenvalues are both nearly zero, indicating an anti-symmetrization of all four constituent states.

Intrigued by these initial findings, we sought further indications for how the observed degeneracies could be contextualized in terms of spin and crystallographic symmetry. Our interpretation centers on a geometric analysis based on **Er-T$_d$**, in which we project eigenvectors of each multiplet from the center of the cluster, scaled by eigenvalue, and generate a three-dimensional visualization of the dipole-coupled magnetic energy surface representing the available quantum space within the low temperature range (Figure 4.3). Figure 4.3 depicts the local magnetic axis of each dipole doublet and highlights the aforementioned degeneracies in three-dimensional space. The convex hull of the available quantum space forms the rhombic dodecahedron, a Catalan solid.[81] Within this, are three subspaces composed of an octahedron, a cube, and a set of points at the origin. States DD$_{0-2}$ are situated orthogonally with respect to each other and take on the configuration of an octahedron (orange, Figure 4.3), following their energetic degeneracies. States DD$_{3-6}$ each project through the center of one of the four COT-rings, generating a cube (cyan, Figure

4.3), highly reminiscent of the ground KDs. State DD_7 projects almost perfectly onto the origin of our geometric representation (magenta, Figure 4.3).

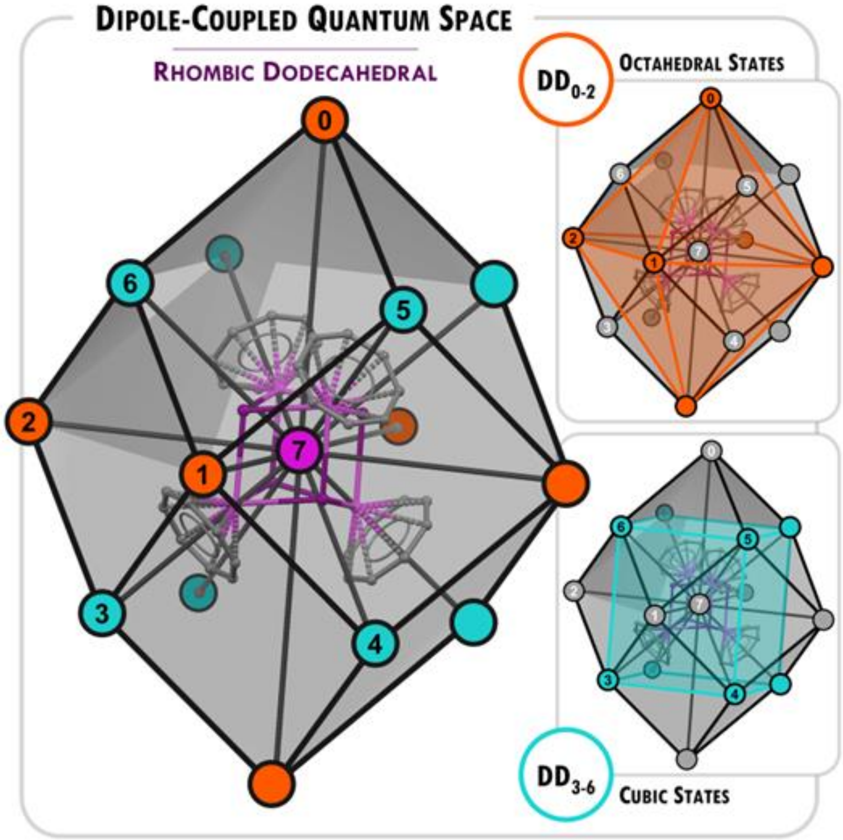

Figure 4.3: Computationally derived quantum space of **Er-T$_d$**. Rhombic dodecahedral dipole-coupled quantum space composed of 8 dipole doublets (DDs), labeled numerically. Color corresponds to octahedral (orange) and cubic (cyan) subspaces, as discussed in the text.

To further discuss transition probabilities within this context, the coordinate system is fixed along the main magnetic axis, aligned with DD_0. The appropriate vector components of each state are projected onto the main magnetic axis (represented with purple dashed arrows, Figure 4.4-top), upholding both the degeneracy and energy of each state. This process retains DD_0 as the ground state and main axis of anisotropy, while fully mixing the projections of its degenerate counterparts, DD_1 and DD_2. States $DD_{3\text{-}6}$ have partial projections and so retain a scaled version of their cubic representation. This is more clearly evidenced in a familiar energy manifold depicted in Figure

4.4-bottom, where each DD is organized by its respective energy and moment. The most(least) likely transition probabilities between states are depicted with red(blue) arrows, relating to

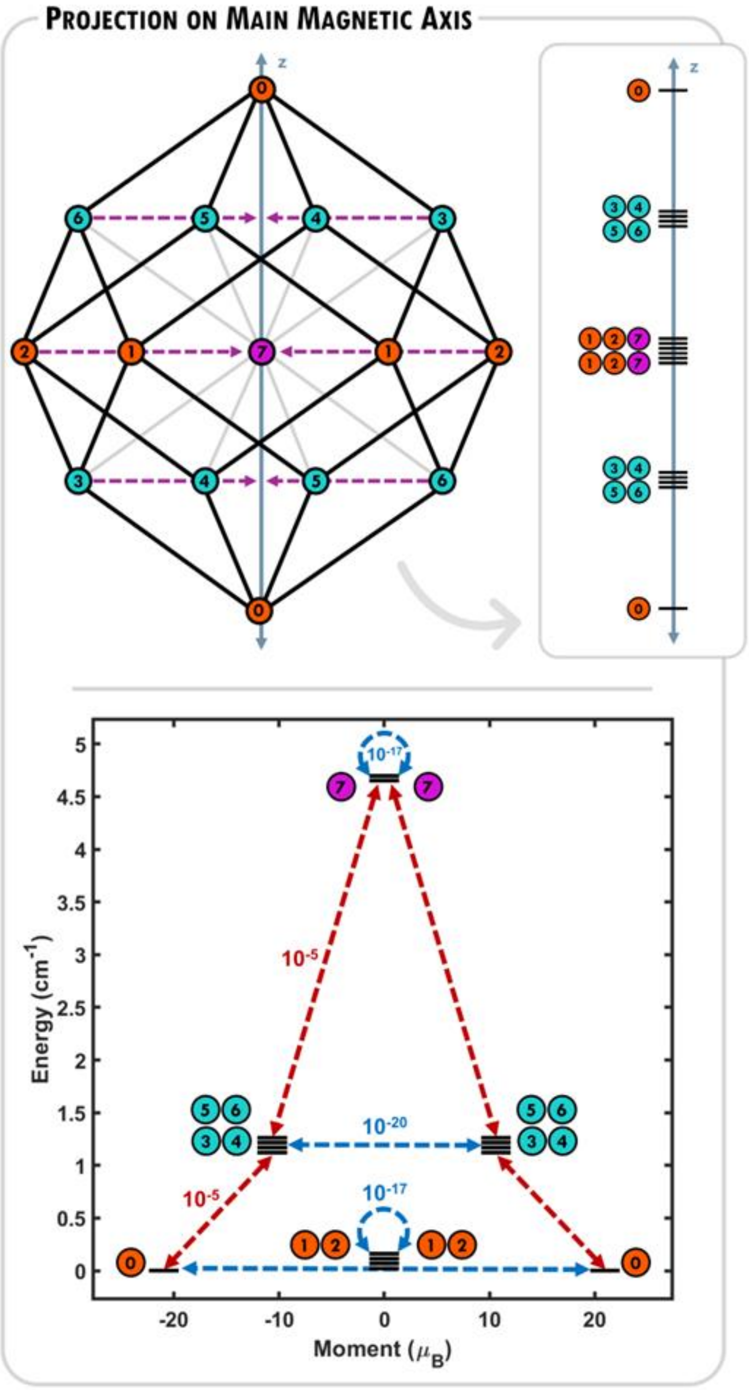

Figure 4.4: Computationally derived quantum space of **Er-T$_d$**. (top) Simplified representation of Figure 4.3, depicting projection of states onto the main magnetic z-axis, to generate (bottom) dipole-coupled energy manifold of states and transition probabilities between them, depicted with as arrows with most (red) and least (blue) probable transitions.

transition matrix elements connecting eigenstates through a Zeeman perturbation.[82]

Within this idealized model, it's possible to clearly see the impact of symmetry and geometry of the quantum space and begin to relate and rationalize experimentally derived data. The experimental findings at low temperatures coincide with our theoretical predictions and computational modeling; DD_0 is the ferromagnetically coupled exchange state responsible for the ZFC/FC and hysteretic behavior seen experimentally within the low-temperature regime. Its two-fold degeneracy arises from the nature of anisotropy, which aligns individual spins, creating an energetic equivalence between the "all-in" and "all-out" configurations. In this context, these are quantized by a total pseudospin of $\tilde{S} = \pm 2$.

The probabilities of transitions follow magnetic dipole-dipole selections rules ($\Delta S = \pm 1$) and are equivalent to a single step on one of the edges connecting to DD_0 on the rhombic dodecahedron. This is equivalent to a single spin-flip and is closely related to the concept of Hamming distance[83] from information theory. The fully ferromagnetically coupled ground state (DD_0, $\tilde{S} = \pm 2$) is most likely to transition to one of the cubic states ($DD_{3\text{-}6}$, $\tilde{S} = \pm 1$), each of which is representative of a "one-in, three-out" (or vice versa) spin configuration. It is unlikely to transition to DD_1 or DD_2 ($\tilde{S} = 0$), which allows it to maintain its large anisotropy. As expected, quantum tunnelling of magnetization (QTM) in the dipole-coupled ground states is greatly suppressed (10^{-17} vs. 10^{-5} in KD_0) and is similarly suppressed within the cubic states (~10^{-20}, Figure 4.4-bottom). There is no direct pathway involving the smallest distance (one edge) between states on either side of the barrier, and QTM becomes a four-step spin-flip process strongly impacted by dipole coupling present amongst spins.

From fitting our experimental data, the predicted dipolar energy splitting was determined to be $D_{eff} = 0.43$ cm^{-1}, whereas the calculated dipolar barrier is $\Delta E(DD_0, DD_7) = 4.7$ cm^{-1}, indicating

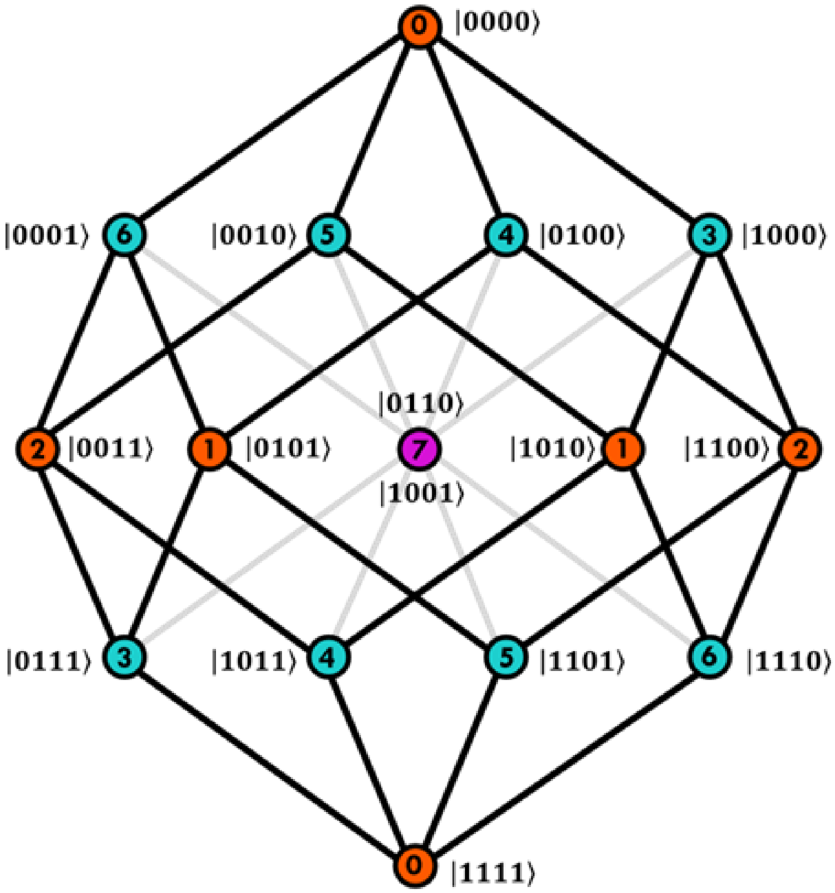

Figure 4.5: Binary computational basis in ket-representations mapped onto the dipole-coupled quantum space. Numerically ordered circles in orange, cyan, and magenta correspond to dipole doublets, as discussed in the text.

that the highest energy state, DD_7, is unlikely to be involved to an appreciable degree. It is further unlikely that the dipolar barrier is composed of DD_2 ($E = 0.52\ cm^{-1}$; Figure S.4.9) as calculated for crystallographic **[Er(hdcCOT)I]$_4$**, as this transition would be disallowed by dipolar selection rules, which is further confirmed through calculated matrix probabilities. Following the analysis of the idealized tetrahedral compound, **Er-T$_d$**, it appears most likely that the dipolar barrier is composed of the cubic states ($E \sim 1\ cm^{-1}$), access to which are allowed by selection rules, and which are within the order of magnitude of the experimentally derived dipolar barrier.

Stimulated by discussion within the field of molecular magnetism towards its applicability to quantum computing, we set out to map a computational basis onto the dipole-coupled quantum space of our tetranuclear compound. To discuss this, we introduce a simple representation of the binary basis in ket-form where the spin at each site is represented by a “0” or “1” (Figure 4.5). In this depiction, the “all-in” state is represented by $|0000\rangle$ and the “all-out” by $|1111\rangle$, corresponding to DD_0. In this context, traversing between states across one edge is directly related to a unit Hamming distance and the equivalence of one spin-flip per step. Furthermore, the computational basis mapped onto our molecular system becomes representative of a quantum Cayley network,[61] proposed by Facer and coworkers, claimed to be adjustable to perfectly route quantum information between nodes (in our molecular system, these correspond to DD states). The depiction from their work shows an identical configuration of states (nodes) and mapped computational basis, however the two center states are separated, as the quantum Cayley network maps onto a four-dimensional hypercube instead of a three-dimensional rhombic dodecahedron, as in our molecular system.

Curiously, the rhombic dodecahedron is a vertex-first parallel-projection of a four-dimensional hypercube into three-dimensional space.[84] We thus hypothesize that the dipole-coupled quantum spaces of **Er-T$_d$** and **[Er(hdcCOT)I]$_4$** may generalize through models that are constructed and manipulated in a higher-dimensional space with projection onto a lower dimensional measurement space only for comparison with experiment. Such models may aid us in rationalizing the superimposed center states (magenta, Figure 4.5), as well as time-reversal symmetry upon this surface. Investigations to understand and mathematically depict this are underway. Furthermore, we hypothesize that this system could be implemented as a molecular manifestation of a quantum Cayley network, wherein particular cubic states could be accessed with an appropriate application of field. The example we presented depicts an application of field along the z-axis of the molecule, however, due to its crystallographic and emergent quantum space symmetries, applications of field in x- or y-directions could stimulate DD_1 or DD_2 to act as the corresponding ground states. The projections of cubic states could remain analogous to the example presented prior but would project different sets of states onto the two sides of the dipole barrier. Further investigations to test the propensity of this system as an accessible quantum network are ongoing.

4.3 Conclusion

In this work we use a geometric approach for discussing the spin structure of a lanthanide cluster, incorporating elements of spin and spatial symmetry to facilitate connection between synthesis, measurement, theory, and computation into a unified hypothesis-driven model of spin architecture design. Our analysis reveals that **$[Er(hdcCOT)I]_4$** has SMM functionality driven by near-tetrahedral symmetry. Computational analysis further shows that this tetrahedral space manifests into a 16-eigenstate dipole-coupled quantum space with a rhombic dodecahedral convex hull composed of octahedral and cubic subspaces. We show that despite vanishingly small energy barriers to relaxation, the additional restrictions on the spin symmetry inhibit QTM, and enforce spin paths that respect magnetic dipole-dipole selection rules. A thermal barrier (U_{eff} = 177 cm^{-1}), well in excess of KD_1, and low-temperature relaxation time of 138 seconds are strong indicators that **$[Er(hdcCOT)I]_4$** is an SMM because of spin-symmetry restrictions on the Hamiltonian, not purely electrostatic restrictions. Furthermore, we've shown that it's possible to map a computational binary basis onto this system that uses synthetic design and symmetry to leverage the advantages of molecules to design quantum interactions bypassing the standard qubit-by-qubit approach. From these results, we envision the opportunity to further expand upon principles for multinuclear magnetic architectures using the precision and predictability of the dipolar interaction to bring the fundamental goal of designing functional quantum spaces closer to reality.

4.4 Associated Supplemental Content

4.4.1 Preparative Details

All manipulations were conducted under anaerobic, anhydrous conditions under an atmosphere of N_2 in Vacuum Technology Inc. and MBraun gloveboxes. All glassware was dried at 160 °C overnight prior to use. Tetrahydrofuran (THF), toluene, hexane, and pentane were dried on an activated alumina column and stored over a 1:1 mixture of 3 and 4 Å molecular sieves for at least two days before use. Erbium triiodide (Alfa Aesar), 1,3,5,7-cyclooctatetraene (Acros Organics), and trimethylaluminum (TMA, Sigma Aldrich) were all used as received. Neutral hdcCOT ligand was synthesized by literature procedure.[u] CHN elemental analyses were performed by Micro-Analysis, Inc., Wilmington, DE, U.S.A.

Synthesis of dipotassium hexahydrodicyclopentacyclooctatetraenide, K_2hdcCOT(thf)$_2$

To a clean piece of excess potassium was added ca. 15-20 mL THF and cooled in a -30°C freezer for 15-20 minutes. During this time, previously prepared hdcCOT (1.175 g; yellow-orange oil) was placed in 10 mL THF and placed in the freezer to cool. The cold solution of hdcCOT in THF was then added slowly and dropwise to the potassium in THF. The reaction progressed from dark orange to brown and was allowed to react overnight at -30°C. The next day, the reaction was allowed to come to RT, upon which the brown solution was removed from the excess potassium and centrifuged to remove insoluble impurities. The supernatant was collected and concentrated

---

[u] Wender, P. A.; Christy, J. P. "Nickel(0)-Catalyzed [2 + 2 + 2 + 2] Cycloadditions of Terminal Diynes for the Synthesis of Substituted Cyclooctatetraenes" *J Am Chem Soc* **2007**, *129*, 13402.

in vacuo to ca. 20 mL total volume and allowed to crystallize overnight at -30°C, yielding yellow-brown needle-like crystals. These were crushed and dried thoroughly, washed with hexanes and pentane, to yield an off-white, pale-yellow powder, used in downstream synthesis. To characterize the compound, X-ray quality light yellow plates were grown via THF/pentane vapor diffusion at -45°C; CCDC identifier: 2311635.

Synthesis of monomeric precursor, Er[hdcCOT]I(thf)$_2$

K_2hdcCOT (0.2403 g, 1 eq.) was dissolved in ca. 8 mL of THF and cooled in a -30°C freezer for 20 minutes, resulting in a vivid yellow-orange solution. During this time, a slurry of ErI_3 (0.5518 g, 1.1 eq.) in ca. 3 mL THF was prepared and also cooled in a -30°C freezer for 20 minutes (white/pale-pink slurry). The cold solution of K_2hdcCOT was then added dropwise into the cold stirring slurry of ErI3, which took on an opaque yellow color upon addition. This was allowed to react, stirring, at -30°C for 18 hours, upon which it took on an opaque peach appearance. The next day, the mixture was allowed to come to RT, upon which it was thoroughly centrifuged to remove insoluble byproducts. The white pellet was discarded, and the peach supernatant was dried *in vacuo* to yield a peach microcrystalline solid. This solid was dissolved in ca. 8 mL of THF, filtered through a glass fiber, and allowed to crystallize at -30°C for 24 hours, yielding X-ray quality pink-orange plates (0.3625 g; 64% yield on first crop); CCDC identifier: 2311633.

Synthesis of tetranuclear cluster, [Er(hdcCOT)I]$_4$

Prior to synthesis, crystals of Er[hdcCOT]I(thf)$_2$ (0.3625 g) were finely ground and suspended in ca. 20 mL of toluene, heated at 70°C. After 20 minutes, a solubilized potion of the compound (12 mL, peach-orange) was removed and filtered through a glass fiber. Additional toluene was added to the remainder to the reaction mixture and allowed to stir at 70°C for another 20 minutes, after which it was filtered as the previous portion. To each filtered portion (ca. 12 mL), excess trimethylaluminum (TMA, in toluene; 2 mL, 2 M) was added and shaken well. The reaction took on a deep orange color and was allowed to sit at room temperature for 18 hours, upon which red-orange crystals began to form. The reaction was then transferred to the freezer at -30°C, from which red-orange X-ray quality crystals were grown over the course of 2-3 days (0.1857 g, yield: 66.6% yield on first crop); CCDC identifier: 2311634. CHN analysis (calculated, found) for [$C_{56}H_{64}Er_4I_4$]: C (35.15%, 34.98%); H (3.37%, 3.46%); N (0.00%, 0.00%).

4.4.2 Sample Characterization

Crystallographic Methods

Single crystal diffraction data were collected on a Bruker Apex II-Ultra CCD with microfocus rotating anode using a Mo(Kα) radiation source. The structures were solved using direct methods via the SHELX routine and refined using full-matrix least-squares procedures with the SHELXL routine.[v] Olex^2 was used as a graphical front end during refinement.[w] Hydrogens were modeled using a riding model for all positions. Supplementary crystallographic data can be accessed from the Cambridge Crystallographic Data Center via deposition numbers: 2311633, 2311634, 2311635.

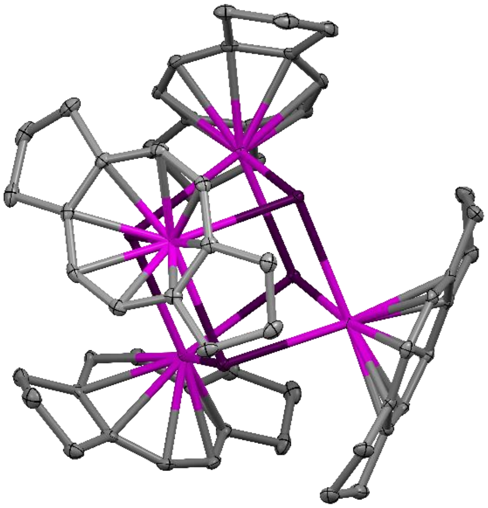

Supplemental Figure 4.1: Crystal structure of **[Er(hdcCOT)I]$_4$**, showing thermal ellipsoids at 50% probability. Atoms are colored by element type: gray (carbon), purple (iodine), pink (erbium). Hydrogen atoms have been omitted for clarity.

---

[v] Sheldrick, G. M. "Structure determination revisited" *Acta Crystallogr A* 2015, *71*, S9; Sheldrick, G. M. "SHELXT - Integrated space-group and crystal-structure determination" *Acta Crystallogr A* **2015**, *71*, 3; Sheldrick, G. M. "Crystal structure refinement with SHELXL" *Acta Crystallogr C* **2015**, *71*, 3.

[w] Dolomanov, O. V.; Bourhis, L. J.; Gildea, R. J.; Howard, J. A. K.; Puschmann, H. "OLEX2: a complete structure solution, refinement and analysis program" *J Appl Crystallogr* **2009**, *42*, 339.

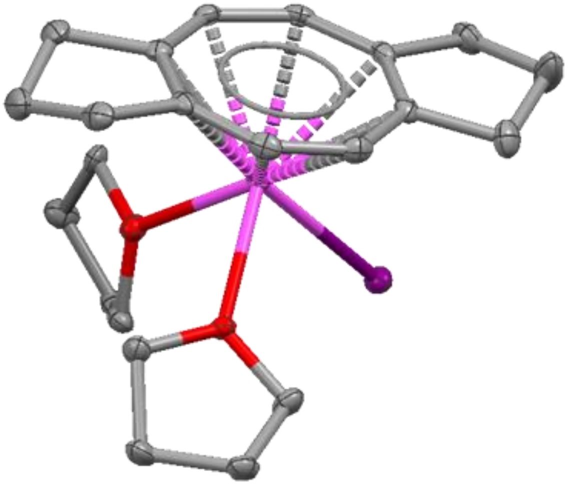

Supplemental Figure 4.2: Crystal structure of **Er[hdcCOT]I(thf)$_2$**, showing thermal ellipsoids at 50% probability. Atoms are colored by element type: gray (carbon), purple (iodine), pink (erbium), red (oxygen). Hydrogen atoms have been omitted for clarity.

Magnetometry Methods

Magnetic data were collected under DC and VSM scan modes using a Quantum Design MPMS3 SQUID Magnetometer with equipped AC susceptibility attachment. Crystal samples were finely crushed and loaded in custom quartz tubes (D&G Glassblowing Inc.), layered with eicosane wax, and subsequently flame-sealed under static vacuum. Eicosane wax was melted within the sealed sample to abate sample torquing and to facilitate thermal conductivity. Diamagnetic corrections for the samples and eicosane wax were calculated using Pascal's constants[x] and subtracted from all static moment data. Thermal magnetic susceptibilities were collected as ZFC and FC data in DC scan mode under applied fields of H = 100, 200, and 1,000 Oe. Isothermal magnetization data were collected in VSM mode between −7 to 7 T at a 60 Oe sec^{-} sweep rate.

---

[x] Bain, G. A.; Berry, J. F. "Diamagnetic corrections and Pascal's constants" *J Chem Educ* **2008**, *85*, 532.

Short and long-timescale AC data were fit to a Debye (Cole-Cole relaxation) model. Details related to the collection and analysis of long-timescale magnetic data are discussed in our previous works[y] and analyzed in a further publication.[z] Temperature and τ data were fit to a multi-term relaxation model shown in Equation S.4.1. MPMS 3 data parsing, fitting, and plotting was performed with our MATLAB package, *Super*.[aa] This object-oriented code package and all applicable documentation is available at [*https://github.com/RinehartGroup/super-matlab*](https://github.com/RinehartGroup/super-matlab) under the MIT License.

$$\tau^{-1} = \tau_0^{-1} exp\left(\frac{-U_{eff}}{k_B T}\right) + CT^n + \tau_D^{-1} exp\left(\frac{-D_{eff}}{k_B T}\right) \qquad \textit{(Eq. S.4.1)}$$

Equation S.4.1. Multi-term relaxation mechanism equation accounting for Orbach, Raman, and dipolar processes, where τ is the fitted relaxation time, τ_0 is the attempt time, U_{eff} is the effective barrier, k_B is the Boltzmann constant, T is the temperature, C is the Raman coefficient, n is the Raman exponent, τ_D is the dipole attempt time, and D_{eff} is the dipole effective barrier.

---

[y] Hilgar, J. D.; Butts, A. K.; Rinehart, J. D. "A method for extending AC susceptometry to long-timescale magnetic relaxation" *Phys Chem Chem Phys* **2019**, *21*, 22302; Orlova, A. P.; Hilgar, J. D.; Bernbeck, M. G.; Gembicky, M.; Rinehart, J. D. "Intuitive Control of Low-Energy Magnetic Excitations via Directed Dipolar Interactions in a Series of Er(III)-Based Complexes" *J Am Chem Soc* **2022**, *144*, 11316; Orlova, A. P.; Varley, M. S.; Bernbeck, M. G.; Kirkpatrick, K. M.; Bunting, P. C.; Gembicky, M.; Rinehart, J. D. "Molecular Network Approach to Anisotropic Ising Lattices: Parsing Magnetization Dynamics in Er Systems with 0-3-Dimensional Spin Interactivity" *J Am Chem Soc* **2023**, *145*, 22265.

[z] Blackmore, W. J. A.; Gransbury, G. K.; Evans, P.; Kragskow, J. G. C.; Mills, D. P.; Chilton, N. F. "Characterisation of magnetic relaxation on extremely long timescales" *Phys Chem Chem Phys* **2023**, *25*, 16735.

[aa] Hilgar, J. D., Orlova, A.P., Bernbeck, M.G., super-matlab (Version 2.0.0), **2022**.

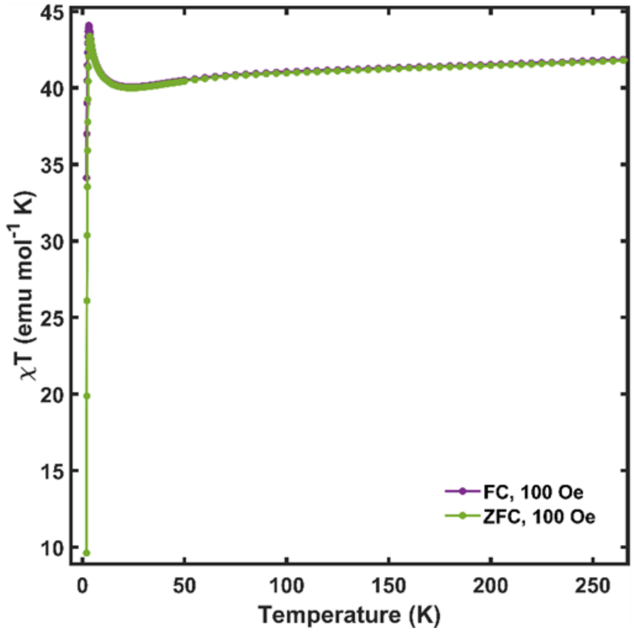

Supplemental Figure 4.3: DC susceptibility data of **[Er(hdcCOT)I]$_4$** under H = 100 Oe applied field in ZFC (green) and FC (purple) collection modes.

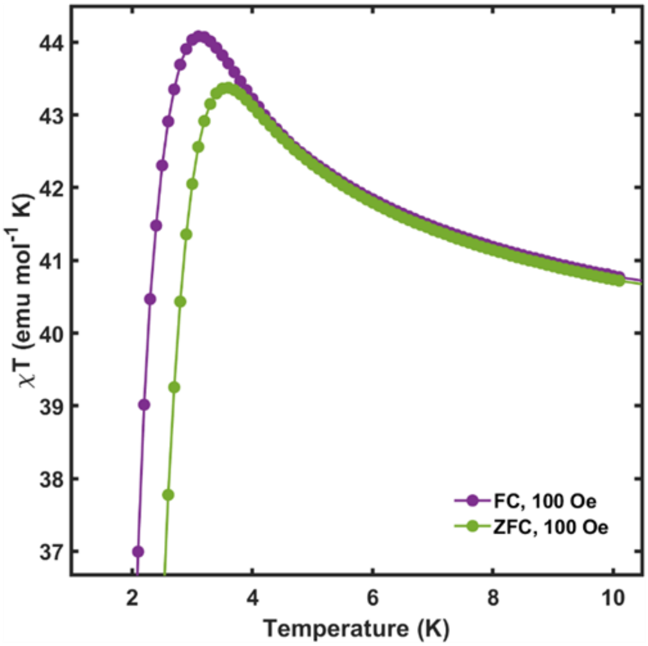

Supplemental Figure 4.4: Zoom of DC susceptibility data of **[Er(hdcCOT)I]$_4$** under H = 100 Oe applied field in ZFC (green) and FC (purple) collection modes.

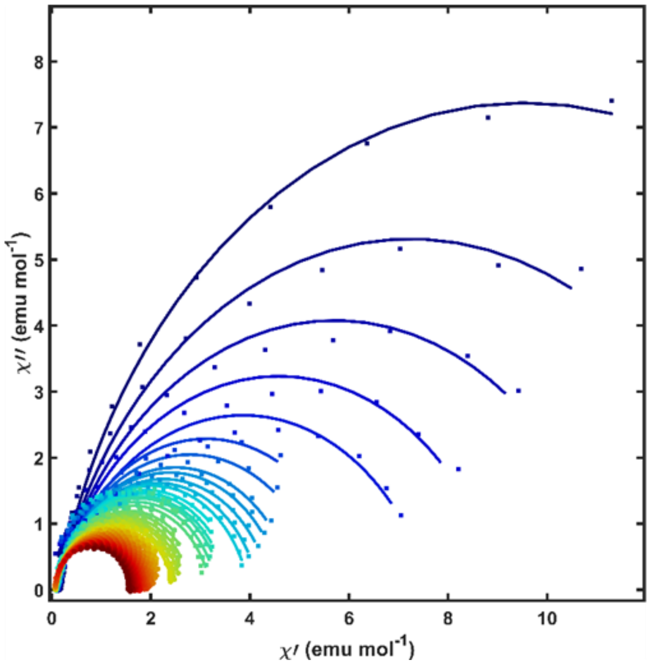

Supplemental Figure 4.5: Cole-cole plot of **[Er(hdcCOT)I]$_4$** collected between T = 2 - 27 K (blue - red). Data points are susceptibilities measured via standard AC measurements (circles) and extracted from Fourier analysis of VSM data (squares). Lines represent fits to a generalized Debye model.

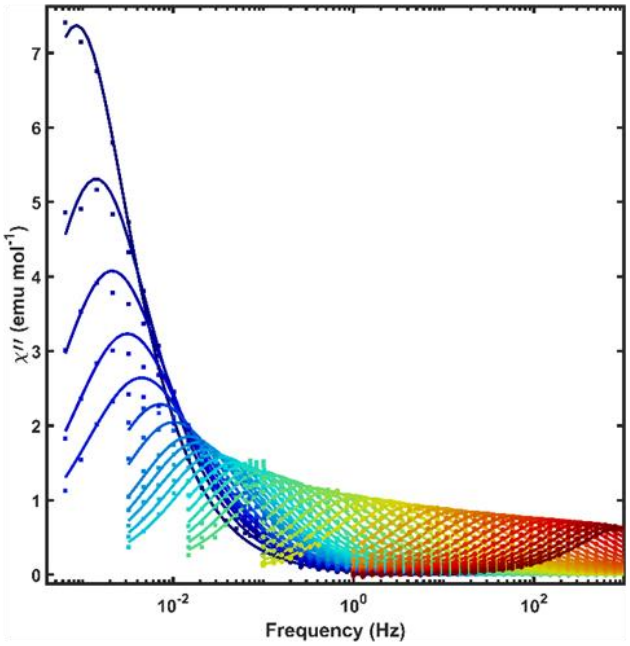

Supplemental Figure 4.6: AC out-of-phase susceptibility (χ'') of **[Er(hdcCOT)I]$_4$** collected between T = 2 - 27 K (blue - red). Data points are susceptibilities measured via standard AC measurements (circles) and extracted from Fourier analysis of VSM data (squares). Lines represent fits to a generalized Debye model.

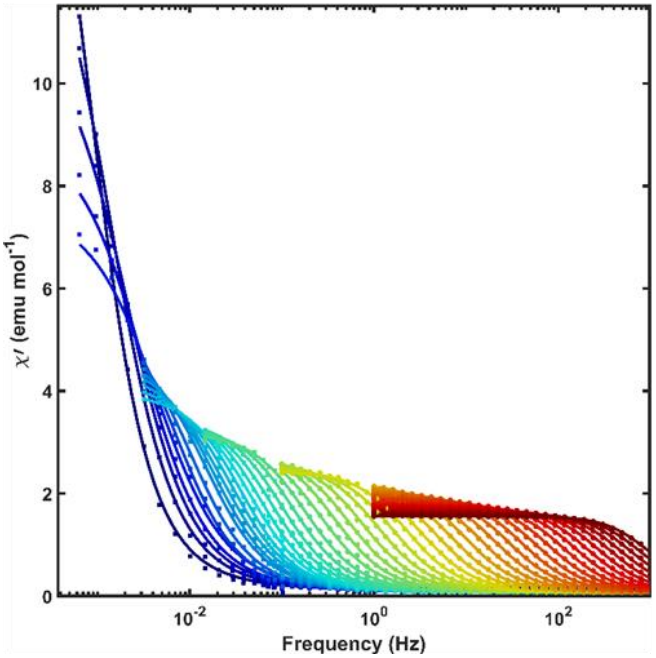

Supplemental Figure 4.7: AC in-of-phase susceptibility (χ'') of **[Er(hdcCOT)I]$_4$** collected between T = 2 - 27 K (blue - red). Data points are susceptibilities measured via standard AC measurements (circles) and extracted from Fourier analysis of VSM data (squares). Lines represent fits to a generalized Debye model.

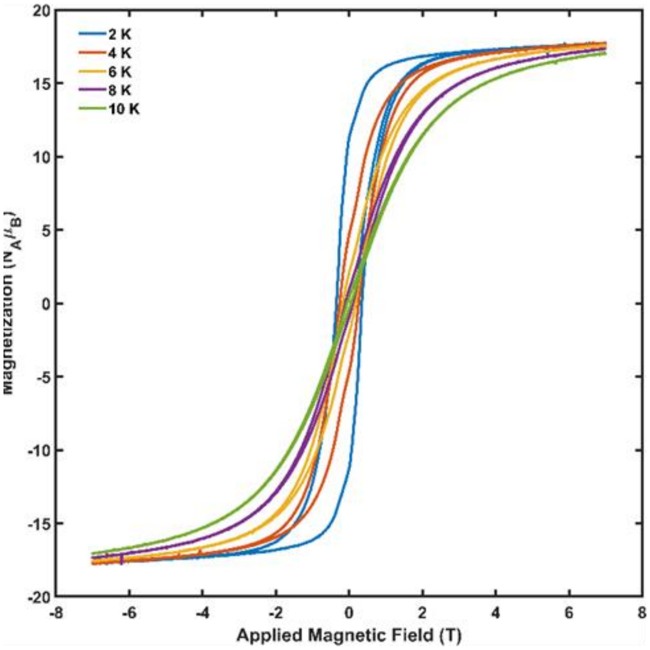

Supplemental Figure 4.8: Isothermal magnetization of **[Er(hdcCOT)I]$_4$** at T = 2, 4, 6, 8, and 10 K collected between $H = -7$ to 7 T at a constant sweep rate of 60 Oe sec^{-1} in VSM mode.

Supplemental Table 4.1: Model fit values for AC and waveform data collected for **[Er(hdcCOT)I]$_4$** between *T* = 2 - 27 K.

T	τ_1	$\tau_{1, error, LB}$	$\tau_{1, error, UB}$	α_1	$\alpha_{1, error, LB}$	$\alpha_{1, error, UB}$	χ_T	$\chi_{T, error, LB}$	$\chi_{T, error, UB}$	χ_S	$\chi_{S, error, LB}$	$\chi_{S, error, UB}$
2	187.47	182.66	192.29	0.15	0.15	0.16	18.94	18.66	19.22	0.13	0.12	0.15
3	113.32	109.43	117.21	0.19	0.17	0.20	14.37	14.12	14.63	0.10	0.08	0.12
4	75.37	72.58	78.17	0.20	0.19	0.21	11.33	11.13	11.54	0.09	0.07	0.11
5	51.03	49.00	53.06	0.21	0.19	0.22	9.08	8.92	9.24	0.08	0.06	0.11
6	35.48	33.71	37.25	0.22	0.21	0.24	7.64	7.48	7.79	0.09	0.06	0.11
7	22.12	21.18	23.07	0.18	0.17	0.19	6.16	6.03	6.30	0.08	0.07	0.10
8	15.62	14.96	16.28	0.18	0.16	0.19	5.50	5.39	5.61	0.08	0.06	0.09
9	10.47	10.11	10.83	0.17	0.16	0.18	4.92	4.84	5.00	0.08	0.06	0.09
9.5	8.60	8.29	8.90	0.16	0.15	0.18	4.67	4.60	4.75	0.07	0.06	0.09
10	6.96	6.70	7.23	0.17	0.15	0.18	4.44	4.36	4.52	0.07	0.06	0.09
10.5	5.48	5.32	5.64	0.15	0.14	0.16	4.19	4.14	4.25	0.07	0.06	0.09
11	4.35	4.24	4.46	0.14	0.12	0.15	3.99	3.94	4.03	0.08	0.06	0.09
11.5	3.37	3.28	3.47	0.13	0.12	0.14	3.77	3.71	3.83	0.08	0.07	0.09
12	2.67	2.61	2.73	0.12	0.12	0.13	3.64	3.60	3.69	0.08	0.07	0.09
12.5	2.08	2.05	2.11	0.13	0.13	0.14	3.55	3.52	3.57	0.08	0.08	0.08
13	1.61	1.57	1.66	0.13	0.11	0.14	3.46	3.41	3.51	0.08	0.06	0.09
13.5	1.20	1.17	1.23	0.13	0.11	0.14	3.34	3.29	3.38	0.08	0.06	0.09
14	0.88	0.86	0.91	0.13	0.12	0.15	3.22	3.18	3.26	0.08	0.06	0.09
14.5	0.60	0.59	0.62	0.14	0.13	0.15	3.04	3.00	3.09	0.07	0.07	0.08
15	0.42	0.41	0.43	0.13	0.12	0.14	2.92	2.90	2.94	0.07	0.07	0.08
15.5	0.30	0.29	0.30	0.13	0.12	0.14	2.81	2.79	2.83	0.07	0.07	0.08
16	0.21	0.21	0.21	0.12	0.12	0.13	2.71	2.70	2.73	0.07	0.07	0.08
16.5	0.14	0.14	0.15	0.12	0.12	0.13	2.63	2.62	2.64	0.07	0.07	0.08
17	0.10	0.10	0.10	0.11	0.11	0.12	2.53	2.52	2.54	0.07	0.07	0.08
17.5	0.07	0.07	0.07	0.11	0.10	0.12	2.46	2.44	2.47	0.07	0.07	0.08
18	0.05	0.05	0.05	0.12	0.12	0.13	2.40	2.38	2.41	0.07	0.06	0.07
18.5	0.03	0.03	0.03	0.12	0.12	0.13	2.34	2.33	2.36	0.06	0.06	0.07
19	0.02	0.02	0.02	0.12	0.12	0.13	2.28	2.26	2.29	0.06	0.06	0.07
19.5	0.02	0.02	0.02	0.12	0.11	0.13	2.22	2.21	2.24	0.06	0.05	0.07
20	0.01	0.01	0.01	0.12	0.11	0.12	2.14	2.13	2.15	0.06	0.05	0.07
20.5	0.01	0.01	0.01	0.11	0.10	0.12	2.08	2.07	2.09	0.06	0.05	0.07
21	0.01	0.01	0.01	0.11	0.10	0.12	2.03	2.02	2.04	0.06	0.05	0.07
21.5	0.00	0.00	0.00	0.11	0.10	0.12	1.98	1.97	1.99	0.06	0.05	0.07
22	0.00	0.00	0.00	0.11	0.10	0.12	1.93	1.92	1.94	0.06	0.05	0.07
22.5	0.00	0.00	0.00	0.11	0.10	0.12	1.89	1.88	1.90	0.05	0.04	0.06
23	0.00	0.00	0.00	0.10	0.09	0.11	1.84	1.83	1.85	0.06	0.04	0.07
23.5	0.00	0.00	0.00	0.10	0.09	0.11	1.80	1.79	1.80	0.06	0.04	0.07
24	0.00	0.00	0.00	0.10	0.09	0.11	1.76	1.76	1.77	0.06	0.04	0.08
24.5	0.00	0.00	0.00	0.09	0.07	0.10	1.72	1.71	1.73	0.08	0.05	0.10

Supplemental Table 4.1: Model fit values for AC and waveform data collected for **[Er(hdcCOT)I]$_4$** between T = 2 - 27 K. (Continued)

25	0.00	0.00	0.00	0.08	0.07	0.09	1.69	1.68	1.69	0.09	0.07	0.11
25.5	0.00	0.00	0.00	0.07	0.06	0.08	1.66	1.65	1.66	0.11	0.09	0.14
26	0.00	0.00	0.00	0.06	0.05	0.07	1.62	1.62	1.63	0.16	0.13	0.19
26.5	0.00	0.00	0.00	0.04	0.03	0.06	1.59	1.58	1.59	0.19	0.16	0.23
27	0.00	0.00	0.00	0.03	0.02	0.05	1.56	1.56	1.56	0.24	0.20	0.27

Computational Methods

All calculations were carried out at the CASSCF level using the OpenMolcas computational package.[bb] Basis functions of the ANO-RCC type were generated with the SEWARD module. The quality of a specific atomic basis function was determined by the atom's connectivity to the Er^{3+} ion (**Er**: ANO-RCC-VTZP; **atoms bound to Er**: ANO-RCC-VDZP; **all other atoms**: ANO-RCC-VDZ). Two-electron integrals were Cholesky decomposed (10^{-6} cutoff). A 7-orbital, 11-electron active space (CAS(11,7)) was selected for the CASSCF calculation, which was carried out using the RASSCF module. In this space, all 35 configuration-interaction (CI)

[bb] Aquilante, F.; Autschbach, J.; Baiardi, A.; Battaglia, S.; Borin, V. A.; Chibotaru, L. F.; Conti, I.; De Vico, L.; Delcey, M.; Fdez. Galván, I.; Ferré, N.; Freitag, L.; Garavelli, M.; Gong, X.; Knecht, S.; Larsson, E. D.; Lindh, R.; Lundberg, M.; Malmqvist, P. Å.; Nenov, A.; Norell, J.; Odelius, M.; Olivucci, M.; Pedersen, T. B.; Pedraza-González, L.; Phung, Q. M.; Pierloot, K.; Reiher, M.; Schapiro, I.; Segarra-Martí, J.; Segatta, F.; Seijo, L.; Sen, S.; Sergentu, D.-C.; Stein, C. J.; Ungur, L.; Vacher, M.; Valentini, A.; Veryazov, V. "Modern quantum chemistry with [Open]Molcas" *The Journal of Chemical Physics* **2020**, *152*, 214117; Fdez. Galván, I.; Vacher, M.; Alavi, A.; Angeli, C.; Aquilante, F.; Autschbach, J.; Bao, J. J.; Bokarev, S. I.; Bogdanov, N. A.; Carlson, R. K.; Chibotaru, L. F.; Creutzberg, J.; Dattani, N.; Delcey, M. G.; Dong, S. S.; Dreuw, A.; Freitag, L.; Frutos, L. M.; Gagliardi, L.; Gendron, F.; Giussani, A.; González, L.; Grell, G.; Guo, M.; Hoyer, C. E.; Johansson, M.; Keller, S.; Knecht, S.; Kovačević, G.; Källman, E.; Li Manni, G.; Lundberg, M.; Ma, Y.; Mai, S.; Malhado, J. P.; Malmqvist, P. Å.; Marquetand, P.; Mewes, S. A.; Norell, J.; Olivucci, M.; Oppel, M.; Phung, Q. M.; Pierloot, K.; Plasser, F.; Reiher, M.; Sand, A. M.; Schapiro, I.; Sharma, P.; Stein, C. J.; Sørensen, L. K.; Truhlar, D. G.; Ugandi, M.; Ungur, L.; Valentini, A.; Vancoillie, S.; Veryazov, V.; Weser, O.; Wesołowski, T. A.; Widmark, P.-O.; Wouters, S.; Zech, A.; Zobel, J. P.; Lindh, R. "OpenMolcas: From Source Code to Insight" *Journal of Chemical Theory and Computation* **2019**, *15*, 5925.; Manni, G. L.; Galván, I. F.; Alavi, A.; Aleotti, F.; Aquilante, F.; Autschbach, J.; Avagliano, D.; Baiardi, A.; Bao, J. J.; Battaglia, S.; Birnoschi, L.; Blanco-González, A.; Bokarev, S. I.; Broer, R.; Cacciari, R.; Calio, P. B.; Carlson, R. K.; Couto, R. C.; Cerdán, L.; Chibotaru, L. F.; Chilton, N. F.; Church, J. R.; Conti, I.; Coriani, S.; Cuéllar-Zuquin, J.; Daoud, R. E.; Dattani, N.; Decleva, P.; de Graaf, C.; Delcey, M. G.; De Vico, L.; Dobrautz, W.; Dong, S. J. S.; Feng, R. L.; Ferré, N.; Filatov, M.; Gagliardi, L.; Garavelli, M.; González, L.; Guan, Y. F.; Guo, M. Y.; Hennefarth, M. R.; Hermes, M. R.; Hoyer, C. E.; Huix-Rotllant, M.; Jaiswal, V. K.; Kaiser, A.; Kaliakin, D. S.; Khamesian, M.; King, D. S.; Kochetov, V.; Krosnicki, M.; Kumaar, A. A.; Larsson, E. D.; Lehtola, S.; Lepetit, M. B.; Lischka, H.; Ríos, P. L.; Lundberg, M.; Ma, D. X.; Mai, S.; Marquetand, P.; Merritt, I. C. D.; Montorsi, F.; Mörchen, M.; Nenov, A.; Nguyen, V. H. A.; Nishimoto, Y.; Oakley, M. S.; Olivucci, M.; Oppel, M.; Padula, D.; Pandharkar, R.; Phung, Q. M.; Plasser, F.; Raggi, G.; Rebolini, E.; Reiher, M.; Rivalta, I.; Roca-Sanjuán, D.; Romig, T.; Safari, A. A.; Sánchez-Mansilla, A.; Sand, A. M.; Schapiro, I.; Scott, T. R.; Segarra-Martí, J.; Segatta, F.; Sergentu, D. C.; Sharma, P.; Shepard, R.; Shu, Y. N.; Staab, J. K.; Straatsma, T. P.; Sorensen, L. K.; Tenorio, B. N. C.; Truhlar, D. G.; Ungur, L.; Vacher, M.; Veryazov, V. "The OpenMolcas: A Community-Driven Approach to Advancing Computational Chemistry" *Journal of Chemical Theory and Computation* **2023**, *19*, 6933.

roots of spin multiplicity 4 and all 112 CI roots of spin multiplicity 2 were included. The RASSI module was used to calculate spin-orbit matrix elements between CAS output wavefunctions. The SINGLE_ANISO module of OpenMolcas was used to calculate relevant magnetic properties based on these multiconfigurational SCF results. The POLY_ANISO module was used to calculate dipolar coupling interactions for the ground Kramers doublets in **[Er(hdcCOT)I]$_4$** and its derivatives, as described below.

Four sets of computational calculations were completed with the utilization of SINGLE_ANISO and POLY_ANISO suites of OpenMolcas. The initial set of calculations were completed iteratively on each erbium center of the tetranuclear compound with input geometries arising from the exact crystallographic coordinates, while substituting the other three centers with yttrium(III), a diamagnetic counterpart to erbium(III) with a similar ionic radius. The tetranuclear cluster, taken as-is, from crystallographic coordinates is of C_2 symmetry, and is referred to as **[Er(hdcCOT)I]$_4$**; **crystallographic**.

The second set of calculations looked to compare the crystallographic compound to one with truncated COT rings, in which the [hdc] groups were removed and replaced with planar hydrogen atoms. This modified tetranuclear cluster is also of C_2 symmetry and is referred to as **[ErCOTI]$_4$; Er-C$_2$**. For the third set of calculations, S_4 symmetry was imposed onto the truncated structure by symmetrizing it with the Largent-Polik-Schmidt algorithm via WebMO.[cc] This modified tetranuclear cluster is of S_4 symmetry and is referred to as **[ErCOTI]$_4$; Er-S$_4$**. The last set of calculations was completed on an idealized tetrahedral compound, referred to as **[ErCOTI]$_4$;**

[cc] Largent, R. J.; Polik, W. F.; Schmidt, J. R. "Symmetrizer: Algorithmic determination of point groups in nearly symmetric molecules" *J Comput Chem* **2012**, *33*, 1637; Polik, W. F.; Schmidt, J. R. "WebMO: Web-based computational chemistry calculations in education and research" *Wires Comput Mol Sci* **2022**, *12*.

Er-T$_d$. Dummy atoms were generated in place of the COT-centroids. These dummy atoms and the Er-I core, were symmetrized to T$_d$ symmetry with the Largent-Polik-Schmidt algorithm. Post-facto, idealized COT rings were generated by placing carbon atoms around the dummy atoms at a distance of 1.85 A (average from crystal structure). Planar hydrogens were placed on each carbon to generate the final structure, **Er-T$_d$**.

In each set of ab initio calculations, the four erbium centers were computed independently from one another to generate the electronic Kramers doublet (KD) manifolds of the compounds via the RASSI, RASSCF, RASSCF2, and SINGLE_ANISO modules of OpenMolcas. These outputs were used as downstream inputs for the POLY_ANISO program, through which the dipolar coupled manifolds of the interacting ground KDs were generated. In its calculations of pseudospin Hamiltonian tensors of each multiplet (pseudospin S = ½, referred to as Dipole Doublets, or DDs), POLY_ANISO provides output written in the coordinate systems of the local magnetic axes of the interacting sites. To generate the 3D surface in Figure 4.3, the main magnetic axis of each multiplet was identified within the g-tensor block and plotted in 3-space scaled by its respective g_z value (scaled by ¼ for visibility) and was added(subtracted) from the coordinates of the center of the cluster. For this compound, the main magnetic axis was depicted by the Z_m vector for each multiplet, with the g_z values corresponding to exactly double the eigenvalues calculated in this coordinate system. The ab initio blocking barrier of Zeeman eigenvalues is calculated within POLY_ANISO after adjusting the coordinate system to the magnetic axes of the whole system, which modifies the eigenvalues to the new coordinate system.

The impact of symmetry on the compound is best exemplified in the tabulation of g-values, eigenvalues, and energies of the KD and DD states (see below). The ground states (KD$_0$) across **Er-crystallographic**, **Er-C$_2$**, **Er-S$_4$**, and **Er-T$_d$** are nearly unchanged. There are differences in states KD_2 and up, however, these are not utilized in the calculations of DDs within POLY_ANISO.

Supplemental Table 4.2: $J = 15/2$ manifold g-values of four centers for **[Er(hdcCOT)I]$_4$** and computed derivatives.

[Er(hdcCOT)I]$_4$; crystallographic												
	Center 1			**Center 2**			**Center 3**			**Center 4**		
KD_n, n =	g_z	g_y	g_x	g_z	g_y	g_x	g_z	g_y	g_x	g_z	g_y	g_x
0	17.962	0.000	0.000	17.954	0.000	0.000	17.969	0.000	0.000	17.967	0.000	0.000
1	15.538	0.002	0.002	15.530	0.002	0.002	15.545	0.003	0.003	15.541	0.003	0.003
2	9.136	3.900	0.942	8.998	3.894	0.927	9.305	3.064	2.090	9.294	3.076	2.071
3	7.935	4.537	1.370	7.879	4.469	1.360	7.712	4.839	3.603	7.679	4.934	3.601
4	1.091	3.591	4.038	1.072	3.572	4.011	3.972	2.580	1.846	3.969	2.591	1.833
5	7.485	1.518	0.900	7.470	1.503	0.888	7.217	0.962	0.150	7.204	0.962	0.149
6	9.616	0.396	0.160	9.604	0.394	0.156	9.723	0.636	0.001	9.703	0.633	0.003
7	8.635	0.817	0.310	8.639	0.808	0.306	8.851	1.108	0.548	8.889	1.100	0.547
[ErCOTI]$_4$; C_2												
	Center 1			**Center 2**			**Center 3**			**Center 4**		
KD_n, n =	g_z	g_y	g_x	g_z	g_y	g_x	g_z	g_y	g_x	g_z	g_y	g_x
0	17.964	0.000	0.000	17.968	0.000	0.000	17.965	0.000	0.000	17.968	0.000	0.000
1	15.541	0.002	0.002	15.545	0.003	0.002	15.542	0.002	0.002	15.544	0.003	0.002
2	11.004	5.212	1.326	9.231	3.629	2.205	11.037	5.229	1.324	9.226	3.632	2.203
3	10.942	1.635	0.477	8.349	3.988	2.752	10.945	1.637	0.483	8.347	3.990	2.749
4	1.842	3.232	3.890	1.976	2.979	3.944	1.847	3.241	3.889	1.974	2.981	3.943
5	7.205	1.000	0.346	7.169	0.954	0.023	7.208	1.000	0.349	7.169	0.954	0.023
6	9.896	0.429	0.040	9.904	0.541	0.029	9.896	0.426	0.039	9.897	0.541	0.029
7	8.571	0.741	0.305	8.945	0.978	0.450	8.573	0.737	0.304	8.950	0.977	0.449
[ErCOTI]$_4$; S_4												
	Center 1			**Center 2**			**Center 3**			**Center 4**		
KD_n, n =	g_z	g_y	g_x	g_z	g_y	g_x	g_z	g_y	g_x	g_z	g_y	g_x
0	17.967	0.000	0.000	17.964	0.000	0.000	17.965	0.000	0.000	17.965	0.000	0.000
1	15.546	0.003	0.003	15.543	0.001	0.001	15.545	0.001	0.001	15.544	0.003	0.003
2	2.773	5.631	8.199	9.906	5.174	2.104	9.926	5.189	2.107	2.768	5.640	8.195
3	1.751	5.017	8.192	10.104	2.261	1.756	10.101	2.268	1.762	1.749	5.016	8.198
4	2.010	3.178	3.930	3.927	2.494	1.494	3.925	2.501	1.498	2.008	3.180	3.928
5	7.097	1.260	0.185	6.974	0.745	0.239	6.976	0.747	0.240	7.097	1.260	0.185
6	10.257	0.699	0.185	10.286	0.268	0.076	10.286	0.269	0.077	10.247	0.700	0.185
7	9.593	1.152	0.554	8.958	0.451	0.256	8.963	0.452	0.257	9.601	1.151	0.554

Supplemental Table 4.2: $J = 15/2$ manifold g-values of four centers for **[Er(hdcCOT)I]$_4$** and computed derivatives. (Continued)

[ErCOTI]$_4$; T$_d$												
	Center 1			**Center 2**			**Center 3**			**Center 4**		
KD_n, n =	g_z	g_y	g_x	g_z	g_y	g_x	g_z	g_y	g_x	g_z	g_y	g_x
0	17.965	0.000	0.000	17.967	0.000	0.000	17.967	0.000	0.000	17.965	0.000	0.000
1	15.552	0.003	0.003	15.549	0.003	0.003	15.55	0.003	0.003	15.551	0.003	0.003
2	0.284	7.666	9.999	0.263	8.449	8.627	0.977	7.879	8.248	0.177	7.830	9.787
3	11.972	0.801	0.61	11.498	1.090	1.020	10.846	1.557	1.481	11.919	0.866	0.669
4	3.619	1.366	1.149	3.641	0.144	0.065	3.638	0.218	0.133	3.621	1.277	0.823
5	6.077	1.127	0.975	6.084	0.981	0.889	6.089	1.033	1.015	6.072	1.322	0.947
6	10.76	0.064	0.035	10.759	0.038	0.014	10.748	0.057	0.012	10.76	0.066	0.023
7	8.390	1.115	0.989	8.400	0.957	0.910	8.417	1.057	0.982	8.404	1.188	1.073

Supplemental Table 4.3: $J = 15/2$ manifolds of four centers and average of all centers for **[Er(hdcCOT)I]$_4$** and computed derivatives.

[Er(hdcCOT)I]$_4$; crystallographic										
	Center 1		**Center 2**		**Center 3**		**Center 4**		**Centers AVG.**	
KD_n, n =	M_z (μ_B)	E (cm^{-1})	M_z (μ_B)	E (cm^{-1})	M_z (μ_B)	E (cm^{-1})	M_z (μ_B)	E (cm^{-1})	M_z (μ_B)	E (cm^{-1})
0	8.98	0.00	8.98	0.00	8.98	0.00	8.98	0.00	8.98	0.00
1	7.77	87.19	7.77	87.19	7.77	85.50	7.77	85.48	7.77	86.34
2	4.57	245.21	4.50	245.21	4.65	243.19	4.65	243.19	4.59	244.20
3	3.97	249.05	3.94	249.05	3.86	251.73	3.84	251.72	3.90	250.39
4	0.55	291.84	0.54	291.84	1.99	292.81	1.98	292.83	1.26	292.33
5	3.74	348.02	3.73	348.02	3.61	351.17	3.60	351.17	3.67	349.60
6	4.81	369.32	4.80	369.32	4.86	367.18	4.85	367.11	4.83	368.23
7	4.32	392.81	4.32	392.81	4.43	393.57	4.44	393.53	4.38	393.18
[ErCOTI]$_4$; C$_2$										
	Center 1		**Center 2**		**Center 3**		**Center 4**		**Centers AVG.**	
KD_n, n =	M_z (μ_B)	E (cm^{-1})	M_z (μ_B)	E (cm^{-1})	M_z (μ_B)	E (cm^{-1})	M_z (μ_B)	E (cm^{-1})	M_z (μ_B)	E (cm^{-1})
0	8.98	0.00	8.98	0.00	8.98	0.00	8.98	0.00	8.98	0.00
1	7.77	89.84	7.77	88.98	7.77	89.85	7.77	88.98	7.77	89.41
2	5.50	245.27	4.62	246.39	5.52	245.28	4.61	246.39	5.06	245.83
3	5.47	252.51	4.17	254.07	5.47	252.51	4.17	254.07	4.82	253.29

Supplemental Table 4.3: $J = 15/2$ manifolds of four centers and average of all centers for **[Er(hdcCOT)I]$_4$** and computed derivatives. (Continued)

4	0.92	291.94	0.99	294.56	0.92	291.94	0.99	294.56	0.95	293.25
5	3.60	351.29	3.58	352.95	3.60	351.29	3.58	352.95	3.59	352.12
6	4.95	371.72	4.95	370.36	4.95	371.72	4.95	370.36	4.95	371.04
7	4.29	395.43	4.47	395.98	4.29	395.43	4.47	395.98	4.38	395.71
[ErCOTI]$_4$; S$_4$										
	Center 1		**Center 2**		**Center 3**		**Center 4**		**Centers AVG.**	
KD_n, n =	M$_z$ (μ_B)	E (cm^{-1})	M$_z$ (μ_B)	E (cm^{-1})	M$_z$ (μ_B)	E (cm^{-1})	M$_z$ (μ_B)	E (cm^{-1})	M$_z$ (μ_B)	E (cm^{-1})
0	8.98	0.00	8.98	0.00	8.98	0.00	8.98	0.00	8.98	0.00
1	7.77	88.46	7.77	87.46	7.77	87.46	7.77	88.46	7.77	87.96
2	1.39	245.84	4.95	243.97	4.96	243.97	1.38	245.84	3.17	244.91
3	0.88	252.80	5.05	250.64	5.05	250.64	0.87	252.80	2.96	251.72
4	1.01	293.63	1.96	290.36	1.96	290.36	1.00	293.63	1.48	291.99
5	3.55	352.47	3.49	351.39	3.49	351.39	3.55	352.47	3.52	351.93
6	5.13	369.52	5.14	368.41	5.14	368.41	5.12	369.52	5.13	368.97
7	4.80	396.25	4.48	394.15	4.48	394.15	4.80	396.25	4.64	395.20
[ErCOTI]$_4$; T$_d$										
	Center 1		**Center 2**		**Center 3**		**Center 4**		**Centers AVG.**	
KD_n, n =	M$_z$ (μ_B)	E (cm^{-1})	M$_z$ (μ_B)	E (cm^{-1})	M$_z$ (μ_B)	E (cm^{-1})	M$_z$ (μ_B)	E (cm^{-1})	M$_z$ (μ_B)	E (cm^{-1})
0	8.98	0.00	8.98	0	8.98	0	8.98	0	8.98	0.00
1	7.77	84.67	7.77	85.31	7.77	84.44	7.77	85.61	7.77	85.01
2	0.32	243.64	0.3	244.37	0.52	244.22	0.27	244.27	0.35	244.12
3	5.98	251.97	5.75	250.14	5.42	249.52	5.96	252.77	5.78	251.10
4	1.81	290.13	1.82	289.14	1.82	289.18	1.81	290.49	1.81	289.74
5	3.04	357.25	3.04	354.46	3.04	354.35	3.03	357.46	3.04	355.88
6	5.37	370.79	5.38	366.74	5.37	366.2	5.37	371.15	5.37	368.72
7	4.19	399.01	4.19	394.74	4.19	394.55	4.19	399.21	4.19	396.88

Supplemental Table 4.4: Dipole coupled state g-values and eigenvalues for **[Er(hdcCOT)I]$_4$** and computed derivatives in the coordinate system of the **local** magnetic axes of each multiplet.

	[Er(hdcCOT)I]$_4$				**[ErCOTI]$_4$; C$_2$**			
DD$_n$, n =	**g_z**	**g_y**	**g_x**	**Eigenvalue**	**g_z**	**g_y**	**g_x**	**Eigenvalue**
0	38.891	0.000	0.000	±19.4456297	39.420	0.000	0.000	±19.7101348
1	40.229	0.000	0.000	±20.1146323	40.264	0.000	0.000	±20.1319046
2	45.046	0.000	0.000	±22.5228523	44.587	0.000	0.000	±22.2933022
3	34.903	0.000	0.000	±17.4514278	35.146	0.000	0.000	±17.5729380
4	34.893	0.000	0.000	±17.4464474	35.144	0.000	0.000	±17.5720855
5	36.921	0.000	0.000	±18.4603020	36.704	0.000	0.000	±18.3518015
6	36.929	0.000	0.000	±18.4644730	36.704	0.000	0.000	±18.3518518
7	1.601	0.000	0.000	±0.8003467	1.251	0.000	0.000	±0.6253811
	[ErCOTI]$_4$; S$_4$				**[ErCOTI]$_4$; T$_d$**			
DD$_n$, n =	**g_z**	**g_y**	**g_x**	**Eigenvalue**	**g_z**	**g_y**	**g_x**	**Eigenvalue**
0	39.863	0.000	0.000	±19.9316030	41.961	0.000	0.000	±20.9802786
1	38.860	0.000	0.000	±19.4298331	41.346	0.000	0.000	±20.6728665
2	45.440	0.000	0.000	±22.7197613	41.159	0.000	0.000	±20.5793409
3	36.024	0.000	0.000	±18.0121769	36.249	0.000	0.000	±18.1244991
4	36.024	0.000	0.000	±18.0122030	36.153	0.000	0.000	±18.0763529
5	35.837	0.000	0.000	±17.9185661	35.704	0.000	0.000	±17.85190712
6	35.834	0.000	0.000	±17.9172300	35.618	0.000	0.000	±17.8089950
7	0.146	0.000	0.000	±0.0731696	0.465	0.000	0.000	±0.2326533

Supplemental Table 4.5: Dipole coupled ab initio blocking barrier (Zeeman Eigenstates) generated by coupling the ground KDs for **[Er(hdcCOT)I]$_4$** and computed derivatives in the coordinate system of the **main** magnetic axes.

	[Er(hdcCOT)I]$_4$		**[ErCOTI]$_4$; C$_2$**		**[ErCOTI]$_4$; S$_4$**		**[ErCOTI]$_4$; T$_d$**	
DD$_n$, n =	**Energy (cm^{-1})**	**Eigenvalue**	**Energy (cm^{-1})**	**Eigenvalue**	**Energy (cm^{-1})**	**Eigenvalue**	**Energy (cm^{-1})**	**Eigenvalue**
0	0.00	±19.4456297	0.00	±19.7101348	0.00	±19.9316030	0.00	±20.9802786
1	0.08	±0.9446066	0.09	±0.7130629	0.02	±0.0865768	0.01	±0.0389920
2	0.52	±0.0045532	0.54	±0.0011535	0.53	±0.0016834	0.02	±0.0389920
3	1.30	±9.2536713	1.31	±9.4992436	1.34	±10.0096392	1.17	±10.6256575
4	1.30	±9.2473517	1.31	±9.4978283	1.34	±10.0085406	1.18	±10.5838503
5	1.36	±10.1965116	1.38	±10.2120447	1.35	±9.9236472	1.19	±10.3936131
6	1.36	±10.1937247	1.38	±10.2111530	1.35	±9.9213790	1.19	±10.3574363
7	4.72	±0.0017664	4.74	±0.0002618	4.84	± 0.0005848	4.69	±0.22922925

Supplemental Table 4.6: Average magnetic moment matrix elements between dipole coupled Zeeman eigenstates for **[Er(hdcCOT)I]$_4$** and computed derivatives.

[Er(hdcCOT)I]$_4$								
OPPOSITE SIDE	**DD$_0$– >**	**DD$_1$– >**	**DD$_2$– >**	**DD$_3$– >**	**DD$_4$– >**	**DD$_5$– >**	**DD$_6$– >**	**DD$_7$– >**
<DD$_0$+	1.50E-20	5.56E-09	5.71E-10	8.72E-13	8.77E-13	4.01E-11	3.98E-11	1.04E-10
<DD$_1$+		5.05E-16	5.05E-10	8.00E-05	8.01E-05	4.08E-11	4.10E-11	1.32E-10
<DD$_2$+			8.52E-13	4.03E-12	3.59E-05	4.37E-11	8.42E-05	4.49E-10
<DD$_3$+				1.42E-18	1.42E-07	2.53E-09	5.09E-09	3.84E-12
<DD$_4$+					3.96E-17	5.20E-09	2.54E-09	3.40E-05
<DD$_5$+						7.14E-16	1.56E-05	7.80E-05
<DD$_6$+							1.06E-16	4.05E-11
<DD$_7$+								2.74E-13
SAME SIDE	**DD$_0$+ >**	**DD$_1$+ >**	**DD$_2$+ >**	**DD$_3$+ >**	**DD$_4$+ >**	**DD$_5$+ >**	**DD$_6$+ >**	**DD$_7$+ >**
<DD$_0$+	x	1.07E-09	5.67E-10	7.95E-05	7.94E-05	3.45E-05	3.47E-05	1.04E-10
<DD$_1$+		x	5.07E-10	8.71E-13	8.91E-13	3.56E-05	3.54E-05	1.32E-10
<DD$_2$+			x	3.57E-05	4.01E-12	8.43E-05	4.38E-11	9.46E-11
<DD$_3$+				x	8.13E-07	5.24E-09	6.25E-10	3.42E-05
<DD$_4$+					x	6.28E-10	5.33E-09	3.82E-12
<DD$_5$+						x	4.04E-06	4.05E-11
<DD$_6$+							x	7.81E-05
<DD$_7$+								x

Supplemental Table 4.6: Average magnetic moment matrix elements between dipole coupled Zeeman eigenstates for **[Er(hdcCOT)I]$_4$** and computed derivatives. (Continued)

[ErCOTI]$_4$; C$_2$								
OPPOSITE SIDE	**DD$_0$– >**	**DD$_1$– >**	**DD$_2$– >**	**DD$_3$– >**	**DD$_4$– >**	**DD$_5$– >**	**DD$_6$– >**	**DD$_7$– >**
<DD$_0$+	2.40E-22	1.83E-09	2.08E-10	1.81E-12	1.80E-12	5.21E-12	5.28E-12	3.70E-11
<DD$_1$+		4.86E-17	2.30E-10	4.05E-05	3.81E-05	5.48E-12	5.02E-12	5.97E-11
<DD$_2$+			4.20E-13	5.33E-12	3.07E-05	6.98E-12	4.43E-05	1.59E-10
<DD$_3$+				1.28E-18	7.39E-07	8.19E-10	1.63E-09	4.18E-12
<DD$_4$+					1.29E-18	1.61E-09	8.30E-10	2.41E-05
<DD$_5$+						1.63E-17	3.34E-06	3.69E-05
<DD$_6$+							1.63E-17	5.81E-12
<DD$_7$+								4.25E-15
SAME SIDE	**DD$_0$+ >**	**DD$_1$+ >**	**DD$_2$+ >**	**DD$_3$+ >**	**DD$_4$+ >**	**DD$_5$+ >**	**DD$_6$+ >**	**DD$_7$+ >**
<DD$_0$+	x	7.23E-10	2.08E-10	3.78E-05	3.80E-05	2.53E-05	2.49E-05	3.71E-11
<DD$_1$+		x	2.26E-10	1.81E-12	1.93E-12	2.40E-05	2.63E-05	6.04E-11
<DD$_2$+			x	2.98E-05	5.18E-12	4.67E-05	7.36E-12	7.41E-11
<DD$_3$+				x	1.72E-06	2.07E-09	8.00E-11	2.38E-05
<DD$_4$+					x	7.48E-11	2.02E-09	4.12E-12
<DD$_5$+						x	1.65E-06	5.78E-12
<DD$_6$+							x	3.67E-05
<DD$_7$+								x

Supplemental Table 4.6: Average magnetic moment matrix elements between dipole coupled Zeeman eigenstates for **[Er(hdcCOT)I]$_4$** and computed derivatives. (Continued)

[ErCOTI]$_4$; S$_4$								
OPPOSITE SIDE	**DD$_0$– >**	**DD$_1$– >**	**DD$_2$– >**	**DD$_3$– >**	**DD$_4$– >**	**DD$_5$– >**	**DD$_6$– >**	**DD$_7$– >**
<DD$_0$+	8.36E-21	4.35E-08	3.73E-10	1.39E-11	1.37E-11	1.39E-12	1.34E-12	7.40E-11
<DD$_1$+		5.58E-15	3.99E-10	1.31E-11	1.44E-11	8.58E-05	9.14E-05	1.01E-10
<DD$_2$+			1.22E-15	6.62E-12	1.03E-04	1.66E-11	2.18E-05	8.07E-10
<DD$_3$+				6.50E-18	1.01E-05	9.53E-09	1.98E-08	8.54E-05
<DD$_4$+					6.19E-18	2.03E-08	9.39E-09	5.44E-12
<DD$_5$+						5.03E-18	2.32E-07	1.50E-11
<DD$_6$+							1.08E-18	1.97E-05
<DD$_7$+								1.82E-15
SAME SIDE	**DD$_0$+ >**	**DD$_1$+ >**	**DD$_2$+ >**	**DD$_3$+ >**	**DD$_4$+ >**	**DD$_5$+ >**	**DD$_6$+ >**	**DD$_7$+ >**
<DD$_0$+	x	1.44E-09	3.66E-10	2.04E-05	2.07E-05	8.82E-05	8.78E-05	7.43E-11
<DD$_1$+		x	3.93E-10	2.14E-05	1.96E-05	1.42E-12	1.33E-12	9.60E-11
<DD$_2$+			x	9.68E-05	6.19E-12	2.31E-05	1.75E-11	3.93E-11
<DD$_3$+				x	6.27E-07	2.42E-08	5.05E-09	5.51E-12
<DD$_4$+					x	4.88E-09	2.42E-08	8.57E-05
<DD$_5$+						x	7.41E-06	1.99E-05
<DD$_6$+							x	1.52E-11
<DD$_7$+								x

Supplemental Table 4.6: Average magnetic moment matrix elements between dipole coupled Zeeman eigenstates for **[Er(hdcCOT)I]$_4$** and computed derivatives. (Continued)

[ErCOTI]$_4$; T$_d$								
OPPOSITE SIDE	**DD$_0$– >**	**DD$_1$– >**	**DD$_2$– >**	**DD$_3$– >**	**DD$_4$– >**	**DD$_5$– >**	**DD$_6$– >**	**DD$_7$– >**
<DD$_0$+	2.16E-17	1.65E-09	1.59E-09	1.60E-13	2.61E-13	1.01E-13	9.29E-14	6.53E-11
<DD$_1$+		2.16E-17	4.26E-09	4.63E-14	4.08E-05	6.62E-14	1.23E-05	5.26E-11
<DD$_2$+			4.91E-14	2.31E-14	3.65E-05	1.28E-05	5.35E-14	4.97E-11
<DD$_3$+				1.54E-17	8.64E-08	2.01E-09	2.48E-09	2.66E-13
<DD$_4$+					1.89E-20	6.01E-09	4.28E-09	1.35E-13
<DD$_5$+						1.42E-20	1.77E-08	3.74E-05
<DD$_6$+							5.93E-21	3.56E-05
<DD$_7$+								8.45E-17
SAME SIDE	**DD$_0$+ >**	**DD$_1$+ >**	**DD$_2$+ >**	**DD$_3$+ >**	**DD$_4$+ >**	**DD$_5$+ >**	**DD$_6$+ >**	**DD$_7$+ >**
<DD$_0$+	x	3.25E-09	2.91E-09	2.11E-05	1.29E-05	3.70E-05	3.89E-05	1.40E-11
<DD$_1$+		x	1.42E-08	3.85E-05	3.27E-14	2.05E-05	4.13E-14	2.96E-11
<DD$_2$+			x	3.84E-05	4.98E-14	7.83E-14	2.17E-05	3.13E-11
<DD$_3$+				x	1.01E-08	1.06E-08	9.82E-09	1.22E-05
<DD$_4$+					x	7.79E-09	6.87E-09	2.01E-05
<DD$_5$+						x	3.25E-08	8.50E-14
<DD$_6$+							x	1.03E-13
<DD$_7$+								x

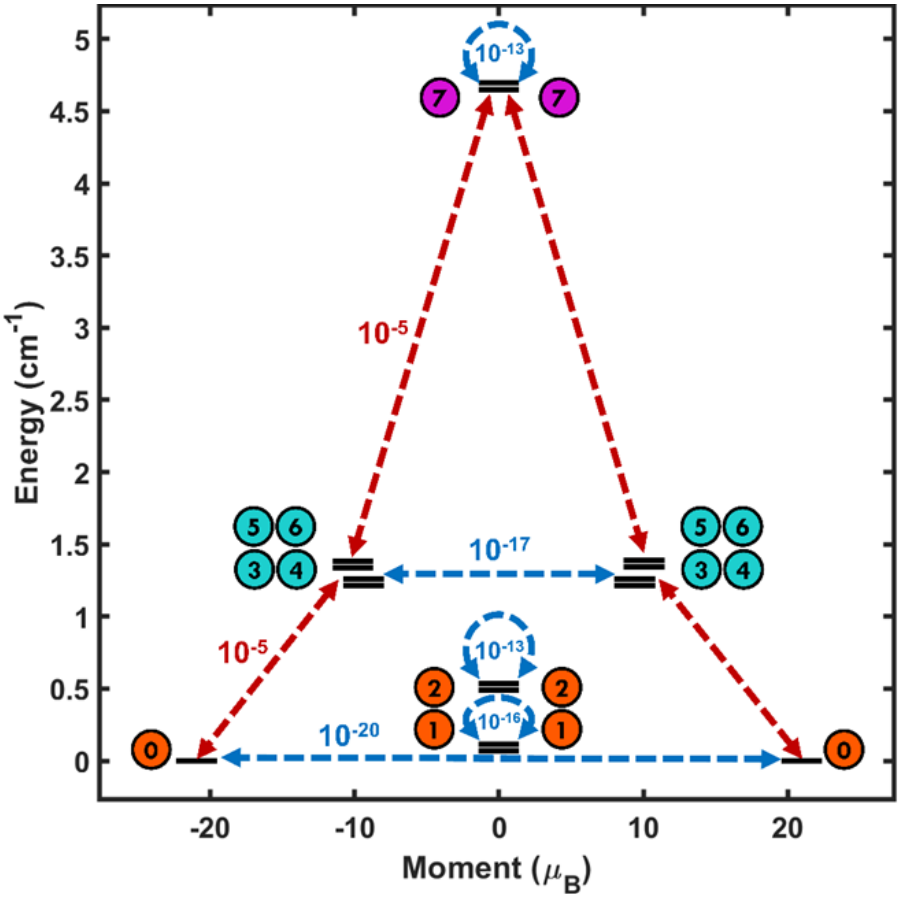

Supplemental Figure 4.9: Dipole-coupled energy manifold of states and transition probabilities between them for crystallographic **[Er(hdcCOT)I]$_4$**.

4.5 Acknowledgements

Chapter 4 is directly adapted from material as it appears in the Journal of the American Chemical Society: Orlova, A.P., Bernbeck, M.G., Rinehart, J.D., "Designing Quantum Spaces of Higher Dimensionality from a Tetranuclear Erbium-Based Single-Molecule Magnet," *J. Amer. Chem. Soc.* **2024**. The dissertation author was the primary researcher and author of this paper.

4.6 References

1. Gaita-Ariño, A.; Luis, F.; Hill, S.; Coronado, E., Molecular spins for quantum computation. Nature Chemistry 2019, 11 (4), 301-309.

2. Wasielewski, M. R.; Forbes, M. D. E.; Frank, N. L.; Kowalski, K.; Scholes, G. D.; Yuen-Zhou, J.; Baldo, M. A.; Freedman, D. E.; Goldsmith, R. H.; Goodson, T.; Kirk, M. L.; McCusker, J. K.; Ogilvie, J. P.; Shultz, D. A.; Stoll, S.; Whaley, K. B., Exploiting chemistry and molecular systems for quantum information science. Nat Rev Chem 2020, 4 (9), 490-504.

3. Stewart, R.; Canaj, A. B.; Liu, S.; Regincós Martí, E.; Celmina, A.; Nichol, G.; Cheng, H.-P.; Murrie, M.; Hill, S., Engineering Clock Transitions in Molecular Lanthanide Complexes. J Am Chem Soc 2024, 146 (16), 11083-11094.

4. Smith, P. W.; Hrubý, J.; Evans, W. J.; Hill, S.; Minasian, S. G., Identification of an X-Band Clock Transition in Cp′3Pr– Enabled by a 4f25d1 Configuration. J Am Chem Soc 2024, 146 (9), 5781-5785.

5. National Academies of Sciences, E.; Medicine, Advancing Chemistry and Quantum Information Science: An Assessment of Research Opportunities at the Interface of Chemistry and Quantum Information Science in the United States. The National Academies Press: Washington, DC, 2023.

6. Chen, Y. C.; Tong, M. L., Single-molecule magnets beyond a single lanthanide ion: the art of coupling. Chem Sci 2022, 13 (30), 8716-8726.

7. Rinehart, J. D.; Long, J. R., Exploiting single-ion anisotropy in the design of f-element single-molecule magnets. Chem Sci 2011, 2 (11), 2078-2085.

8. Hilgar, J. D.; Bernbeck, M. G.; Flores, B. S.; Rinehart, J. D., Metal-ligand pair anisotropy in a series of mononuclear Er-COT complexes. Chem Sci 2018, 9 (36), 7204-7209.

9. Wäckerlin, C.; Cahlík, A.; Goikoetxea, J.; Stetsovych, O.; Medvedeva, D.; Redondo, J.; Svec, M.; Delley, B.; Ondrácek, M.; Pinar, A.; Blanco-Rey, M.; Kolorenc, J.; Arnau, A.; Jelínek, P., Role of the Magnetic Anisotropy in Atomic- Spin Sensing of 1 D Molecular Chains. Acs Nano 2022, 16 (10), 16402–16413.

10. Briganti, M.; Lucaccini, E.; Chelazzi, L.; Ciattini, S.; Sorace, L.; Sessoli, R.; Totti, F.; Perfetti, M., Magnetic Anisotropy Trends along a Full 4f-Series: The fn+7 Effect. J Am Chem Soc 2021, 143 (21), 8108-8115.

11. Gatteschi, D., Physical techniques for the investigation of molecular magnetic clusters. J Phys Chem B 2000, 104 (42), 9780-9787.

12. Li, D. F.; Parkin, S.; Wang, G. B.; Yee, G. T.; Clerac, R.; Wernsdorfer, W.; Holmes, S. M., An=6 cyanide-bridged octanuclear FeNi complex that exhibits slow relaxation of the magnetization. J Am Chem Soc 2006, 128 (13), 4214-4215.

13. Li, D. F.; Parkin, S.; Wang, G. B.; Yee, G. T.; Holmes, S. M., Early metal di- and tricyanometalates: Useful building blocks for constructing magnetic clusters. Inorganic Chemistry 2006, 45 (7), 2773-2775.

14. Maniaki, D.; Pilichos, E.; Perlepes, S. P., Coordination Clusters of 3d-Metals That Behave as Single-Molecule Magnets (SMMs): Synthetic Routes and Strategies. Front Chem 2018, 6:461, 1-28.

15. Mertes, K. M.; Suzuki, Y.; Sarachik, M. P.; Myasoedov, Y.; Shtrikman, H.; Zeldov, E.; Rumberger, E. M.; Hendrickson, D. N.; Christou, G., Mn12-acetate: a prototypical single molecule magnet. Solid State Communications 2003, 127 (2), 131-139.

16. Boskovic, C.; Brechin, E. K.; Streib, W. E.; Folting, K.; Bollinger, J. C.; Hendrickson, D. N.; Christou, G., Single-molecule magnets:: A new family of Mn clusters of formula [MnOX(OCPh)L]. J Am Chem Soc 2002, 124 (14), 3725-3736.

17. Han, H. T.; Li, X. L.; Zhu, X. F.; Zhang, G. S.; Hang, X. X.; Tang, J. K.; Liao, W. P., Single-Molecule Magnetic Behavior in a Calix[8]arene-Capped Heterometallic {DyCo} Square-Antiprismatic Cluster. European Journal of Inorganic Chemistry 2017, (41), 4879-4883.

18. Li, M. Y.; Lan, Y. H.; Ako, A. M.; Wernsdorfer, W.; Anson, C. E.; Buth, G.; Powell, A. K.; Wang, Z. M.; Gao, S., A Family of 3d-4f Octa-Nuclear [MnLn] Wheels (Ln = Sm, Gd, Tb, Dy, Ho, Er, and Y): Synthesis, Structure, and Magnetism. Inorganic Chemistry 2010, 49 (24), 11587-11594.

19. Mereacre, V.; Akhtar, M. N.; Lan, Y. H.; Ako, A. M.; Clérac, R.; Anson, C. E.; Powell, A. K., Structures and magnetic properties of MnLn aggregates with a "square-in-square" topology. Dalton Transactions 2010, 39 (20), 4918-4927.

20. Perfetti, M.; Rinck, J.; Cucinotta, G.; Anson, C. E.; Gong, X. J.; Ungur, L.; Chibotaru, L.; Boulon, M. E.; Powell, A. K.; Sessoli, R., Single Crystal Investigations Unravel the Magnetic Anisotropy of the "Square-In Square" CrDy SMM Coordination Cluster. Front Chem 2019, 7:6, 1-8.

21. Pineda, E. M.; Heesing, C.; Tuna, F.; Zheng, Y. Z.; McInnes, E. J. L.; Schnack, J.; Winpenny, R. E. P., Copper Lanthanide Phosphonate Cages: Highly Symmetric {CuLnP} and {CuLnP} Clusters with C and D Symmetry. Inorganic Chemistry 2015, 54 (13), 6331-6337.

22. Vignesh, K. R.; Langley, S. K.; Swain, A.; Moubaraki, B.; Damjanovic, M.; Wernsdorfer, W.; Rajaraman, G.; Murray, K. S., Slow Magnetic Relaxation and Single-Molecule Toroidal Behaviour in a Family of Heptanuclear {CrLn} (Ln=Tb, Ho, Er) Complexes. Angew Chem Int Edit 2018, 57 (3), 779-784.

23. Xiang, H.; Lu, W. G.; Jiang, L.; Zhang, W. X.; Lan, Y. H., A Family of Double Cubanes {CrLnO} (Ln = Tb, Ho, Er, Yb, Y) Based on Sulfate: Single-Molecule Magnet Behavior in the Terbium and Erbium Analogues. European Journal of Inorganic Chemistry 2016, (6), 907-912.

24. Zheng, Y. Z.; Evangelisti, M.; Tuna, F.; Winpenny, R. E. P., Co-Ln Mixed-Metal Phosphonate Grids and Cages as Molecular Magnetic Refrigerants. J Am Chem Soc 2012, 134 (2), 1057-1065.

25. Stati, D.; van Leusen, J.; Ahmed, N.; Kravtsov, V. C.; Kögerler, P.; Baca, S. G., A {CoIII2DyIII4} Single-Molecule Magnet with an Expanded Core Structure. Cryst Growth Des 2023, 23 (1), 395-402.

26. Han, T.; Ding, Y. S.; Zheng, Y. Z., Lanthanide Clusters Toward Single-Molecule Magnets. Struct Bond 2017, 173, 209-314.

27. Ungur, L.; Lin, S. Y.; Tang, J. K.; Chibotaru, L. F., Single-molecule toroics in Ising-type lanthanide molecular clusters. Chemical Society Reviews 2014, 43 (20), 6894-6905.

28. Pedersen, K. S.; Vindigni, A.; Sessoli, R.; Coulon, C.; Clérac, R., Single-Chain Magnets. In Molecular Magnetic Materials, 2017; pp 131-159.

29. Huang, G.; Daiguebonne, C.; Calvez, G.; Suffren, Y.; Guillou, O.; Guizouarn, T.; Le Guennic, B.; Cador, O.; Bernot, K., Strong Magnetic Coupling and Single-Molecule-Magnet Behavior in Lanthanide-TEMPO Radical Chains. Inorganic Chemistry 2018, 57 (17), 11044-11057.

30. Huang, G.; Fernandez-Garcia, G.; Badiane, I.; Camarra, M.; Freslon, S.; Guillou, O.; Daiguebonne, C.; Totti, F.; Cador, O.; Guizouarn, T.; Le Guennic, B.; Bernot, K., Magnetic Slow Relaxation in a Metal-Organic Framework Made of Chains of Ferromagnetically Coupled Single-Molecule Magnets. Chem-Eur J 2018, 24 (27), 6983-6991.

31. Journaux, Y.; Ferrando-Soria, J.; Pardo, E.; Ruiz-Garcia, R.; Julve, M.; Lloret, F.; Cano, J.; Li, Y. L.; Lisnard, L.; Yu, P.; Stumpf, H.; Pereira, C. L. M., Design of Magnetic Coordination

Polymers Built from Polyoxalamide Ligands: A Thirty Year Story. European Journal of Inorganic Chemistry 2018, (3-4), 228-247.

32. Orlova, A. P.; Varley, M. S.; Bernbeck, M. G.; Kirkpatrick, K. M.; Bunting, P. C.; Gembicky, M.; Rinehart, J. D., Molecular Network Approach to Anisotropic Ising Lattices: Parsing Magnetization Dynamics in Er Systems with 0-3-Dimensional Spin Interactivity. J Am Chem Soc 2023, 145 (40), 22265-22275.

33. Yang, Z. X.; Gong, F.; Lin, D. M.; Huo, Y., Recent advances in polyoxometalate-based single-molecule magnets. Coordination Chemistry Reviews 2023, 492, 215205.

34. Manna, F.; Oggianu, M.; Avarvari, N.; Mercuri, M. L., Lanthanide-Based Metal-Organic Frameworks with Single-Molecule Magnet Properties. Magnetochemistry 2023, 9 (7), 190.

35. Lin, P. H.; Korobkov, I.; Wernsdorfer, W.; Ungur, L.; Chibotaru, L. F.; Murugesu, M., A Rare mu(4)-O Centred Dy-4 Tetrahedron with Coordination-Induced Local Chirality and Single-Molecule Magnet Behaviour. European Journal of Inorganic Chemistry 2011, (10), 1535-1539.

36. Anwar, M. U.; Thompson, L. K.; Dawe, L. N.; Habib, F.; Murugesu, M., Predictable self-assembled [2 x 2] Ln(III)(4) square grids (Ln = Dy,Tb)-SMM behaviour in a new lanthanide cluster motif. Chem Commun 2012, 48 (38), 4576-4578.

37. Chandrasekhar, V.; Das, S.; Dey, A.; Hossain, S.; Sutter, J. P., Tetranuclear Lanthanide (III) Complexes Containing Dimeric Subunits: Single-Molecule Magnet Behavior for the Dy-4 Analogue. Inorganic Chemistry 2013, 52 (20), 11956-11965.

38. Guo, P. H.; Liu, J. L.; Zhang, Z. M.; Ungur, L.; Chibotaru, L. F.; Leng, J. D.; Guo, F. S.; Tong, M. L., The First {Dy-4} Single-Molecule Magnet with a Toroidal Magnetic Moment in the Ground State. Inorganic Chemistry 2012, 51 (3), 1233-1235.

39. Wang, B.; Wei, C. Y., Structures, fluorescent properties and single-molecule-magnet behavior of two Ln (Ln = Tb and Dy) clusters. J Mol Struct 2020, 1216, 128241.

40. Orlova, A. P.; Hilgar, J. D.; Bernbeck, M. G.; Gembicky, M.; Rinehart, J. D., Intuitive Control of Low-Energy Magnetic Excitations via Directed Dipolar Interactions in a Series of Er(III)-Based Complexes. J Am Chem Soc 2022, 144 (25), 11316-11325.

41. Hilgar, J. D.; Bernbeck, M. G.; Rinehart, J. D., Million-fold Relaxation Time Enhancement across a Series of Phosphino-Supported Erbium Single-Molecule Magnets. J Am Chem Soc 2019, 141 (5), 1913-1917.

42. Bernbeck, M. G.; Hilgar, J. D.; Rinehart, J. D., Probing axial anisotropy in dinuclear alkoxide-bridged Er-COT single-molecule magnets. Polyhedron 2020, 175, 114206.

43. Bernbeck, M. G.; Orlova, A. P.; Hilgar, J. D.; Gembicky, M.; Ozerov, M.; Rinehart, J. D., Dipolar Coupling as a Mechanism for Fine Control of Magnetic States in ErCOT-Alkyl Molecular Magnets. J Am Chem Soc 2024, 146 (11), 7243–7256.

44. Abbas, G.; Lan, Y. H.; Kostakis, G. E.; Wernsdorfer, W.; Anson, C. E.; Powell, A. K., Series of Isostructural Planar Lanthanide Complexes [Ln(μ-OH)(mdeaH)(piv)] with Single Molecule Magnet Behavior for the Dy Analogue. Inorganic Chemistry 2010, 49 (17), 8067-8072.

45. Biswas, S.; Das, S.; Gupta, T.; Singh, S. K.; Pissas, M.; Rajaraman, G.; Chandrasekhar, V., Observation of Slow Relaxation and Single-Molecule Toroidal Behavior in a Family of Butterfly-Shaped Ln Complexes. Chem-Eur J 2016, 22 (51), 18532-18550.

46. Blagg, R. J.; Ungur, L.; Tuna, F.; Speak, J.; Comar, P.; Collison, D.; Wernsdorfer, W.; McInnes, E. J. L.; Chibotaru, L. F.; Winpenny, R. E. P., Magnetic relaxation pathways in lanthanide single-molecule magnets. Nature Chemistry 2013, 5 (8), 673-678.

47. Chen, H. M.; Wang, W. M.; Li, X. Q.; Chu, X. Y.; Nie, Y. Y.; Liu, Z.; Huang, S. X.; Shen, H. Y.; Cui, J. Z.; Gao, H. L., Luminescence and magnetocaloric effect of Ln clusters (Ln = Eu, Gd, Tb, Er) bridged by CO deriving from the spontaneous fixation of carbon dioxide in the atmosphere. Inorganic Chemistry Frontiers 2018, 5 (2), 394-402.

48. Gao, H. L.; Huang, S. X.; Zhou, X. P.; Liu, Z.; Cui, J. Z., Magnetic properties and structure of tetranuclear lanthanide complexes based on 8-hydroxylquinoline Schiff base derivative and β-diketone coligand. Dalton Transactions 2018, 47 (10), 3503-3511.

49. Gao, H. L.; Zhou, X. P.; Bi, Y. X.; Shen, H. Y.; Wang, W. M.; Wang, N. N.; Chang, Y. X.; Zhang, R. X.; Cui, J. Z., A Dy4 single-molecule magnet and its Gd(), Tb(), Ho(), and Er() analogues encapsulated by an 8-hydroxyquinoline Schiff base derivative and a-diketonate coligand. Dalton Transactions 2017, 46 (14), 4669-4677.

50. Li, X. L.; Li, F. C.; Zhang, X. L.; Liu, Y. F.; Wang, A. L.; Tian, J. F.; Xiao, H. P., Synthesis, crystal structures and magnetic properties of two tetranuclear lanthanide-hydroxo cubane clusters. Synthetic Met 2015, 209, 220-224.

51. Lin, S. Y.; Sun, B. D.; Xu, Z. K., Syntheses, structures and magnetic properties of chiral lanthanide tetrahedral clusters supported by symmetrical amidate ligands. Inorg Chim Acta 2017, 464, 119-124.

52. Luan, F.; Yan, P. F.; Zhu, J.; Liu, T. Q.; Zoua, X. Y.; Li, G. M., A salen-type Dy single-molecule magnet with an enhanced energy barrier and its analogues. Dalton Transactions 2015, 44 (9), 4046-4053.

53. Pajerowski, D. M.; Li, Q.; Hyun, J.; Dennis, C. L.; Phelan, D.; Yan, P. F.; Chen, P.; Li, G. M., Chloride-bridged, defect-dicubane {Ln} core clusters: syntheses, crystal structures and magnetic properties. Dalton Transactions 2014, 43 (31), 11973-11980.

54. Zhang, H. F.; Zhang, J.; Li, Y. H.; Qin, Y. R.; Chen, Y. M.; Liu, W.; Gao, D. D.; Li, W., A series of tetranuclear [Ln] clusters with defect-dicubane cores including a Dy single-molecule magnet. J Coord Chem 2015, 68 (16), 2798-2809.

55. Feng, W. X.; Zhang, Y.; Zhang, Z.; Lü, X. Q.; Liu, H.; Shi, G. X.; Zou, D.; Song, J. R.; Fan, D. D.; Wong, W. K.; Jones, R. A., Anion-Induced Self-Assembly of Luminescent and Magnetic Homoleptic Cyclic Tetranuclear Ln(Salen) and Ln(Salen) Complexes (Ln = Nd, Yb, Er, or Gd). Inorganic Chemistry 2012, 51 (21), 11377-11386.

56. Sukhikh, T. S.; Bashirov, D. A.; Kuratieva, N. V.; Smolentsev, A. I.; Bogomyakov, A. S.; Burilov, V. A.; Mustafina, A. R.; Zibarev, A. V.; Konchenko, S. N., New NIR-emissive tetranuclear Er(III) complexes with 4-hydroxo-2,1,3-benzothiadiazolate and dibenzoylmethanide ligands: synthesis and characterization. Dalton Transactions 2015, 44 (12), 5727-5734.

57. Zhao, J. Y.; Yang, C.; Bian, X. Y.; Qiu, J.; Ren, S. Y.; Fang, M., A tetranuclear Er(III)-based cluster with bifunctional properties: Efficient conversion of CO2 and slow magnetic relaxation behavior. Inorg Chim Acta 2023, 556, 121560.

58. Koo, B. H.; Lim, K. S.; Ryu, D. W.; Lee, W. R.; Koh, E. K.; Hong, C. S., A unique tetranuclear Er-4(III) cluster exhibiting field-induced single-molecule magnetism. Chem Commun 2012, 48 (19), 2519-2521.

59. Bramwell, S. T.; Gingras, M. J. P., Spin Ice State in Frustrated Magnetic Pyrochlore Materials. Science 2001, 294 (5546), 1495-1501.

60. Feigel'man, M. V.; Ioffe, L. B.; Geshkenbein, V. B.; Dayal, P.; Blatter, G., Superconducting tetrahedral quantum bits. Phys Rev Lett 2004, 92 (9), 098301.

61. Facer, C.; Twamley, J.; Cresser, J., Quantum Cayley networks of the hypercube. Phys Rev A 2008, 77 (1), 012334.

62. Saha, D.; Iyengar, S. S.; Richerme, P.; Smith, J. M.; Sabry, A., Mapping Quantum Chemical Dynamics Problems to Spin-Lattice Simulators. Journal of Chemical Theory and Computation 2021, 17 (11), 6713-6732.

63. Rosiak, D.; Okuniewski, A.; Chojnacki, J., Novel complexes possessing Hg–(Cl, Br, I)···OC halogen bonding and unusual Hg2S2(Br/I)4 kernel. The usefulness of τ4′ structural parameter. Polyhedron 2018, 146, 35-41.

64. Okuniewski, A.; Rosiak, D.; Chojnacki, J.; Becker, B., Coordination polymers and molecular structures among complexes of mercury(II) halides with selected 1-benzoylthioureas. Polyhedron 2015, 90, 47-57.

65. Yang, L.; Powell, D. R.; Houser, R. P., Structural variation in copper(i) complexes with pyridylmethylamide ligands: structural analysis with a new four-coordinate geometry index, τ4. Dalton Transactions 2007, (9), 955-964.

66. Hilgar, J. D.; Butts, A. K.; Rinehart, J. D., A method for extending AC susceptometry to long-timescale magnetic relaxation. Phys Chem Chem Phys 2019, 21 (40), 22302-22307.

67. Blackmore, W. J. A.; Gransbury, G. K.; Evans, P.; Kragskow, J. G. C.; Mills, D. P.; Chilton, N. F., Characterisation of magnetic relaxation on extremely long timescales. Phys Chem Chem Phys 2023, 25 (25), 16735-16744.

68. Hilgar, J. D.; Flores, B. S.; Rinehart, J. D., Ferromagnetic coupling in a chloride-bridged erbium single-molecule magnet. Chem Commun 2017, 53 (53), 7322-7324.

69. Xue, T. J.; Ding, Y. S.; Reta, D.; Chen, Q. W.; Zhu, X. F.; Zheng, Z. P., Closely Related Organometallic Er(III) Single-Molecule Magnets with Sizably Different Relaxation Times of Quantum Tunneling of Magnetization. Cryst Growth Des 2023, 23 (1), 565-573.

70. Chen, S.-M.; Xiong, J.; Zhang, Y.-Q.; Yuan, Q.; Wang, B.-W.; Gao, S., A soft phosphorus atom to "harden" an erbium(iii) single-ion magnet. Chem Sci 2018, 9 (38), 7540-7545.

71. Meng, Y.-S.; Wang, C.-H.; Zhang, Y.-Q.; Leng, X.-B.; Wang, B.-W.; Chen, Y.-F.; Gao, S., (Boratabenzene)(cyclooctatetraenyl) lanthanide complexes: a new type of organometallic single-ion magnet. Inorganic Chemistry Frontiers 2016, 3 (6), 828-835.

72. Ungur, L.; Le Roy, J. J.; Korobkov, I.; Murugesu, M.; Chibotaru, L. F., Fine-tuning the Local Symmetry to Attain Record Blocking Temperature and Magnetic Remanence in a Single-Ion Magnet**. Angew Chem Int Edit 2014, 53 (17), 4413-4417.

73. Le Roy, J. J.; Ungur, L.; Korobkov, I.; Chibotaru, L. F.; Murugesu, M., Coupling Strategies to Enhance Single-Molecule Magnet Properties of Erbium–Cyclooctatetraenyl Complexes. J Am Chem Soc 2014, 136 (22), 8003-8010.

74. Le Roy, J. J.; Korobkov, I.; Murugesu, M., A sandwich complex with axial symmetry for harnessing the anisotropy in a prolate erbium(iii) ion. Chem Commun 2014, 50 (13), 1602-1604.

75. Meihaus, K. R.; Long, J. R., Magnetic Blocking at 10 K and a Dipolar-Mediated Avalanche in Salts of the Bis(η8-cyclooctatetraenide) Complex [Er(COT)2]−. J Am Chem Soc 2013, 135 (47), 17952-17957.

76. Aquilante, F.; Autschbach, J.; Baiardi, A.; Battaglia, S.; Borin, V. A.; Chibotaru, L. F.; Conti, I.; De Vico, L.; Delcey, M.; Fdez. Galván, I.; Ferré, N.; Freitag, L.; Garavelli, M.; Gong, X.; Knecht, S.; Larsson, E. D.; Lindh, R.; Lundberg, M.; Malmqvist, P. Å.; Nenov, A.; Norell, J.; Odelius, M.; Olivucci, M.; Pedersen, T. B.; Pedraza-González, L.; Phung, Q. M.; Pierloot, K.; Reiher, M.; Schapiro, I.; Segarra-Martí, J.; Segatta, F.; Seijo, L.; Sen, S.; Sergentu, D.-C.; Stein, C. J.; Ungur, L.; Vacher, M.; Valentini, A.; Veryazov, V., Modern quantum chemistry with [Open]Molcas. The Journal of Chemical Physics 2020, 152 (21), 214117.

77. Fdez. Galván, I.; Vacher, M.; Alavi, A.; Angeli, C.; Aquilante, F.; Autschbach, J.; Bao, J. J.; Bokarev, S. I.; Bogdanov, N. A.; Carlson, R. K.; Chibotaru, L. F.; Creutzberg, J.; Dattani, N.; Delcey, M. G.; Dong, S. S.; Dreuw, A.; Freitag, L.; Frutos, L. M.; Gagliardi, L.; Gendron, F.; Giussani, A.; González, L.; Grell, G.; Guo, M.; Hoyer, C. E.; Johansson, M.; Keller, S.; Knecht, S.; Kovačević, G.; Källman, E.; Li Manni, G.; Lundberg, M.; Ma, Y.; Mai, S.; Malhado, J. P.; Malmqvist, P. Å.; Marquetand, P.; Mewes, S. A.; Norell, J.; Olivucci, M.; Oppel, M.; Phung, Q. M.; Pierloot, K.; Plasser, F.; Reiher, M.; Sand, A. M.; Schapiro, I.; Sharma, P.; Stein, C. J.; Sørensen, L. K.; Truhlar, D. G.; Ugandi, M.; Ungur, L.; Valentini, A.; Vancoillie, S.; Veryazov, V.; Weser, O.; Wesołowski, T. A.; Widmark, P.-O.; Wouters, S.; Zech, A.; Zobel, J. P.; Lindh, R., OpenMolcas: From Source Code to Insight. Journal of Chemical Theory and Computation 2019, 15 (11), 5925-5964.

78. Manni, G. L.; Galván, I. F.; Alavi, A.; Aleotti, F.; Aquilante, F.; Autschbach, J.; Avagliano, D.; Baiardi, A.; Bao, J. J.; Battaglia, S.; Birnoschi, L.; Blanco-González, A.; Bokarev, S. I.; Broer, R.; Cacciari, R.; Calio, P. B.; Carlson, R. K.; Couto, R. C.; Cerdán, L.; Chibotaru, L. F.; Chilton, N. F.; Church, J. R.; Conti, I.; Coriani, S.; Cuéllar-Zuquin, J.; Daoud, R. E.; Dattani, N.; Decleva, P.; de Graaf, C.; Delcey, M. G.; De Vico, L.; Dobrautz, W.; Dong, S. J. S.; Feng, R. L.; Ferré, N.; Filatov, M.; Gagliardi, L.; Garavelli, M.; González, L.; Guan, Y. F.; Guo, M. Y.; Hennefarth, M. R.; Hermes, M. R.; Hoyer, C. E.; Huix-Rotllant, M.; Jaiswal, V. K.; Kaiser, A.; Kaliakin, D. S.; Khamesian, M.; King, D. S.; Kochetov, V.; Krosnicki, M.; Kumaar, A. A.; Larsson, E. D.; Lehtola, S.; Lepetit, M. B.; Lischka, H.; Ríos, P. L.; Lundberg, M.; Ma, D. X.; Mai, S.; Marquetand, P.; Merritt, I. C. D.; Montorsi, F.; Mörchen, M.; Nenov, A.; Nguyen, V. H. A.; Nishimoto, Y.; Oakley, M. S.; Olivucci, M.; Oppel, M.; Padula, D.; Pandharkar, R.; Phung, Q. M.; Plasser, F.; Raggi, G.; Rebolini, E.; Reiher, M.; Rivalta, I.; Roca-Sanjuán, D.; Romig, T.; Safari, A. A.; Sánchez-Mansilla, A.; Sand, A. M.; Schapiro, I.; Scott, T. R.; Segarra-Martí, J.; Segatta, F.; Sergentu, D. C.; Sharma, P.; Shepard, R.; Shu, Y. N.; Staab, J. K.; Straatsma, T. P.; Sorensen, L. K.; Tenorio, B. N. C.; Truhlar, D. G.; Ungur, L.; Vacher, M.; Veryazov, V.; Voss, T. A.; Weser, O.; Wu, D. H.; Yang, X. C.; Yarkony, D.; Zhou, C.; Zobel, J. P.; Lindh, R., The OpenMolcas: A Community-Driven Approach to Advancing Computational Chemistry. Journal of Chemical Theory and Computation 2023, 19 (20), 6933-6991.

79. Largent, R. J.; Polik, W. F.; Schmidt, J. R., Symmetrizer: Algorithmic determination of point groups in nearly symmetric molecules. J Comput Chem 2012, 33 (19), 1637-1642.

80. Polik, W. F.; Schmidt, J. R., WebMO: Web-based computational chemistry calculations in education and research. Wires Comput Mol Sci 2022, 12 (1), 1-22.

81. Catalan, E., Mémoire sur la théorie des polyèdres. Journal de l'École Polytechnique 1865, 24, 1-71.

82. Ungur, L.; Thewissen, M.; Costes, J.-P.; Wernsdorfer, W.; Chibotaru, L. F., Interplay of Strongly Anisotropic Metal Ions in Magnetic Blocking of Complexes. Inorganic Chemistry 2013, 52 (11), 6328-6337.

83. Hamming, R. W., Error Detecting and Error Correcting Codes. Bell Syst Tech J 1950, 29 (2), 147-160.

84. Coxeter, H. S. M., Regular Polytopes. Dover Publications, 1973.